DEPARTMENT OF ELECTRICAL AND COMPUTER ENGINEERING

NUMERICAL SIMULATION OF HELIUM ATMOSPHERIC PRESSURE PLASMA

CONSTANTINOS LAZAROU

A dissertation submitted to the University of Cyprus in partial fulfillment of the requirements for the degree of Doctor of Philosophy

April 2019

VALIDATION PAGE

Doctoral Candidate: **Constantinos Lazarou**

Doctoral Thesis Title: **Numerical simulation of helium atmospheric pressure plasma.**

The present Doctoral Dissertation was submitted in partial fulfillment of the requirements for the degree of Doctor of Philosophy at the ***Department of Electrical and Computer Engineering*** *and was approved on the 15th of April 2019 by the members of the* ***Examination Committee.***

Examination Committee:

Research Supervisor:

Prof. George E. Georghiou

Committee Chair:

Prof. Stavros Iezekiel

Committee Member:

Prof. Marcos Antoniades

Committee Member:

Prof. Triantafyllos Stylianopoulos

Committee Member:

Prof. George Naidis

DECLARATION OF DOCTORAL CANDIDATE

The present doctoral dissertation was submitted in partial fulfillment of the requirements for the degree of Doctor of Philosophy of the University of Cyprus. It is a product of original work of my own, unless otherwise mentioned through references, notes, or any other statements.

Constantinos Lazarou [Full Name of Doctoral Candidate]

……..[Signature]

Abstract

Helium dielectric barrier discharges (DBD) operated at atmospheric pressure and low temperature have gained tremendous attention in the last years, due to low production costs and wide range of applications such as plasma medicine, surface modification, sterilization etc. The ability of DBD plasma sources to have such a diverse set of applications arises from the wide range of reactive species, ions, high electric fields and UV photons they can generate. In such discharges, the presence of air impurities is unavoidable and should be considered as it significantly affects the plasma composition and consequently the discharge evolution. Deep understanding of the physics behind helium discharges, how the fundamental processes are affected by the presence of air impurities and how plasma interacts with surfaces is a prerequisite for the optimization and stabilization of helium DBD devices.

In this work, an accurate numerical model has been developed which is able to describe helium DBD in the presence of the dominant air constituents, i.e. nitrogen, oxygen and water. Due to the high complexity of the model, its development is split into three steps, starting with a simple model (pure Helium) and then upgrading it by adding more details (N_2 then O_2 and subsequently water species). At each step, the simulation model is validated with experimental results, in order to ensure its correctness. This systematic and gradual methodology provides confidence for the validity of the developed model. For each model, the level of air contaminants was varied, and the effect of air contaminants on the evolution of the discharge, reaction kinetics, discharge characteristics and important ion species are investigated. The results clearly demonstrate that the plasma chemistry and consequently the discharge evolution is significantly affected by the concentration level of air contaminants in the mixture. In this study, for the first time a reasonable explanation is given for the well-known rule of thumb that low concentration of air helps the ignition of the helium DBD, while higher levels stop the discharge ignition. Subsequently, the validated model which considers helium, nitrogen and oxygen species, is used to numerically investigate a helium atmospheric pressure plasma jet (APPJ) device with and without the presence of oxygen admixtures and its interaction with a dielectric surface. Oxygen admixtures are important for biomedical applications of helium APPJ where it has been observed that a small amount of oxygen in the helium gas increases its effectiveness against cancer cells. Through this

work, new insight is gained into the fundamental processes of helium APPJ, the effect of the presence of oxygen admixtures and its interaction with dielectric surfaces. For example the model gives an explanation as to why the helium plasma jet has a torus/ring like shape and it also explains why the addition of oxygen admixtures causes the plasma bullet to change to a sphere like shape. The shape of the plasma bullet plays a crucial role in its interaction with the surface. If the plasma bullet has a torus like shape, this means that the plasma parameters take their maximum values off axis. On the other hand, if the plasma bullet has a sphere like shape means that the plasma parameters take their maximum values on the axis of symmetry. However, for potential applications, it is preferred to have maximum of plasma parameters at the point of interaction. For the plasma jet the point of interaction is the axis of symmetry. For that reason, the sphere like shape of the plasma bullet is preferable for applications. Furthermore, the model shows how a low level of oxygen impurities increases the induced electric field (IEF) on the dielectric surface, which is very important for biomedical applications of helium plasma jets.

Περίληψη

Οι απορρίψεις διηλεκτρικού φραγμού ηλίου (DBD) που λειτουργούν σε ατμοσφαιρική πίεση και χαμηλή θερμοκρασία έχουν κερδίσει μεγάλη προσοχή τα τελευταία χρόνια, λόγω του χαμηλού κόστους παραγωγής τους και του μεγάλου εύρους εφαρμογών τους. Μερικές από τις εφαρμογές τους βρίσκονται στους τομείς της ιατρική πλάσματος, της τροποποίησης επιφανειών, της αποστείρωσης επιφανίων κλπ. Η ικανότητα τους να έχουν ένα τόσο ευρύ φάσμα εφαρμογών, έγκειται στο γεγονός ότι παράγουν μία μεγάλη ποικιλία αντιδραστικών ειδών, φορτισμένων σωματιδίων, υψηλών ηλεκτρικών πεδίων και υπεριώδους ακτινοβολίας. Ωστόσο, σε τέτοιες απορρίψεις η παρουσία σωματιδίων αέρα στο αέριο ηλίου είναι αναπόφευκτη, και πρέπει να λαμβάνεται υπόψη καθώς επηρεάζει σημαντικά την χημεία του πλάσματος και κατά συνέπεια την εξέλιξη της απόρριψης. Η βαθιά κατανόηση της φυσικής πίσω από τις απορρίψεις ήλιου, του τρόπου με τον οποίο οι θεμελιώδεις διεργασίες επηρεάζονται από την παρουσία προσμίξεων του αέρα και πώς το πλάσμα αλληλοεπιδρά με τις επιφάνειες αποτελεί σημαντική προϋπόθεση για τη βελτιστοποίηση και σταθεροποίηση αυτών συσκευών.

Σε αυτή την διατριβή, ένα ακριβές αριθμητικό μοντέλο έχει αναπτυχθεί προκειμένου να μοντελοποιεί απορρίψεις ηλίου στην παρουσία των κυριάρχων σωματιδίων του αέρα (δηλ. αζώτου, οξυγόνου και νερού). Λόγο της πολυπλοκότητας του μοντέλου, η ανάπτυξη του χωρίστηκε σε τρία στάδια, αρχίζοντας από ένα απλό μοντέλο (καθαρό ήλιο) και στην συνέχεια αναβαθμίζοντας το προσθέτων τας σε αυτό τα κυρίαρχα συστατικά του αέρα (N_2, O_2 και H_2O). Σε κάθε στάδιο, κρίθηκε απαραίτητο το μοντέλο να επαληθεύεται με πειραματικά αποτελέσματα προκειμένου να διασφαλίζεται η ορθότητα του. Η συστηματική και βαθμιαία αυτή μεθοδολογία, προσδίδει εμπιστοσύνη στην εγκυρότητα της ανάπτυξης του μοντέλου. Επιπλέον, σε κάθε στάδιο, τα επίπεδα των σωματιδίων που εισάγονταν στο μοντέλο (ως προσμίξεις) μεταβάλλονταν και η επίδραση τους στην εξέλιξη της απόρριψης, στην χημεία του πλάσματος, στα ηλεκτρικά χαρακτηριστικά της απόρριψης και στην δημιουργία ιόντων στο μίγμα διερευνήθηκαν. Τα αποτελέσματα έδειξαν ότι η χημεία του πλάσματος και κατά συνέπεια η εξέλιξη της απόρριψης επηρεάζεται σημαντικά από τα επίπεδα συγκέντρωσης των σωματιδίων του αέρα στο μείγμα. Σε αυτή τη μελέτη, για πρώτη φορά έχει δοθεί εξήγηση πίσω από το γνωστό φαινόμενο ότι η χαμηλή συγκέντρωση αέρα βοηθά στην ανάφλεξη της απόρριψης ηλίου, ενώ υψηλότερα επίπεδα

σταματούν την ανάφλεξη της απόρριψης ηλίου. Στην συνέχεια, το επικυρωμένο μοντέλο (το οποίο λαμβάνει υπόψη τα είδη ηλίου, αζώτου και οξυγόνου) χρησιμοποιήθηκε για να διερευνήσει αριθμητικά μια συσκευή πίδακα πλάσματος ηλίου η οποία λειτουργεί σε ατμοσφαιρική πίεση (APPJ) με και χωρίς την παρουσία προσμείξεων οξυγόνου και την αλληλεπίδρασή της με μια διηλεκτρική επιφάνεια. Οι προσμίξεις οξυγόνου είναι σημαντικές για τις βιοϊατρικές εφαρμογές του πίδακα πλάσματος ηλίου αφού έχει παρατηρηθεί ότι μικρή ποσότητα οξυγόνου στο αέριο ηλίου αυξάνει την αποτελεσματικότητα του στην καταπολέμηση των καρκινικών κυττάρων. Μέσα από αυτή την μελέτη, αποκτήθηκε νέα γνώση πίσω από τις βασικές ιδιότητες του πίδακα πλάσματος ηλίου, η επίδραση των προσμείξεων οξυγόνου στην λειτουργία του και η αλληλεπίδραση του πίδακα πλάσματος με διηλεκτρικές επιφάνειες. Για παράδειγμα το μοντέλο έδωσε ερμηνεία γιατί το σχήμα της σφαίρας πλάσματος (για τον πίδακα πλάσματος ηλίου) έχει σχήμα δακτυλίου ενώ όταν προστεθεί οξυγόνο στο μίγμα το σχήμα της σφαίρας πλάσματος γίνεται σφαιρικό. Το σχήμα της σφαίρας πλάσματος παίζει σημαντικό ρόλο στην αλληλεπίδραση της με την επιφάνεια. Εάν η σφαίρα πλάσματος έχει σχήμα τόρου, αυτό σημαίνει ότι οι παράμετροι του πλάσματος λαμβάνουν τις μέγιστες τιμές εκτός άξονα συμμετρίας. Από την άλλη πλευρά, αν η σφαίρα πλάσματος έχει σφαιρικό σχήμα αυτό σημαίνει ότι οι παράμετροι του πλάσματος λαμβάνουν τις μέγιστες τιμές τους στον άξονα συμμετρίας. Ωστόσο, για πιθανές εφαρμογές, προτιμάται οι μέγιστες τιμές των παραμέτρων του πλάσματος να επιτυγχάνονται στο σημείο της αλληλεπίδρασης. Για τον πίδακα πλάσματος το σημείο αλληλεπίδρασης είναι ο άξονας συμμετρίας. Για το λόγο αυτό, προτιμάται το σφαιρικό σχήμα της σφαίρας πλάσματος για εφαρμογές. Επιπλέον, το μοντέλο δείχνει πώς ένα χαμηλό επίπεδο προσμείξεων οξυγόνου αυξάνει το διεγειρόμενο ηλεκτρικό πεδίο (IEF) στην διηλεκτρική επιφάνεια, το οποίο είναι πολύ σημαντικό για βιοϊατρικές εφαρμογές πιδάκων πλάσματος ηλίου.

List of publications

Dissertation journal articles

[1] **Lazarou C**, Chiper A S, Anastassiou C, Topala I, Mihaila I, Pohoata V and Georghiou G E 2019 Numerical simulation of the effect of water admixtures on the evolution of a helium/dry air discharge *J. Phys. D. Appl. Phys.* **52** 195203

[2] **Lazarou C**, Anastassiou C, Topala I, Chiper A S, Mihaila I, Pohoata V and Georghiou G E 2018 Numerical simulation of a capillary helium and helium-oxygen atmospheric pressure plasma jet: propagation dynamics and interaction with dielectric *Plasma Sources Sci. Technol.* **27** 105007

[3] **Lazarou C**, Belmonte T, Chiper A S and Georghiou G E 2016 Numerical modelling of the effect of dry air traces in a helium parallel plate dielectric barrier discharge *Plasma Sources Sci. Technol.* **25** 055023

[4] **Lazarou C**, Koukounis D, Chiper A S, Costin C, Topala I and Georghiou G E 2015 Numerical modeling of the effect of the level of nitrogen impurities in a helium parallel plate dielectric barrier discharge *Plasma Sources Sci. Technol.* **24** 035012

Dissertation conference papers

[1] **Lazarou C**, Anastassiou C, Topala I, Chiper AS, Mihaila I, Pohoaţa V and Georghiou G E 2019 The effect of oxygen admixtures on the electric field induced by an atmospheric pressure helium plasma jet *6th International Workshop on Plasma for Cancer Treatment*

[2] Anastassiou C, **Lazarou C**, Mihai C,Topala I, Chiper A S, Mihaila I, Pohoaţa V and Georghiou G E 2019 Helium Atmospheric Plasma Jet Treating Breast Cancer Cells *6th International Workshop on Plasma for Cancer Treatment*

[3] **Lazarou C**, Anastassiou C, Topala I, Chiper AS, Mihaila I, Pohoaţa V and Georghiou G E 2019 On the plasma bullet shape of He and He/O_2 capillary plasma jet devices and interaction with dielectric surface *DPG conference in München*

[4] **Lazarou C**, Anastassiou C, Topala I, Chiper AS, Mihaila I, Pohoaţa V and Georghiou G E 2018 Numerical modelling of the effect of water admixtures in a helium/air parallel plate dielectric barrier discharge *24th Europhysics Conference on Atomic and Molecular Physics of Ionized Gases*

[5] Anastassiou C, **Lazarou C**, Topala I, Mihaila I, Chiper AS, Pohoata V and Georghiou G E 2018 Capillary He and He-O_2 plasma jet simulation and experimental data 7th *International Conference on Plasma Medicine*

[6] Anastassiou C, **Lazarou C**, Mihai C T, Topala I and Georghiou G E 2018 Helium atmospheric pressure plasma jet aiding chemotherapy for the treatment of breast cancer 7th *International Conference on Plasma Medicine*

[7] **Lazarou C**, Anastassiou C, Klute F D, Franzke J and Georghiou G E 2017 The influence of air impurities on the evolution of plasma species in a capillary helium plasma jet *33th International Conference on Phenomena in Ionized Gases*

[8] **Lazarou C**, Chiper A S, Anastassiou C, Pohoata V, Mihaila I, Topala I and Georghiou G E 2017 Numerical and experimental investigation of the effect of N_2 and O_2 admixtures in a helium dielectric barrier discharge *17th international conference on plasma physics and applications*

[9] Anastassiou C, **Lazarou C**, Chiper A S, Pohoata V, Mihaila I, Topala I and Georghiou G E 2017 Understanding the bullet evolution and its interaction with dielectrics in a capillary helium plasma jet *17th international conference on plasma physics and applications*

[10] Anastassiou C, Charalambous N, **Lazarou C** and Georghiou G E 2017 Numerical study of electroporation of cells by helium atmospheric pressure plasma jet *Electroporation-Based Technologies and Treatments*

[11] **Lazarou C**, Anastassiou C, Topala I, Chiper A S, Mihaila I, Pohoata V and Georghiou G E 2017 The effect of oxygen impurities of helium atmospheric pressure plasma jet on the redox chemistry of cells *6th Young Professionals Workshop on Plasma Medicine*

[12] **Lazarou C** and Georghiou G E 2016 Investigation of the influence of electron impact cross section from different databases on the simulation results of helium barrier discharge with dry air impurities *23th Europhysics Conference on Atomic and Molecular Physics of Ionized Gases*

[13] **Lazarou C**, Anastassiou C and Georghiou G E 2016 Numerical investigation of the electric field produced by the interaction of helium plasma jet with normal and cancer cells *6th International Conference on Plasma Medicine*

[14] **Lazarou C**, Jijie R, Pohoata V, Mihaila I, Topala I and Georghiou G E 2014 Numerical investigation of the influence of nitrogen impurity levels on the dielectric barrier discharge in helium *22th Europhysics Conference on Atomic and Molecular Physics of Ionized Gases*

[15] Demeter A, **Lazarou C**, Jijie R, Nastuta A V, Pohoata V, Mihaila I, Georghiou E G and Topala I 2013 Experimental investigation and modeling of atmospheric pressure helium plasma jet for direct treatment of living tissues *16th international conference on plasma physics and applications*

Table of Contents

1. **Introduction** **1**

1.1 Introduction 1

1.2 Motivation, objectives and general methodology 4

1.3 General assumptions 9

1.4 Novelty 10

1.5 Outline of the proposal 11

2. **Simulation model** **12**

2.1 Introduction 12

2.2 Model selection 12

2.3 Plasma fluid model (PFM) 16

2.4 Boundary conditions of the plasma fluid model 20

2.5 Gas dynamic model (GDM) 21

2.6 Boundary conditions of the gas dynamic model 23

2.7 Simulation procedure 24

3. **Simulation model of a helium-nitrogen mixture** **26**

3.1 Introduction 26

3.2 Experimental setup and computational domain 27

3.3 Input parameters for the model 28

3.4 Results and discussion 31

3.4.1 Model Validation 31

3.4.1 Effect of Nitrogen impurity levels 34

3.5 Conclusions 44

4. **Simulation model of a helium-nitrogen-oxygen mixture** **45**

4.1 Introduction 45

4.2 Experimental setup 45

4.3 Input parameters for the model 46

4.4 Results and discussion 50

4.4.1 Model validation 51

4.4.2 Effect of dry air concentration in helium DBD 52
4.4.3 150 ppm level of air impurity 53
4.4.4 Effect of air concentration on the most important reactions for ion production 63
4.4.5 Influence of air concentration on the discharge ignition and symmetry 67
4.5 Conclusions 72

5. **Simulation model of a helium-nitrogen-oxygen-water mixture 73**
5.1 Introduction 73
5.2 Experimental setup 73
5.3 Input parameters for the model 76
5.4 Results and discussion 79
5.4.1 Comparison of the simulation model with the experimental results 79
5.4.2 Effect of water admixtures on the discharge characteristics of a He/dry air (500 ppm) DBD 81
5.4.3 Effect of water admixtures on the ion composition of a He/dry air (500 ppm) DBD 84
5.5 Conclusions 90

6. **Capillary He and He/O_2 plasma jet: simulations and experimental validation 91**
6.1 Introduction 91
6.2 Experimental setup 92
6.3 Model 94
6.4 Input parameters for the model 95
6.5 Results and discussion 97
6.5.1 Comparison of the simulation model with the experiment for a He and He+O2 (1000 ppm) plasma jet 99
6.6 Conclusions 105

7. **Numerical simulation of a capillary helium and helium-oxygen atmospheric pressure plasma jet: propagation dynamics and interaction with dielectric 106**
7.1 Introduction 106
7.2 Experimental Setup 106
7.3 Experimental results 108
7.4 Analysis of the simulation results 109
7.4.1 Evolution of the pure helium plasma jet 110
7.4.2 Evolution of the He+O_2 (1000 ppm) plasma jet 117

7.4.3 Effects of different level of oxygen admixtures on the plasma evolution and interaction with the dielectric surface 124

7.5 Conclusions 126

8. **Conclusions and Future work** **128**

8.1 Conclusions 128

8.2 Future Work 131

9. **Appendix A: Rate coefficients for helium and nitrogen reactions and mesh independency analysis.** **132**

10. **Appendix B: Rate coefficients for helium, nitrogen and oxygen reactions.** **134**

11. **Appendix C: Rate coefficients for helium, nitrogen, oxygen and water reactions.** **139**

12. **Appendix D: Rate coefficients for helium, nitrogen and oxygen reactions.** **147**

13. **Appendix E: Supplementary simulation results for the plasma jet** **150**

14. **References** **154**

List of Figures

Figure 1: Four states of matter. 2

Figure 2: DBD-based plasma devices: (a) coplanar parallel plate configuration with plasma generated between the two dielectrics; (b) pin to plane configuration with plasma generated between the pin and the dielectric; (c) plasma jet with two metal ring electrodes outside the tube, the plasma is generated inside dielectric tube; (d) plasma jet with one metal electrode outside and a concentric needle electrode inside, the plasma is generated inside the dielectric tube. The blue colour shows the surface being treated, the black colour indicates the electrodes and the grey colour indicates the dielectric. 4

Figure 3: Schematic diagram presenting the process of the model development. 7

Figure 4: Schematic diagram presenting the fundamental equations governing the plasma behaviour. 13

Figure 5: Schematic diagram presenting the procedure for the plasma model selection. 15

Figure 6: Schematic diagram summarizing the simulation model procedure. 25

Figure 7: Simulation domain. 28

Figure 8: Comparison of the different EEDFs as a function of electron energy, with temperature = 350 K, electron density = 10^{18} m^{-3} and mole fraction of He_m* = 10^{-7}. 31

Figure 9: Simulation and experimental current and applied voltage as a function of time. The amplitude, frequency and rise time of the applied voltage are 3 kV, 2 kHz and 33 μs respectively. 32

Figure 10: Simulated current as a function of time for three different ionization degrees: 10^{-2}, 10^{-4} and 10^{-7}, with temperature = 350 K, electron density = 10^{18} m^{-3} and mole fraction of He_m* = 10^{-7}. 33

Figure 11: Comparison between the experimental and simulation applied voltage and current (a) as obtained in [63] and (b) obtained by our simulation model for 100 ppm N_2. The amplitude and frequency of the applied voltage are 3 kV and 25 kHz respectively. 34

Figure 12: Temporal variation of the simulated spatial averaged plasma properties for a He-N_2 mixture (1 ppm of N_2) over a voltage cycle. The amplitude, frequency and rise time of the applied voltage are 3 kV, 2 kHz and 33 μs respectively. 36

Figure 13: Simulation of the average reaction rates for (a) the production and (b) the destruction of He_2^+ as a function of time for 1 ppm nitrogen impurities. 40

Figure 14: Simulation of the average reaction rates for (a) the production and (b) the destruction of N_2^+ as a function of time for 1 ppm nitrogen impurities. 40

Figure 15: Simulated (a) average concentration of charged species at breakdown, (b) discharge current and (c) breakdown voltage as a function of the level of nitrogen impurities. The amplitude, frequency and rise time of the applied voltage are 3 kV, 2 kHz and 33 μs respectively. 41

Figure 16: Comparison of the different EEDFs as a function of electron energy, at a mean electron energy of 4 eV. The legend represents the air content in the mixture. 49

Figure 17: Comparison between (a) the experimental results reported in [21] for atmospheric pressure DBD working in He (purity 99.999 vol%) and (b) our simulation results for DBD in He with 80 ppm air impurities. The black line represents the discharge current, the dashed red line the applied voltage, the dotted black line the gap voltage and the dashed dotted blue line the memory voltage. 52

Figure 18: Simulation results of (a) the applied voltage, gap voltage and discharge current, and (b-d) the spatially-temporally resolved density distribution of electrons, O_2^+ and absolute magnitude of the electric field respectively (150 ppm), over a voltage cycle. The amplitude and frequency of the applied voltage are 1 kV and 10 kHz respectively. 55

Figure 19: Simulation results of (a) the applied voltage, gap voltage, discharge current and average electron temperature, and (b) the average concentration of positive ion species for a He-air mixture (150 ppm) over a voltage cycle. The amplitude and frequency of the applied voltage are 1 kV and 10 kHz respectively. 57

Figure 20: Simulation of the average rates for (a) production and (b) destruction of O_2^+ as a function of time for 150 ppm dry air. 58

Figure 21: Schematic diagram of the most important reaction pathways for ion production. 59

Figure 22: Simulation result of (a) the applied voltage and discharge current, and (b) the average concentration of negative charge species for a He-air mixture (150 ppm) over a voltage cycle. The amplitude and frequency of the applied voltage are 1 kV and 10 kHz respectively. 61

Figure 23: Simulation of the average rates for (a) production and (b) destruction of electrons as a function of time for 150 ppm dry air. 63

Figure 24: Simulated (a) breakdown voltage and (b-d) peak of the average reaction rates as a function of the concentration of air. The amplitude and frequency of the applied voltage are 1 kV and 10 kHz respectively. 64

Figure 25: Simulation results of (a) the applied voltage, gap voltage and discharge current, (b) the average concentration of positive ion species, and (c) the average concentration of negative ion species for a He-air mixture (500 ppm) over a voltage cycle. The amplitude and frequency of the applied voltage are 1 kV and 10 kHz respectively. 68

Figure 26: Simulation results of (a) the applied voltage, gap voltage and discharge current, (b) the average concentration of electrons, and (c) the surface charge density for a He-air mixture (1100 ppm) over a voltage cycle. The amplitude and frequency of the applied voltage are 1 kV and 10 kHz respectively..... 71

Figure 27: Experimental configuration. 75

Figure 28: Stainless steel cylindrical chamber where the parallel plate BDB was inserted for operation. 75

Figure 29: Comparison between simulation and experimental discharge characteristics (current and voltage). 80

Figure 30: Simulation results of (a) the applied voltage and discharge current, and (b) the spatio-temporal evolution of the total ionization rate in logarithmic scale over a voltage cycle. 81

Figure 31: Simulation results of the discharge characteristics (applied voltage, gap voltage and discharge current) for (a) 50 ppm and (b) 500 ppm of water admixtures in a He/dry air (500 ppm) DBD. 82

Figure 32: Simulation results of the breakdown voltage, second peak of the gap voltage and amplitude of the discharge current at different levels of water in a He/dry air (500 ppm) DBD. The amplitude and frequency of the sinusoidal applied voltage are 2.5 kV peak to peak and 10 kHz respectively. 84

Figure 33: Simulation results of the surface charge density on the dielectrics at different levels of water admixtures (50, 500 and 1000 ppm) over a voltage cycle. The symbols B1 and B2 in the graph refer to the surface (contacted with the plasma) of dielectric layers which cover the ground contact and the contact of the applied voltage respectively. 84

Figure 34: Average concentrations of the positive ions during the breakdown, for different levels of water admixtures in the helium/dry air (500 ppm) discharge. The amplitude and frequency of the sinusoidal applied voltage are 2.5 kV peak to peak and 10 kHz respectively. 86

Figure 35: Schematic diagram of the most important reaction pathways for positive ion production. 86

Figure 36: Average concentrations of the electrons and the negative ions during the breakdown, for different levels of water admixtures in the helium/dry air (500 ppm) discharge. The amplitude and frequency of the sinusoidal applied voltage are 2.5 kV peak to peak and 10 kHz respectively. 87

Figure 37: Simulation results of the average reaction rates of electron production during the breakdown, for different levels of water admixtures in the helium/dry air (500 ppm) discharge. The amplitude and frequency of the sinusoidal applied voltage are 2.5 kV peak to peak and 10 kHz respectively. 88

Figure 38: Simulation results of the average reaction rates of electron destruction during the breakdown, for different levels of water admixtures in the helium/dry air (500 ppm) discharge. The amplitude and frequency of the sinusoidal applied voltage are 2.5 kV peak to peak and 10 kHz respectively. 89

Figure 39: Experimental arrangement. 93

Figure 40: Experimental configuration of the helium plasma jet interacting with a dielectric surface placed normal to the jet axis. 94

Figure 41: Axi-symmetric simulation domain for the gas and the plasma fluid model. 95

Figure 42: Optical emission spectra for (a) pure helium plasma jet and (b) He+O_2 (1000 ppm) plasma jet. 99

Figure 43: Helium−air mixing for the pure helium plasma jet. 100

Figure 44: Measured relative intensity distributions of He line at 706.5 nm (experiment, top), compared with calculated reaction rate for the transition of He($3s3S$) → $He2p3P$ (simulation, bottom) for He plasma jet. The edges of the capillary tube are marked out by a white thick line. The tube exit (z=0 mm), the dielectric surface (z=2 mm) and the axis of symmetry (r=0 mm) are marked out by a white and red dashed line respectively, and t=0 ns corresponds to the maximum of the emission intensity being at the tube exit. 101

Figure 45: Measured relative intensity distributions of He line at 706.5 nm (experiment, right), compared with calculated reaction rate for the transition of He($3s3S$) → $He2p3P$ (simulation, left) for He plasma jet at the z=1 mm plane. 101

Figure 46: Position of the measured maximum intensity at 706.5 nm and simulated peak of reaction rate for the transition of He($3s3S$) to He($2p3P$) for pure helium jet. Time 0 ns corresponds to the radiation intensity that coincides with the tube exit (z=0 mm)..... 102

Figure 47: Measured relative intensity distributions of He line at 706.5 nm (experiment, top), compared with calculated reaction rate for the transition of He($3s3S$) → $He2p3P$ (simulation, bottom) for He+O_2 (1000 ppm) plasma jet. The edges of the capillary tube are marked out by a white thick line. The tube exit (z=0 mm), the dielectric surface (z=2 mm) and the axis of symmetry (r=0 mm) are marked out by a white and red dashed line respectively, and t=0 ns corresponds to the maximum of the emission intensity being at the tube exit..... 103

Figure 48: Measured relative intensity distributions of He line at 706.5 nm (experiment, right), compared with calculated reaction rate for the transition of He($3s3S$) → $He2p3P$ (simulation, left) for He+O_2 (1000 ppm) plasma jet at the z=1 mm plane. 104

Figure 49: Position of the measured maximum intensity at 706.5 nm and simulated peak of reaction rate for the transition of He($3s3S$) to He($2p3P$) for He+O_2 (1000 ppm) jet. Time 0 ns corresponds to the radiation intensity that coincides with the tube exit (z=0 mm)..... 104

Figure 50. Experimental arrangement..... 107

Figure 51: Spatio-temporal evolution of the plasma bullet for (a) He and (b) He+O_2 (1000 ppm) plasma jet. Time 0 ns corresponds to the plasma bullet just about the exit of the tube. The three dashed lines indicate the axial distance from the tube nozzle for z=0, 1 and 2 mm..... 109

Figure 52: Helium-air mixture for the case of pure helium plasma jet obtained from the gas dynamic model. The white line shows the air at 1%. 110

Figure 53: Positions and corresponding times of the streamer head (total ionization rate) propagation for the He plasma jet. The time 0 ns corresponds to the streamer head coinciding with the tube exit (z=0 mm)..... 111

Figure 54: Simulation results of the spatio-temporal evolution of the total ionization rate (time snapshots as in Figure 53), for the He plasma jet. The total ionization rate has units of mol/m^3s. 112

Figure 55: Simulation results of electron production rate in logarithmic scale for the He plasma jet at time -152 ns..... 113

Figure 56: Simulation results of the secondary emission flux of electrons (SEFE) attributed to the different ions for the times (a) 121 ns and (b) 190 ns, for the He plasma jet. 115

Figure 57: Simulation results of the (a) surface charge density, (b) electric field in z direction (axial) and (c) electric field in radial direction during the propagation of the streamer, for the He plasma jet. 116

Figure 58: Simulation results of the spatio-temporal evolution of the total ionization rate along the dielectric surface (time snapshots as in Figure 53), for the He plasma jet. The total ionization rate has units of mol/m^3s..... 117

Figure 59: Positions and corresponding times of the streamer head (total ionization rate) propagation for the He+O_2 (1000 ppm) plasma jet. The time 0 ns corresponds to the streamer head coinciding with the tube exit (z=0 mm)..... 118

Figure 60: Simulation results of the spatio-temporal evolution of the total ionization rate (same time snapshots as in Figure 59), for He+O_2 (1000 ppm) plasma jet. The total ionization rate has units of mol/m^3s. 119

Figure 61: Simulation results of electron production rate in logarithmic scale for He+O_2 (1000 ppm) plasma jet at time – 181 ns. 120

Figure 62: Simulation results of secondary emission flux of electrons (SEFE) attributed to the different ions for the times (a) 163 ns and (b) 261 ns, for He+O_2 (1000 ppm) plasma jet. 121

Figure 63: Simulation results of the (a) surface charge density, (b) electric field in z direction and (c) electric field in r direction during the propagation of the streamer for He+O_2 (1000ppm) plasma jet..... 123

Figure 64: Simulation results of time snapshots of the total ionization rate of He+O_2 (1000 ppm) plasma jet, during the propagation of the streamer along the dielectric surface. The total ionization rate has units of mol/m^3s..... 124

Figure 65: Simulation results of the axial position of the streamer head as a function of time.. 125

Figure 66: Induced electric field on the dielectric surface at different level of oxygen admixtures. 126

Figure A1: Simulation results of the discharge current peak for different mesh densities. Mo represents the mesh density of 1000 elements in the plasma region. 133

Figure E1: Simulation results of the electron production rate for the He plasma jet at z=0.1 mm and time -152 ns (i.e. streamer head location at z=-0.75 mm, same time snapshot as Figure 51a). 150

Figure E2: Simulation results of the spatio-temporal evolution of the total ionization rate for He plasma jet without considering the Penning reactions in the kinetic scheme. 150

Figure E3: Simulation results of the electron production rate for the He plasma jet (a) at z=1 mm and time 0 ns (i.e. streamer head location at z=0 mm, same time snapshot as Figure 51c), (b) at z=1.85 and time 121 ns (i.e. streamer head location at z=1 mm, same time snapshot as Figure 51e). The dotted grey lines are a visual aid to highlight the peak shift between the two curves. 151

Figure E4: Simulation results of the spatio-temporal evolution of the total ionization rate for He plasma jet where the seec is set to zero..... 151

Figure E5: Simulation results of the electron production rate for the He+O_2 (1000ppm) plasma jet at z=0.1 mm and time -181 ns (i.e. plasma bullet location z= -0.75 mm, same time snapshot as Figure 57a). 152

Figure E6: Simulation results of the electron production rate for the He+O_2 (1000 ppm) plasma jet (a) at z=1 mm and time 0 ns (i.e. the plasma bullet location just about the exit of the tube, same time snapshot as Figure 57c), (b) at z=1.85 and time 163 ns (i.e. plasma bullet location z= 1 mm, same time snapshot as Figure 57e). 152

Figure E7: Simulation results of the spatio-temporal evolution of the total ionization rate for He+O_2 (1000 ppm) plasma jet without considering the Penning reactions in the kinetic scheme. 153

Figure E8: Simulation results of the spatio-temporal evolution of the total ionization rate for He+O_2 (1000 ppm) plasma jet where the seec is set to zero..... 153

List of Tables

Table 1: Operational parameters. 28

Table 2: Surface reactions. 30

Table 3: Boundary conditions considered for the simulation model. The letters A-H correspond to the ones in Figure 6. 31

Table 4: Different cases considered in the simulations. 35

Table 5: Operational parameters of experimental setup from [21]. 46

Table 6: Input parameters for the Boltzmann solver [48,105]. 49

Table 7: Surface reactions, reaction probabilities, seec and mese. 50

Table 8: Different cases considered in the simulations. 53

Table 9: Operational parameters of the experimental setup. 75

Table 10: Species included in the model chemistry. 77

Table 11: Air impurities considered for the comparison of the simulation model with the experiment results of section 5.2. 78

Table 12: Surface reactions, reaction probabilities, seec and mese. 78

Table 13: Boundary conditions considered for the plasma fluid model. The letters A–O correspond to the ones found in Figure 41. 97

Table 14: Boundary conditions considered for the gas fluid model. The letters A–O correspond to the ones found in Figure 41. 97

Table 15: Probable reactions for the production of He($3s3S$), $N2 + B2\Sigma u +$ and $O35P$. 99

Table A1: Rate coefficient for helium and nitrogen reactions. 132

Table B1: Rate coefficients for helium, nitrogen and oxygen reactions. 134

Table C1: Rate coefficients for helium, nitrogen, oxygen and water reactions. 139

Table D1: Rate coefficients for helium, nitrogen and oxygen reactions. 147

Nomenclature

Abbreviations

DBD	Dielectric barrier discharge
LTAPP	Low temperature atmospheric pressure plasma
APPJ	Atmospheric pressure plasma jet
ICCD	Intensified charged coupled device
APGD	Atmospheric pressure glow discharge
APTD	Atmospheric pressure Townsend discharge
EEDF	Electron energy distribution function
CAPP	Cold atmospheric pressure plasma
IEF	Induced electric field
GDM	Gas dynamic model
PFM	Plasma fluid model
SEEC	Secondary electron emission coefficient
MESE	Mean energy secondary electrons

Chapter 1

Introduction

1.1 Introduction

Low temperature atmospheric pressure plasma (LTAPP) has gained tremendous attention in recent years due to its low production cost and wide range of applications ranging from surface modification [1,2], plasma medicine [3,4], sterilization [5,6] etc. Its main benefit lies in the fact that it operates at atmospheric pressure without the need for costly, complicated and limiting vacuum equipment. The absence of a vacuum system coupled with the low plasma temperature (close to room temperature) enhances its applicability.

In order to understand LTAPP we must first describe plasma in general. Plasma is the fourth state of matter, the others being solid, liquid and gas (see Figure 1). Plasma is an ionized gas made up of a large number of electrons and positive/negative atoms and molecules, in addition to neutral atoms and molecules, which are also present in a normal (non-ionized) gas. The energy required to ionize atoms and molecules can come from electrical, thermal or optical sources. In most applications, externally applied electric fields are used to heat electrons, ions and neutral charge species in the gaseous state producing ionization, excitation and other chemical reactions. In particular, the gas mixture (depending on the application requirements), passes through a region of high electric field (e.g. between an anode and a cathode). The free electrons (which exist due to cosmic radiation: air, cosmic, terrestrial background) are accelerated by the electric field and then release further electrons due to the ionization of neutral atoms/molecules. The remaining ionized atoms/molecules are positively charged species. However, some of the electrons may not have sufficient energy for ionization, causing excitation. This species “soup” is what is generally referred to as plasma.

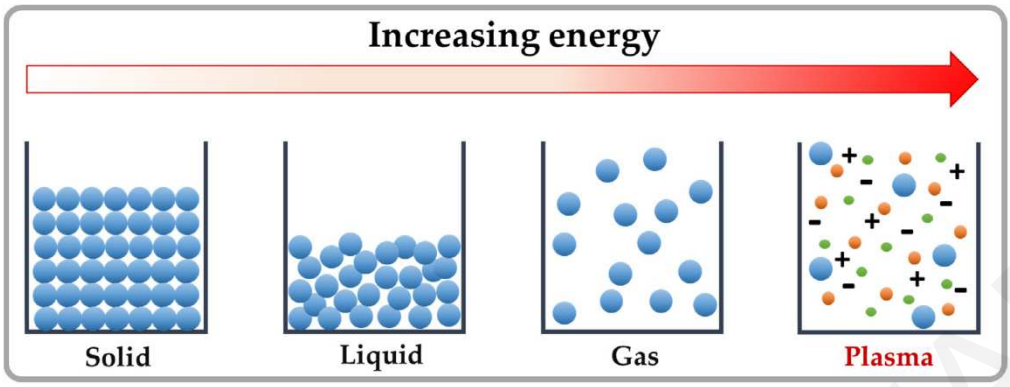

Figure 1: Four states of matter.

In most applications, a high electric field is required for the production of the desired density of species in the mixture. This causes the plasma to reach the arc regime which is a high temperature state and is known as thermal plasma, where the temperatures of the electrons ($T_{electrons}$), ions (T_{ions}) and gas (T_{gas}) are about the same i.e. $T_{electrons} \sim T_{ions} \sim T_{gas} > 1000$ ℃. However, the high temperatures are not desirable for temperature sensitive applications. An effective solution to **avoid high plasma temperatures** is achieved by covering the **electrodes with dielectric layers**. This configuration inhibits the transition to arcing, keeping the plasma at room temperature. Particularly, during breakdown, the charges accumulate on the dielectric layers creating an electric field in the opposite direction to that of the external electric field. As a result, the total voltage in the plasma region decreases significantly, and heating of the plasma species is avoided. This type of discharge is called **dielectric barrier discharge (DBD)**. In this plasma, $T_{electrons} \gg T_{ions} \sim T_{gas} \sim 30 - 50$ ℃ hence the term low temperature plasma.

The DBD plasma sources fit into two major categories: **direct** and **indirect plasma** sources. In most cases, direct plasma sources consist of two electrodes, where one or both of the electrodes are covered with a dielectric layer, and gas flows in the region between the electrodes (see Figure 2a and Figure 2b). For direct plasma sources, the surface to be processed is placed in the plasma generating region (i.e. between the electrodes, wherein the plasma is formed). On the other hand, the indirect plasma sources usually consist of a dielectric tube, a high voltage electrode placed either around the tube or inside the tube (see Figure 2c and Figure 2d), and gas flows into the tube. In this case, plasma is first produced and then delivered like a jet to the surface being processed. This type of plasma sources are known as **atmospheric pressure plasma jet (APPJ**). During the last decades a great deal of attention has been given to both plasma sources, direct and indirect

showing very promising results in biomedical applications, such as sterilization [6], bacterial inactivation [7], dentistry [8], wound healing [4], treatment of cancer cells [9], genetics and DNA [10]. The ability of DBD plasma sources to have such a great range of applications arises from the wide range of reactive species, ions, high electric fields and UV photons they can generate.

In the European Union more than two million people die from cancer every year. These results demonstrate the need for finding new treatments against the cancer. APPJ has been found to be very effective in treating cancer cells without damaging normal cells. This selectivity, gives to the APPJ an important advantage over the conventional methods against cancer. In the literature there are several studies showing this selectivity of APPJ [9,11,12]. Particularly, Mirpour et al [12] investigated the effect of helium APPJ on human breast cancer and normal cells. It was found that, APPJ reduces significantly the viability of cancer cells while leaving the normal cells with no significant damage. When the helium APPJ operated with O_2 admixtures, the cancer cells viability reduced more. In this study, the viability of cancer cells was compared to that provided by a common chemotherapy drug (Doxorubicin). It was found that the APPJ operated with He/O_2 gas reduces more the viability of cancer cells in comparison to that of the chemotherapy drug. In addition to this, the normal cells viability was compared in this case (APPJ with He/O_2 gas vs chemotherapy drug), where with the APPJ treatment, the damage of normal cells was lower by 20 %. The small effect of APPJ on normal cells was also seen by the minor influence on their morphology.

The beneficial effect of APPJ on the treatment of cancer cells is not limited only to the selectivity (i.e. induces apoptosis in cancer cells, while leaving healthy cells without any significant damage). Some other important observations made the last few years for the interaction of plasma - cancer cells are: the viability of cancer cells continues be decreased after the end of treatment with plasma [13] and after the end of the treatment the immune system may be activated against the type of cancerous cells that have treated [14]. These results are very promising for the treatment of cancer with plasma, as it eliminates the probability of metastasis which is considered vital for the patient life.

An important prerequisite for developing and optimizing these applications is to understand the physics behind the operation of these plasma sources. In this work, we investigate the physics behind such plasma discharges for both direct and indirect sources.

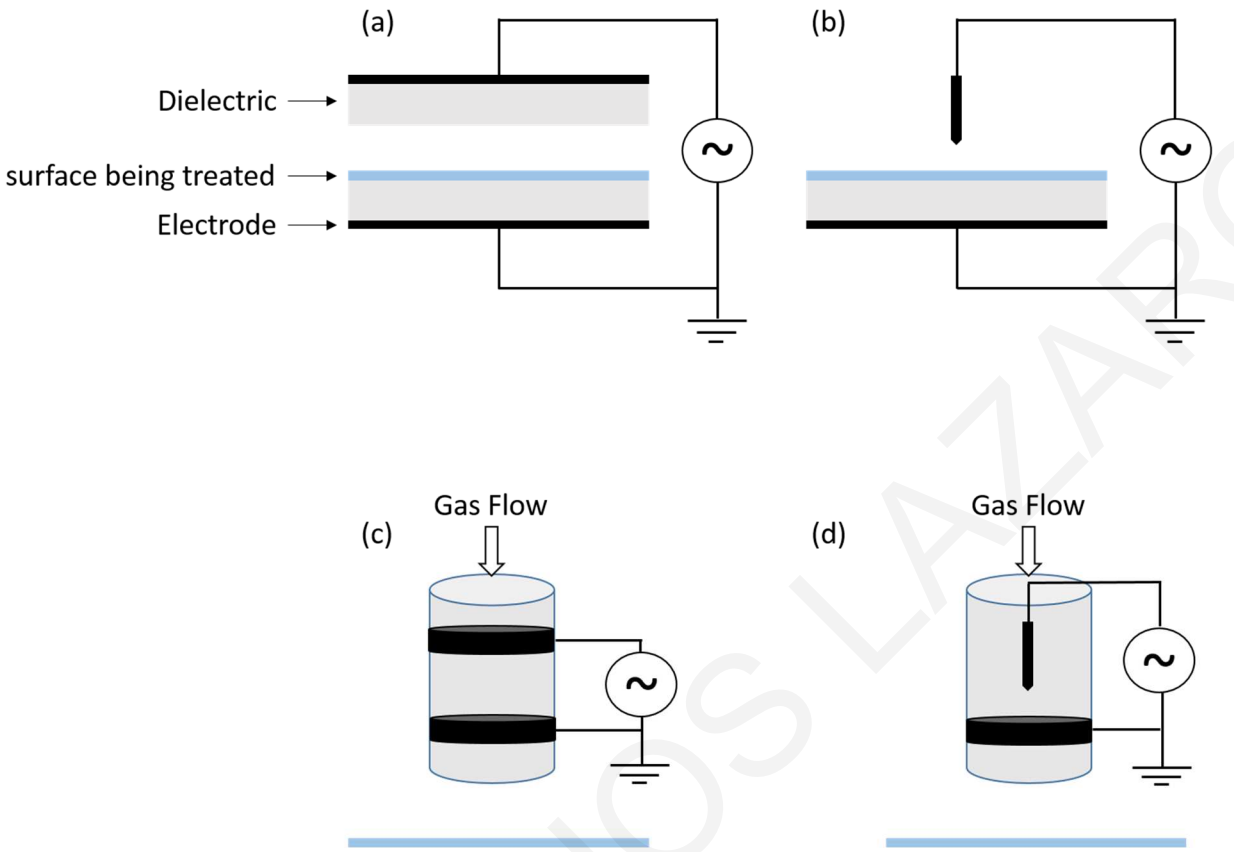

Figure 2: DBD-based plasma devices: (a) coplanar parallel plate configuration with plasma generated between the two dielectrics; (b) pin to plane configuration with plasma generated between the pin and the dielectric; (c) plasma jet with two metal ring electrodes outside the tube, the plasma is generated inside dielectric tube; (d) plasma jet with one metal electrode outside and a concentric needle electrode inside, the plasma is generated inside the dielectric tube. The blue colour shows the surface being treated, the black colour indicates the electrodes and the grey colour indicates the dielectric.

1.2 Motivation, objectives and general methodology

There are several commercially available direct and indirect DBD plasma sources (working at atmospheric pressure), and their designs differ depending on the application needs. Such plasma sources usually operate with inert gases such as argon, neon or helium. These gases are preferred because they create the conditions for lower power requirements and they produce a wide range of reactive species. At atmospheric pressure (where the discharges are operated), it is not realistic to have only pure gases (argon, neon or helium in the plasma region) and in most cases air impurities are present, usually in the form of molecular nitrogen, oxygen and water. Furthermore, in several applications, extra admixtures of nitrogen or oxygen species are added to the inert gases, in order to enhance the production of reactive species. **These impurities significantly affect** the

plasma composition and consequently **the discharge evolution**. It is therefore imperative to understand how these impurities affect the mechanisms behind the evolution of DBDs, in order to be able to optimize their application. Numerical modelling provides a very useful way of studying the processes behind such discharges and can thus help in optimizing them depending on the particular application.

However, due to the very complex chemistry behind this type of discharges (dozens of species and hundreds to thousands of reaction channels), mainly ***zero dimensional global models*** are used for these simulations. These models are computationally efficient, but have limitations, as they ***do not consider*** the spatial evolution (***diffusion and convective transport***) of the different species in the mixture. The effect of water admixtures on helium discharges through global models has been investigated by several researchers [15–20]. Particularly, Liu et al. [18] investigated the plasma chemistry of a He/H_2O mixture. The main species and dominant reaction pathways over a wide range of water admixtures (0-3000 ppm) were highlighted. The simulation results showed that water charged species dominate over helium charged species for levels of water admixtures above 30 ppm. It was shown that the electronegativity of the discharge increases as the level of water increases in the helium mixture. In addition, Liu et al. [19] investigated the effect of H_2O admixtures on the chemistry of a He+O_2 plasma. It was observed that even at low concentrations of water in the mixture, hydrated ions are abundant. In that study, the ratio between water and oxygen was kept constant at 0.5%. It was found that the ratio H_2O/O_2 of around one provides the highest amount of reactive species in the mixture. The effect of humid air on the plasma composition of a He+O_2 (0.5%) plasma was investigated by Murakami et al. [15–17]. It was found that as the level of humid air increases in the mixture, the electronegativity of the plasma composition increases while the concentration of reactive oxygen species decreases. Recently, through a global model, Schröter et al. [20] showed the importance of the surface reaction probabilities (for the species H, O and OH) and the reactor geometry on the composition of the reactive species in the mixture for a He+H_2O plasma. It was observed that the surface reaction probabilities especially for low mass species (such as H) influence significantly the concentration levels of the reactive species in the mixture. It was also found that as the size of the reactor cross section increases, the densities of H, O and OH increase with H experiencing the most dramatic increase due to its high diffusion and therefore lower surface losses. As shown by global models, even at low levels of water admixtures in the helium plasma, the hydrated ions become dominant.

However, hydration changes the mass of ions and consequently their transport coefficients. ***Global models cannot capture this effect on the plasma dynamics.***

The **main objective** of this work is the **development of a validated** with experimental results **model** that considers the **spatial evolution** of the different species for a **helium DBD plasma in the presence of nitrogen, oxygen and water species.** However, due to the complexity of creating such a model, a step by step process is followed starting from a simple model and verifying it with experimental results, and then improving it by adding more detail (addition of impurities). This procedure provides confidence about the validity of the developed model. The **methodology** followed for the model development is summarized in Figure 3. The first step focuses on the description of the helium DBD in the presence of nitrogen admixtures (see step 1 in Figure 3). The nitrogen species is the first admixture because it constitutes the highest concentration in air (approximately 79%). In the second step (Figure 3), the oxygen species are added, as they constitute almost the rest of the amount of air (approximately 21% of air). The third step (see Figure 3) considers the addition of water species in the model chemistry (0.01 - 0.02 % of air). **At each step**, the **simulation model is validated with experimental results** and specifically electrical measurements. For the three stages of the model development, the configuration of the parallel plate DBD (operated in the homogenous mode) is used, because these experiments are more accurate, as they are executed in a controlled chamber. It is noted that the simulation models have been developed by the University of Cyprus, while the experiments have been performed by the Alexandru Ioan Cuza University of Iasi, with the exception of chapter 4, where the experimental results have been taken from the literature [21].

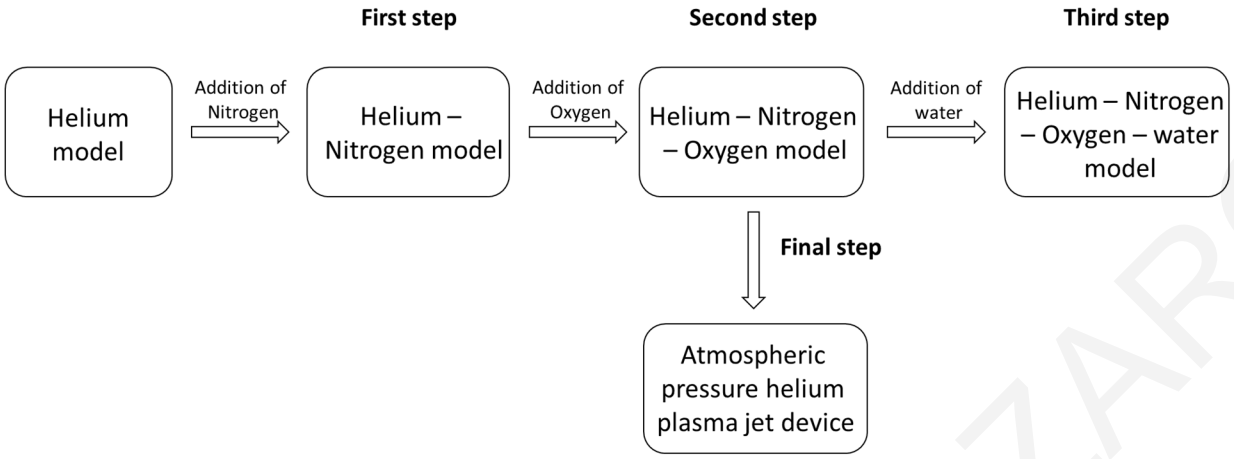

Figure 3: Schematic diagram presenting the process of the model development.

The second objective of this work is to **use the validated model** created for the description of helium DBD in the presence of nitrogen and oxygen species for the **investigation of a plasma device** (final step in Figure 3). Here, the atmospheric pressure plasma jet (APPJ) device is chosen as it shows very promising results in applications ranging from plasma medicine [22], to sterilization [6], to material surface modification [2], etc. To further ensure the model captures correctly the physics behind such discharges, **additional validation** is performed with the APPJ device. The validation is based on the comparison of the experimental spatio-temporal resolved emission (taken by an ICCD camera) with the appropriate reaction rates calculated by the simulation model.

In the literature, there are remarkable simulation studies investigating the evolution of helium plasma jet devices providing insight into the fundamental processes during the discharge [23–36]. The numerical simulation studies indicate that the plasma bullet has the characteristics of an ionizing wave (streamer) [23–25,27,29]. The ring structure of the plasma bullet has been successfully captured in many numerical simulation studies [26,27,29,30,36]. Brenden et al. [27] showed the importance of helium-air channel for the successful propagation of the ionizing wave. Naidis [28] showed that increasing the applied voltage and the helium flow rate increases the propagation speed of the ionizing wave as well as the propagation length. On the other hand, increasing the tube radius for the same flow rate results in the decrease of the propagation length. Boeuf et al. [29] showed that by increasing the voltage pulse amplitude or rise time or preionization density the plasma bullet speed increases. In the same study, decreasing the tube radius shows an increase of the electron density on the plasma bullet head. The effect of air admixtures on the

evolution of a helium plasma jet has been investigated by Naidis [31]. It was observed that the ring structure of a helium plasma jet disappeared when air admixtures were introduced into the helium gas due to the smoothing of the radial uniformity of plasma parameters inside the streamer channel. The effect of nitrogen impurities on the dynamic evolution of a helium plasma gun setup was investigated by Bourdon et al. [32]. It was shown that two and three body penning reactions are crucial for the discharge dynamics. It was also found that higher amplitudes of the applied voltage cause an increase of the ionization front velocity, confirming the results from Naidis et al. [32] and Boeuf et al. [29]. However, the ionization front velocity at different level of nitrogen admixtures in the helium gas was shown to be dependent on a complex coupling between the kinetics of the discharge, the photoionization and the 2D structure of the discharge in the tube. Norberg et al. [33] investigated the production of reactive oxygen and nitrogen species (RONS) for a He/O_2 plasma jet. It was shown that high flow rates and low repetition frequency results in the production of RONS that flow outside the tube. Furthermore, a higher applied voltage results in a higher production rate of RONS. Logothetis et al. [34] investigated the interaction of helium plasma jet with air. A flow alteration was observed when plasma was activated due to an induced electro hydrodynamic force acting on the fluid. Recently Lietz et al. [35] discussed processes in the He/air gas phase that heat up the gas and may cause the disturbance of the helium-air channel.

However, for practical applications, the importance of plasma jet lies on the interaction with surfaces (such as plastics, metals, biological tissue, liquids). Due to that, in the last few years emphasis is placed on numerical simulation studies of the plasma surface interaction [37–41]. Norberg et al. [37] investigated the interaction of a He/O_2 plasma jet with different surfaces (dielectrics with relative permittivity in the range of 2-80 and metal). It was observed that as the relative permittivity increases, the speed of the ionizing wave increases as well as the density of plasma species. The metal surface presents similar features as the high permittivity surfaces (a conductive channel between the surface and the tube) but with negligible propagation of the ionizing wave along the metal. On the other hand, dielectrics with lower permittivity show a higher penetration of the electric field into the dielectric and a greater propagation of the ionizing wave along them. Similar observation has been made by Wang et al. [39], for a helium plasma jet impinging into dielectrics with different relative permittivities. Yan and Economou [40] investigated a helium plasma jet in ambient oxygen impinging on metal and dielectric surface. A conductive channel was observed to be developed between the plasma jet device and the metal

surface without surface ionizing waves (SIW), while for the case of a dielectric surface SIW was developed similar to the one reported by Norberg et al. [37] and Wang et al. [39].

In this thesis, for the ***first time*** to our knowledge, ***the effect of oxygen admixtures*** on ***the evolution and interaction of a capillary helium plasma jet device with a dielectric surface*** is investigated numerically and observed experimentally. Several components such as secondary emission flux of electrons (SEFE), Penning reactions, and oxygen admixtures are all considered and integrated into the numerical model. The use of capillary tubes for plasma generation [42,43], as is done in this thesis, is gaining attention for biomedical applications. Capillaries are small and flexible and generate low volume plasma streams that can be delivered to previously inaccessible anatomical structures. Furthermore, it has been observed that a small amount of oxygen admixtures into the helium increases the effectiveness of APPJ against cancer cells [44,12]. Since the plasma bullet mainly determines the interaction of the plasma jet with the surface, it is important to understand how the bullet and its interaction is affected by the introduction of O_2 into the helium gas.

1.3 General assumptions

For the validation of the simulation models developed in steps one to three, the experimental results of a parallel plate DBD operated in the homogenous mode are used. In order to simplify the simulations, the following two assumptions are considered:

- The plasma quantities vary only in the direction vertical to the surface of the electrodes. This is possible due to the homogeneous characteristics of the parallel plate DBD and its symmetric shape.
- The disturbance of the electric field at the edges of the parallel electrodes is not considered. This is possible due to the much smaller distance between the electrodes in comparison to their surface dimensions.
- The residence time of helium atoms inside the electrode gap is much higher than the inter-pulse period. Thus, any gas flow of the helium can be ignored in the one-dimensional model case.

Because of these assumptions, the simulations can be performed in one, two or three dimensions without affecting significantly the simulation results. In this work, the simulations have been performed in one and two dimensions for computational efficiency.

1.4 Novelty

Atmospheric pressure and low temperature helium DBD devices have been extensively used in the last decades in many applications, due to low production cost and ease of use. In such discharges, the presence of air impurities is unavoidable and should be taken into account as they affect the discharge characteristics and evolution. Furthermore, in many biomedical applications nitrogen, oxygen and water species play an important role for the effectiveness and use of plasma devices. In the literature, there is a very limited number of studies regarding the effect of these impurities on the evolution of helium DBD. This work aims to close this knowledge gap by using novel methodologies, developments and investigations. Specifically, the **novelty** of this work is:

- The **development** and **validation** of a **state of the art** numerical **model** for the description of a helium DBD in the presence of nitrogen, oxygen and water species.
- The **investigation** and deep **understanding** of the effects of nitrogen, oxygen and water impurities on the plasma evolution of a helium DBD.
- The **development** of a **state of the art** numerical **model** for the investigation of APPJ devices and their interaction with dielectric materials.

This work has yielded important and novel results and insights into DBD devices. Specifically, novel insight is given in Chapter 3 where it is shown that as the nitrogen impurities increase (0.1-500 ppm) in a helium DBD, the breakdown voltage, the dominant ion species and the discharge current are all affected and are interconnected. It can be shown for example, how the dominant ion species are affected by varying the level of nitrogen impurities in the mixture. Three different dominant ions were found, which are strongly dependent on the level of nitrogen impurities. These are: He_2^+ (0.1–35 ppm), N_2^+ (35–150 ppm) and N_4^+ (150–500 ppm). Furthermore, important insight can also be seen in Chapter 4 where oxygen impurities are added along with the nitrogen ones and this allowed for the investigation of dry air impurities into the DBD plasma. It is shown that a small amount of dry air impurities can help plasma ignition, while **higher level of dry air** in the helium mixture causes first **instabilities** and eventually **extinction** of the discharge unless a

higher gap voltage is applied. In this work, for the first time a detailed explanation was given behind this phenomenon, which was also observed experimentally. Furthermore, new insights into fundamental processes of helium DBD operated in air surroundings are gained which are highly relevant for applications, e.g. in plasma medicine. In chapter 5, important insight into the effect of water admixtures on the evolution of a He/air DBD is provided. This study showed that a low level of water in the mixture helps the ignition of the discharge, while higher levels (>600 ppm), causes an increase in the ignition voltage. Additionally, despite the low levels of water in the mixture, it was found that the predominant ions in the mixture are H_2O^+ for 20 - 100 ppm of water admixtures and $H_{11}O_5^+$ for 100 - 2000 ppm of admixtures. In chapters 6 and 7, new insights are gained into the fundamental processes of helium APPJ devices, the effect of the presence of oxygen admixtures and interaction with dielectric surfaces. For example the model gives an explanation as to why the helium plasma jet has a **torus/ring like shape** and it also explains why the addition of oxygen admixtures causes the plasma bullet to change to a **sphere like shape.** Furthermore, the model shows how a low level of oxygen impurities increases the induced electric field (IEF) on the dielectric surface, which is very important for biomedical applications of helium plasma jets.

1.5 Outline of the proposal

The proposal is divided and organized into eight chapters. Specifically, chapter 1 is the introduction and includes the motivation, general methodology, assumptions, novelty and research objectives of the work. Chapter 2 provides the criteria for the selection procedure of the simulation model for plasma description along with a detailed description of the equations and boundary conditions of the selected plasma model. Chapter 3 investigates the evolution of helium DBD in a wide range of nitrogen impurities. In chapter 4, the oxygen impurities are added, in order to investigate the evolution of helium DBD in the presence of dry air impurities. In Chapter 5, the water admixtures were introduced in the model, and their effect on the evolution of a He/air DBD is investigated. The evolution of a capillary helium plasma jet with and without the presence of oxygen admixtures and its interaction with a dielectric surface is investigated in chapters 6 and 7. Chapter 8 contains the conclusions with the summary of the thesis achievements so far and future planned work for this thesis.

Chapter 2

Simulation model

2.1 Introduction

In this chapter, the procedure followed for the selection of the appropriate model for the plasma description is presented. In literature, there are several models for the description of plasma. However, for low temperature plasma at atmospheric pressure with hundreds of reactions, the plasma fluid model provides accurate results at reasonable simulation time.

2.2 Model selection

Plasma is the state of matter with such high concentration of charged particles, that its dynamic behaviour is dominated by the electromagnetic forces. Therefore, one would expect that its description would be an easy task, since the fundamental charged-particle motion is well known (Newton's Law, classical electromagnetic theory and the Lorentz force equation). Through this approach, the motion of charged particles can be calculated in a self-consistent way, by following the next four steps summarized in detail in Figure 4. In the first step, the position and velocity of all particles is calculated from the solution of Newton's law and the Lorentz force. Based on the position and velocity of each particle, in the second step, the charge and current density are calculated by averaging over a macroscopically small volume. In the third step, the electric and magnetic fields are calculated from the solution of Maxwell's equations based on the charge and current density in the domain. In the last step, the Lorentz force is calculated from the electric and magnetic fields. This methodology, constitutes a self-consistent way for the description of the plasma. Although this approach in theory is able to describe plasma phenomena, in practice it is not very practical due to the very large ($\sim 10^{25}$) number of particles that would need to be tracked. Furthermore, the velocity and position of each particle cannot be measured experimentally, and thus cannot be compared with simulation results. Typically, the experimental measurements are for a group of particles in a small volume (such as particle density, bulk plasma velocity etc.). With

the model described above it will be very difficult and complicated to derive the previous measurable quantities. Another important drawback of this model is that it disregards atomic processes such as ionization, excitation, attachment etc. The above lead to the conclusion that there is a need for the description of the behaviour of large quantities of particles. This can be achieved by describing plasma through a statistical approach and then averaging over a large number of particles. As plasma has many common properties with gases, the kinetic theory of gases (statistical approach for gas description) can be used for the description of plasma phenomena. Such an approach, uses a velocity-space distribution function (f(r,v,t)) for the description of particle positions and velocities.

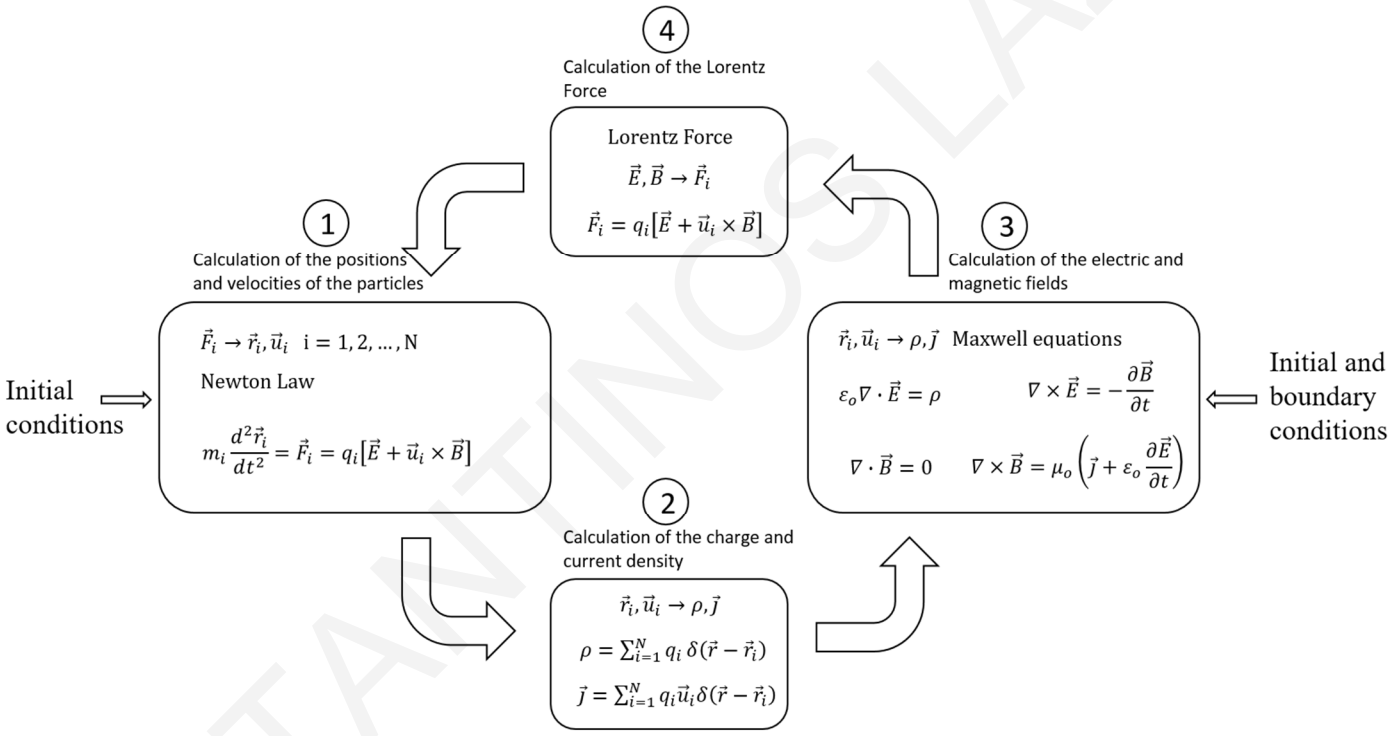

Figure 4: Schematic diagram presenting the fundamental equations governing the plasma behaviour.

The f(r,v,t)d^3r d^3v gives the total number of particles inside a six-dimensional phase space volume d^3r d^3v at the position and velocity (r, v) at time t. By knowing the distribution function *f*(r,v,t), one can calculate the density of particles at position r and time t, $n(r,t)$, through the following integral:

$$n(r,t) = \int f(\mathrm{r,v,t})\ \mathrm{dv} \tag{1}$$

The distribution function can be used to calculate any macroscopic quantity (i.e. temperature, flux, current, etc.), by averaging that quantity (g(r,v,t)) over the velocities (dv):

$$g_{av}(r,t) = \frac{1}{n(r,t)} \int g(r,v,t)\, f(\mathrm{r,v,t})\ \mathrm{dv} \tag{2}$$

The quantity of interest is averaged over the velocity space giving the result as a function of space and time, which allows comparison with experimental results. The time variation of the distribution function is given by Boltzmann's equation:

$$\frac{\partial f}{\partial t} + v \cdot \nabla_r f + \alpha \cdot \nabla_v f = \left(\frac{\partial f}{\partial t}\right)_{coll} \tag{3}$$

where v is the velocity, ∇_r is the differential operator in space, α is the acceleration, ∇_v is the differential operator in velocity and $\left(\frac{\partial f}{\partial t}\right)_{coll}$ represents the particle flow due to collisions. It is important to note that v and α are independent. By solving Boltzmann's equation for each species in the mixture, the distribution function and therefore any other macroscopic quantity can be calculated. This model is well known in the literature as kinetic approach. However, the solution of Boltzmann's equation is computationally costly and cannot deal with arbitrary plasma chemistry. Nevertheless, in most applications there is no need to have the distribution function. So, instead of solving Boltzmann's equation for each species which is complicated and time consuming, one can solve the moments of Boltzmann's equation, which are the equations for the macroscopic quantities of interest (e.g. number density, mean velocity, mean energy etc.). Through this procedure, knowledge of the distribution function is not required. The procedure for deriving the moments of Boltzmann's equation, is by multiplying it with powers of the velocity and then integrating on the velocity space. An important question is how many moments are needed, in order to have a satisfactory and accurate description of the plasma. In the continuum regime, the mass, momentum, and energy balance equations are assumed to be sufficient for the description of plasma. These correspond to the first three moments (velocity to the power of 0, 1 and 2). The mass, momentum, and energy balance equations form the foundation of the plasma fluid model.

The analytical derivation of these equations is well described in several studies in the literature [45–47]. These equations have been adopted in our model for the description of electrons and electron energy. However, for the description of the rest of the species in the mixture (heavy species) the multicomponent diffusion equation (that uses the mixture-averaged diffusion coefficient) is used. This equation provides more accurate results as the diffusive driving force of each species depends on the mixture composition, temperature, and pressure. It is noted that an energy balance equation is not taken into account for the heavy species because the ion energy does not affect the ionization rates significantly.

Another approach for the plasma description is the hybrid method that treats some of the components of the plasma through the fluid model and others through the kinetic model. Usually, the electrons are treated kinetically by solving the Fokker-Planck equation (which is a simplified version of Boltzmann's equation) or using the Monte Carlo method, while the heavy species are described by the fluid model. This method is more accurate than the plasma fluid model, but requires more computational time. For discharges with low Knudsen numbers, at low temperature and atmospheric pressure, as is the case in this thesis, the hybrid and plasma fluid models give similar results. Therefore, in order to save computational time without affecting the overall results, the plasma fluid model is used. The equations used for our plasma fluid model are described in the next section.

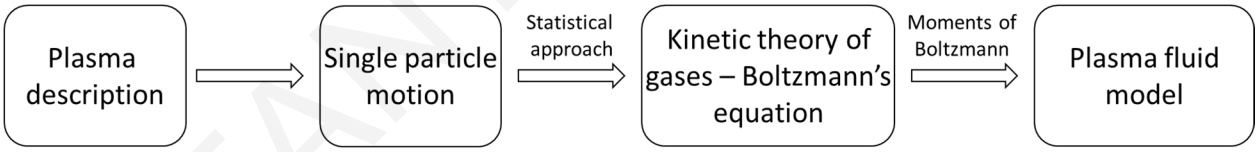

Figure 5: Schematic diagram presenting the procedure for the plasma model selection.

In summary, the procedure for the model selection is presented in Figure 5. Originally, the single particle model that treats each particle separately was considered as a possible model for the description of the plasma. However, the high number of particles at atmospheric pressure (10^{25}) makes the application of this model impractical. Then, a statistical model was considered as a possible approach for the description of the plasma. Such a model describes the particles through a distribution function in the six-dimensional phase space (kinetic theory of gases). However, the distribution function is obtained from the solution of Boltzmann's equation, which for arbitrary chemistries is computationally very expensive. In order to simplify the solution, we use the first

three moments of Boltzmann's equation which correspond to the mass, momentum, and energy balance equations for the description of the plasma. This model is known as the plasma fluid model.

2.3 Plasma fluid model (PFM)

For the simulation of the helium DBD the fluid approach was used. The electrons are described by the first three moments of Boltzmann's equation, which after simplification reduce to the continuity equations for the description of the electron density and electron energy density [48]. The remaining species in the mixture were considered as heavy and described by a multicomponent diffusion equation which used the mixture-averaged diffusion coefficient [49,50].

The equation which describes the electron density is

$$\frac{\partial n_e}{\partial t} + \nabla \cdot \vec{\Gamma_e} = S_e - (u \cdot \nabla) n_e \tag{4}$$

where n_e is the electron density, $\vec{\Gamma_e}$ is the electron flux term, S_e is the source or sink for the electron density and u is the mass average velocity of the mixture. The flux term is derived from the momentum transfer equation and is expressed based on the drift diffusion approximation [48]

$$\vec{\Gamma_e} = -\mu_e \vec{E} n_e - D_e \nabla n_e \tag{5}$$

where μ_e and D_e are the mobility and diffusion coefficient for the electrons respectively and $\vec{E}$ is the electric field. The source term for electrons is given by

$$S_e = \sum_{j=1}^{M} c_{j,e} R_j \tag{6}$$

where $c_{j,e}$ is the stoichiometric number for electrons in the reaction j, R_j the reaction rate and M is the number of electron reactions. The equation for the description of the electron energy density is the following:

$$\frac{\partial n_\varepsilon}{\partial t} + \nabla \cdot \vec{\Gamma}_\varepsilon = S_\varepsilon - (u \cdot \nabla) n_\varepsilon \tag{7}$$

where n_ε is the electron energy density, $\vec{\Gamma}_\varepsilon$ is the flux term for the electron energy density and S_ε represents the energy loss or gain due to elastic and inelastic collisions and the energy gained from the electric field.

The flux and the source term are defined as [48]

$$\vec{\Gamma}_\varepsilon = -\mu_\varepsilon \vec{E} n_\varepsilon - D_\varepsilon \nabla n_\varepsilon \tag{8}$$

$$S_\varepsilon = -e\vec{\Gamma}_e \cdot \vec{E} - \sum_{j=1}^{P} c_{j,e} R_j \varepsilon_j \tag{9}$$

where μ_ε and D_ε are the mobility and diffusion coefficient for the electron energy density respectively, P is the number of elastic and inelastic collisions and ε_j is the energy lost or gained in the collision and is taken equal to the reaction threshold. For Q heavy species in the mixture, the $Q - 1$ species are described by a multi-component diffusion equation [49,50]

$$\rho \frac{\partial}{\partial t}(\omega_i) + \rho (u \cdot \nabla) \omega_i = \nabla \cdot \vec{j}_i + S_i \quad i = 1, \dots, Q - 1 \tag{10}$$

where ρ is the density of the mixture, ω_i is the mass fraction of the species i, $\vec{j}_i$ is the diffusive flux vector and S_i is the source term. The density of the background gas is given from the equation (conservation of mass)

$$\omega = 1 - \sum_{i=1}^{Q-1} \omega_i \tag{11}$$

The diffusive flux vector is defined as follows

$$\vec{j}_i = \rho \omega_i \left(D_{i,m} \frac{\nabla \omega_i}{\omega_i} + D_{i,m} \frac{\nabla M_n}{M_n} - z_i \mu_{i,m} \vec{E} \right) \tag{12}$$

where $D_{i,m}$ is the mixture-averaged diffusion coefficient, M_n is the mean molar mass, z_i is the charge number of species i and $\mu_{i,m}$ is the mixture-averaged mobility. The mixture-averaged diffusion is calculated through the binary diffusion [49,50]. In the case where the binary diffusion cannot be predicted from the kinetic theory [51,52], it is calculated from the experimental value of the mobility using the local field approximation [53]. For the neutral species the last term on the right hand side of equation (12) is zero. The mixture-averaged mobility is calculated from Einstein's relation

$$\mu_{i,m} = \frac{qD_{i,m}}{k_b T} \tag{13}$$

where q is the electron charge, k_b is the Boltzmann constant and T is the gas temperature. Finally, the electric field is calculated from Poisson's equation

$$-\nabla \cdot (\varepsilon_r \nabla \varphi) = \rho_v \tag{14}$$

where ε_r is the dielectric constant of the material, φ is the potential and ρ_v is the local charge in the gap.

Due to the high degree of nonlinearity inherent in the drift diffusion equation, the electron number density can span 10 orders of magnitude over a very small distance. In this region (the plasma sheath), the difference in the mobility and diffusivity between the ions and electrons creates a separation of space charge. This in turn produces a large electric field which can lead to a substantial increase in the mean electron energy. For that reason, a log formulation is used for the description of electron density and electron energy density. This constitutes the best handling from the numerical point of view. The electron and electron energy equations are now written as follows.

$$\frac{n_e \partial N_e}{\partial t} + \nabla \cdot \left[-n_e\left(\mu_e \vec{E}\right) - n_e D_e \nabla N_e\right] = S_e + R_e - n_e (u \cdot \nabla) N_e \tag{15}$$

$$\frac{n_\varepsilon \partial E_n}{\partial t} + \nabla \cdot \left[-n_\varepsilon\left(\mu_\varepsilon \vec{E}\right) - n_\varepsilon D_\varepsilon \nabla E_n\right] + \vec{E} \cdot \vec{\Gamma}_e = S_e + R_\varepsilon - n_\varepsilon (u \cdot \nabla) E_n \tag{16}$$

where $N_e = \ln(n_e)$ is the log formulation of electron density, $E_n = \ln(n_\varepsilon)$ is the log formulation of electron energy density and $R_{e,\varepsilon}$ is a stabilization term for the electron and electron energy density respectively. In particular, to avoid zero values in the log formulation, a stabilization term has been added in the above equations. This term acts as a source term preventing the density of the electrons and electron energy from approaching zero. When the particle density increases, this term becomes exponentially smaller and eventually becomes negligible for high particle densities.

$$R_e = N_A \exp(-\zeta ln n_e) \tag{17}$$

$$R_\varepsilon = N_A \exp(-\zeta ln n_\varepsilon) \tag{18}$$

where N_A is the Avogadro constant and ζ is a tuning parameter ($0 < \zeta < 1$).

The description of the heavy species in the plasma mixture is handled in a similar manner. In particular, due to the large variation in mass fraction of the heavy plasma species, a logarithmic scalling is used. The multicomponent diffusion equation is now written as follows.

$$\rho\omega_i \frac{\partial}{\partial t}(W_i) + \rho\omega_i (u \cdot \nabla) W_i = \nabla \cdot \vec{J}_i + S_i + R_i \quad i = 1, \dots, Q-1 \tag{19}$$

$$\vec{J}_i = \rho\omega_i \left(D_{i,m} \nabla W_i + D_{i,m} \nabla \ln M - z_k \mu_{k,m} \vec{E} \right) \tag{20}$$

where $W_i = \ln(\omega_i)$ is the log formulation of mass fraction of species i and R_i is an extra stabilization term defined as follows:

$$R_i = \exp\left(-\zeta \ln(n_i)\right) \tag{21}$$

where n_i is the density of species i. In the simulation model, the parameter ζ is set to 0.25 (for both electron and heavy species) as it provides the best stability for the algorithm.

2.4 Boundary conditions of the plasma fluid model

The boundary conditions considered for the flux of electrons and electron energy at the solid surface are given by the following equations:

$$\vec{n} \cdot \vec{\Gamma_e} = \left(\frac{1}{2} v_{e,th} n_e - a n_e \mu_e \vec{E} \cdot \vec{n}\right) - \sum_{k=1}^{Q} \gamma_k N_A \vec{n} \cdot \vec{j}_k \tag{22}$$

$$\vec{n} \cdot \vec{\Gamma_\varepsilon} = \left(\frac{5}{6} v_{e,th} n_\varepsilon - a n_\varepsilon \mu_\varepsilon \vec{E} \cdot \vec{n}\right) - \sum_{k=1}^{Q} \gamma_k \varepsilon_k N_A \vec{n} \cdot \vec{j}_k \tag{23}$$

where $\vec{n}$ is the normal pointing towards the solid surface, $v_{e,th}$ is the thermal velocity, μ_e and μ_ε are the electron and electron energy mobility respectively, γ_k is the secondary electron emission coefficient (seec) of species k, N_A is the Avogadro constant, $\vec{j}_k$ is the flux of the heavy species k, ε_k is the mean initial energy of secondary electrons (mese) emitted from the solid surface and a is a switching function that depends on the product of $\vec{E}$ and $\vec{n}$ defined as follows:

$$a = \begin{cases} 1 \left(sgn(q)\vec{E} \cdot \vec{n} > 0\right) \\ 0 \left(sgn(q)\vec{E} \cdot \vec{n} \leq 0\right) \end{cases} \tag{24}$$

where q is the charge of the considered species. The two terms in the parenthesis, on the right hand side of equation 22 represent the loss of electrons on the solid surface, due to the random motion of electrons and the flux of electrons due to the electric field. On the other hand, the last term on the right hand side of equation 22 represents the gain of electrons due to secondary electron emission. Similar explanation applies to equation 23 concerning the electron energy.

The normal component of the heavy species flux at the solid surface is given by:

$$\vec{n} \cdot \vec{j}_k = M_k R_{surf,k} + a M_k \omega_k \mu_{k,m} z_k \left(\vec{n} \cdot \vec{E}\right) \tag{25}$$

where M_k is the molar weight of species k, $R_{surf,k}$ is the surface reaction rate, ω_k represents the mass fraction of species k, $\mu_{k,m}$ is the mixture-averaged mobility and z_k is the charge number of species k. The first term on the right hand side of equation 25 $\left(R_{surf,k}\right)$ is linked to the way species

are created or lost on the solid surfaces, while the second term represents the loss of ions due to the movement driven by the electric field. For the neutral species, the second term on the right hand side of equation 25 is zero. The surface reaction rate is given by:

$$R_{surf,k} = c_k \sum_{i=1}^{N} v_{i,k} \frac{\gamma_i}{(1-\gamma_i/2)} \frac{1}{4} \sqrt{\frac{8RT_g}{\pi M_n}} \tag{26}$$

where N is the number of surface reactions, $v_{i,k}$ is the stoichiometric number of species k on the i^{th} surface reaction, γ_i is the probability of the reaction to occur (sticking coefficient), R is the universal constant, T_g is the gas temperature and M_n is the mean mass of the mixture. The reaction rate (equation 26) is attributed to the random motion of species with Maxwellian velocity distribution function times the probability of a collision happening (sticking coefficient). The term $1/(1-\gamma_i/2)$ represents the Motz–Wise correction, which is a corrector term for reactions with high probability, when the velocity distribution of the species is non-Maxwellian. The field generated by the charge accumulated on the dielectrics is calculated from the following equation:

$$\hat{n} \cdot \left(\vec{D}_1 - \vec{D}_2\right) = \rho_s \tag{27}$$

where $\vec{D}_1$ and $\vec{D}_2$ are the electric displacement field above and below the boundary and ρ_s is the surface charge density which can be obtained from the following ordinary differential equation on the boundary:

$$\frac{\partial \rho_s}{\partial t} = \vec{n} \cdot \vec{J}_e + \vec{n} \cdot \vec{J}_i \tag{28}$$

where $\vec{J}_i$ and $\vec{J}_e$ are the ion and electron current densities on the wall respectively.

2.5 Gas dynamic model (GDM)

The gas dynamic model is used only in chapters 6 and 7 in order to describe the flow of the helium jet into the ambient air. This model has not been used for the parallel plate DBD simulations, because these experiments have been performed in controlled chambers and the residence time of helium gas in the chamber was much higher than the interpulse period. For that reason, the flow of the helium gas between the dielectrics can be ignored for these cases. The

model considers only two species, helium and air. The helium-air mixing is obtained from solving the steady-state multi-component mass transport equation, without considering the chemical reaction term. This equation is appropriate when the species concentrations in the mixture are of the same order of magnitude and none of the species acts as a solvent. On the other hand, the mass average velocity of the mixture is obtained from solving the steady-state equations of the conservation of total mass and momentum. As an approximation for the present analysis, the heating of the gas is not considered (from the solution of the energy conservation equation), since it has been observed that it does not affect significantly the structure of the flow [54].

The multi-component mass transport equation is given below:

$$\nabla \cdot \left(\rho D_i^M \nabla \omega_i + \rho \omega_i D_i^M (\nabla M/M)\right) + \rho (u \cdot \nabla)\omega_i = 0, \;\; i = 1, \dots, Q-1 \tag{29}$$

where ρ is the mixture gas density, D_i^M the mixture average diffusivity of species i, ω_i the mass fraction of species i, M the molar mass of the mixture, u the mass average velocity of the mixture and Q is the number of species in the mixture. For a binary system, as in this case, the multicomponent mass transport equation reduces to one equation. Equation (29) is solved only for the helium species and the air mass fraction is calculated from the equation:

$$\omega_{Air} = 1 - \omega_{He} \tag{30}$$

Due to the low gas speeds with a Mach number < 0.2 the gases can be considered incompressible and the density of the mixture can be computed from the species composition and gas temperature [54]. The mass average velocity field of the mixture is calculated from the equations of the conservation of the total mass and momentum:

$$\nabla \cdot (\rho u) = 0 \tag{31}$$

$$\rho (u \cdot \nabla) u = \nabla \cdot (\mathrm{pI} + \mu(\nabla u + (\nabla u)^T) - 2/3\, \mu (\nabla \cdot u)\mathrm{I}) + F \tag{32}$$

where p is the pressure, I the unit matrix, μ the dynamic viscosity of the mixture and F is the body force field. The dynamic viscosity is calculated from Wilke's formula [55]. The body force field is considered as the buoyancy force exerted in helium gas due to the mixing of the gases:

$$F = g(\rho - \rho_{Air}) \tag{33}$$

where g is the gravity constant.

2.6 Boundary conditions of the gas dynamic model

The multi-component mass transport equation deals only with helium species. The flux of helium species (N_i) from the solid surfaces is considered to be zero:

$$\begin{gathered} -\vec{n} \cdot N_i = 0 \\ N_i = \rho D_i^M \nabla \omega_i + \rho \omega_i D_i^M (\nabla M/M) + \rho (u \cdot \nabla) \omega_i \end{gathered} \tag{34}$$

where $\vec{n}$ is the normal vector pointing towards the solid surface. The helium mass fraction is set to 1 at the entrance point of the tube nozzle, while the helium mass fraction is set to zero at boundaries located away from the tube. Regarding equations 31 and 32 describing the mass average velocity field, the following boundary condition is used for points away from the tube:

$$(-\mathrm{pI} + \mu(\nabla u + (\nabla u)^T) - 2/3\,\mu(\nabla \cdot u)\mathrm{I})\vec{n} = -p_0 \vec{n} \tag{35}$$

where $p_0 = 1$ atm. This condition takes into account the normal stress but not the tangential one (it assumes the boundary is so far that there is no tangential flow). At the entrance point of the tube nozzle, the uniform axial velocity (u_0) is calculated from the helium flow rate in the tube. On the tube surface, the velocity is set to zero (no-slip condition) [56].

The equations presented in section 2.3 to 2.6 are solved on an Intel Xenon E5-2630 V2 2.6 kHz (with 12 core) server using the chemical reaction engineering module (for GDM) and the plasma module (for PFM) of the COMSOL multiphysics simulation package [57]. The equations for the GDM and the PFM are discretized by the Galerkin finite element method using linear element shape functions, and the resulting system is solved using the direct solver PARDISO. For the time integration (PFM) the backward Euler method is used.

2.7 Simulation procedure

The main aim of this section is to provide a complete picture of the model, with the ultimate goal of making the reading of the next chapters more understandable. With this in mind, we summarize all the information's of the model in the schematic diagram presented in Figure 6. As it can be seen from the schematic diagram, in the first step, the kinetic scheme is defined. This includes all the reactions between the species. The rate coefficients of these reactions are taken from the literature mainly from experimental studies, while the rate coefficients of the electron impact reactions are calculated from the solution of the Boltzmann equation with the two term approximation using the program Bolsig$^+$ [48]. The solution also gives the transport properties of electron and electron energy. Next, the simulation domain is designed based on the experimental configuration and discharge characteristics. It is noted that the experimental setup is described in detail at each chapter and based on that the simulation domain is designed. Then, since the simulation domain is defined, the boundary conditions are set. Subsequently, the input parameters (i.e. reaction channels, species transport properties, applied voltage, gas temperature) of the heavy species, electron and electron energy and the initial conditions (i.e. initial electron and heavy species densities and initial electron energy density) are set. All the above information is presented in detail at each chapter and specifically in the sections, experimental setup and input parameters for the model. Then the simulation model is run as it is shown in the schematic diagram, by coupling the continuity equations of the heavy species, electron and electron energy densities with the Poisson equation for the electric field and their boundary conditions.

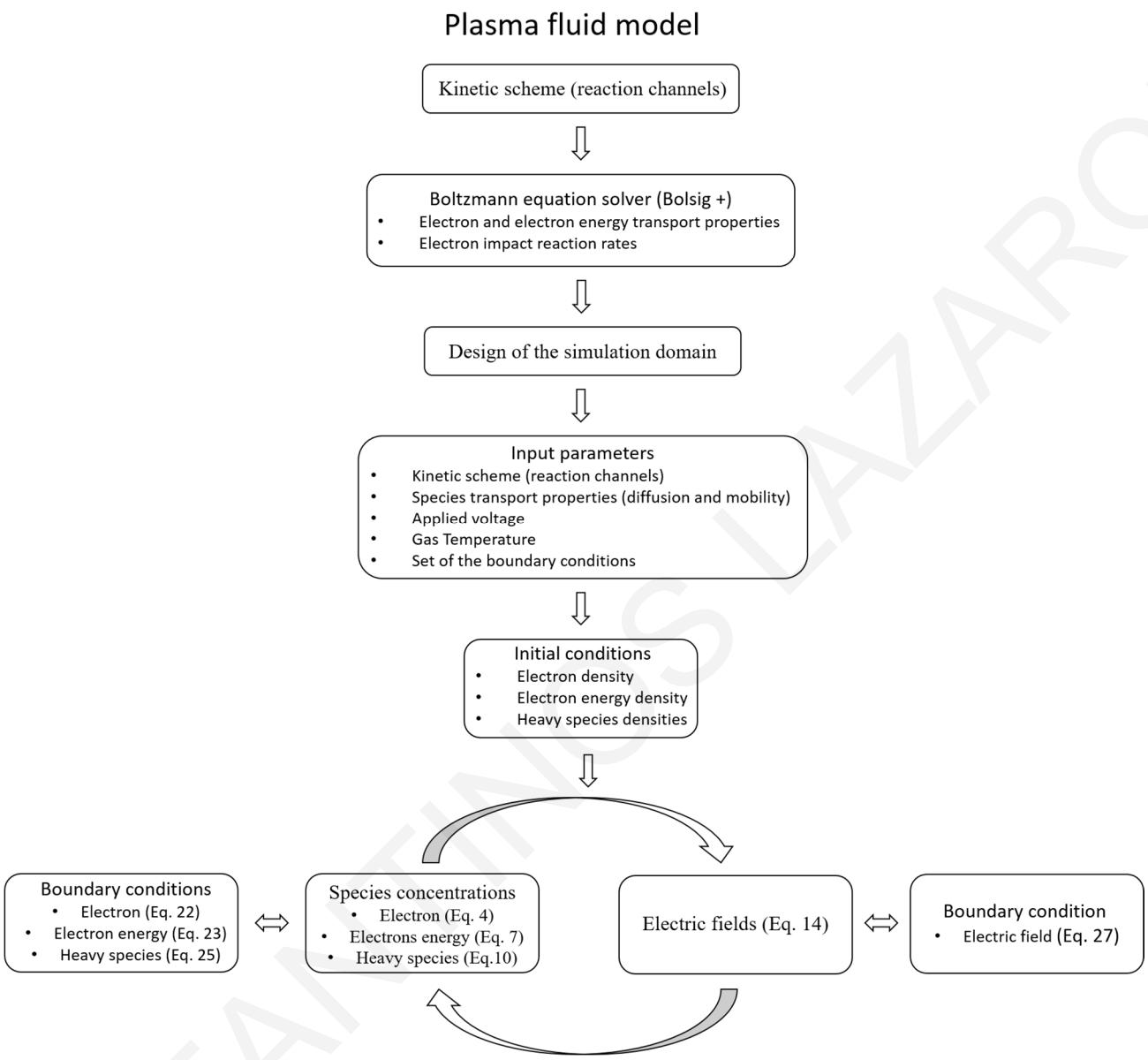

Figure 6: Schematic diagram summarizing the simulation model procedure.

Chapter 3

Simulation model of a helium-nitrogen mixture

3.1 Introduction

The main aim of this chapter is to present the model developed for the description of a helium DBD in the presence of nitrogen species. The plasma species in the model are governed by the plasma equations presented in chapter 2 (without considering the flow of the gas), with the appropriate chemistry for the helium-nitrogen species and boundary conditions. As a first step, the model was validated with experimental results, and was subsequently used to study the effect of different level of nitrogen impurities on the evolution of the discharge. The amount of impurities studied ranges between 0.1 – 500 ppm. It is noted that, in the entire range of impurities, the DBD exhibits a homogenous mode, also known as diffuse mode. The latter usually appears in two forms: atmospheric pressure glow discharge (APGD) and atmospheric pressure Townsend discharge (APTD) [58]. The APGD mainly consists of the cathode fall, Faraday dark space and positive column [59,60]. The concentration of electrons and ions is almost the same and the maximum value occurs near the cathode (~ 10^{11} cm^{-3}). This value is large enough to disturb the electric field. On the other hand the Townsend discharge mode does not exhibit a clear discharge structure. In such a discharge the concentration of ions (~ 10^{10} cm^{-3}) is about 2-3 orders of magnitude higher than the concentration of electrons. This charge is not enough to disturb the electric field. Additionally, in the Townsend mode the discharge current is in the range of 0.1-10 mA/cm^2 as opposed to 10-100 mA/cm^2 for the glow mode. The physics behind such discharges is very important in order to improve the practical applications of atmospheric pressure plasma devices. As a result, understanding the effect of nitrogen impurities on the discharge characteristics is very important for the utilization of atmospheric pressure plasma devices.

3.2 Experimental setup and computational domain

In order to validate the numerical model, experimental data were compared with simulation results. A DBD reactor was investigated, running under the following conditions: 30 mm diameter copper electrodes deposited on 1 mm glass discs, separated by a 5 mm gap. Helium (6.0 spectral purity) was continuously circulating inside the reactor, with 3 slpm flow rate. One electrode was powered using high voltage pulses, at 2 kHz frequency, delivered by an amplification chain (Tabor WW5064 function generator and Trek PD07016 amplifier) and the opposite electrode was grounded.

An oscilloscope (Tektronix TDS5034B), voltage and current probes (Tektronix 6015A and Pearson 6585 respectively) were used to continuously monitor the applied voltage and the discharge current. The voltage probe signal is monitoring the high voltage pulses applied on the power electrode, while the current monitor is placed on the ground line and gives information on the electrical current through the gap. Experimental results obtained using these probes have been presented in previous work [61–63]. The amplitude and rise time of the applied voltage pulses considered here are 3 kV and 33 μs respectively. The pressure and the gas temperature are 1 atm and 350 K respectively. The gas temperature was estimated using the rotational distribution in the emission spectrum of the first negative system of N_2^+ ($(B^2\sum_u^+, v_B=0) \rightarrow (X^2\sum_g^+, v_X=0)$), by Boltzmann plot method, under the assumption that the translational and rotational degrees of freedom have equal temperatures [64,65] because of rotational relaxation under atmospheric pressure conditions. Therefore, a constant gas temperature for all calculations seems to be a good approximation since the rotational temperature variation is below 10% with the addition of nitrogen impurities to helium [65] and for the range of impurity levels considered here. For calculation simplicity a constant gas temperature was considered in our simulations.

The computational domain fits all geometrical details of the plasma reactor. In additon, the operational parameters are presented in Table 1.

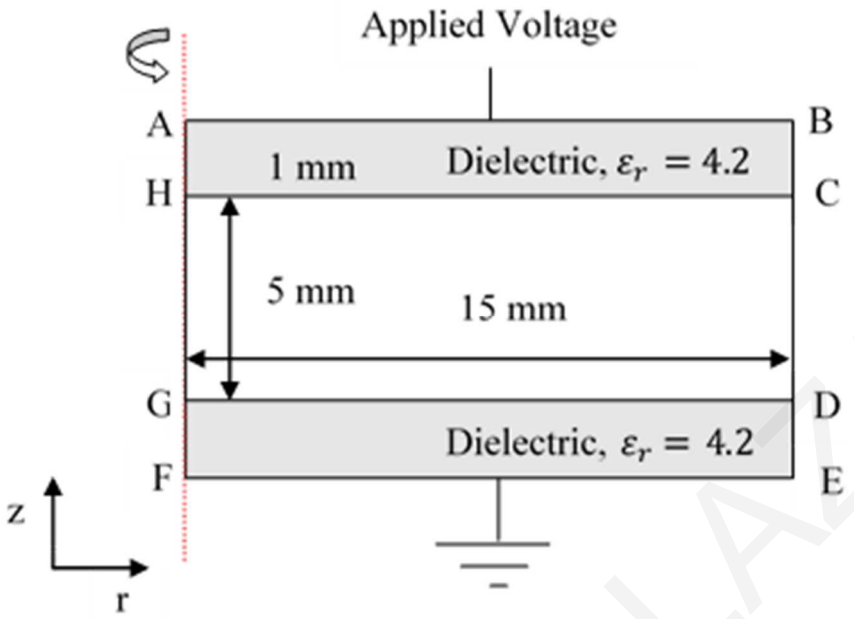

Figure 7: Simulation domain.

Table 1: Operational parameters.

Gas pressure (atm)	1
Gas temperature (K)	350
Vp-p (kV)	3
Wave form	Square monopolar
Frequency (kHz)	2
Rise time (μs)	33
Voltage Pulse width (μs)	250

3.3 Input parameters for the model

For an accurate description of the experimental discharge, 46 reactions and 10 species were used. The kinetic scheme used is taken from [66]. However, it is considered necessary to include a few but mandatory three body reactions, involved in Penning and charge transfer processes together with associated two body reactions [67]. The importance of these reactions on the discharge propagation is clearly shown in [68]. The species included in the model are electrons, He^+ and He_2^+ ions, He ground-state atoms, He_2* excimers, He_m* and He** metastable atoms, N^+, N_2^+ and N_4^+ ions, N_2 ground state molecules and N atoms. The reaction rate coefficients are given in Table A1 (in Appendix A). The rate coefficients for the first ten reactions are functions of the mean

electron energy. The rate and the transport coefficients (mobility and diffusion) of the electrons and electron energy are calculated from the electron energy distribution function (EEDF) [48].

The EEDF describes the population of electrons at different energy states. In the existing literature there are four main EEDFs. The first one is obtained by solving Boltzmann's equation with the two term approximation [48] and the remaining three are predefined functions (Maxwellian, Druyvesteyn, Generalized). Figure 8 depicts the four main EEDFs versus electron energy for a constant mean electron energy of 4 eV. In particular, for the EEDF that is obtained from Boltzmann's equation, three different ionization degrees are considered (10^{-2}, 10^{-4} and 10^{-7}) to establish its effect on the EEDF. The ionization degree is very important as it affects the shape of the EEDF and it determines if the gas is highly or weakly ionized. A value of 10^{-2} represents a highly ionized gas, and 10^{-7} represents a weakly ionized gas. It is also worth noting that in order to obtain the EEDF from Boltzmann's equation, additional input parameters such as the electron temperature, electron density and mole fraction are required. The other parameters for the experimental setup are as follows: temperature = 350 K, electron density = $10^{18}\ m^{-3}$ and mole fraction of He_m* = 10^{-7}. The chosen EEDF is considered correct if the simulation and experimental currents do not differ by more than 5%.

In our simulation, the EEDF obtained by solving Boltzmann's equation with ionization degree 10^{-7} gave the best results in reproducing the experimental discharge current and hence this has been used in the model to study the effect of nitrogen impurities. From Figure 8, it is noted that the EEDFs taken from the solution of Boltzmann's equation by using ionization degrees $10^{-2}, 10^{-4}$ and 10^{-7} approach the EEDFs obtained by the Maxwellian, Generalized and Druyvesteyn predefined functions respectively.

The diffusion coefficient for the species He, He_m*, He**, N and N_2 is calculated from the kinetic theory [51,52]. The diffusion coefficient of He_2* is taken from [69] and the mobilities of He^+, He_2^+, N^+, N_2^+ and N_4^+ are taken from experimental values [70,71].

The surface reactions considered on the dielectric surface are given in Table 2. After collision with the dielectrics the helium and nitrogen species are converted to the ground state species. The secondary electron emission was not taken into account in this study as their effect is limited [69,72]. Specifically, in the case of glow mode the discharge is sustained by the electrons trapped

in the positive column region. In this region, the concentration of electrons remains high (due to the low electric field) [59] and these act as seeds for the next breakdown. Moreover, the plasma chemistry considered in this model includes a number of reactions related to excited and metastable helium. Consequently, the ionization procedure is enhanced by these metastable species through Penning ionization. Furthermore, the effect of plasma chemistry and the transport and rate coefficients have a great effect on the discharge development and characteristics. As the purpose of this work is to study the effect of reaction channels on the evolution of the discharge, more emphasis is given on the plasma chemistry and the transport and rate coefficients, and therefore the effect of secondary electron emission was not considered. The boundary conditions are presented in Table 3. The mesh consists of 1050 elements, of which 1000 are in the plasma region. It is noted that the simulation results (the discharge current) have been compared with those obtained with a finer mesh and a maximum difference of 0.5 % was obtained. In Figure A1, the mesh independency analysis of the model is presented. As it can be seen, by increasing the mesh density, the peak of the discharge current convergences to a specific value. In particular, above 1000 elements in the discharge region, the current peak remains almost constant. On the other hand, increasing the number of elements in the plasma region, increases considerably the simulation time. For that reason 1000 elements is considered to be a good choice as it provides accurate results in a reasonable simulation time.

Table 2: Surface reactions.

consumed		created
He_m*	→	He
He**	→	He
He^+	→	He
He_2^+	→	2He
He_2*	→	2He
N	→	$0.5N_2$
N^+	→	$0.5N_2$
N_2^+	→	N_2
N_4^+	→	$2N_2$

Table 3: Boundary conditions considered for the simulation model. The letters A-H correspond to the ones in Figure 6.

Boundary	n_e	n_ε	n_i	n_n	φ
AB	0	0	0	0	Applied Voltage
BC, DE, FG, HA	0	0	0	0	$\partial\varphi/\partial r = 0$
CD, GH	$-\vec{n}\cdot\vec{\Gamma}_e = 0$	$-\vec{n}\cdot\vec{\Gamma}_\varepsilon = 0$	$-\vec{n}\cdot\vec{j}_k = 0$	$-\vec{n}\cdot\vec{j}_k = 0$	$\partial\varphi/\partial r = 0$
CH, DG	Equation 22	Equation 23	Equation 25	Equation 25	Equation 27
EF	0	0	0	0	Ground

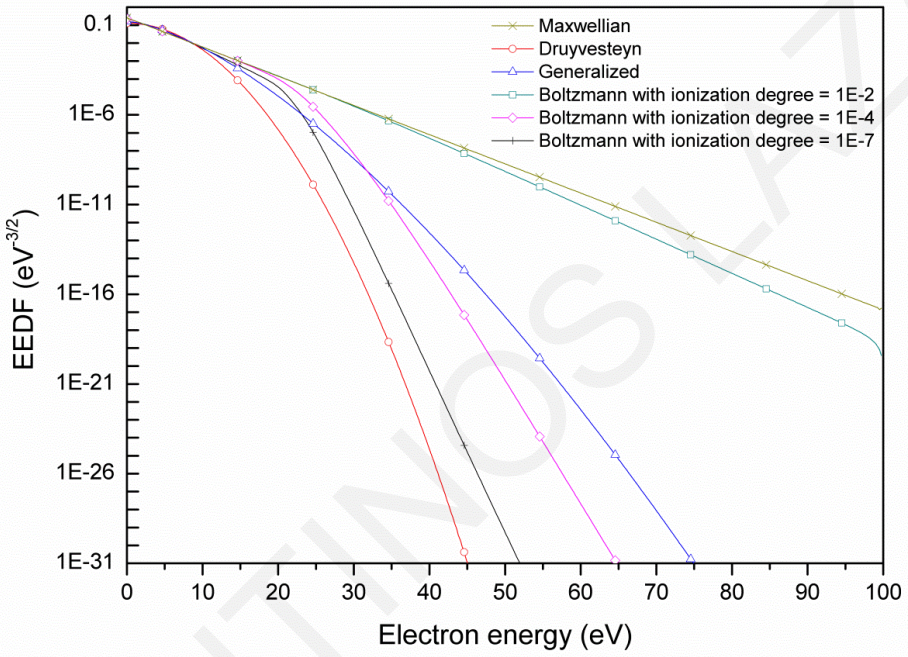

Figure 8: Comparison of the different EEDFs as a function of electron energy, with temperature = 350 K, electron density = 10^{18} m^{-3} and mole fraction of $He_m^* = 10^{-7}$.

3.4 Results and discussion

Initially, the model was validated with experimental results in order to ensure that it captures correctly the physics of the discharges and then the effect of the level of impurities was investigated.

3.4.1 Model Validation

From Figure 9, it can be observed that the experimental results as described in section 3.2 are in good agreement with the simulation results for 1 ppm nitrogen impurities. The discharge current for the same simulation model, but using different EEDF for the calculation of the model input

parameters is presented in Figure 10. The three different cases considered are obtained by solving Boltzmann's equation with the two-term approximation for three different ionization degrees: 10^{-2}, 10^{-4} and 10^{-7}. It can be observed that the discharge current is lower and wider for higher values of the ionization degree. This is attributed to the lower gap voltage needed to trigger breakdown for higher values of the ionization degree.

In order to further ascertain the validity of the model, supplementary verification with experimental and numerical results obtained from the literature was carried out. The experimental configuration and results can be found in [66]. In this case, the same model as presented above was used and the level of nitrogen impurities was set to 100 ppm. The experimental and simulation applied voltage and current measured in [66] is presented in Figure 11a and the results taken from our simulation are presented in Figure 11b, demonstrating good agreement. This provides confidence about the ability of the model to capture the physics behind this kind of discharge and as a result, it was subsequently used to study the effect of nitrogen impurities on the discharge evolution.

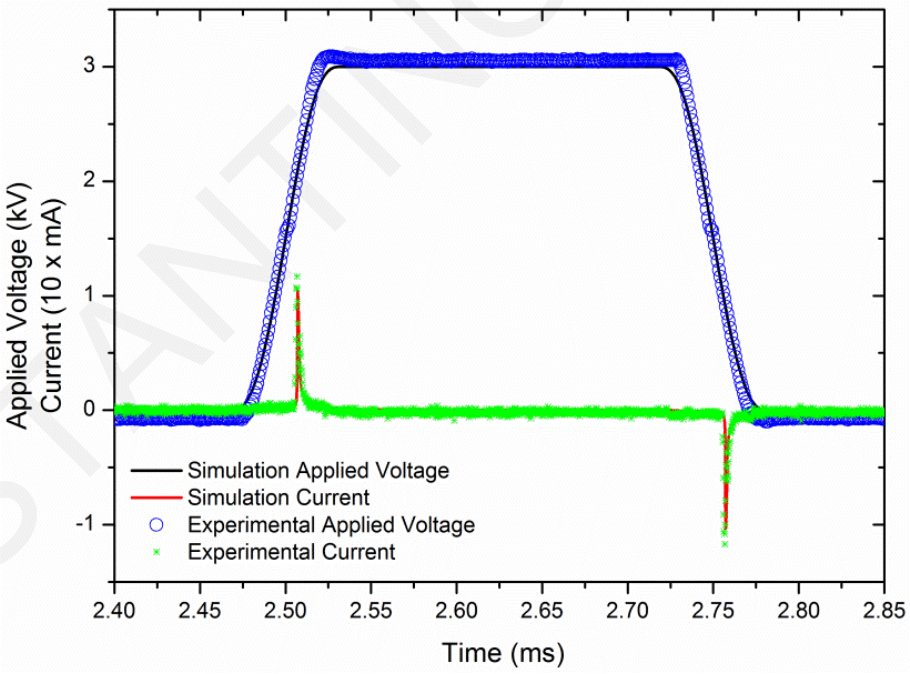

Figure 9: Simulation and experimental current and applied voltage as a function of time. The amplitude, frequency and rise time of the applied voltage are 3 kV, 2 kHz and 33 μs respectively.

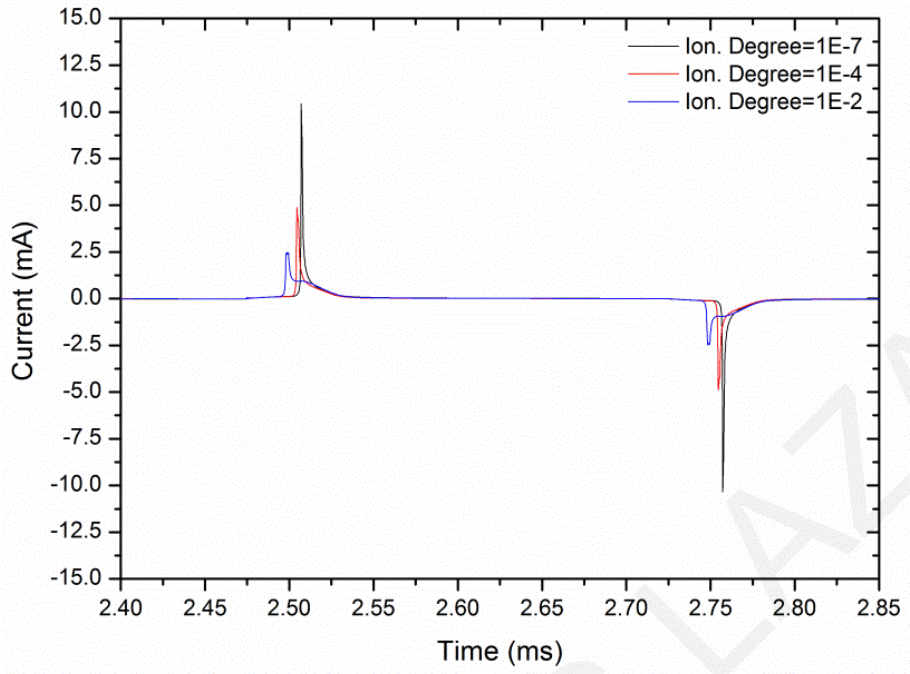

Figure 10: Simulated current as a function of time for three different ionization degrees: 10^{-2}, 10^{-4} and 10^{-7}, with temperature = 350 K, electron density = 10^{18} m^{-3} and mole fraction of He_m* = 10^{-7}.

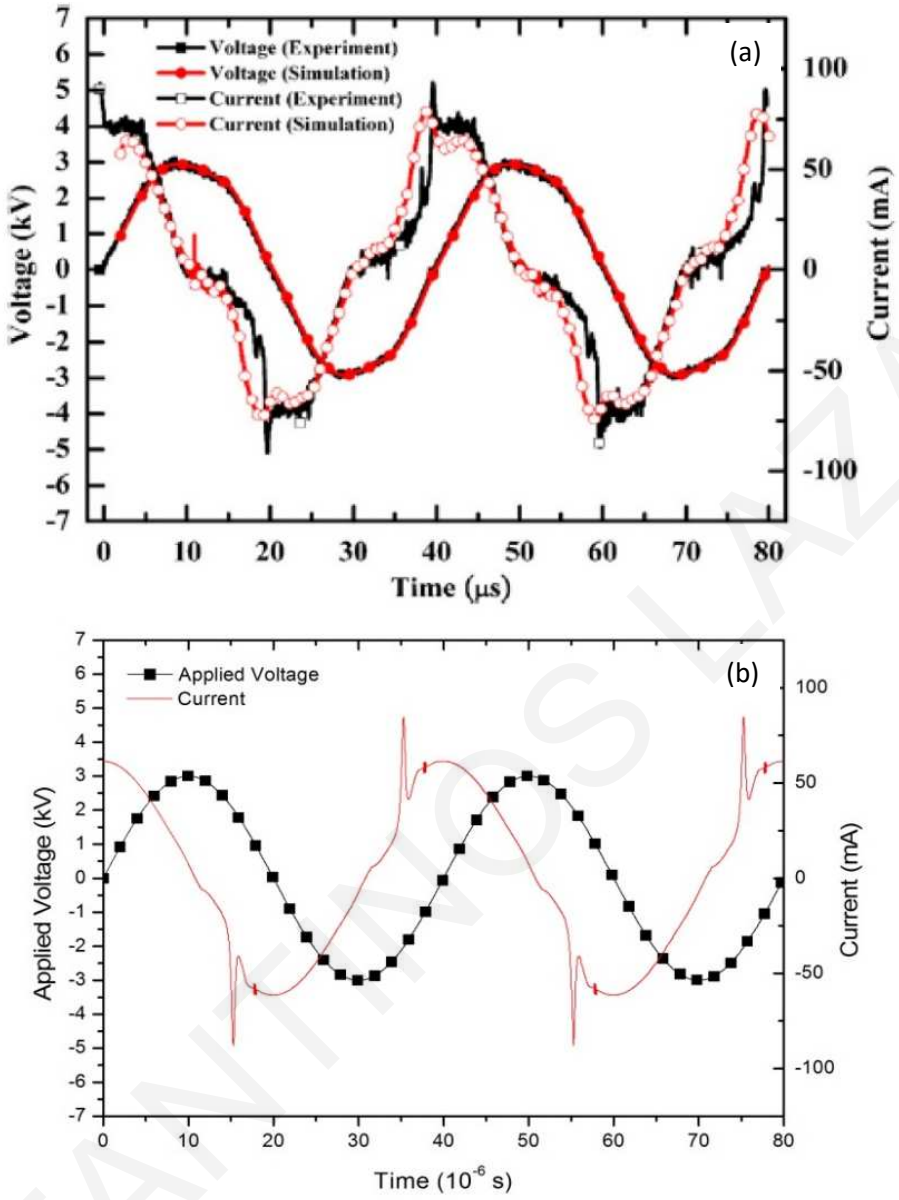

Figure 11: Comparison between the experimental and simulation applied voltage and current (a) as obtained in [63] **and (b) obtained by our simulation model for 100 ppm N_2. The amplitude and frequency of the applied voltage are 3 kV and 25 kHz respectively.**

3.4.1 Effect of Nitrogen impurity levels

The level of nitrogen impurities under investigation was in the range 0.1 – 500 ppm. This range was divided into five sub ranges by using three important criteria: the dominant charged species at breakdown, the trend of breakdown voltage and discharge current (Table 4). With the term trend, we mean how the discharge current or the breakdown voltage change (increase, decrease or remain constant) as a function of the level of nitrogen impurities.

In order to gain a better understanding of the processes that occur in the discharge gap, initially a detailed analysis will be presented. The following quantities are considered: applied voltage, gap voltage, discharge current, electron temperature, total average charge concentration, total average ion concentration, average electron concentration and average concentration of all charged species. Additionally, it is helpful to present the most important average reaction rates for the production and destruction of the most important charged species in the mixture as a function of time in order to shed more light into the processes that affect the evolution of the discharge.

Table 4: Different cases considered in the simulations.

Case	Level of nitrogen impurity (ppm)	Dominant ions species	Discharge current	Gap Voltage
1	0.1 – 3	He_2^+	Reduced	Reduced
2	3 – 35	He_2^+	Reduced	Increased
3	35 – 100	N_2^+	Increased	Reduced
4	100 – 150	N_2^+	Reduced	Reduced
5	150 – 500	N_4^+	Reduced	Reduced

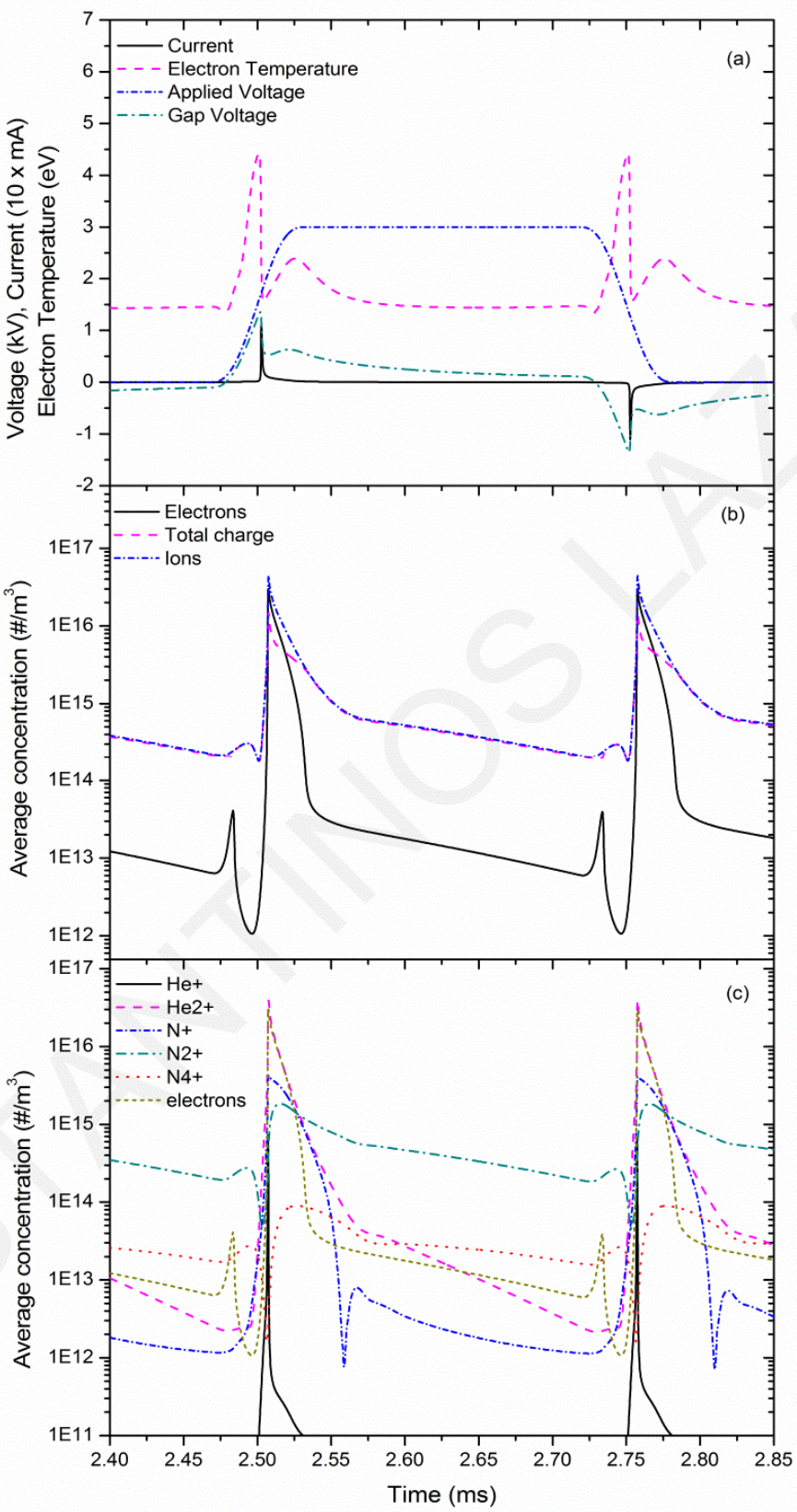

Figure 12: Temporal variation of the simulated spatial averaged plasma properties for a He-N_2 mixture (1 ppm of N_2) over a voltage cycle. The amplitude, frequency and rise time of the applied voltage are 3 kV, 2 kHz and 33 µs respectively.

The case of 1 ppm is studied below. As can be seen from Figure 12a, the discharge current exhibits the same behaviour during the first (rising part of the applied voltage) and second breakdown (falling part) but with opposite sign. The discharge also exhibits the characteristics of a glow discharge, evidenced by the very similar charge densities between electrons and positive ions on the first and second breakdown (Figure 12b) and due to the high discharge current (Figure 12a). As can be seen from Figure 12a breakdown occurs when the discharge current reaches its maximum value. Next, the behaviour of the most important ion species in the mixture is analyzed and useful information about the physics behind the evolution of the discharge and the way the nitrogen impurities affect the discharge characteristics is obtained.

From Figure 12b it can be observed that the concentration of electrons is generally much lower compared to the concentration of ions. The only instance where the concentration of electrons and ions is similar is during breakdown. While the applied voltage increases, the concentration of electrons increases as well (see first maximum of the electron concentration in Figure 12b). This happens because the electrons gain energy and they can cause ionization and excitation. Later the concentration of electrons reduces because of their movement towards the boundaries due to the presence of the electric field. Similar behaviour is exhibited by the ions but to a much lesser extent. The decrease in the concentration of electrons is much quicker than the ions since the electrons are much lighter. The concentration of electrons, ions and total charge increases sharply by the further increase of the applied voltage until breakdown. The term 'total charge' refers to the sum of the average concentration of ions minus the average concentration of electrons. From Figure 12c, it is observed that the sharp increase in the concentration of ions during breakdown is mainly caused by He_2^+, which subsequently reduces and stabilizes to approximately $\sim 2\ x\ 10^{14}\ atoms/m^3$ and consists mainly of charged N_2^+. To explain this point further the most important average reaction rates which are responsible for the production and destruction of He_2^+ as a function of time are presented in Figure 13a and Figure 13b. Similarly, Figure 14a and Figure 14b present the most important reaction rates for the production and destruction of charged N_2^+. The species He_2^+ and N_2^+ are studied more closely since they are the most important charged species in the mixture at breakdown and after breakdown respectively. From Figure 13a it is evident that the sharp increase of He_2^+ at breakdown is caused by reaction 18 (He**+He=>He_2^++He) [73]. However, the average rate of this reaction reduces sharply after breakdown. This can be explained by studying the electron temperature that represents the energy of electrons. From Figure 12a, it can be seen that

the electron temperature presents two peaks which occur before and after the breakdown and stabilizes at 1.5 eV. The significant increase of the electron temperature at the first peak is due to the increase of the applied voltage. The second peak results from the electron concentration decreasing faster than the ions because electrons are being lost on the boundaries. The remaining ions cause the increase of the gap voltage and consequently the electron temperature. With this high temperature before the breakdown, the electrons are able to cause ionization and excitation of the helium and nitrogen ground state species. This increases the concentration of species He_m*, He** and He^+ and consequently the concentration of He_2^+ through reaction 18 (Figure 13a). The thresholds for ionization and excitation of the helium reactions are higher than those of nitrogen as shown in Table A1, however due to the low level of impurities the dominant species at breakdown are the helium species. Finally the electron temperature after the breakdown decreases since the created charge carriers accumulate on the dielectrics (ions on the side of cathode and electrons on the side of anode) inducing an opposite electric field to the one created as a result of the applied voltage, thus canceling each other out and reducing the gap voltage and electron temperature. The low electron temperature means that the electrons are not able to cause ionization and excitation and as a consequence the concentration of He_m*, He** and He^+ reduces, causing a decrease in the concentration of He_2^+. From Figure 13a it is observed that the main reaction which contributes to the production of He_2^+ after the breakdown is reaction 26 (He_2*+He_2*=>He_2^++2He+e) since the concentration of He_2* remains high and constant between two successive breakdown events [72,73]. However, at higher level of impurities this is not valid. Finally, He_2^+ are mainly converted to N_2^+ and N^+ through the linked reactions 32 (He_2^++N_2=>N_2^++2He), 45 (He_2^++N_2+He=>N_2^++3He) and 33 (He_2^++N_2=>N^++N+2He) respectively (Figure 13b). As already mentioned, the total ion concentration remains constant at about $\sim 2\,x\,10^{14}\ atoms/m^3$ due to N_2^+. The concentration of N_2^+ increases during breakdown mainly due to reactions 28 (He_m*+N_2=>e+N_2^++He), 32, 44 (He_m*+N_2+He=>2He+N_2^++e) and 45 and remains constant because of reaction 29 (He_2*+N_2=>e+N_2^++2He), following the breakdown (Figure 14a). The rate for reactions 32, 28, 44 and 45 reduces after breakdown since the species He_2^+ and He_m* reduce as explained above, while the rate for reaction 29 remains constant since He_2* has constant concentration between two successive breakdown events [72,73]. From Figure 14b it can be seen that N_2^+ is mainly converted to N_4^+ through the linked reaction 41

(N_2^++He+N_2=>N_4^++He), but the major part of N_4^+ is converted back to N_2^+ through reaction 43 (N_4^++He=>N_2^++He+N_2) (Figure 14a).

At this point, it should be emphasized that the positive charge that accumulates at the cathode dielectric is mainly formed by He_2^+ since this forms the bulk of the ionizing wave. Additionally, the concentration of N_2^+ is increased when the gap voltage is significantly decreased due to shielding from the surface charge accumulation. This is an additional reason why the concentration of N_2^+ remains constant after the breakdown.

If only pure helium (first 27 reactions in Table A1) was considered, the total ions would follow the concentration of He_2^+ (Figure 12c). With the introduction of nitrogen impurities (46 reactions in Table A1) the concentration of ions remains at higher levels due to N_2^+. As a result, He_2^+ which is responsible for the breakdown has to contribute less on the total charge concentration in order to reach the appropriate value to trigger the breakdown. As shown above, the concentration of He_2^+ is highly dependent on the electron temperature. Since lower concentration of He_2^+ is needed, the required electron temperature for breakdown is lower too. This means that breakdown can occur at lower gap voltage. The above analysis highlights the reason for the decrease of the breakdown voltage by the introduction of the nitrogen impurities.

The same process is repeated for the falling part of the applied voltage. During this time, the surface charge accumulation is no longer shielded by the external electric field, thus the gap voltage is increased in the opposite direction until the next breakdown.

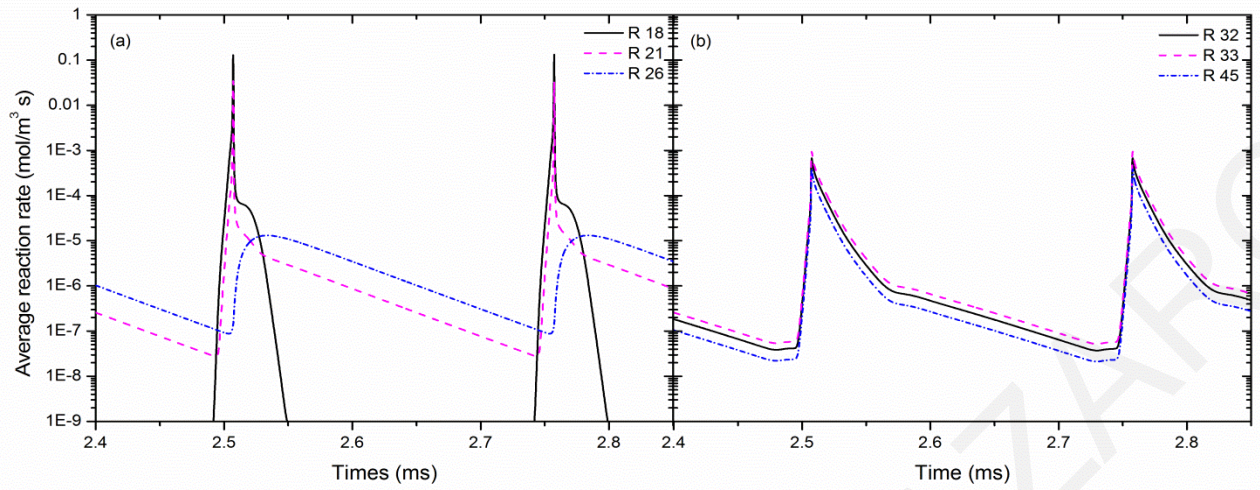

Figure 13: Simulation of the average reaction rates for (a) the production and (b) the destruction of He_2^+ as a function of time for 1 ppm nitrogen impurities.

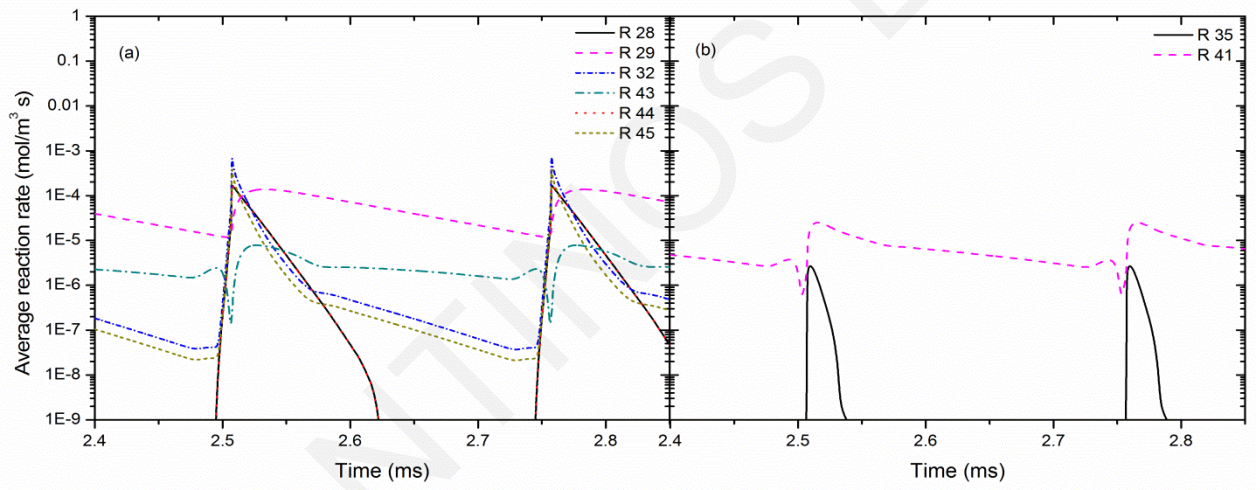

Figure 14: Simulation of the average reaction rates for (a) the production and (b) the destruction of N_2^+ as a function of time for 1 ppm nitrogen impurities.

The above detailed analysis highlights the processes occurring in the discharge gap, over a voltage cycle for the case of 1 ppm. With this in mind it is easy to understand the analysis that follows, which considers the influence of nitrogen impurities on: the dominant ions at breakdown, the discharge current and the breakdown voltage. In the entire range of impurities, the discharge current was symmetric (same magnitude during the rising and falling part of the applied voltage) and the discharge exhibits the characteristics of a glow mode. For this reason, the above detailed analysis (for the case of 1 ppm) will not be repeated for other levels of nitrogen impurities, as the processes occurring in the discharge gap are similar. Next, the different cases are further analysed.

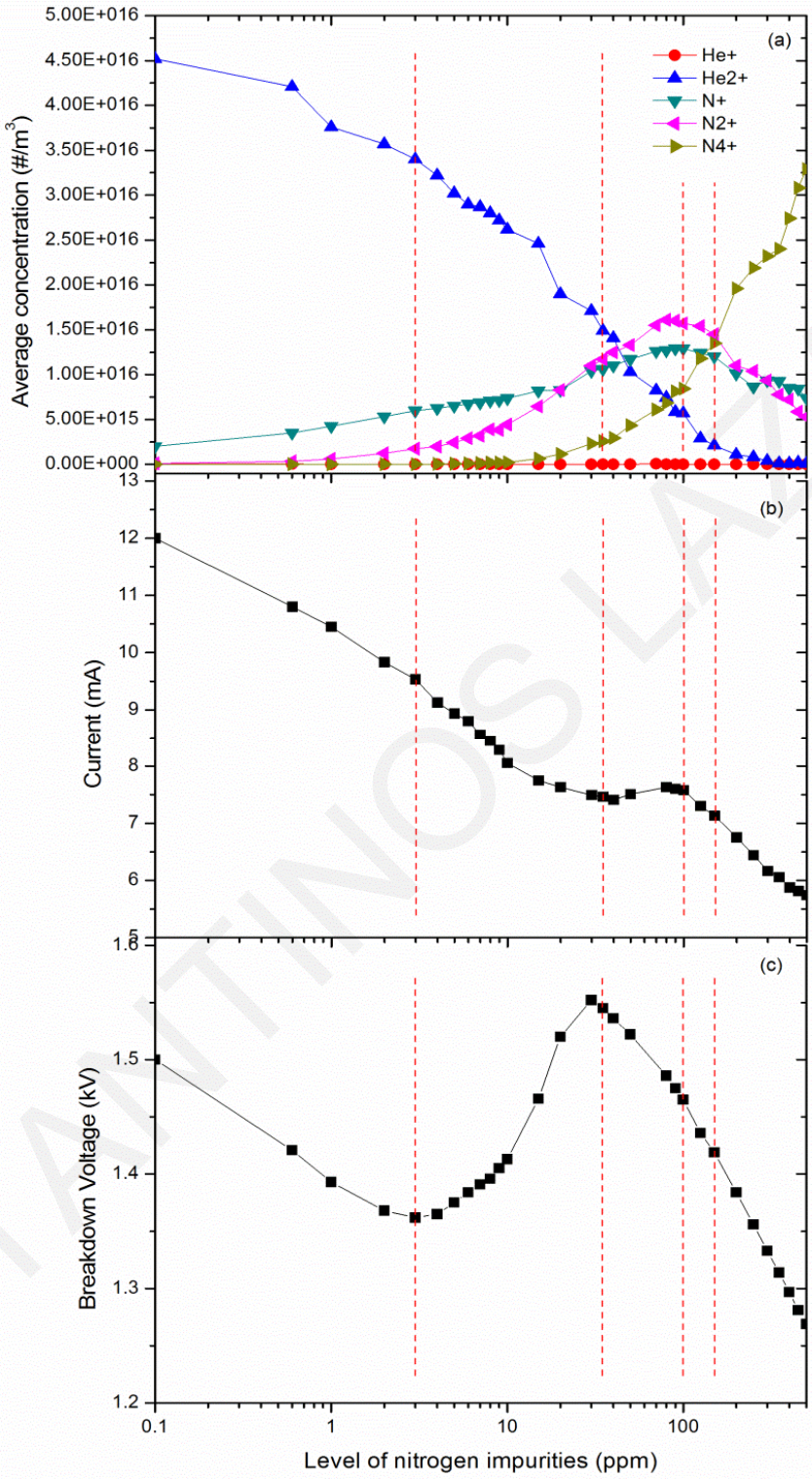

Figure 15: Simulated (a) average concentration of charged species at breakdown, (b) discharge current and (c) breakdown voltage as a function of the level of nitrogen impurities. The amplitude, frequency and rise time of the applied voltage are 3 kV, 2 kHz and 33 µs respectively.

0.1 to 3 ppm: The charge species He_2^+ is the dominant ion at breakdown in this range of nitrogen impurities, as can be seen in Figure 15a. The concentration of this species is much higher at breakdown compared to other charged species, confirming that it is the species responsible for the breakdown. From Figure 15b and Figure 15c, it is observed that, as the impurity level increases, the discharge current and breakdown voltage decrease. The reduction of these two important quantities is attributed to the reduction of the concentration of He_2^+, which is the responsible species for the breakdown. In order to trigger the breakdown, the total charge has to reach a specific value. As the impurity level increases, the concentration of total ions ends up at a higher value before the next breakdown. As a result, smaller contribution is needed from the species He_2^+, in order to reach the appropriate value and trigger the breakdown as explained earlier (see Figure 12c). The charged species N_2^+ is responsible for the high concentration of total ions before the next breakdown. Consequently, lower concentration of He_2^+ at breakdown means lower electron temperature and breakdown voltage. Additionally, the lower the concentration of He_2^+ at breakdown, the smaller the ion current density that will reach the cathode dielectric after the breakdown and as a result, the discharge current will be lower.

3 to 35 ppm: In this range of nitrogen impurities, the charged species He_2^+ remains the dominant ion at breakdown (see Figure 15a). However, the breakdown does not depend entirely on this species, but also on N^+ and N_2^+. As the impurity level increases from 3 to 35 ppm, the discharge current decreases whereas the breakdown voltage increases. The increase of the breakdown voltage is attributed to the slower ionization rate of the total ions. The increase of N_2 benefits reactions 32, 33 and 45 that convert He_2^+ (during breakdown) to N^+ and N_2^+. Due to this, the total charge needs more time to reach the appropriate value and trigger the breakdown. This means that the applied voltage will reach a higher value, and simultaneously the breakdown voltage will increase since they are proportional. On the other hand, the discharge current continues to decrease as a function of the level of nitrogen impurities due to the decrease of He_2^+. The reduction rate of the discharge current is lower at the end of this region, since the charged species N^+ and N_2^+ start to contribute to the breakdown (Figure 15a).

35 to 100 ppm: For the level of nitrogen impurities in the range of 35 – 100 ppm the charged species N_2^+ starts to become the dominant ion at breakdown (see Figure 15a). Important contribution to the breakdown is also provided by the charged species N^+. As the amount of the

impurities increases (from 35 to 100 ppm) the discharge, current increases slightly while the breakdown voltage decreases (Figure 15b and Figure 15c). The increase of N_2, benefits the production of N^+ and N_2^+ through reactions 33 (for N^+) and 28, 32, 44, 45 (for N_2^+). The species which contribute to these reactions are He, He_2^+, He_m*, and N_2. The concentration of He is constant since this is the bulk gas. So for higher concentration of N_2, lower concentration is needed from the species He_2^+ and He_m, in order for the charged species N^+ and N_2^+ to reach appropriate values to cause breakdown. Lower concentration of He_2^+ and He_m* means lower electron temperature and lower gap voltage. The above analysis highlights the reason of the reduction of the breakdown voltage as a function of the level of nitrogen impurities. Despite the decrease of the breakdown voltage, the concentration of N^+ and N_2^+ increases and this causes the small increase of the discharge current.

100 to 150 ppm: The charged species N_2^+ continues to be the dominant ion at breakdown up to 150 ppm. As the impurity level increases, the breakdown voltage and the discharge current decrease. In this range, the contribution of N_4^+ at breakdown increases while the contribution of N_2^+ and N^+ decreases. Due to the lower drift velocity of N_4^+, compared to the charged species N^+ and N_2^+, the flux of the ion current density towards the dielectric wall decreases. This explains the decrease of the discharge current. The decrease of the breakdown voltage is attributed to the lower contribution needed from the species He_2^+ and He_m* during breakdown, due to the high concentration of N_2.

150 to 500 ppm: The dominant ion species at breakdown is the charge species N_4^+ in this region, as reaction 41 is affected more by the increase of the nitrogen impurities [74]. The species that contribute to reaction 41 are He, N_2 and N_2^+. The concentration of He remains constant since this is the background gas while N_2 depends on the level of nitrogen impurities. For higher concentration of N_2, lower concentration of N_2^+ is needed in order for N_4^+ to reach the desirable value, which will cause breakdown. The concentration of N_2^+ during breakdown depends on the concentration of He_m* and He_2^+ (reactions 28, 32, 44 and 45). For lower concentration of N_2^+, the concentration of He_m* and He_2^+ has to be lower. This happens at lower value of electron temperature and consequently lower gap voltage. The above analysis highlights the reason for the decrease of the breakdown voltage by the increase of the nitrogen impurities in this range. The discharge current continues to decrease as a function of the level of the impurities, despite the fact

that the concentration of N_4^+ is increased. This is attributed to the lower drift velocity of N_4^+. It can also be seen that the higher the concentration of N_2, the higher the percentage of N_4^+ forming the ionizing wave. Due to the low, drift velocity of N_4^+, the flux of the ion current density towards the dielectric wall decreases. This explains the decrease of the discharge current and the reason of the wider current peak.

3.5 Conclusions

In this chapter, a plasma fluid model was used for the description of a helium barrier discharge in the presence of nitrogen impurities. The model was validated with experimental results and then was used to investigate the effect of nitrogen impurities on the evolution of the discharge. The level of nitrogen impurities in the model ranged from 0.1 – 500 ppm. The entire range was divided into five sub domains based on the following characteristics: (a) the dominant ion at breakdown, (b) the trend of the discharge current and (c) the trend of the breakdown voltage. Each domain was analysed separately, in order to understand how the level of nitrogen impurities affects the dominant ion and the discharge characteristics (discharge current and breakdown voltage). It was observed that the dominant ion at breakdown is significantly affected by the concentration of N_2. Specifically, at low level of impurities (0.1 to 35 ppm), the dominant ion at breakdown is the charged species He_2^+. As the impurity levels increase in the range of 35 – 150 ppm, the helium species He_m*, He^+ and He_2^+ are quickly converted to N_2^+ (during breakdown) which becomes the dominant ion. For higher levels of impurities (between 150 – 500 ppm), the charged species N_4^+ is the dominant ion. Furthermore, it has been found that, as the impurity level increases the breakdown voltage decreases. This was attributed to the lower contribution needed during breakdown from the helium species that are strongly dependent on the electron temperature and the gap voltage. However, an increase of the breakdown voltage in the range of 3 – 35 ppm was observed, due to the decrease of the ionization rate of the total ions. Finally, the discharge current is mostly reduced for the level of nitrogen impurities considered, with the exception of the range 35-100 ppm. At low levels of impurities, this was attributed to the decrease of the concentration of the dominant ion (He_2^+), while at higher levels it was attributed to the low drift velocity of the charged species N_4^+.

Chapter 4

Simulation model of a helium-nitrogen-oxygen mixture

4.1 Introduction

The purpose of this chapter is to present the numerical model developed for the study of helium DBD in the presence of dry air (79% N_2 and 21% O_2) impurities. The plasma species in the model are governed by the equations and boundary conditions presented in chapter 2, with the appropriate chemistry for the helium-nitrogen-oxygen species. Initially, the model is validated with experimental results to ensure its correctness and then was used to numerically investigate the influence of air traces in the evolution of the helium DBD. The level of dry air impurity was in the range from 0 to 1500 ppm, which corresponds to the most commonly encountered range in atmospheric pressure discharge experiments. In the literature, there are several studies investigating numerically the effect of impurities in helium discharges, He+N_2 [32,74–80], He+O_2 [81–83] and He+air [23,28,66,84,85]. However, there is no published work regarding the effect of dry air impurities on the discharge evolution in a wide range of compositions. In order to be able to characterize and optimize applications that are based on helium DBDs, it is very important to understand the effect of the air traces on the discharge evolution.

4.2 Experimental setup

The experimental setup that was used for the validation mainly consists of two parallel electrodes covered by dielectric layers of the same thickness. On one of the electrodes, a high voltage is applied, while the other is grounded. The gap between the dielectric layers is filled with helium gas (purity of 99.999 vol %) at atmospheric pressure, after the discharge cell was pumped down to 10 Pa. The experimental setup and operational parameters, reported in [21], are summarized in Table 5. It is noted that the discharge exhibits the characteristics of the homogenous mode.

Table 5: Operational parameters of experimental setup from [21]**.**

Relative permittivity (ε_r)	9.4
Gap between dielectrics (mm)	5
Dielectric thickness (mm)	0.7
Electrode area (cm^2)	4
Gas pressure (atm)	1
Gas temperature (K)	300
$Voltage_{p\text{-}p}$ (kV)	2
Voltage waveform	sinusoidal
Frequency (kHz)	10
Helium gas purity (%)	99.999

4.3 Input parameters for the model

For the description of the experiment presented in section 4.2, 27 species and 153 reaction channels were considered. The species included in the model are electrons, He^+ and He_2^+ ions, He ground-state atoms, He_2* excimers, He_m excitation to metastable atoms He(2^3S) and He(2^1S), N_2^+ and N_4^+ ions, N_2 ground state molecules and N atoms, $N_2(A)$, $N_2(B)$, $N_2(a)$ and $N_2(C)$ nitrogen excited species, O, O_2 and O_3 ground state atoms, molecules and polyatomic molecules, $O_2(v)$ vibrational excited states $(v = 1 - 4)$, O^-, O_2^-, O_3^-, O_2^+ and O_4^+ ions, O^1S and O^1D excited atoms, $O_2(a_1\Delta_g)$ and $O_2(b^1\Sigma_g^+)$ excited molecules. Based on the idea of [86], the species $N_2(A)$ represents the excitation of N_2 at $N_2\left(A^3\Sigma_u^+ (v = 0 - 4)\right)$, $N_2\left(A^3\Sigma_u^+ (v = 5 - 9)\right)$ and $N_2\left(A^3\Sigma_u^+ (v > 9)\right)$, the species $N_2(B)$ represents the excitation of N_2 at $N_2\left(B^3\Pi_g\right)$, $N_2(W^3\Delta_u)$ and $N_2(B^3\Sigma_u^-)$, the species $N_2(a)$ represents the excitation of N_2 at $N_2(a^1\Sigma_u^-)$, $N_2\left(a^1\Pi_g\right)$ and $N_2(W^1\Delta_u)$ and the species $N_2(C)$ represents the excitation of N_2 at $N_2(C^3\Pi_u)$, $N_2\left(E^3\Sigma_g^+\right)$ and $N_2(a^1\Sigma_g^+)$. The NOx molecules were not considered in the kinetic scheme because they increase the computational time without affecting significantly the simulation results. The kinetic scheme (reaction channels) used is mainly taken from [15,66,67,80,81,86,87].

The electron transport parameters and the rate coefficients of reactions 1-4, 28-41 and 63-74 (see Table B1 in Appendix B), which are used as input parameters in the fluid model, are calculated by averaging specific quantities and the electron impact cross sections over the electron energy

distribution function (EEDF) [48,88]. This indicates the importance of the chosen EEDF and electron impact cross sections on the simulation results. The electron impact cross sections are available on the open access LXCat website [89].

In the literature, there are two approaches to solve Boltzmann's equation: either kinetic [48] or statistical [90,91]. However, for the case of helium, both methods give similar results [92]. This is not true for other gases. In this work, the two term-approximation (kinetic) as described by [48] is used to solve Boltzmann's equation.

Moreover, input parameters such as electron concentration, gas temperature, ionization degree, mole fractions of some species and the electron impact cross sections are required to solve Boltzmann's equation. The gas temperature is set the same as the temperature of the experiment, while the electron density is estimated from the experimental discharge current. Since the discharge in the experiment exhibits the characteristics of the homogeneous mode, the gas is assumed to be weakly ionized [58,93]. The mole fraction of species $\mathrm{He_m}, \mathrm{O}, \mathrm{O_2(v)}, \mathrm{O_2(a)}$ and $\mathrm{O_2(b)}$ is estimated from [81], based on the level of oxygen impurities that is used in the simulation model. For this study, the concentration of air was set at 80 ppm because this value gave the best agreement with the experimental results.

From the above analysis, the input parameters for the Boltzmann solver are defined as follows: gas temperature $\mathrm{T_g} = 300$ K, electron density= $10^{20}\ m^{-3}$, ionization degree = 10^{-7}, mole fraction of $\mathrm{He_m} = 2 \cdot 10^{-9}$, $\mathrm{O} = 10^{-7}, \mathrm{O_2}(b) = 10^{-8}$, $\mathrm{O_2}(a) = 5 \cdot 10^{-8}$, $\mathrm{O_2}(v) = 6 \cdot 10^{-9}$ and mole fraction of air = 0.8×10^{-4} (79% N_2 and 21% O_2). The chosen electron impact cross sections will be analysed in the following paragraph. It is also worth noting that the electron impact cross sections affect both the calculation of the EEDF and the rate coefficients. The EEDF calculated at 80 ppm level of air was used for all air concentrations, since it does not change significantly in the range of air concentrations considered in this study (see Figure 16).

Concerning the electron impact cross sections, these should be complete and consistent [92,94,95]. The term 'complete' means that the chosen database should be able to describe the main electron momentum-loss, energy-loss and number-changing processes (ionization, attachment, and recombination). On the other hand, 'consistent' refers to the ability of the database to predict correctly the electron swarm parameters when this database is used as input to the Boltzmann

solver [48]. More details about the different databases for electron impact cross section and the chosen criteria are described in the literature [92,94,95]. In this study, the Morgan database is used for the description of the electron scattering cross section with the He gas, while for the N_2 and O_2 gases, the IST-Lisbon database was used [96,97]. These databases are complete and predict the swarm parameters with good accuracy [92,98]. For the electron impact excitation of O atoms to $O(^1S)$ and the attachment of $O_2(a_1\Delta_g)$, $O_2(b^1\Sigma_g^+)$ [96] and $O_2(v)$ [99], the Morgan and TRINITI databases are used. All the parameters used for the calculation of the EEDF are summarized in Table 6.

The diffusion coefficients for the species He, He_m, N, N_2, $N_2(A)$, $N_2(B)$, $N_2(a)$, $N_2(C)$, O, O_2, O_3, O^1S, O^1D, $O_2(a_1\Delta_g)$ and $O_2(b^1\Sigma_g^+)$ are calculated from the kinetic theory [51,52]. For the excited species, the diffusion coefficient is considered the same as for their corresponding neutral species. The diffusion coefficient of He_2* is taken from [100] and the mobilities of He^+, He_2^+, N_2^+, N_4^+, O_2^+, O_4^+, O^-, O_2^- and O_3^- are taken from experimental values [70,71,101].

The surface reactions, reaction probabilities, seec and mese considered on the dielectric surface are given in Table 7. The surface reactions and reaction probabilities are taken from [18,81,102]. On the other hand, the electrons emitted from the dielectric surface are attributed to the intrinsic electrons and the trapped electrons in the shallow traps of dielectric surfaces. The latter mechanism has the most important contribution, since these electrons require less energy to be released [58]. However, the secondary electron emission coefficient is not trivial because the surface charges on the dielectrics are not known and in most cases this is considered as an "adjustable parameter" [103,104]. For that reason, the seec is varied until simulation and experimental results match. It is important to note that the energy required to release electrons from the dielectric surfaces is taken mainly from the ions and excited species that remain in the discharge gap from the previous breakdown [58].

For the case of atmospheric pressure glow discharge (APGD), this energy is mainly provided by the "memory" ions that remain in the positive column region [59] from the previous breakdown. On the other hand, for atmospheric pressure, Townsend discharge (APTD), this energy is provided by the "memory" excited species, which are created close to the anode from the previous breakdown. More details on this point can be found in [58]. As in the experiment [21], the discharge has the characteristics of the APGD and it was assumed that only "memory" ions are

responsible for extracting electrons from the dielectrics. In our simulation, the seec which gave the best results in reproducing the experimental results is summarized in Table 7.

The mean initial energy of the released electrons depends on the ion energy (ionization energy). It is noted that the helium ions have higher energy compared to the nitrogen and oxygen ions (see Appendix B, Table B1). For the helium ions, a mean initial energy of 5 eV for the secondary electrons was used which was the same as in [53], while for nitrogen and oxygen a mean initial energy of 3 eV was used since these ions have lower intrinsic energy.

For all the species in the mixture, a uniform initial density of $10^{13}\ 1/m^3$ was set (except for the He which is the background gas, and the densities of N_2 and O_2 which are defined based on the level of air content in the mixture). Different initial densities have also been used in the range of $10^{11} - 10^{14}\ 1/m^3$ yielding similar simulation results.

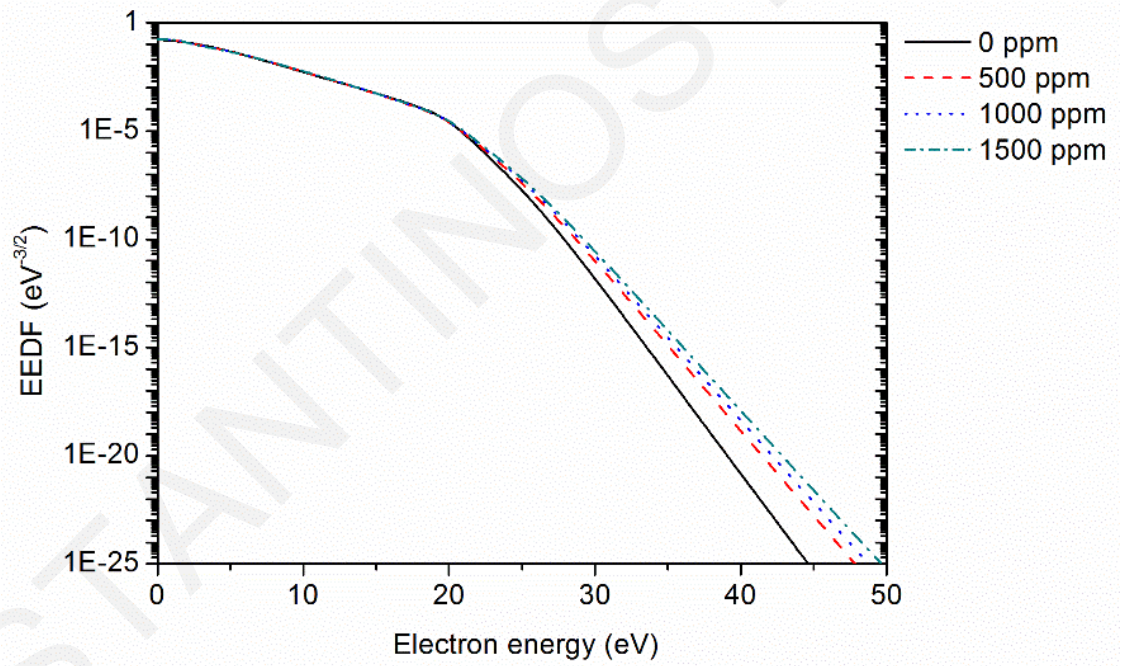

Figure 16: Comparison of the different EEDFs as a function of electron energy, at a mean electron energy of 4 eV. The legend represents the air content in the mixture.

Table 6: Input parameters for the Boltzmann solver [48,105]**.**

Gas temperature	300 K
Electron density	$10^{20}\ m^{-3}$
Ionization degree	10^{-7}
He_m mole fraction	$2 \cdot 10^{-9}$
O mole fraction	$1 \cdot 10^{-7}$
O_2(b) mole fraction	$1 \cdot 10^{-8}$

O_2(a) mole fraction	$5 \cdot 10^{-8}$
O_2(v) mole fraction	$6 \cdot 10^{-9}$
N_2 mole fraction	6.32×10^{-5} (79% of 80 ppm of Air)
O_2 mole fraction	1.68×10^{-5} (21% of 80 ppm of Air)

Table 7: Surface reactions, reaction probabilities, seec and mese.

No	Surface Reaction [a)]	Reaction probability[a)]	seec	mese
1	$He_m^* + Surface \rightarrow He$	1	0	0
2	$He_2^* + Surface \rightarrow 2He$	1	0	0
3	$He^+ + Surface \rightarrow He$	1	$2 \cdot 10^{-2}$	5
4	$He_2^+ + Surface \rightarrow 2He$	1	$2 \cdot 10^{-2}$	5
5	$N + Surface \rightarrow 0.5N_2$	0.01	0	0
6	$N_2(A) + Surface \rightarrow N_2$	0.5	0	0
7	$N_2(B) + Surface \rightarrow N_2$	0.5	0	0
8	$N_2(a) + Surface \rightarrow N_2$	0.5	0	0
9	$N_2(C) + Surface \rightarrow N_2$	0.5	0	0
10	$N_2^+ + Surface \rightarrow N_2$	1	$1 \cdot 10^{-3}$	3
11	$N_4^+ + Surface \rightarrow 2N_2$	1	$1 \cdot 10^{-3}$	3
12	$O + Surface \rightarrow 0.5O_2$	0.02	0	0
13	$O(^1D) + Surface \rightarrow O$	1	0	0
14	$O(^1S) + Surface \rightarrow O$	1	0	0
15	$O_2(v) + Surface \rightarrow O_2$	0.2	0	0
16	$O_2(a) + Surface \rightarrow O_2$	0.0004	0	0
17	$O_2(b) + Surface \rightarrow O_2$	0.02	0	0
18	$O_3 + Surface \rightarrow O_3$	1	0	0
19	$O^- + Surface \rightarrow 0.5O_2$	1	0	0
20	$O_2^- + Surface \rightarrow O_2$	1	0	0
21	$O_3^- + Surface \rightarrow O_3$	1	0	0
22	$O_2^+ + Surface \rightarrow O_2$	1	$2 \cdot 10^{-5}$	3
23	$O_4^+ + Surface \rightarrow 2O_2$	1	$2 \cdot 10^{-5}$	3

[a] ref [18,81,102]

4.4 Results and discussion

An important part of this study is the development of an appropriate model for the description of helium discharges in the presence of dry air impurities. In order to ensure its correctness, the model was validated with experimental results [21]. Then, the level of air impurities was varied and its effect on plasma dynamics and chemistry was studied. Given that the breakdown has the

characteristics of the homogeneous mode, the use of a one dimensional model to interpret the experimental results is justified.

4.4.1 Model validation

The validation of the model is based on the electrical measurements from the experiment described in [21]. The quantities, which were compared with the simulation results, are the discharge current, the breakdown voltage, the memory voltage and the amplitude of the applied voltage when breakdown occurs. Figure 17 shows the comparison between the experimental results reported in [21], for atmospheric pressure DBD working in He (purity 99.999 vol %) after 99.99% of the air from the discharge chamber was previously removed, and our simulation results for DBD in He with 80 ppm air impurities. Here the air concentration was set at 80 ppm because this gave the best reproduction of the experimental results. From Figure 17, a very good agreement is observed. In particular, the simulation discharge current and breakdown voltage have an error of less than 2.5 and 10 % respectively compared to the experimental results. These errors are within acceptable limits. Furthermore, breakdown occurred at about 0.7 kV, both for the simulation and experiment. The simulation results presented correspond to the 9^{th} voltage cycle after steady-state has been reached. Specifically, steady state is typically reached 2–3 ac cycles after the first breakdown.
The above validation of the simulation results provides us confidence about the ability of the model to capture the physics behind this kind of discharges and as a result, it was subsequently used to study the effect of dry air traces on the discharge evolution.

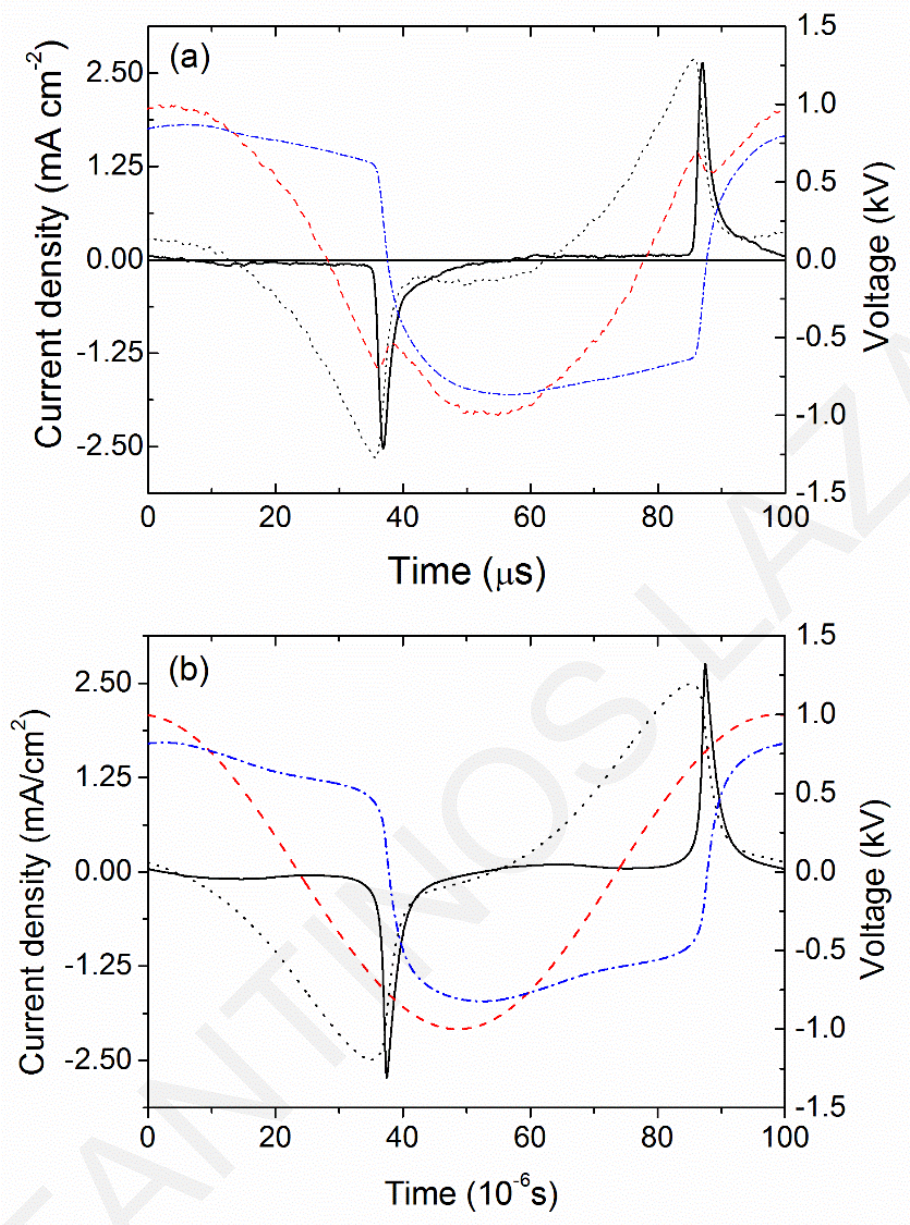

Figure 17: Comparison between (a) the experimental results reported in [21] **for atmospheric pressure DBD working in He (purity 99.999 vol%) and (b) our simulation results for DBD in He with 80 ppm air impurities. The black line represents the discharge current, the dashed red line the applied voltage, the dotted black line the gap voltage and the dashed dotted blue line the memory voltage.**

4.4.2 Effect of dry air concentration in helium DBD

The dry air contents in the helium DBD were investigated in the range from 0 to 1500 ppm. For a better interpretation of the results, this range was divided into four sub-ranges based on the following criteria: the discharge ignition, the discharge mode and the symmetry of the discharge current. With the term symmetric current, we mean that the current exhibits the same behaviour

during both parts of the voltage cycle, but with a different sign. The four different cases are presented in Table 8.

Before proceeding with the analysis of Table 8, it was considered necessary to describe in detail the main processes that occur in the discharge gap over a voltage cycle. This will help us thereafter in the interpretation of the results presented in Table 8. In order to simplify the analysis, the case of 150 ppm air was chosen, as it exhibits symmetric characteristics.

Table 8: Different cases considered in the simulations.

Case	Level of air impurity (ppm)	Discharge ignition	Discharge mode	Discharge current
1	0 – 55	No	---	---
2	55 – 225	Yes	Glow	Symmetric
3	225 – 1000	Yes	Glow	Non-symmetric
4	1000 – 1500	No	---	---

4.4.3 150 ppm level of air impurity

As can be seen from Table 8, for the 150 ppm concentration of dry air, the discharge exhibits the characteristics of the glow mode and the discharge current is symmetric. The dominant positive and negative species are O_2^+ and electrons respectively, as will be demonstrated below. In glow-like discharges, the concentration of dominant ions reaches its maximum value near the cathode ($\sim 10^{17}\ 1/m^3$), thus disturbing the electric field [58]. The spatio-temporal concentration of the O_2^+ and electrons, and the absolute magnitude of the electric field are presented in Figure 18, together with the applied voltage, gap voltage and discharge current. It is noted that the vertical axis in Figure 18b-d represents the spatial position across the parallel plate barrier discharge. In the simulation, the voltage is applied at the 6.4 mm point, while the point at 0 mm is grounded. Consequently, for positive polarity of the applied voltage, the 6.4 mm point represents the anode while the 0 mm point the cathode. The polarity of the applied voltage is illustrated on the graph.

From Figure 18a, it is observed that two individual breakdown events occur during the voltage cycle, with a single current peak per half period. The first breakdown occurs during the falling part of the applied voltage, while the second breakdown occurs during the rising part of the applied voltage. These breakdown events are a result of the voltage increase in the gap. As displayed in Figure 18a, the gap voltage follows a pattern similar to the applied voltage and reaches its

maximum value at the time of breakdown. After the breakdown, the gap voltage is reduced and approaches zero because of the surface charge accumulation on the dielectrics, which shields the electric field of the applied voltage. For this reason, a single current peak is observed at each breakdown event. The symmetric characteristics of the discharge are evident from the same behaviour and absolute magnitude of the discharge current during both breakdown events. The opposite sign of the discharge current arises from the inversion of the voltage polarity. On the other hand, evidence of the glow-like discharge, is the maximum values attained by the electrons and the O_2^+ (dominant ions in the mixture) near the cathode during the breakdown events (see Figure 18b and Figure 18c). This high concentration of ions disturbs the electric field near the cathode (Figure 18d), which is also a characteristic of the glow mode [58,106].

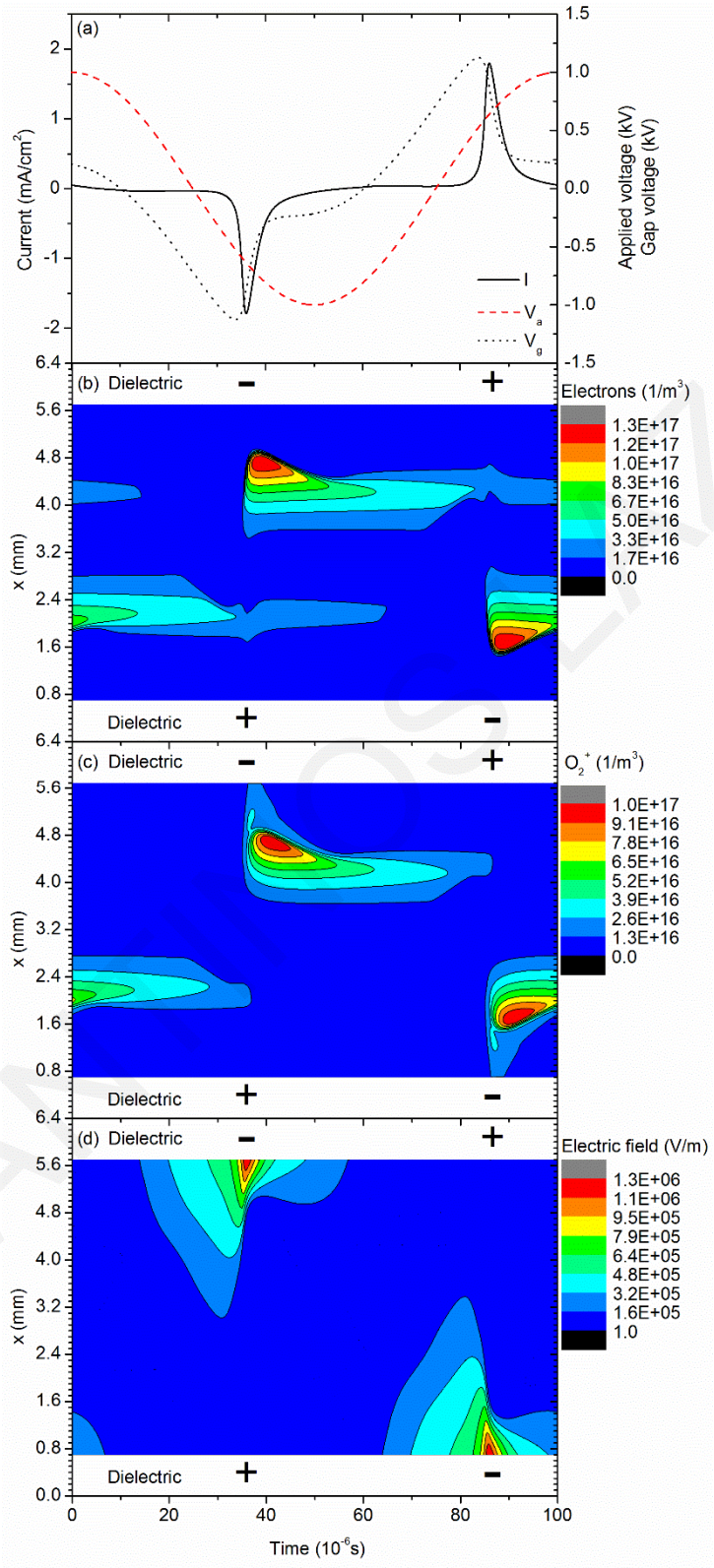

Figure 18: Simulation results of (a) the applied voltage, gap voltage and discharge current, and (b-d) the spatially-temporally resolved density distribution of electrons, O_2^+ and absolute magnitude of the electric field respectively (150 ppm), over a voltage cycle. The amplitude and frequency of the applied voltage are 1 kV and 10 kHz respectively.

In order to further understand the physics behind the discharge event, the evolution of positive and negative ions in the mixture during a voltage cycle is further analysed. Initially the positive ions are investigated. The average concentration of positive ions during a voltage cycle is captured in Figure 19, together with the applied voltage, gap voltage, electron temperature and discharge current. As shown in Figure 19, the concentration of ions is increased during the increase in the electron temperature. After the breakdown events, the ion concentrations are mostly reduced because of the reduction of the electron temperature. It is noted that the electron temperature follows a pattern similar to the absolute value of the gap voltage [79].

Figure 19b clearly indicates that the most important positive ion in the mixture is O_2^+. This proves that even a weak concentration of impurity has a great influence on plasma composition, despite the much higher concentration of helium in the mixture. In comparison to O_2^+, the density of O_4^+ is lower and remains almost constant between the two consecutive breakdowns. On the other hand, the nitrogen ions (N_2^+ and N_4^+) are not as important as O_2^+, despite the higher concentration of nitrogen molecules in the air. Regarding the helium ions (He^+ and He_2^+), these have negligible densities compared to the nitrogen and oxygen ions during the breakdown events.

In order to shed more light into the processes that affect the evolution of ions, the most important processes of dominant positive ion (O_2^+) production and destruction in the mixture are presented in Figure 20. The criterion used for choosing the production and destruction processes was to have a maximum value higher than $8 \cdot 10^{-5}$ and $4 \cdot 10^{-5}$ $[\mathrm{mol/m^3 s}]$ respectively. Reactions with lower maximum values compared to the mentioned ones appear not to affect the simulation results and hence their choice as thresholds.

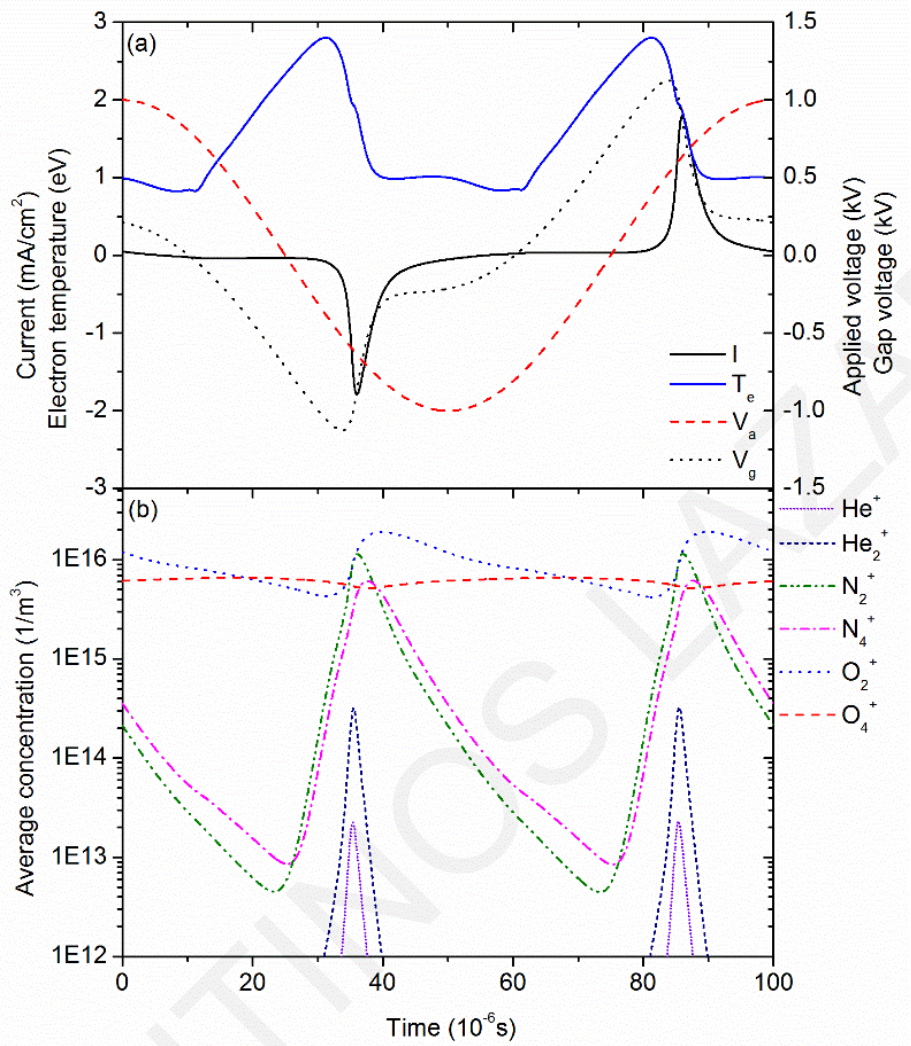

Figure 19: Simulation results of (a) the applied voltage, gap voltage, discharge current and average electron temperature, and (b) the average concentration of positive ion species for a He-air mixture (150 ppm) over a voltage cycle. The amplitude and frequency of the applied voltage are 1 kV and 10 kHz respectively.

From Figure 20a, it can be seen that the Penning ionization ($He_m+O_2=>O_2^++He+e^-$, R107) of O_2 by He_m is the most important reaction for O_2^+ production. The remaining important reactions for O_2^+ production are more than one order of magnitude lower. These processes are the Penning ionization of O_2 by He_2* ($He_2*+O_2=>O_2^++2He+e^-$, R108), the direct ionization of ground state O_2 molecules ($e+O_2=>2e+O_2^+$, R74) and the charge transfer reactions ($He_2^++O_2=>2He+O_2^+$, $N_2^++O_2=>N_2+O_2^+$ and $N_4^++O_2=>2N_2+O_2^+$ R110, R134 and R135 respectively) associated with the helium and nitrogen ions. This also explains the lower concentration of helium and nitrogen ions (He_2^+, N_2^+ and N_4^+) during the breakdown events (see Figure 19b), as they are converted to oxygen ions.

Our calculations show that the destruction of O_2^+ is almost completely determined by the losses at the boundaries (B1 and B2, see Figure 20b). B1 and B2 refer to the dielectric layers which cover the ground contact and the contact of the applied voltage respectively. On the contrary, the loss of O_2^+ due to volume processes is more than one order of magnitude lower. From these processes, the three-body charge transfer reaction ($O_2^+ + O_2 + He => O_4^+ + He$, R106) is the most important. Other loss processes are determined by the recombination of O_2^+ with electrons ($e^- + O_2^+ => 2O$, R75) and with O_2^- ($O_2^+ + O_2^- + He => 2O_2 + He$, R113).

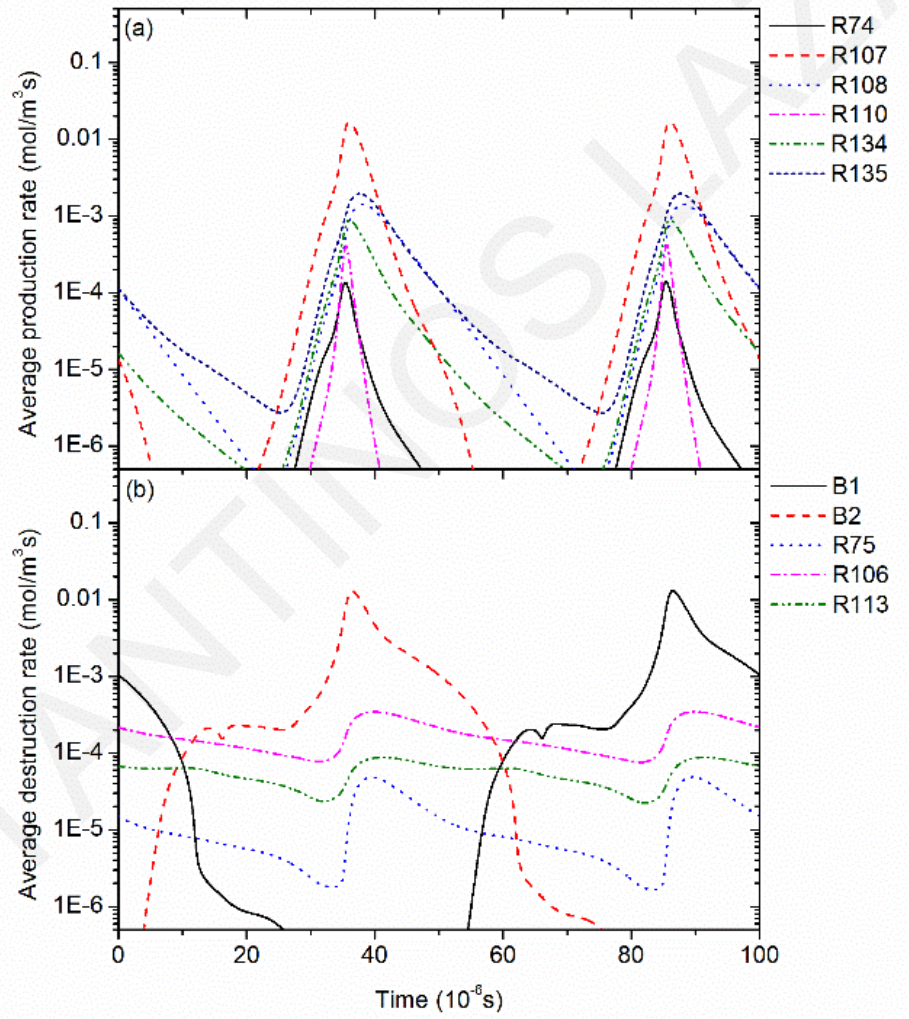

Figure 20: Simulation of the average rates for (a) production and (b) destruction of O_2^+ as a function of time for 150 ppm dry air.

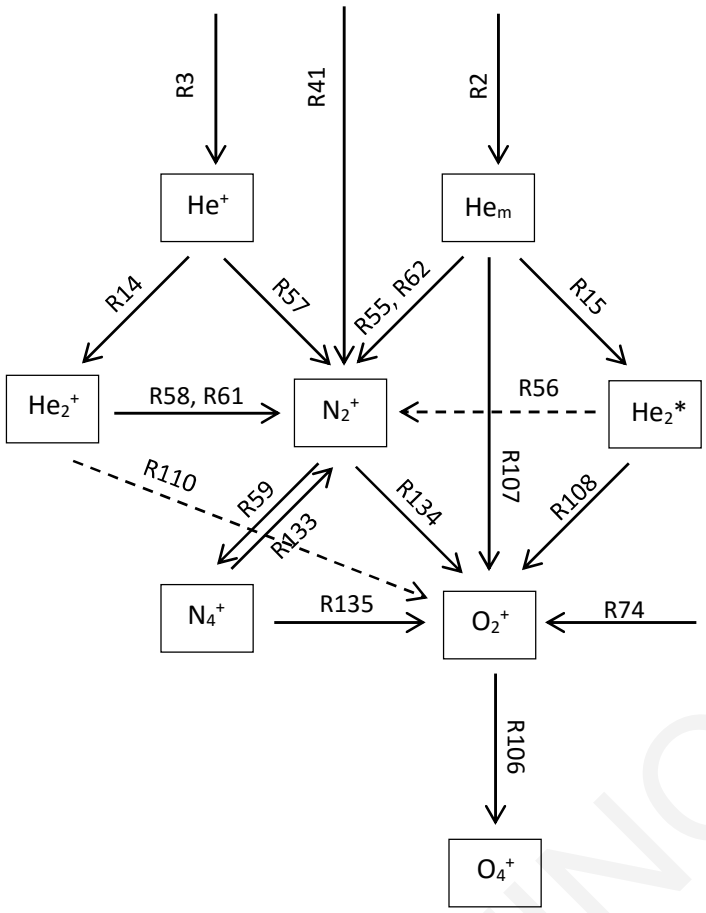

R2: $e^- + He \rightarrow e^- + He_m$
R3: $e^- + He \rightarrow 2e^- + He^+$
R14: $He^+ + 2He \rightarrow He_2^+ + He$
R15: $He_m + 2He \rightarrow He_2^* + He$
R41: $e^- + N_2 \rightarrow 2e^- + N_2^+$
R55: $He_m + N_2 \rightarrow e^- + N_2^+ + He$
R56: $He_2^* + N_2 \rightarrow e^- + N_2^+ + 2He$
R57: $He^+ + N_2 \rightarrow N_2^+ + He$
R58: $He_2^+ + N_2 \rightarrow N_2^+ + 2He$
R59: $N_2^+ + He + N_2 \rightarrow N_4^+ + He$
R61: $He_2^+ + N_2 + He \rightarrow N_2^+ + 3He$
R62: $He_m + N_2 + He \rightarrow N_2^+ + 2He + e^-$
R74: $e^- + O_2 \rightarrow 2e^- + O_2^+$
R106: $O_2^+ + O_2 + He \rightarrow O_4^+ + He$
R107: $He_m + O_2 \rightarrow O_2^+ + He + e^-$
R108: $He_2^* + O_2 \rightarrow O_2^+ + 2He + e^-$
R110: $He_2^+ + O_2 \rightarrow O_2^+ + 2He$
R133: $N_4^+ + O_2 \rightarrow O_2 + N_2 + N_2^+$
R134: $N_2^+ + O_2 \rightarrow N_2 + O_2^+$
R135: $N_4^+ + O_2 \rightarrow 2N_2 + O_2^+$

Figure 21: Schematic diagram of the most important reaction pathways for ion production.

The most important reaction pathways for ion production are presented in Figure 21 to elucidate the underlying mechanisms responsible for the above results. As illustrated in the schematic diagram, the increase of ion densities is almost completely determined by the increase of He_m and He^+. The concentration of the former species is increased during the increase of the electron temperature (see Figure 19a). After the breakdown, the production of He_m and He^+ is reduced because of the low electron temperature.

From Figure 21, it can be seen that the helium metastable atoms (He_m) are mainly de-excited by producing He_2*, N_2^+ and O_2^+ through reactions 15, 55, 62 and 107. After that, He_2* is decomposed during the production of N_2^+ and O_2^+ through the Penning reactions 56 and 108 respectively. On the other hand, the He^+ ions are immediately converted to He_2^+ and N_2^+ through the charge conversion reaction 14 and the charge transfer reaction 57 respectively. This explains the reason

of the low concentration of He^+ during the breakdown. Moreover, the low concentration of He_2^+ at breakdown events is attributed to its fast conversion to N_2^+ and O_2^+ through reactions 58, 61 and 110.

The above processes increase the concentration of N_2^+ and O_2^+ in the mixture. As shown in the schematic diagram, the N_2^+ is mainly converted to N_4^+ and O_2^+ through the charge conversion reaction 59 and the charge transfer reaction 134. Subsequently, the N_4^+ is converted to N_2^+ and O_2^+ through the linked reactions 133 and 135 respectively. It is also noted that N_2^+ and O_2^+ are produced from direct ionization of the ground state nitrogen and oxygen molecules (reactions 41 and 74). However, the former reactions are not the main source of N_2^+ and O_2^+ production, for the range of air concentration considered in this study. Finally, the O_4^+ is created from the charge transfer of O_2^+, reaction 106.

The above discussion highlights the processes behind ion production during the increase of the gap voltage and clearly shows that finally the oxygen ions survive. Although the O_2^+ is finally converted to O_4^+ in the range of air concentrations considered in this study, the rate of this conversion is small and thus O_2^+ remains the dominant ion in the mixture. This was also observed from the global model [81].

At this point, it is also worth analyzing the negative charge species in the mixture. The concentration of the negative charge species over a voltage cycle is presented in Figure 22 together with the applied voltage and discharge current. Figure 22b shows that the electrons are the dominant negative species in the mixture. In contrast, the negative oxygen ions have negligible concentration during the voltage cycle. These have densities more than two orders of magnitude lower than the electron density. In order to further analyse the negative charge species, the most important processes for the production and destruction of the dominant negative charge species in the mixture (electrons) are presented in Figure 23. The criterion for the chosen production and destruction processes was to have a maximum value higher than $8 \cdot 10^{-5}$ and $4 \cdot 10^{-5}$ $[\mathrm{mol/m^3 s}]$ respectively for the reasons explained earlier.

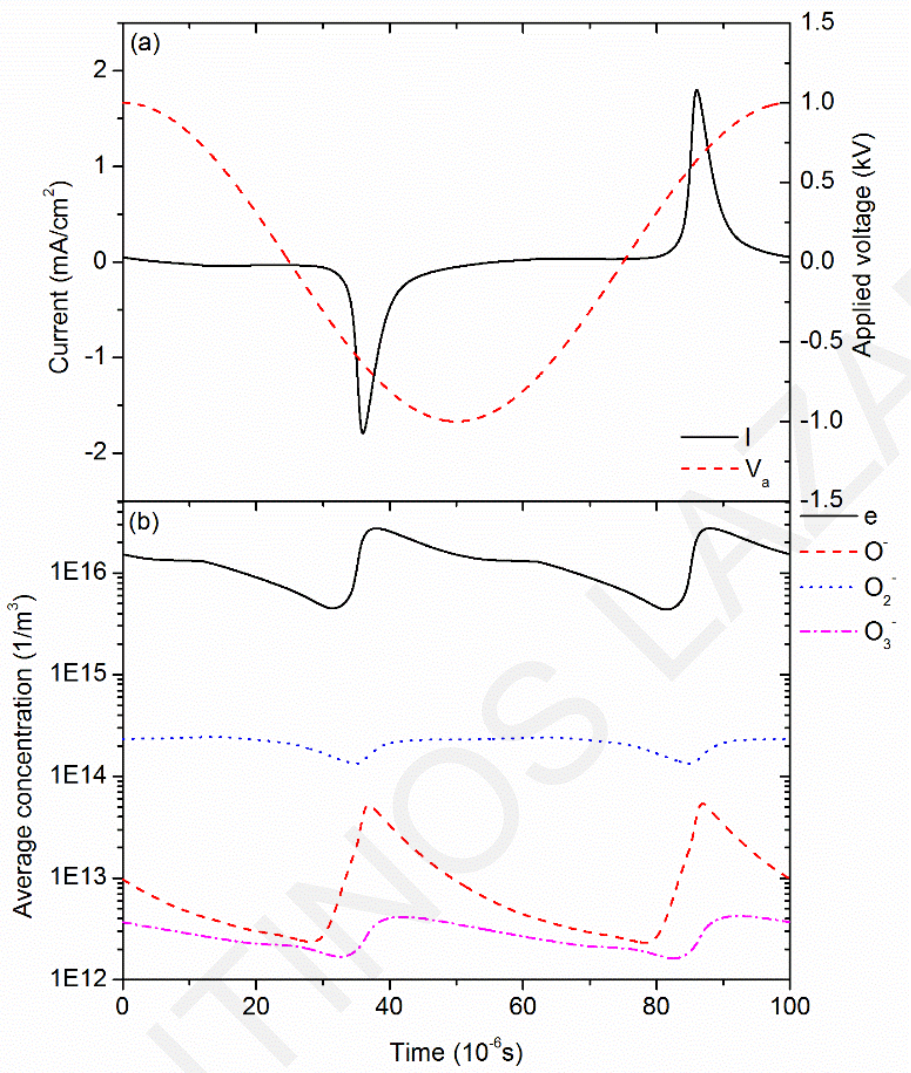

Figure 22: Simulation result of (a) the applied voltage and discharge current, and (b) the average concentration of negative charge species for a He-air mixture (150 ppm) over a voltage cycle. The amplitude and frequency of the applied voltage are 1 kV and 10 kHz respectively.

Figure 23a shows that the Penning ionization of nitrogen and oxygen molecules by helium metastable atoms (R55, R62 and R107) constitute the most important reactions for electron production during breakdown. Additional important reactions are the direct ionization of helium atoms ($e^-+He=>2e^-+He^+$, R3), and the Penning ionization of nitrogen and oxygen molecules by helium dimmers (R56 and R108). It is important to note that the production of electrons during the afterglow stage is completely determined by the Penning ionization of N_2 and O_2 by He_2*. A smaller contribution towards electron production is provided by the direct ionization of ground

state nitrogen and oxygen molecules, reaction 41 and 74 respectively. The above results are in agreement with the schematic diagram presented in Figure 21.

As in the case of O_2^+ (the dominant positive ions), the loss at the boundaries is the dominant mechanism for the destruction of electrons (see Figure 23b). In comparison to surface processes, electron destruction due to volume processes is not as important. Nonetheless, these reactions are the recombination of electrons with N_2^+, N_4^+, O_2^+ and O_4^+ (R43, R46, R75 and R95) and the two and three-body electron attachment with oxygen molecules (R64 and R105). Up to this point, the most important processes that occur in the discharge gap have been analysed. Furthermore, the reaction pathways presented in the schematic diagram of Figure 21 hold for the range of air concentration considered in this study. However, there is no insight regarding the effect of air on the magnitude of the rate of these reactions.

In order to complete the picture of the analysis and proceed towards the analysis of Table 8, it is necessary to provide an insight into the effect of the air content on the most important reactions of ion production in the mixture (reactions of the schematic diagram of Figure 21). With this in mind, the magnitude of the peak of these reaction rates is captured in Figure 24 as a function of the concentration of air, together with the breakdown voltage. The results of the reactions are split into three groups based on the following criteria: production of ions through the reaction pathways associated with (a) helium ions, (b) helium metastable atoms and dimmers and (c) nitrogen and oxygen species. This analysis is presented only in the symmetric case where the magnitude of the reaction rates is the same during both breakdown events.

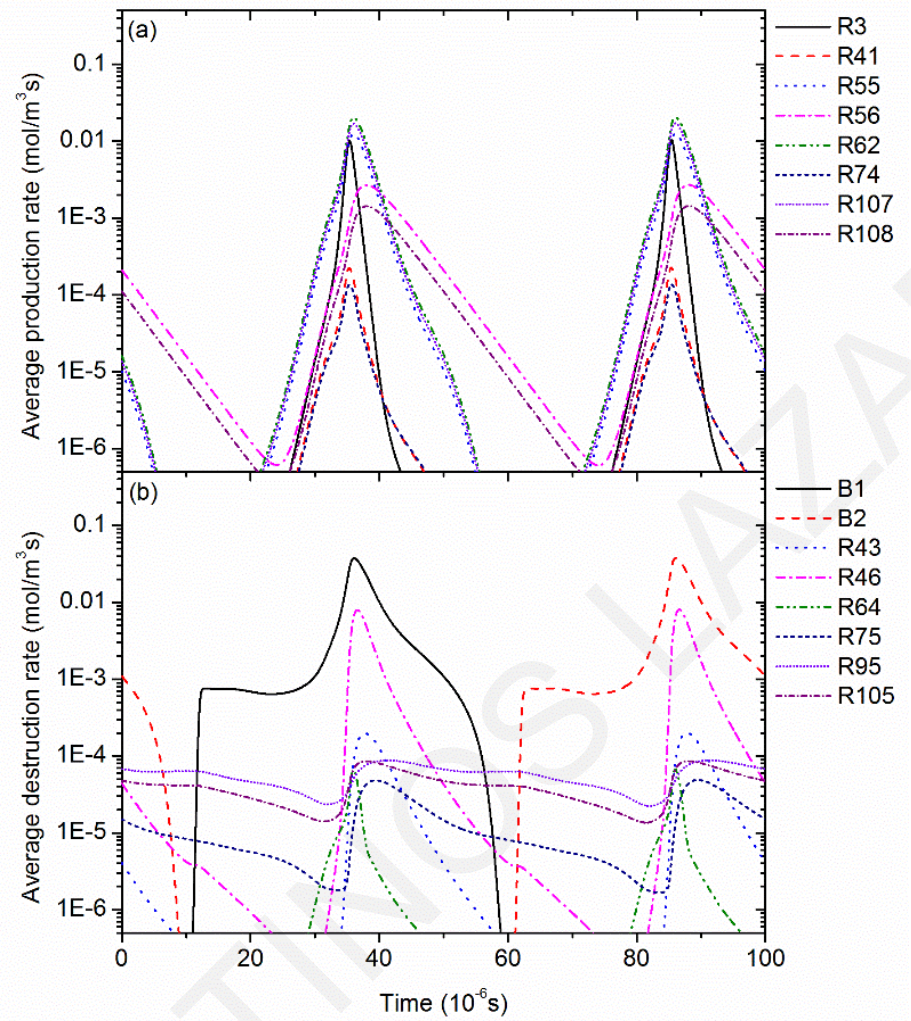

Figure 23: Simulation of the average rates for (a) production and (b) destruction of electrons as a function of time for 150 ppm dry air.

4.4.4 Effect of air concentration on the most important reactions for ion production

From the schematic diagram (see Figure 21) it has been proved that ion production is mainly governed by the increase in He_m and He^+ in the mixture. For a constant concentration of air, the discharge is ignited when the He_m and He^+ reach appropriate values for the production of adequate ions that are able to trigger breakdown. However, the increase in air concentration benefits the reactions associated with the ground state nitrogen and oxygen molecules (see reactions of the schematic diagram in Figure 21). As a result, a lower concentration of He_m and He^+ is required for ion production. The concentration of the former species is highly dependent on the electron temperature and consequently on the gap voltage [79]. The lower the concentration of these species, the lower the breakdown voltage.

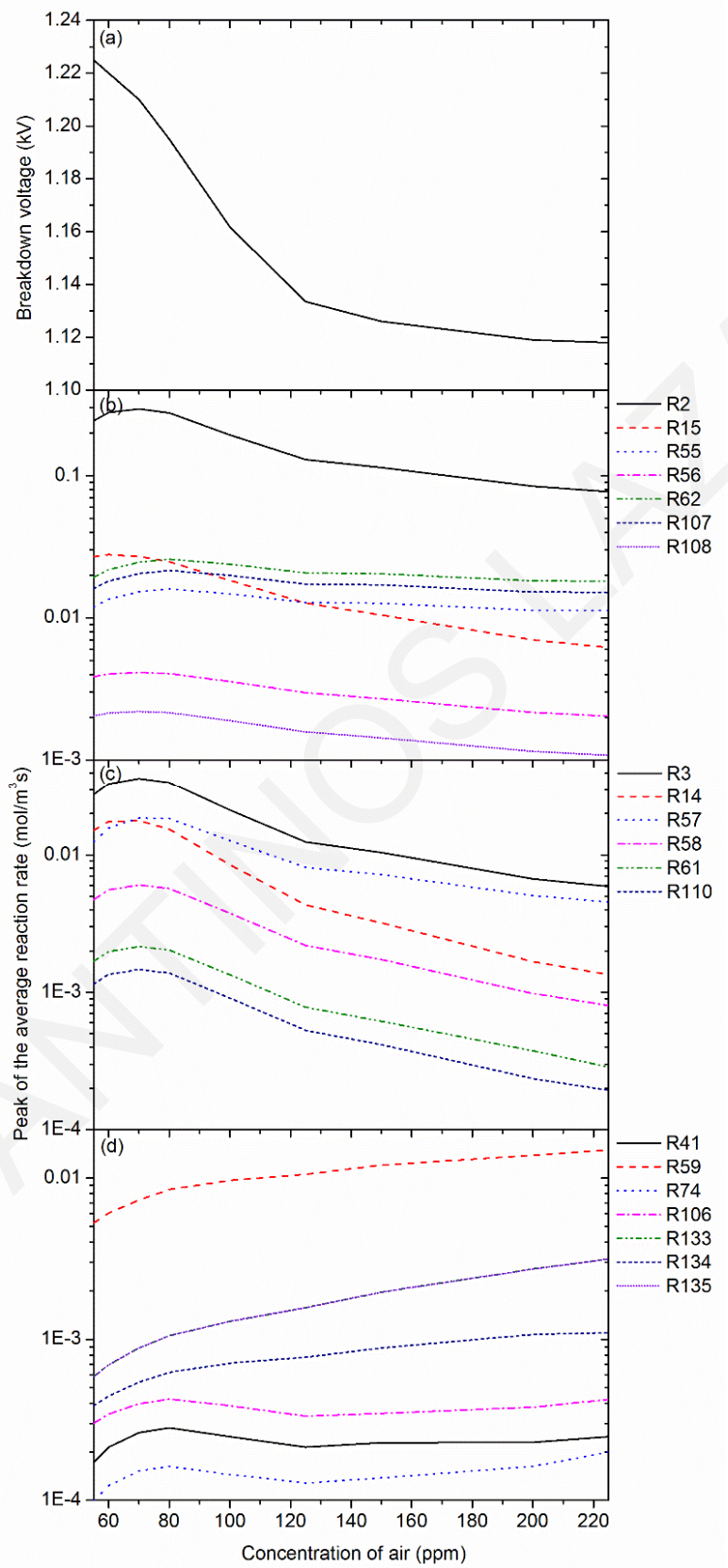

Figure 24: Simulated (a) breakdown voltage and (b-d) peak of the average reaction rates as a function of the concentration of air. The amplitude and frequency of the applied voltage are 1 kV and 10 kHz respectively.

The decrease in the breakdown voltage and the production rates of He_m and He^+ (R2 and R3) as the concentration of air increases in the mixture are clearly depicted in Figure 24a-Figure 24c. In the range between 55 and 70 ppm, however, an increase in the reaction rates is observed. This is attributed to the increase in the production rate of electrons, due to the increase in air concentration in the mixture. As a result, despite lower breakdown voltage and thus lower coefficient rate of reactions 2 and 3, the higher concentration of electrons increases the rate of these reactions. Beyond 80 ppm of air, the rate of electron production is reduced for the reasons that will be explained below.

Initially, the production of ions through the reaction pathways associated with the helium metastable atoms is analysed. The He_m mainly produces He_2*, N_2^+ and O_2^+ through reaction pathways R15, R55, R62 and R107 (see Figure 21). Furthermore, the He_2* decomposes and produces N_2^+ and O_2^+ through the linked reactions 56 and 108 respectively. As shown in Figure 24a, the production of N_2^+ and O_2^+ through reaction pathways linked to He_m and He_2* (R55, R56, R62, R107 and R108) mostly decreases, with the exception at low air concentration (up to 70-80 ppm). As expected, these reaction rates follow a pattern similar to the production rate of He_m. In the range from 80 to 225 ppm, the reactions R55, R62 and R107 experience a slower decrease because of the higher amount of N_2 and O_2 in the mixture, and consequently the higher amount of He_m lost through these reactions. Moreover, the production of electrons is mainly governed by the reactions 55, 62 and 107 during the breakdown and the reactions 56 and 108 during the afterglow. These reactions decrease as the air concentration increases in the mixture, thus reducing the production rate of electrons.

The other important species responsible for the production of ions in the mixture is He^+ (see Figure 21). The He^+ is mainly converted into He_2^+ and N_2^+ through reactions 14 and 57 respectively. Subsequently, the He_2^+ is converted quickly into N_2^+ and O_2^+ through reactions 58, 61 and 110. From Figure 24c, it can be observed that the production rates of N_2^+ and O_2^+ through the reaction pathways associated with the He^+ and He_2^+ (57, 58, 61 and 110) experience an increase up to 70 ppm and then they decrease for higher air concentration. This behaviour is similar to the production rate of He^+. Furthermore, the rate of reaction 57 decreases more slowly (between 70-225 ppm) due to the increase in N_2 in the mixture, and consequently the higher amount of He^+ lost in this reaction.

The reaction pathways associated with helium species (He_m, He^+, He_2* and He_2^+) increase the concentration of N_2^+ and O_2^+ in the mixture. From Figure 24d, it can be seen that the N_2^+ is mostly converted into N_4^+ (R59), while a smaller concentration of N_2^+ is lost through the production of O_2^+ (R135). By increasing air concentration, the rate of the former reactions increases due to the higher concentration of N_2/O_2 in these reactions. Similar behaviour is demonstrated for the rate of reactions 133 and 135 for the production of N_2^+ and O_2^+ through N_4^+. On the other hand, the production rates of N_2^+ and O_2^+ through direct ionization show a peak at ~80 ppm, and then they increase again for impurity levels higher than 125 ppm. The peak of these reaction rates is caused by the increase in the electron concentration (for the reasons already mentioned). On the other hand, the increase in the reaction rates for impurity levels higher than 125 ppm is caused by the increase in N_2 and O_2 in the mixture (despite the lower breakdown voltage).

The production of O_4^+ is only determined by reaction 106. Consequently, the rate of this reaction, as expected has a similar trend to the sum of the production rates of O_2^+ (R74, R107, R108, R110, R134 and R135). As can be seen from Figure 24d, the rate of reaction 106 follows a pattern similar to the rate of reaction 107 (most important reaction for O_2^+ production) up to 125 ppm. For impurity levels higher than 125 ppm, the production rate of O_4^+ experiences a small increase due to the increase in the production rate of O_2^+ (R134 and R135).

In summary, the production of positive ions through the reaction pathways associated with the helium species is mostly reduced, while the production of positive ions through the nitrogen and oxygen species mostly increases as air concentration increases in the mixture. On the other hand, the production of electrons mostly decreases because these are governed by the reaction pathways associated with helium species. Furthermore, the production of He_2* and He_2^+ (R15 and R14) is more affected by the increase in the impurities, indicating that at higher air concentrations these species will become unimportant.

Having in mind the above analysis and the most important processes that occur in the discharge gap over a voltage cycle, it is easy to interpret the results of Table 8, which consider the influence of air concentration on the discharge ignition and symmetry.

4.4.5 Influence of air concentration on the discharge ignition and symmetry

0 to 55 ppm: Our calculations show that in this range of air concentration, no breakdown occurs. This is attributed to the low ion production during the increase/decrease in the applied voltage. In order to ignite the breakdown in this range, the production rate of ions has to be increased. This can be achieved by increasing the applied voltage.

55 to 225 ppm: Another way to increase the rate of ion production is by increasing the level of air impurities in the mixture. As shown in the previous section, this benefits the reactions of ion production associated with N_2 and O_2. As a result, at about 55 ppm of air, the ions reach appropriate values to cause breakdown. The increase in air concentration between 55 and 225 ppm decreases the breakdown voltage (see Figure 24a), and thus the discharge ignites in this range.

Furthermore, the discharge exhibits symmetric characteristics because of the adequate concentration of electrons before each breakdown. From the previous section, it has been demonstrated that the most important reactions for electron production are 3, 55, 56, 62, 107 and 108. The rate of these reactions is mostly reduced as air concentration increases (see Figure 24b-Figure 24c) and for that reason, the concentration of electrons is reduced. Nonetheless, in this range of impurities, the electron concentration after breakdown is not low enough to require a higher gap voltage for the next breakdown.

225 to 1000 ppm: By increasing further the air concentration, the breakdown voltage is reduced and so are the production rates of electrons. This decreases the concentration of electrons and as a result the next breakdown requires higher gap voltage to ignite. For that reason, the discharge does not exhibit symmetric characteristics. To elucidate this phenomenon, the average concentration of ions over a voltage cycle is presented in Figure 25, together with the applied voltage, gap voltage and discharge current. For this analysis, the case of 500 ppm of air was chosen. The results of Figure 25 are repeatable at each voltage cycle.

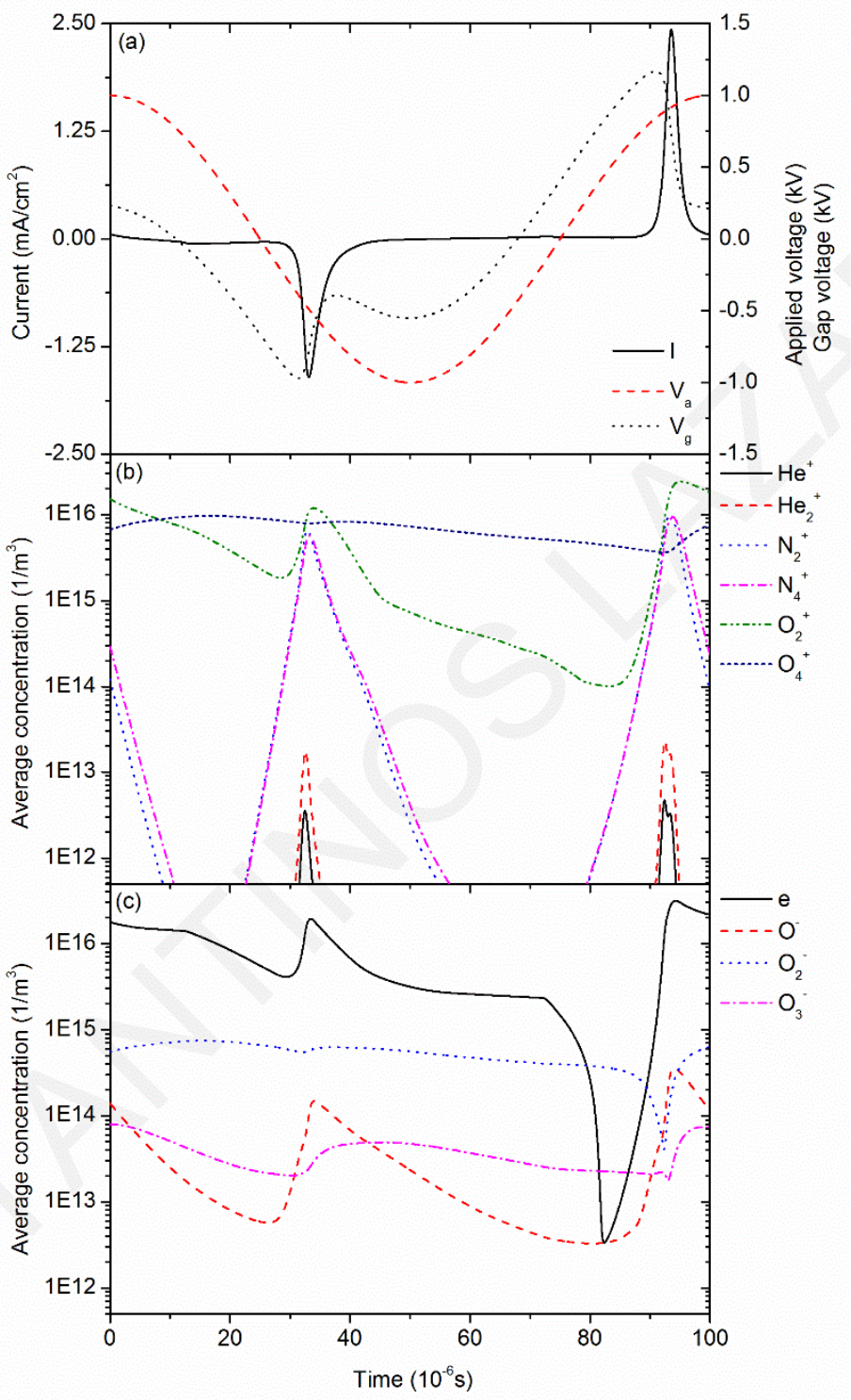

Figure 25: Simulation results of (a) the applied voltage, gap voltage and discharge current, (b) the average concentration of positive ion species, and (c) the average concentration of negative ion species for a He-air mixture (500 ppm) over a voltage cycle. The amplitude and frequency of the applied voltage are 1 kV and 10 kHz respectively.

From Figure 25a, it is obvious that the discharge does not exhibit symmetric characteristics, as the magnitude of the discharge current is different during the falling and rising parts of the applied voltage. Additionally, the dominant positive and negative species during the breakdown events are O_2^+ and electrons respectively (see Figure 25b and Figure 25c). In order to explain the reason for the discharge asymmetry, the concentration of electrons over a voltage cycle is further analysed.

As illustrated in Figure 25c, the concentration of electrons is different before the first (during the falling part of the applied voltage) and the second breakdown (during the rising part of the applied voltage). In particular, the concentration of electrons is much lower before the second breakdown. This is attributed to the lower breakdown voltage of the first discharge (0.97 kV) compared to the second breakdown (1.17 kV), which results in lower electron production. As demonstrated in the previous section, the increase in air concentration in the mixture decreases the breakdown voltage and thus the first breakdown occurs at a lower gap voltage. The lower the breakdown voltage, the lower the production rates of He_m and He^+ and thus of electrons (R3, R55, R56, R107 and R108). Consequently, the concentration of electrons before the second breakdown is lower. Furthermore, the concentration of electrons after the first breakdown is further reduced during the change of voltage polarity in the gap (loss of electrons at the boundaries). For the aforementioned reasons, the concentration of electrons before the second breakdown is reduced significantly as can be seen in Figure 25c. As a result, a higher gap voltage is required for the second breakdown to occur. After the second discharge, the concentration of electrons is not reduced significantly because of the higher breakdown voltage (see Figure 25c). This explains the asymmetry observed in the discharge current in Figure 25a.

In summary, the increase of air concentration in the mixture decreases the breakdown voltage and consequently the production rates of electrons. As a result, the concentration of electrons decreases after the breakdown and thus, a higher gap voltage is required to cause the next breakdown. In this range of air concentration, the applied voltage of 1 kV is able to ignite the discharge even during the second breakdown event and so the discharge takes place during the falling and rising part of the applied voltage. Similar discharge asymmetries, during the increase in the O_2 content in He DBD were also observed experimentally in [107].

1000 to 1500 ppm: In this range of air impurities the discharge ignition stops after a few voltage cycles. This is caused by the significant reduction of electrons after the breakdown and because

the gap voltage does not reach a high enough value which is able to ignite the discharge. In order to examine this phenomenon, the average concentration of electrons is captured over some voltage cycles, together with the applied voltage, gap voltage, discharge current and surface charge density (see Figure 26). The results in Figure 26 are obtained after the completion of the third voltage cycle, and thereafter show the instance where the ignition of the discharge stops. For this analysis, the case of 1100 ppm for air concentration is chosen. Moreover, the symbols B1 and B2 in the graph refer to the surface (contacted with the plasma) of dielectric layers which cover the ground contact and the contact of the applied voltage respectively.

As illustrated in Figure 26a, the ignition of the discharge stops after the third breakdown event. This is due to the combined effect of low electron concentration after the third breakdown event (see Figure 26b) and because the gap voltage during the fourth event does not reach a high enough value which is able to ignite the discharge. In particular, during breakdown the charges accumulate on the dielectric layers creating an electric field in the opposite direction to that of the applied voltage. However, for an ac voltage source, these surface charges enhance the gap voltage during the change of the voltage polarity. In this case, the surface charge density created during the third breakdown event is lower in comparison to the previous discharges (see Figure 26c). As a result, the surface charge density (from the third breakdown event) contributes less to the gap voltage during the rising part of the applied voltage (during the fourth event). Due to that, a lower gap voltage is reached, which is not able to ignite the discharge with this low initial electron density. Moreover, as it can be seen from Figure 26b, the concentration of electrons after the first breakdown event reaches slightly lower values compared to the third one. However, the discharge is ignited in this case because the gap voltage reaches higher values due to the higher surface charge density.

Finally, in order to cause breakdown in this range, the applied voltage has to be increased. The need for the increase in the burning voltage due to the increase in the impurities content in the mixture was also observed experimentally [107].

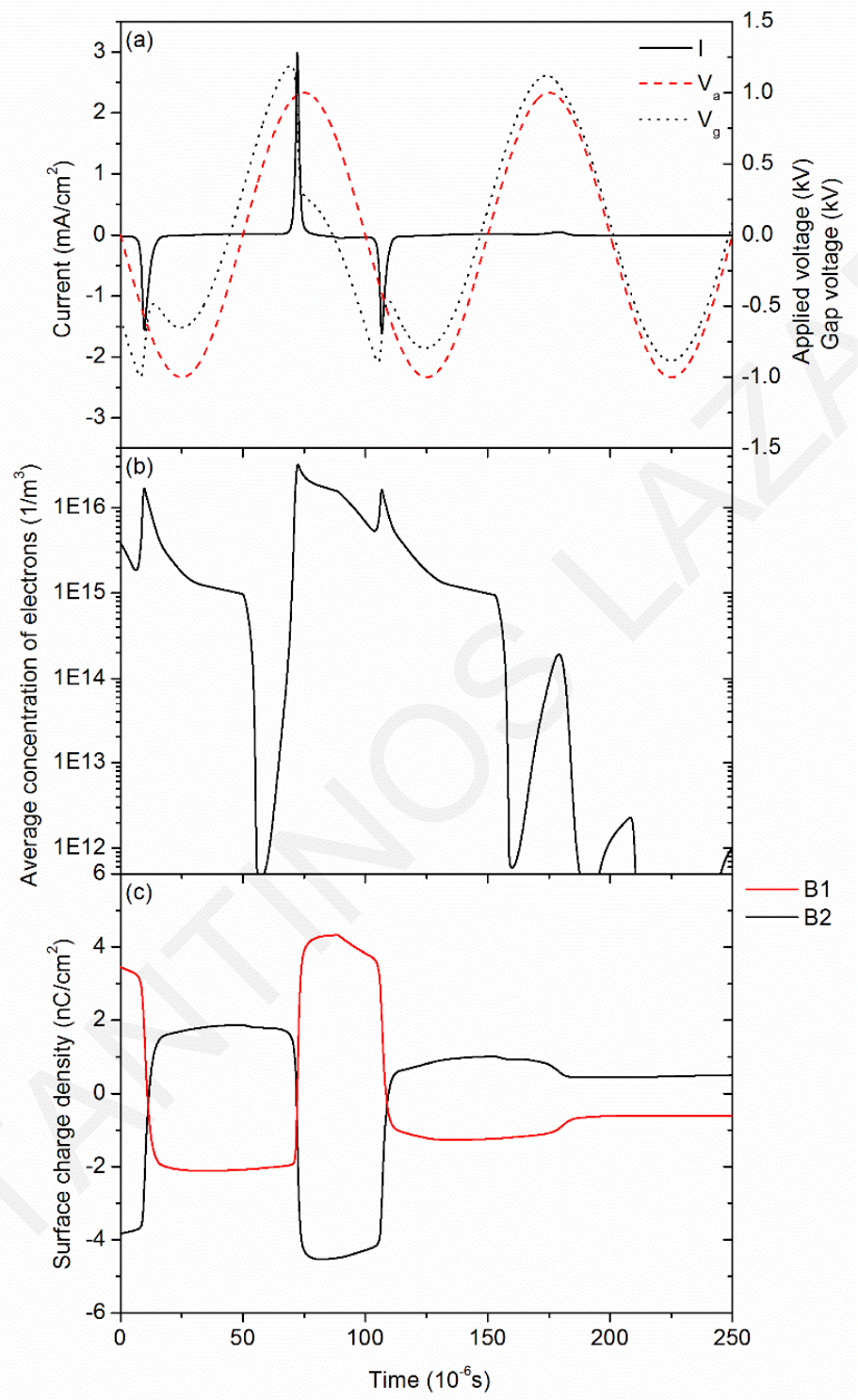

Figure 26: Simulation results of (a) the applied voltage, gap voltage and discharge current, (b) the average concentration of electrons, and (c) the surface charge density for a He-air mixture (1100 ppm) over a voltage cycle. The amplitude and frequency of the applied voltage are 1 kV and 10 kHz respectively.

4.5 Conclusions

In this chapter, a plasma fluid model was used for the physical description of a helium barrier discharge with dry air impurities. This model takes into account 27 species and 153 reaction channels. The model was validated with experimental results in order to ensure its correctness. Subsequently, the concentration of dry air considered as impurities, was varied in the range from 0 to 1500 ppm in the numerical model, in order to investigate its effect on the discharge evolution, discharge ignition and discharge symmetry. The results that dry air significantly affects the helium-air plasma chemistry and consequently the discharge evolution. In particular, four different regions were observed based on the discharge ignition and discharge symmetry. It was observed that at low air concentration (0-55 ppm), the discharge was not ignited due to the low amount of ions created during the increase/decrease of the applied voltage. As air concentration increases in the mixture, the production of ions through the reaction pathways associated with the ground state nitrogen and oxygen molecules benefit. For that reason, the breakdown voltage is reduced and thus the discharge is ignited in the range from 55 to 225 ppm. Furthermore, in this range, the discharge exhibits symmetric characteristics, due to the adequate concentration of electrons before each breakdown. By increasing the air concentration further, in the range from 225 to 1000 ppm, the discharge characteristics become asymmetric. This was caused by the decrease in the breakdown voltage and thus the production rate of electrons. As a result, after the breakdown, the electron concentration is reduced significantly and a higher gap voltage is required to ignite the next discharge. Furthermore, between 225 and 1000 ppm, the applied voltage of 1 kV is able to trigger the breakdown, which requires higher gap voltage. For air concentration higher than 1000 ppm, the ignition of the discharge stops. This is due to the combined effect of the low concentration of electrons after the breakdown and because the gap voltage does not reach a high enough value which is able to ignite the discharge.

Chapter 5

Simulation model of a helium-nitrogen-oxygen-water mixture

5.1 Introduction

The purpose of this chapter is to present the numerical model developed for the description of a helium DBD in the presence of air admixtures (nitrogen, oxygen and water species). The plasma species in the model are governed by the equations and boundary conditions presented in chapter 2. The model considers 56 species and 496 reaction channels and it is verified with experimental results in order to ensure its correctness. Subsequently, the level of dry air (79% N_2 and 21% O_2) is kept constant at 500 ppm (a plausible value for atmospheric pressure discharges without any vacuum equipment) and the effect of water admixtures (20 to 2000 ppm) on the discharge evolution is investigated.

Helium dielectric barrier discharges (DBD) at atmospheric pressure have shown very promising results in biomedical applications, such as wound healing [4], treatment of cancer [9], bacterial inactivation etc. [5]. In such discharges the presence of water impurities is unavoidable and has been shown to highly affect the plasma chemistry and dynamic evolution [77,108–120]. In practice, water impurities are due to the operation of the plasma in the ambient humid air and also due to the plasma interaction with biotic surfaces in wet and moist environments. As the discharge evolution is mainly determined by the ions, understanding the effect of the water admixtures on the ion composition is a prerequisite for effective utilization of these devices.

5.2 Experimental setup

In order to ensure the correctness of the numerical model, experimental data are compared with simulation results. The experimental setup is shown in Figure 27. It consists of two parallel plate copper electrodes (10.4 cm x 5.0 cm) deposited on a dielectric layer of fussed quartz vitreosil 077 (UQG Optics LTD, ε_r=8) with thickness of 1.2 mm each. The distance between the dielectrics

is kept constant at 5.0 mm. A high-voltage amplifier (Trek, Inc., model PD07016) driven by an arbitrary waveform generator (Tektronix, model AFG3022C) is used to operate the discharge. This feeds the upper electrode, through a current limiting resistor (5 kOhms), with a sinusoidal voltage of 2.5 kV amplitude peak to peak and frequency of 10 kHz. The other electrode is grounded. The electrode-dielectrics assembly, forming the discharge gap, is placed in the center of a stainless steel chamber, connected to the vacuum system and the helium flow meter output [121]. Before conducting the experiments, the stainless steel chamber (see Figure 28) is heated and pumped down to 10^{-5} torr. The flow of helium (4.6 spectral purity, Linde) is controlled using mass flow controller (MKS 1179A coupled) and is kept constant at 2.2 l/min (0.7 s residence time inside the gap). The pressure is kept slightly higher than ambient, at 780 torr to reduce the possibility of air intake into the chamber due to leakage.

The applied voltage, measured close to the HV electrode using a high-voltage probe (Tektronix P6015A), and the current measured on the ground line by a current monitor (Pearson 6585), are displayed and stored using a digital oscilloscope (Tektronix TDS 5034B, 350 MHz Bandwidth and 5 GS/s Sample Rate). The average of 50 consecutive acquisitions is considered here. The gas temperature is estimated using the rotational distribution in the emission spectrum of the first negative system of N_2^+ ($(B^2\sum_u^+, v_B=0) \rightarrow (X^2\sum_g^+, v_X=0)$), by the Boltzmann plot method, under the assumption that the rotational temperature reflects that of the gas molecules inside the plasma [64,65]. Using this method, the gas temperature is estimated to be around 300 K. The experimental setup is shown in Figure 27 and operational parameters are summarized in Table 9.

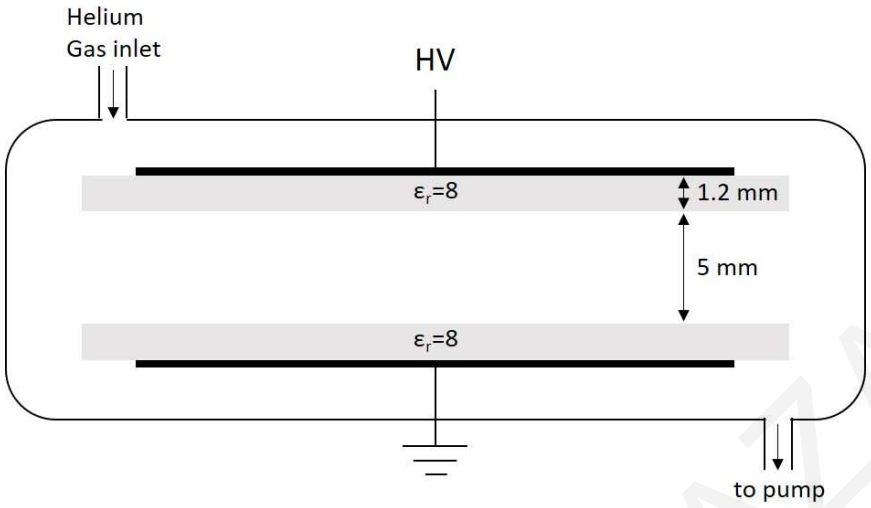

Figure 27: Experimental configuration.

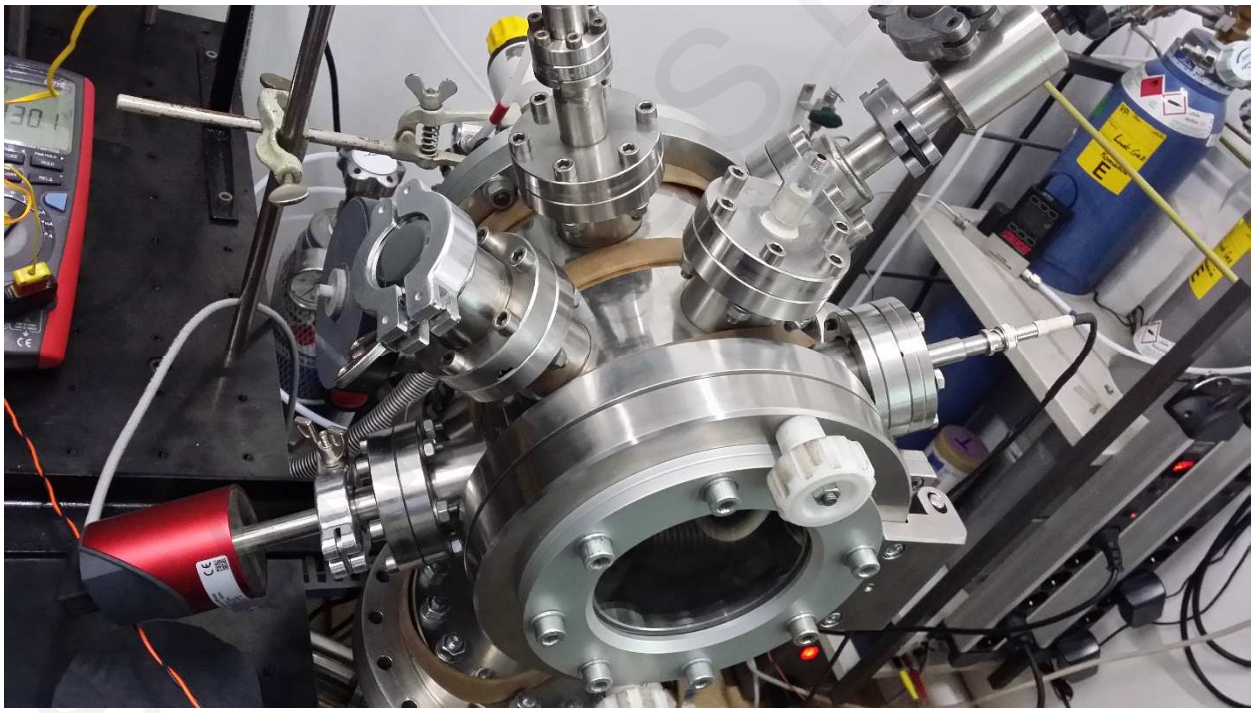

Figure 28: Stainless steel cylindrical chamber where the parallel plate BDB was inserted for operation.

Table 9: Operational parameters of the experimental setup.

Relative permittivity (ε_r)	8
Gap between dielectrics (mm)	5.0
Dielectric thickness (mm)	1.2
Electrode area (cm^2)	52
Gas pressure (torr)	780

Gas temperature (K)	300
$Voltage_{p-p}$ (kV)	2.5
Voltage waveform	sinusoidal
Frequency (kHz)	10
Helium gas purity (%)	99.996
Total gas flow rate (l/min)	2.2

5.3 Input parameters for the model

The plasma chemistry of the model considers 56 species and 496 reaction channels. The species considered in the model and the reaction channels are presented in Table 10 and Table C1 (in Appendix C) respectively. The rate coefficients of the reactions 1-3, 25-38, 63-78, 159-169 and the transport properties of the electrons and electron energy are calculated from the solution of Boltzmann's equation in the two term approximation [48]. This procedure is described in detail in the previous chapter. The mobilities of the species He^+, He_2^+, N_2^+, N_4^+, O_2^+, O_4^+, O^-, O_2^-, O_3^-, H_2O^+, H_3O^+, $H_5O_2^+$, $H_7O_3^+$, $H_9O_4^+$, $H_{11}O_5^+$, $H_{13}O_6^+$, $H_{15}O_7^+$, $H_{17}O_8^+$, $H_{19}O_9^+$, H^-, OH^-, $H_3O_2^-$, $H_5O_3^-$, H^+, H_2^+, OH^+, $H_4O_2^+$, $H_2O_3^+$, HeH^+ are taken from [115,122]. The diffusion coefficients for the species He, O_2, O_3, H_2O, H_2, HO_2, H, H_2O_2 and $H_2O_2^-$ are calculated from the kinetic theory [51,52] and the diffusion coefficient for the He_m, He_2*, N, N_2, N_2(v), N_2(A), N_2(B), N_2(a), N_2(C), O, O(^{1}S), O(^{1}D), O_2(v), O_2(a), O_2(b), OH and OH(A) are taken from the literature [69,115].

The air impurities considered in the model (for comparison purposes with the experiment of section 5.2) are presented in Table 11, unless otherwise stated. These are due to the air remaining in the discharge chamber after its heating and pumping down to 10^{-5} Torr, and air impurities from the helium bottle. The low level of relative humidity (10%) considered in the air remaining in the discharge chamber, is due to the heating of the discharge chamber. The levels of N_2, O_2 and H_2O impurities from the helium bottle were lower than the maximum values given by the producer because a brand-new full helium bottle was used and the heavier N_2, O_2 and H_2O species have a lower probability of being exported from the bottle compared to He. In summary, the heating and pumping of the chamber, the continuous flow and the higher pressure of helium than atmosphere in the chamber ensures a high helium purity in the discharge chamber. The numerical model confirmed this, as a low level of air impurities (as seen in Table 11) was required for matching with the experimental results.

The surface reactions, reaction probabilities, secondary electron emission coefficient (seec) and mean energy of secondary electrons (mese) considered on the dielectric surfaces are given in Table 12. The surface reactions and reaction probabilities are taken from [18,20,81,102,115]. The SEEC is set to 0.015 because it gives the best agreement with the experimental results. It is noted that such coefficients in simulation models are adjusted [104,123] to match the experimental results.

For all the species in the mixture, a uniform initial density of 10^{13} m^{-3} was set (except for the He which is the background gas, and the densities of N_2, O_2 and H_2O which are defined based on the level of air content in the mixture (see Table 11). It is noted that different initial densities have also been used in the range of $10^{11} - 10^{14}$ m^{-3} yielding similar simulation results.

The equations of the plasma fluid model are solved using the plasma module of the COMSOL multiphysics simulation package [57] on an Intel Xenon E5-2667 V4 3.2 kHz (with 16 core) server. These equations are discretized by the Galerkin finite element method using linear element shape functions. The resulting system is solved using the direct solver PARDISO [124]. For the time integration, the backward Euler method is used. The model considers 554 elements and 26556 degrees of freedom, with the smaller mesh size of 10 μm located in the region of the plasma and the larger mesh size of 50 μm located in the dielectrics. Each simulation required about two (2) days to be performed.

Table 10: Species included in the model chemistry.

Species		
Electrons		e^-
Helium	Ions	He^+, He_2^+
	Neutrals	He, He_m, He_2*
Nitrogen	Ions	N_2^+, N_4^+
	Neutrals	N, N_2, N_2(v), N_2(A), N_2(B), N_2(a), N_2(C)
Oxygen	Ions	O_2^+, O_4^+, O^-, O_2^-, O_3^-
	Neutrals	O, O_2, O_3, O(^{1}S), O(^{1}D), O_2(v), O_2(a), O_2(b)
Water	Ions	H_2O^+, $H_2O_3^+$, H_3O^+, $H_4O_2^+$, $H_5O_2^+$, $H_7O_3^+$, $H_9O_4^+$, $H_{11}O_5^+$, $H_{13}O_6^+$, $H_{15}O_7^+$, $H_{17}O_8^+$, $H_{19}O_9^+$, $H_3O_2^-$, $H_5O_3^-$
	Neutrals	H_2O
Others	Ions	H^+, H_2^+, OH^+, HeH^+, H^-, OH^-, $H_2O_2^-$
	Neutrals	H, H_2, OH, OH(A), HO_2, H_2O_2

He_m represents He(2^3S) and He(2^1S); He_2^*represents $He_2(a^3\Sigma_u^+)$; $N_2(v)$ represents the vibrational excited states of $N_2(v = 1 - 10)$; $N_2(A)$ represents $N_2\left(A^3\Sigma_u^+ (v = 0 - 4)\right)$, $N_2\left(A^3\Sigma_u^+ (v = 5 - 9)\right)$ and $N_2\left(A^3\Sigma_u^+ (v > 9)\right)$; $N_2(B)$ represents $N_2\left(B^3\Pi_g\right)$, $N_2(W^3\Delta_u)$ and $N_2(B^3\Sigma_u^-)$; $N_2(a)$ represents $N_2(a^1\Sigma_u^-)$, $N_2\left(a^1\Pi_g\right)$ and $N_2(W^1\Delta_u)$; $N_2(C)$ represents

$N_2(C^3\Pi_u)$, $N_2(E^3\Sigma_g^+)$ and $N_2(a^1\Sigma_g^+)$; $O_2(a)$ represents $O_2(a^1\Delta_g)$; $O_2(b)$ represents $O_2(b^1\Sigma_g^+)$; $O_2(v)$ represents the vibrational excited states of $O_2(v = 1-4)$.

Table 11: Air impurities considered for the comparison of the simulation model with the experiment results of section 5.2.

Species	Discharge Chamber (ppm)[a]	Helium Bottle (ppm)[b]	Total (ppm)
N_2	15.8 (79% of air)	10	25.8
O_2	4.2 (21% of air)	1	5.2
H_2O	0.05 (10% relative humidity)	1.5	1.55

[a] Air impurities (20 ppm) remaining in the chamber after heating and pumping down to 10^{-5} Torr.

[b] Air impurities in the helium bottle. The suppliers quote maximum impurity levels in the 99.996% grade helium as being N_2 20 ppm, O_2 5 ppm and H_2O 5 ppm.

Table 12: Surface reactions, reaction probabilities, seec and mese.

No	Surface Reaction [a]	Reaction probability[a]	seec	mese
1	$He_m + Surface \rightarrow He$	1	1.5e-2	5
2	$He_2^* + Surface \rightarrow 2He$	1	1.5e-2	5
3	$He^+ + Surface \rightarrow He$	1	1.5e-2	5
4	$He_2^+ + Surface \rightarrow 2He$	1	1.5e-2	5
5	$N + Surface \rightarrow 0.5N_2$	0.01	0	0
6	$N_2(A) + Surface \rightarrow N_2$	0.5	1.5e-2	1
7	$N_2(B) + Surface \rightarrow N_2$	0.5	1.5e-2	1
8	$N_2(a) + Surface \rightarrow N_2$	0.5	1.5e-2	1
9	$N_2(C) + Surface \rightarrow N_2$	0.5	1.5e-2	1
10	$N_2^+ + Surface \rightarrow N_2$	1	1.5e-2	3
11	$N_4^+ + Surface \rightarrow 2N_2$	1	1.5e-2	3
12	$O + Surface \rightarrow 0.5O_2$	0.02	0	0
13	$O(^1D) + Surface \rightarrow O$	1	0	0
14	$O(^1S) + Surface \rightarrow O$	1	0	0
15	$O_2(v) + Surface \rightarrow O_2$	0.2	0	0
16	$O_2(a) + Surface \rightarrow O_2$	0.0004	0	0
17	$O_2(b) + Surface \rightarrow O_2$	0.02	0	0
18	$O_3 + Surface \rightarrow O_3$	1	0	0
19	$O^- + Surface \rightarrow 0.5O_2$	1	0	0
20	$O_2^- + Surface \rightarrow O_2$	1	0	0
21	$O_3^- + Surface \rightarrow O_3$	1	0	0
22	$O_2^+ + Surface \rightarrow O_2$	1	1.5e-2	3
23	$O_4^+ + Surface \rightarrow 2O_2$	1	1.5e-2	3
24	$H + Surface \rightarrow 0.5H_2$	0.03	0	0
25	$H^+ + Surface \rightarrow H$	1	1.5e-2	3
26	$H^- + Surface \rightarrow H$	1	0	0
27	$H_2^+ + Surface \rightarrow H_2$	1	1.5e-2	3
28	$OH(a) + Surface \rightarrow OH$	1	0	0
29	$OH + Surface \rightarrow 0.5H_2O_2$	0.03	0	0
30	$OH^+ + Surface \rightarrow OH$	1	1.5e-2	3
31	$OH^- + Surface \rightarrow OH$	1	0	0
32	$HeH^+ + Surface \rightarrow He + H$	1	1.5e-2	3

33	$H_2O^+ + \text{Surface} \rightarrow H_2O$	1	1.5e-2	3
34	$H_2O_3^+ + \text{Surface} \rightarrow H_2O + O_2$	1	1.5e-2	3
35	$H_3O^+ + \text{Surface} \rightarrow H + H_2O$	1	1.5e-2	3
36	$H_4O_2^+ + \text{Surface} \rightarrow 2H_2O$	1	1.5e-2	3
37	$H_5O_2^+ + \text{Surface} \rightarrow H + 2H_2O$	1	1.5e-2	3
38	$H_7O_3^+ + \text{Surface} \rightarrow H + 3H_2O$	1	1.5e-2	3
39	$H_9O_4^+ + \text{Surface} \rightarrow H + 4H_2O$	1	1.5e-2	3
40	$H_{11}O_5^+ + \text{Surface} \rightarrow H + 5H_2O$	1	1.5e-2	3
41	$H_{13}O_6^+ + \text{Surface} \rightarrow H + 6H_2O$	1	1.5e-2	3
42	$H_2O_2^- + \text{Surface} \rightarrow H_2O_2$	1	0	0
43	$H_3O_2^- + \text{Surface} \rightarrow OH + H_2O$	1	0	0
44	$H_5O_3^- + \text{Surface} \rightarrow OH + 2H_2O$	1	0	0

[a] ref [18,20,81,102,115]

5.4 Results and discussion

5.4.1 Comparison of the simulation model with the experimental results

In order to ensure the validity of the numerical model, the simulation results are compared with experimental measurements. The comparison is based on the electrical characteristics as taken from the experiment and the numerical model. Figure 29 presents the discharge current and the applied voltage as measured from the experimental configuration presented in section 5.2 and the simulation model with level of air impurities (31 ppm) as determined in Table 11. The experimental results were obtained for DBD working in continuous He flow at 780 Torr. From Figure 29, it can be observed that the measured voltage collapses during the rise of the discharge current. Similar collapse is also observed in other experimental studies [125]. For the simulation, the applied voltage presented in the figure is the input sinusoidal voltage on the upper electrode.

As it can be observed, there is good agreement between the experimental discharge current and simulation results, with an error on the peak value less than 10%. Furthermore, in both cases the discharge current occurs at the same time during the rising and falling part of the applied voltage. The above analysis gives us confidence on the ability of the model to capture the physics behind this kind of discharges and can be used to study the effect of water admixtures on the evolution of He/air discharges.

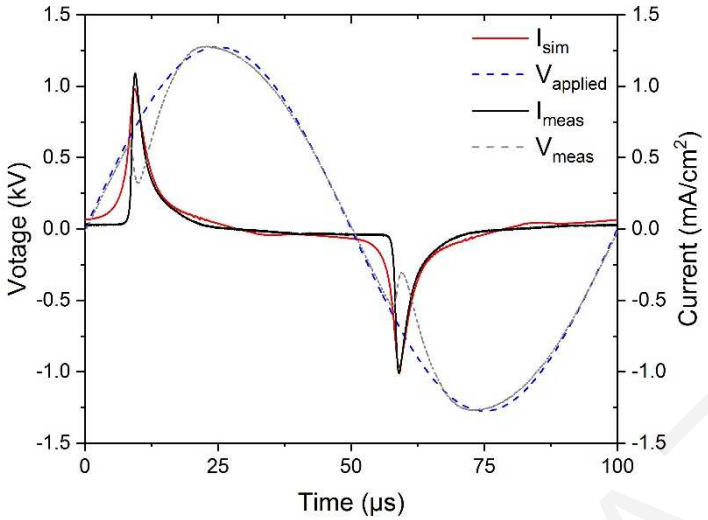

Figure 29: Comparison between simulation and experimental discharge characteristics (current and voltage).

In order to investigate the discharge development, the spatio-temporal evolution of the total ionization rate in logarithmic scale is presented in Figure 30. In the simulation, the voltage is applied at the 7.4 mm point, while the point at 0 mm is grounded. The polarity of the applied voltage is illustrated in the graph. As it can be seen, during the rising part of the applied voltage, the ionization wave begins from the anode and propagates towards the cathode, which is characteristic of a glow discharge. The maximum of the ionization rate occurs at the peak of the discharge current and close to the cathode. After the breakdown, charges accumulate on the dielectric surface, creating an electric field in the opposite direction to that of the applied voltage. The reduced voltage in the gap causes the ionization rate to reduce as well after breakdown. During the falling part of the applied voltage, the voltage polarity in the gap changes (as can be seen from Figure 30), and the ionization wave propagates in the opposite direction. The maximum of the ionization rate occurs at the peak of the discharge current and close to the cathode, indicating that the discharge exhibits glow characteristics.

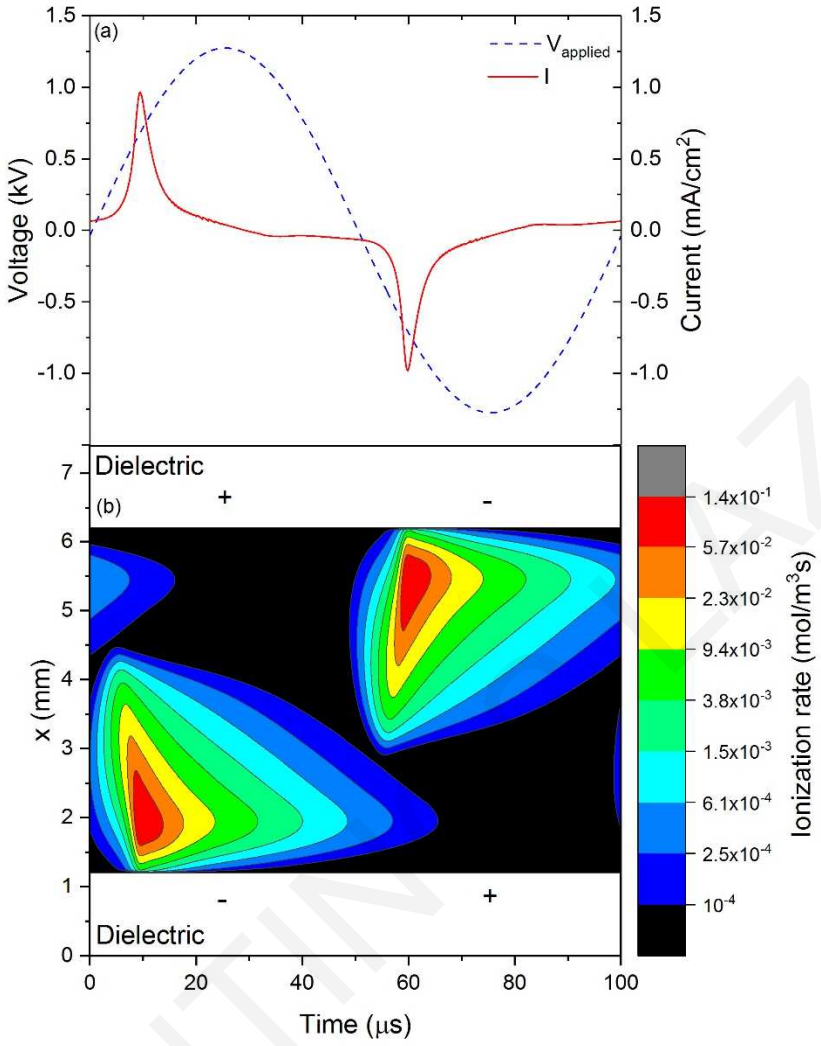

Figure 30: Simulation results of (a) the applied voltage and discharge current, and (b) the spatio-temporal evolution of the total ionization rate in logarithmic scale over a voltage cycle.

5.4.2 Effect of water admixtures on the discharge characteristics of a He/dry air (500 ppm) DBD

In this section, the level of water admixtures is varied in the range of 20-2000 ppm and its effect on the discharge characteristics of a helium/dry air discharge is investigated. The level of dry air in the helium DBD is considered to be 500 ppm (79% N_2 and 21% O_2), as this is a plausible value for atmospheric pressure discharges without any vacuum equipment [17]. In the range of water admixtures considered in this study, the discharge exhibits symmetric characteristics. Figure 31 presents the discharge characteristics (applied voltage, gap voltage and discharge current) for two different levels of water admixtures (50 and 500 ppm). As can be seen, in both cases the

discharge characteristics are symmetric, with one current pulse per half voltage cycle, at the same absolute amplitude and shape. After the breakdown, the gap voltage reduces significantly due to the charge accumulation on the dielectric surfaces shielding the electric field of the applied voltage [126]. As the applied voltage increases and just prior to its maximum, there is a second peak of the gap voltage. However, that gap voltage is not sufficient to ignite a second discharge.

Comparing the discharge characteristics for these two cases of water admixtures (50 and 500 ppm), two differences can be observed regarding the discharge current and the gap voltage. The amplitude of the discharge current is higher for the case of 500 ppm water admixture, however, its current pulse width is narrower. On the other hand, the breakdown voltage is lower for the case of 500 ppm, while, its secondary gap voltage peak is higher. Similar observations have be made in literature [75].

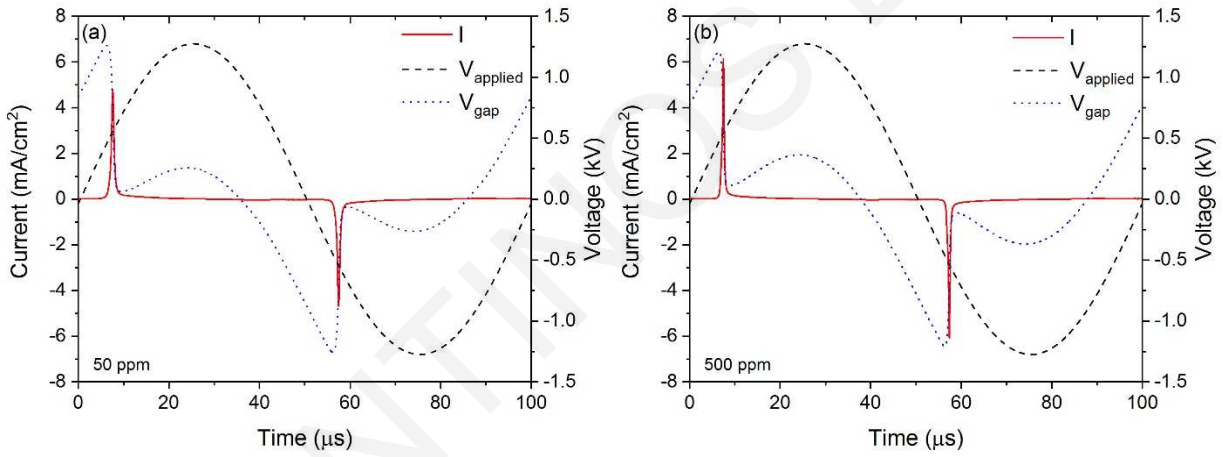

Figure 31: Simulation results of the discharge characteristics (applied voltage, gap voltage and discharge current) for (a) 50 ppm and (b) 500 ppm of water admixtures in a He/dry air (500 ppm) DBD.

In order to further investigate the effect of water admixtures on the discharge characterisitcs, the breakdown voltage, the amplitude of the discharge current and the second peak of the gap voltage at different levels of water admixtures are presented in Figure 32. As it can be seen, the breakdown voltage reduces as the level of water increases in the mixture (up to ~ 600 ppm). This is due to the enhancement of water-related reactions (such as the Penning ionization reaction, charge transfer reaction, etc.). From the schematic diagram of Figure 35 it can be seen that the ion production is initiated by the increase of He_m and He^+ (this is consistent with our previous chapter 4). Although the energy threshold for the production of He_m and He^+ is higher in comparison to the direct ionization of N_2, O_2 and H_2O, direct ionization is not important for low levels of

impurities, as can be seen in Figure 37. For low levels of impurities, the ionization of these species is mainly due to Penning ionization with He_m. The discharge is ignited when the He_m and He^+ reach the necessary values for the production of adequate ions which are able to trigger breakdown. By increasing the concentration of water in the mixture, the reactions associated with water, (i.e. reactions …, 221, 222, 223, … 286, 287, 288, …) also benefit, and as a result a lower concentration of He_m and He^+ is required for ion production. Since the concentration of He_m and He^+ depends on the gap voltage, the reduction in He_m and He^+ will result in a lower breakdown voltage. As the water impurities increase (higher than 600 ppm) the attachment of electrons becomes important, and the breakdown voltage starts increasing.

From Figure 32 it can be observed that the amplitude of the discharge current has a sharp increase for up to 600 ppm of water and at higher levels it starts approaching a constant value. The sharp increase of the discharge current peak is caused by the benefit of H_2O-related reactions that increases the ionization rate and consequently the amplitude of the discharge current. However, above 600 ppm of water, the attachment of electrons becomes important. The two effects balance each other out resulting in a somewhat constant current above 600 ppm.

The second peak of the gap voltage shows a similar behaviour to the discharge current amplitude (see Figure 32). Specifically, it shows a sharp increase for up to 600 ppm water in the mixture, while for higher levels it approaches a constant value. This behaviour can be explained by the surface charge accumulation on the dielectrics during the breakdown. In particular, as the level of water increases in the mixture (up to 600 ppm), the amplitude of the discharge current increases but its pulse width becomes narrower (see Figure 31). Due to the narrower width, the total charge accumulation on the dielectrics and the shielding of the applied voltage decreases (see Figure 33, presenting the surface charge density on the dielectrics at different levels of water admixtures over a voltage cycle). For that reason, the gap voltage increases significantly. However, above 600 ppm of water, the discharge current pulse amplitude, width and charge accumulation generally remain constant. This results in somewhat constant shielding and therefore, constant second peak of the gap voltage.

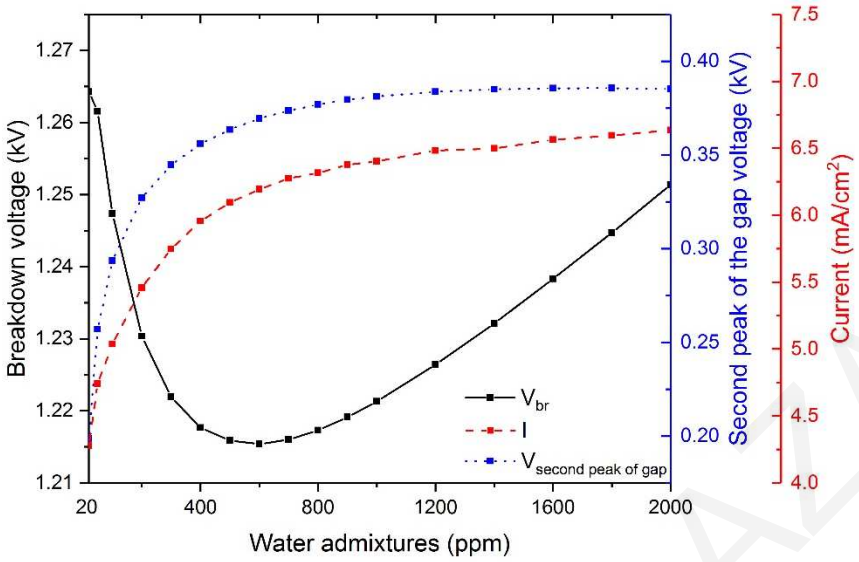

Figure 32: Simulation results of the breakdown voltage, second peak of the gap voltage and amplitude of the discharge current at different levels of water in a He/dry air (500 ppm) DBD. The amplitude and frequency of the sinusoidal applied voltage are 2.5 kV peak to peak and 10 kHz respectively.

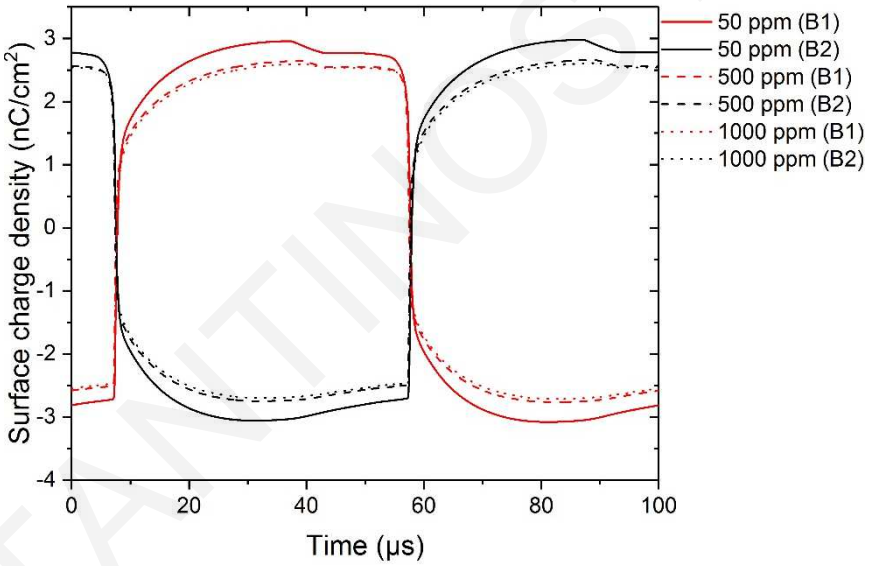

Figure 33: Simulation results of the surface charge density on the dielectrics at different levels of water admixtures (50, 500 and 1000 ppm) over a voltage cycle. The symbols B1 and B2 in the graph refer to the surface (contacted with the plasma) of dielectric layers which cover the ground contact and the contact of the applied voltage respectively.

5.4.3 Effect of water admixtures on the ion composition of a He/dry air (500 ppm) DBD

In Figure 34, the average concentrations of the positive ions during the breakdown are presented, for different levels of water admixtures (20 - 2000 ppm). As can be observed, the dominant positive ion from 20 to 100 ppm of water is H_2O^+, while from 100 - 2000 ppm it is $H_{11}O_5^+$. It is noted that at 2000 ppm of water, the concentrations of $H_{11}O_5^+$ and $H_{13}O_6^+$ coincide.

At this level, the concentrations of $H_{11}O_5^+$ and $H_{13}O_6^+$ have a negative and positive slope respectively, indicating that $H_{13}O_6^+$ will become the dominant ion in the mixture after 2000 ppm.

To analyze the evolution of positive ions concentrations, the most important reaction pathways for ion production are presented in the schematic diagram of Figure 35. The analysis of the simulation results shows that Penning ionization processes (associated with He_m) are the most important reactions for ion production.

At low levels of water in the mixture (up to 50 ppm), He_m species are mainly lost in the Penning ionization reactions 52, 59 and 115 (see Figure 37 that presents the most important reactions for electron production) for the production of nitrogen and oxygen positive ions. However, the nitrogen and oxygen ions are quickly converted to H_2O^+ and $H_2O_3^+$ and for that reason are not the dominant ions, even at these low levels of water in the mixture. As the level of water further increases in the mixture, the amount of He_m lost in Penning ionization reactions with H_2O species increases (reactions 283, 285, 286, 287, 288 and 289, see Figure 37), and particularly through reaction 286. For the above reasons, H_2O^+ is the dominant ion in the range of 20 - 100 ppm. The concentration of H_2O^+ (OH^+, H^+ and HeH^+, the other ions produced through Penning ionization reactions of He_m with water species), presents a maximum and then decreases as the level of water admixtures increases. This occurs due to the hydration of these species or their conversion to higher order cluster ions. In particular, above ~ 90 ppm of water in the mixture, OH^+ and H^+ are quickly converted to H_2O^+. Similarly, H_2O^+ and HeH^+, after 60 and 300 ppm respectively are converted to H_3O^+. However, the concentration of H_3O^+ does not become the dominant one at any level of water in the mixture, because it is immediately converted to $H_5O_2^+$. Similar behavior is also observed for $H_5O_2^+$ and $H_7O_3^+$. In particular, the $H_5O_2^+$ is immediately converted to $H_7O_3^+$ which it then immediately converted to $H_9O_4^+$. As the level of water increases in the mixture (100-2000 ppm), the most dominant ion becomes $H_{11}O_5^+$ due to the fast hydration of the lightest water clusters. Similar results were also observed in the global model [18,114].

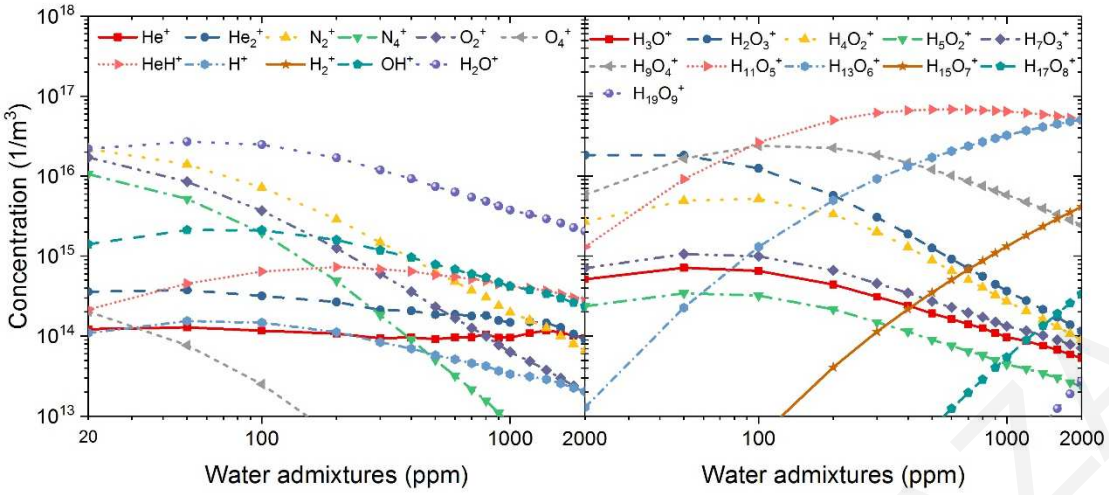

Figure 34: Average concentrations of the positive ions during the breakdown, for different levels of water admixtures in the helium/dry air (500 ppm) discharge. The amplitude and frequency of the sinusoidal applied voltage are 2.5 kV peak to peak and 10 kHz respectively.

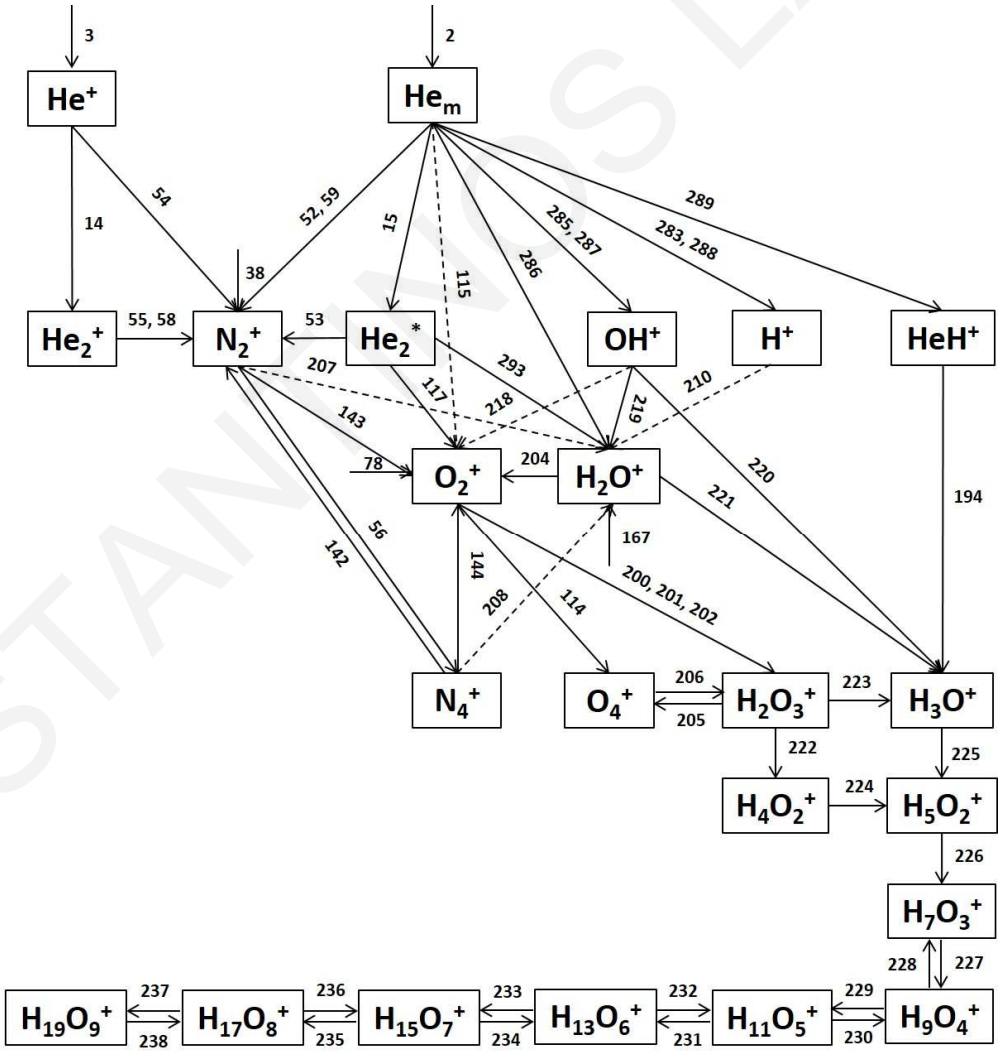

Figure 35: Schematic diagram of the most important reaction pathways for positive ion production.

The effect of water admixtures on the concentration of the negative charge species is presented in Figure 36. As it can be seen, electrons are the most important negative species in the mixture for the range of water admixtures considered in this study. The concentration of negative ions is at least one order of magnitude lower. Furthermore, it can be observed that the concentration of the negative ions $H_5O_3^-$, $H_2O_2^-$, OH^-, $H_3O_2^-$ and H^- exhibit an upward trend as the level of water increases in the mixture, that shows an increase of the electronegative character of the plasma. On the other hand, the oxygen negative ions (O^- and O_3^-) show a downward trend as the level of water increases in the mixture, similar to the results presented in [17], while the concentration of O_2^- remains generally constant for the different levels of water in the mixture.

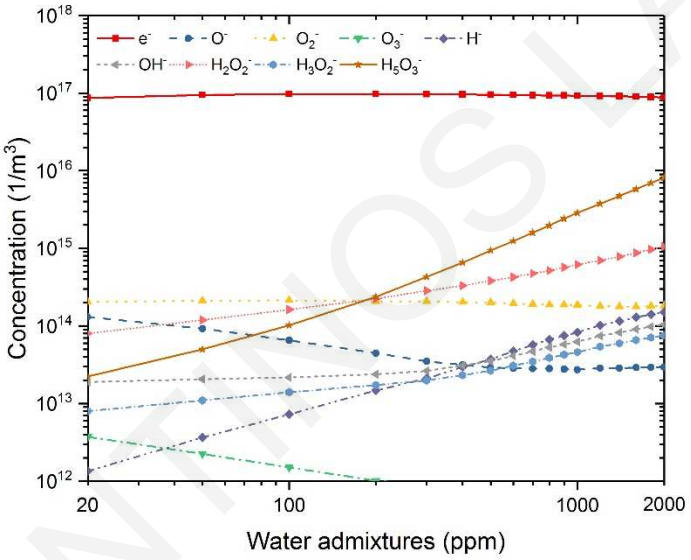

Figure 36: Average concentrations of the electrons and the negative ions during the breakdown, for different levels of water admixtures in the helium/dry air (500 ppm) discharge. The amplitude and frequency of the sinusoidal applied voltage are 2.5 kV peak to peak and 10 kHz respectively.

As electrons are the most abundant in the mixture, it is important to investigate the reaction pathways behind their production and destruction. The average reaction rates for electron production during the breakdown are presented in Figure 37. As it can be seen, at low levels of water in the mixture (up to 50 ppm), the most important reactions for electron production are the Penning ionization of He_m with N_2 and O_2 (reactions 52, 59 and 115), similar to prior work [126]. However, as the level of water increases in the mixture (>50 ppm), the loss of He_m in Penning ionization reactions with H_2O species increases and hence reaction 286 (H_2O^+ production) becomes the dominant reaction for electron production. The other Penning ionization reactions of

He_m with H_2O (for the production of OH^+, H^+ and HeH^+, reactions 287, 288 and 289) have a similar trend to reaction 286 but to a lesser extent. The increase of loss of He_m species with water species (through Penning reactions) reduces the amount lost with the rest ground state species in the mixture (such as He, N_2 and O_2). For that reason, the Penning ionization reactions 52, 59 and 115 (associated with N_2 and O_2 species) decrease as the level of water increases in the mixture. Similar behavior occurs for reactions 53 and 117, as He_2^* is mainly produced through He_m species and He species.

Regarding the direct ionization processes, it can be seen that the direct ionization of He, N_2 and O_2 (reactions 3, 38 and 78 respectively) present an almost constant value for the different levels of water in the mixture. Furthermore, these reactions are less important in comparison to the Penning ionization reactions (associated with He_m species). On the other hand, as expected, the direct ionization of H_2O (reaction 167) increases as the level of water increases. Finally, it is noted that only the detachment collisional reaction 188 approaches the contribution of reaction 286 (most important Penning ionization reaction of electron production) at high levels of water in the mixture (> 1500 ppm). Similar trend is also present for the detachment collisional reaction 189 but to a lesser extent.

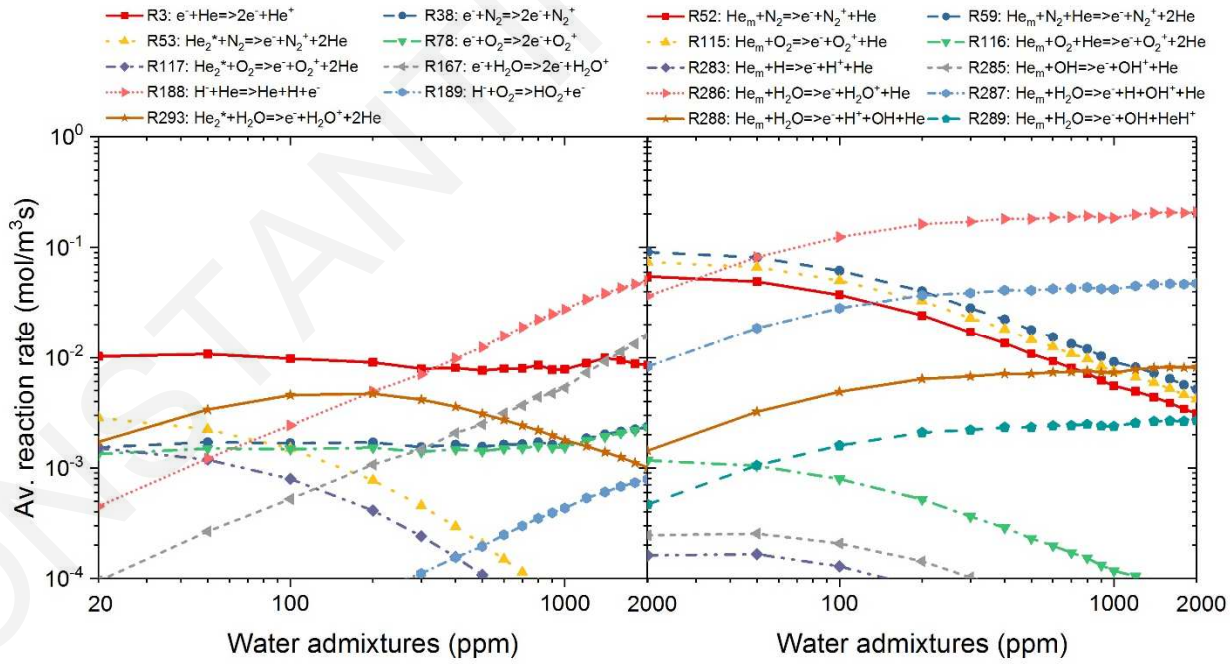

Figure 37: Simulation results of the average reaction rates of electron production during the breakdown, for different levels of water admixtures in the helium/dry air (500 ppm) discharge. The amplitude and frequency of the sinusoidal applied voltage are 2.5 kV peak to peak and 10 kHz respectively.

The average reaction rates for electron destruction during the breakdown are presented in Figure 38. The most important reaction for electron destruction up to 70 ppm of water admixtures, is the dissociative recombination of electrons with $H_9O_4^+$ positive ions (reaction 182), while from 70 and up to 1500 the dissociative recombination with $H_{11}O_5^+$ (reaction 183). As the level of water increases more than 1500 ppm, it can be observed that the dissociative attachment of electrons with H_2O molecules (reaction 160, for the production of H^-) becomes the dominant reaction for electron destruction. It is noted that H^- is quickly converted to OH^- (through reaction 211) which is then converted to $H_3O_2^-$ (through reaction 240) and which is finally converted to $H_5O_3^-$ (through the reaction 242). For that reason for high levels of water in the mixture, $H_5O_3^-$ is the next most important negative species in the mixture after electrons (see Figure 36).

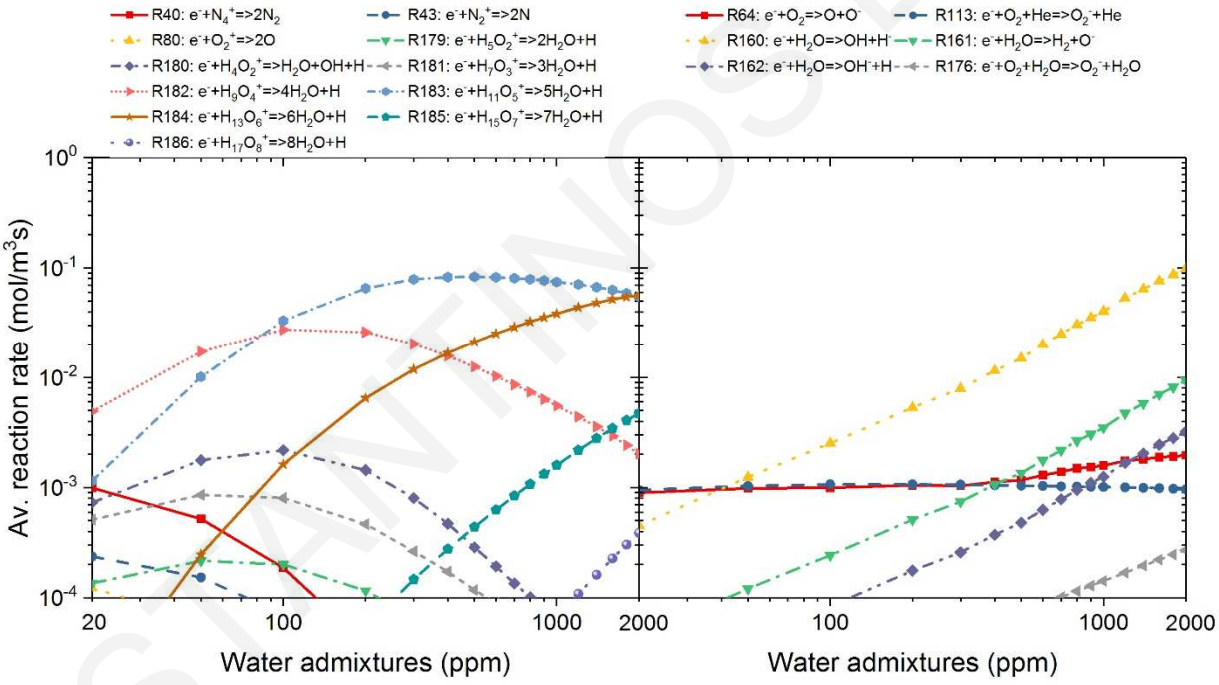

Figure 38: Simulation results of the average reaction rates of electron destruction during the breakdown, for different levels of water admixtures in the helium/dry air (500 ppm) discharge. The amplitude and frequency of the sinusoidal applied voltage are 2.5 kV peak to peak and 10 kHz respectively.

5.5 Conclusions

In this study a one-dimensional plasma fluid model is used to investigate the effect of water admixtures on the evolution of a helium/dry air (500 ppm, 79% N_2 and 21% O_2) DBD. The level of water in the mixture is varied in the range of 20-2000 ppm. The simulation results show that water admixtures highly affect the discharge characteristics and the dominant ions in the mixture. In particular, the increase of water in the mixture benefits the H_2O-related reactions. This causes the discharge current peak to increase, and the discharge to ignite at lower voltages (up to 600 ppm of water). However, the further increase of water (above 600 ppm) enhances the attachment of electrons with water molecules which causes the discharge to ignite at higher voltages. Despite the higher breakdown voltage, the discharge current peak remains almost constant, due to the high attachment of electrons with water molecules. Furthermore, the increase of water in the mixture causes the discharge current pulse width to become narrower. This reduces the total charge accumulation on the dielectrics and consequently the shielding of the applied voltage.

The simulation results show that the dominant ion for water admixtures in the range of 20 to 100 ppm is H_2O^+. By further increasing the water in the mixture, the water ion clusters are quickly converted to heavier water ion clusters. For that reason, from 100 ppm of water and up to 2000 ppm, the $H_{11}O_5^+$ is the most abundant ion in the mixture. The processes behind ion production and interaction are summarized in a schematic diagram. This diagram provides a simple yet complete picture for ion evolution and the dependence on the level of admixtures in the He discharge. Finally, from 20 to 2000 ppm of water admixtures, the most important negative charge species are found to be electrons. It is also observed that as the level of water increases in the mixture the electronegative character of the plasma increases.

Chapter 6

Capillary He and He/O_2 plasma jet: simulations and experimental validation

6.1 Introduction

The aim of this chapter is to use the validated model developed in the previous chapters to simulate a helium plasma device. In particular, the validated model developed in chapter 4 which considers helium, nitrogen and oxygen species, is used here to simulate a helium atmospheric pressure plasma jet (APPJ) device. These devices have gained a lot of attention in recent years due to the very promising results in applications ranging from plasma medicine [127–129], to decontamination [130,131], material surface modification [1,132], etc. The versatility of APPJ arises from its ability to produce almost simultaneously a wide range of reactive species, ions, high electric fields and UV photons, targeting a specific object. Furthermore, oxygen admixtures are shown to be very important for biomedical applications of helium plasma jets as these increase its effectiveness against cancer treatment [44,12]. In order to increase the understanding behind the operation of APPJ and to overcome some of the practical experimental limitations, numerical modelling has been increasingly used to simulate APPJ devices. However, it is very important to ensure that the simulation model capture correctly the experimental results.

The purpose of this chapter is the simulation of a capillary He and He/O_2 plasma jet device and the comparison of the simulation results with the experimental measurements. The plasma jet interacts with a dielectric surface placed normal to the jet axis to bring this model closer to applications. The model is compared with experimental results based on the measured spatial distribution of the 706.5 nm helium spectral line intensity with the reaction rate for the transition $He(3s^3S) \rightarrow He(2p^3P)$. The comparison is realized both, for axial and radial measurements. This procedure provides a more complete picture for the plasma bullet shape.

6.2 Experimental setup

The experimental setup is presented in Figure 39 and Figure 40 (real picture). It mainly consists of a soda lime glass tube of 20 cm length with a high voltage electrode tape wrapped around it. The inner and outer diameter of the tube is 0.9 and 1.35 mm respectively. The tape electrode is located approximately 1.5 mm from the tube exit. The plasma jet interacts with a dielectric slab (made of fused quartz vitreosil 077) placed 2 mm from the tube exit. The working length (where significant interaction is expected) from this type of plasma jet device is less than 1 cm (beyond that the plasma is very weak) [42,133–140]. The dielectric was placed at 2 mm because this still allows for measurements to be made with sufficient resolution and simulations to be completed at a reasonable computational time. The flow of helium (4.6 spectral purity, Linde) and oxygen (4.5 spectral purity, Linde) is independently controlled using mass flow controllers (MKS 1179A coupled with MKS type 247 four channel readout). The total gas flow rate is 1 slm. For the experimental study, He and He+O_2 (1000 ppm) are considered. An intensified charge coupled device (ICCD) camera consisting of a high resolution (1344 x 1024 pixels) CCD camera (Hamamatsu, model C8484-05G) and an image intensifier unit (Hamamatsu, model C9546-03) is used to capture the dynamic evolution of the plasma bullet. Using an appropriate bandpass filter with central wavelength of 714 ± 2 nm and 20 nm full width half-maximum bandwidth, the spatio-temporal distribution of the radiation intensity for helium spectral lines at 706.5 nm and 728.1 nm in the discharge gap is studied.

Square positive voltage pulses with amplitude of 4.0 kV, duration 50 μs, rise/fall time 7.3 μs and frequency of 10 kHz are used to excite the discharge. A 2-channel function generator (Tektronix AFG 3022C) is used to supply a voltage pulse to the HV amplifier (Trek PD07016) and the gate command for the camera intensifier (Figure 39). Moreover, the TTL output of the same function generator is used to trigger the 4-channels oscilloscope (Tektronix TDS5034B). The HV pulses and total current are monitored close to the HV electrode, using a Tektronix P6015A voltage probe and a Pearson 6585 current probe. The ICCD response monitor signal is also recorded using the oscilloscope. The camera gate width was 20 ns, while the integration time was set to 1 s, which corresponds to light collection from 10^4 individual current pulses during the rise

time of HV pulse. After storage, the plasma bullet images were artificially colored (ImageJ v1.51) in order to better observe the low intensity regions.

The emission spectra are recorded using a high-resolution spectrometer (Horiba Jobin Yvon, model Triax 550) equipped with a CCD camera (Horiba Jobin–Yvon, model Symphony) as detector.

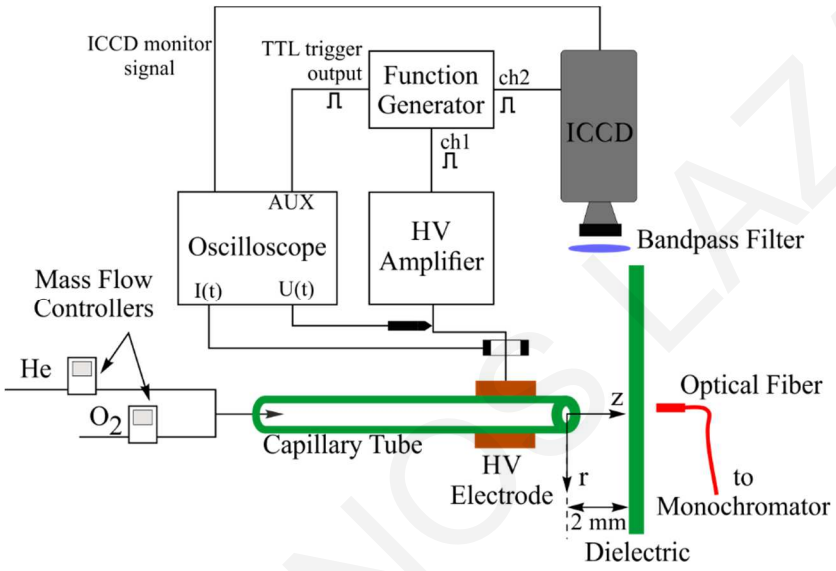

Figure 39: Experimental arrangement.

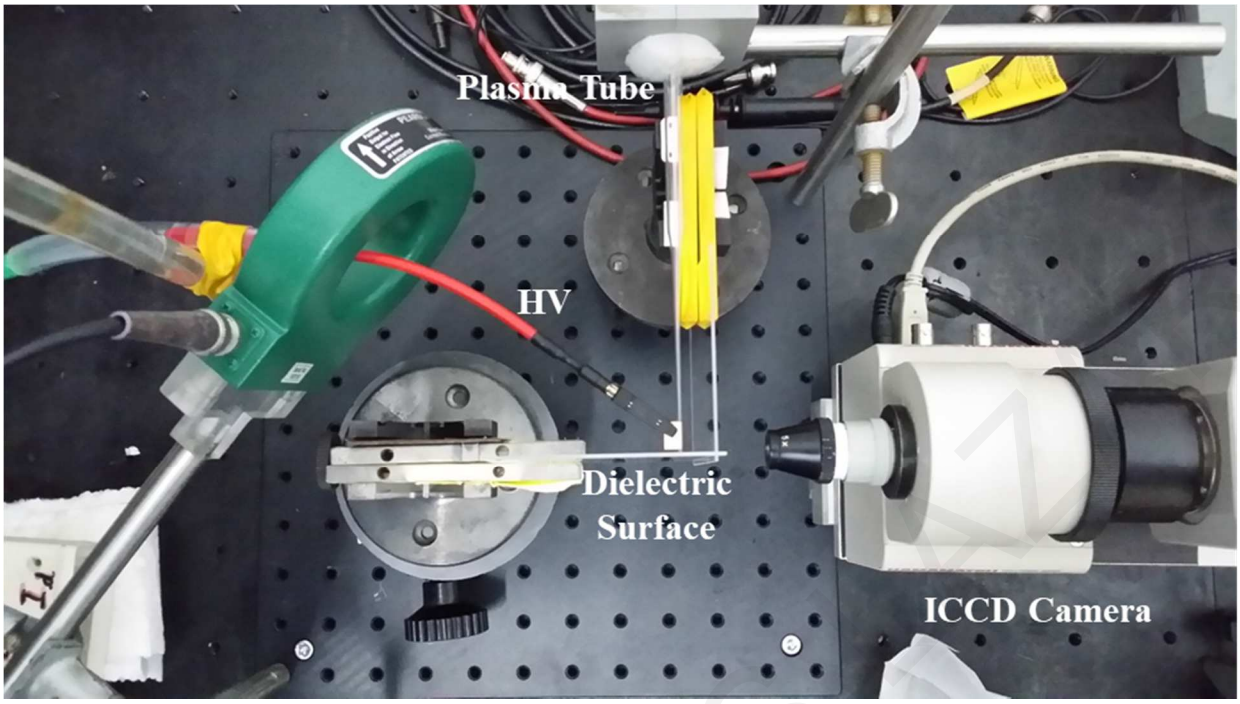

Figure 40: Experimental configuration of the helium plasma jet interacting with a dielectric surface placed normal to the jet axis.

6.3 Model

For the simulation of the helium plasma jet a two-dimensional axi-symmetric model is used. The simulation procedure is divided into two parts. In the first part the mixing of the helium jet and the ambient air, where the air is treated as a single species, is evaluated through the gas dynamic model presented in chapter 2. Due to the much slower speed of the fluid (~ 50 m/s) compared to that of the plasma bullet (~ 10^4 m/s), the gas dynamic model is solved in steady state. The calculated profiles of the air mole fraction and the mass average velocity are then fed into the second part of the simulation dealing with the time dependent plasma evolution (see chapter 2). It is noted that the gas dynamic model is solved only one time (before the plasma fluid model) and the air mole fraction is fed to the plasma fluid model as initial condition for the N_2 (79% of air) and O_2 (21% of air) species. Furthermore, for the initial concentrations of N_2 and O_2 an extra 40 ppm of air is added in the helium channel (79% and 21% of 40 ppm respectively), due to the air impurities in the helium bottle (99.996% purity). This procedure is followed by many published studies [27,30,39,41] and it assumes that for the time scales of interest these species can be considered to be in local equilibrium. The simulation domain, material properties and dimensions are presented in Figure 41. The gas dynamic model is solved in the region ADML, while the

plasma fluid model in the region HENO. At the flow rate of interest of 1 *l/min*, the Reynold's number, R_e ~ 190 and therefore the flow is laminar. For laminar flow the necessary length for the velocity profile to be fully developed in the tube is given by $0.05 \cdot Diameter \cdot R_e \approx 8.6\, mm$ [141]. Therefore, the additional length of 10 mm in the simulation domain for the gas dynamic model is sufficient for the helium gas velocity profile to be fully developed. In order to save simulation time and to focus on the plasma interaction with the dielectric surface, the plasma fluid model is solved in a smaller domain.

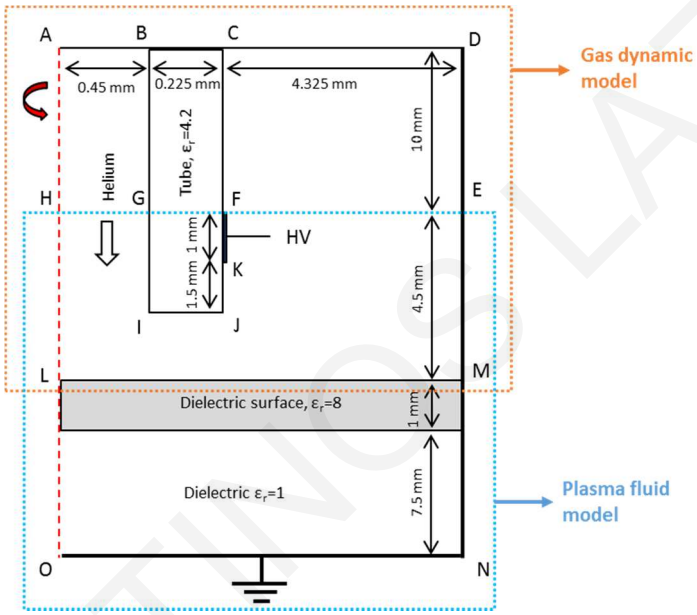

Figure 41: Axi-symmetric simulation domain for the gas and the plasma fluid model.

6.4 Input parameters for the model

For the simulation of the plasma fluid model, 108 reaction channels (see Table D1 in Appendix D) and 16 species are considered. The species are electrons, He ground state atoms, He_m metastable species $He(2s^3S)$ and $He(2s^1S)$, $He(3s^3S)$ and $He(2p^3P)$, He_2^m, He^+ and He_2^+ positive helium ions, N_2 ground state molecules, N_2^+ and N_4^+ positive nitrogen ions, O_2 ground state molecules, O_2^+ and O_4^+ positive oxygen ions, O^-, O_2^- negative oxygen ions. The helium species $He(3s^3S)$ and $He(2p^3P)$ are introduced in the model in order to allow a direct comparison between the simulation and experimental results. In particular, the reaction rate for the transition of $He(3s^3S) \rightarrow He(2p^3P)$ as calculated from the simulation model will be compared with the emitted light of the 706.5 nm line measured from the experiment. The excitation reactions for the

production of N_2 at the vibrational states ($v = 1 - 4$) and at the states of $N_2(A^3\Sigma_u^+ (v = 0 - 4))$, $N_2(A^3\Sigma_u^+ (v = 5 - 9))$, $N_2(A^3\Sigma_u^+ (v > 9))$, $N_2(B^3\Pi_g)$, $N_2(W^3\Delta_u)$, $N_2(B^3\Sigma_u^-)$, $N_2(a^1\Sigma_u^-)$, $N_2(a^1\Pi_g)$, $N_2(W^1\Delta_u)$, $N_2(C^3\Pi_u)$, $N_2(E^3\Sigma_g^+)$, $N_2(a^1\Sigma_g^+)$ are considered in the chemistry of the model in order to calculate the electron energy lost through these reactions. However, in order to save simulation time these species are not tracked separately in the model (they are all treated as N_2), similar to [39]. In the same way, the excitation of O_2 at the vibrational states ($v = 1 - 4$) and at the states of $O_2(a^1\Delta_g)$ and $O_2(b^1\Sigma_g^+)$ are taken into account for the electron energy loss but in the simulation model they are all treated as O_2.

In Appendix D (Table D1), the rate coefficient of reactions 1-3, 24-38 and 52-60 are calculated from the solution of Boltzmann's equation with the two term approximation [48]. The procedure followed for these calculations is described in detail in our previous chapter. The above calculations also provide the transport parameters of the electrons and electron energy. The transport and rate coefficients are calculated only once and stored in tables as a function of the mean electron energy and air mole fraction. For these calculations, the air mole fraction was varied in the range of 10^{-5} to 1 (10 steps for every decade, i.e.$10^{-5}, 2 \cdot 10^{-5}$ ... $10^{-4}, 2 \cdot 10^{-4}$, ... 1). The interpolation between the different values of air mole fraction was linear. These coefficients are then retrieved from the tables during the operation of the plasma fluid model. The transport parameters for all the heavy species and their reaction with solid surfaces are the same as defined in [126]. As the surface charge accumulation on the dielectrics is not known, the secondary electron emission coefficient (seec) is considered as an adjustable parameter. For the positive ions in the mixture, the seec is set to 0.1 since that value gives good agreement between the experimental and numerical results. Furthermore, this value lies in the acceptable range as estimated experimentally [142]. The energy of the secondary electrons is set to 5 eV for the helium ions, and 3 eV for the nitrogen and oxygen ions. No secondary electrons are considered from other species in the mixture. The boundary conditions for the plasma fluid model and gas dynamic model are presented in detailed in Table 13 and Table 14 respectively. Photoionization is not considered in this study, but instead a uniform background density of electrons and positive/negative ions is used, similar to other published works [30,39–41]. The density of the different species in the mixture is as follows: electrons are set to 10^{13} m^{-3}, heavy species (He_m, He_2^m, He_2^+, N_2^+, N_4^+, O_2^+, O_4^+, O^-, and O_2^-) are set to one order of magnitude lower than electrons i.e. 10^{12} m^{-3}

(electroneutrality through the concentration of He^+ is hence satisfied), He^+ is set to a value that satisfies electroneutrality in the mixture, N_2 and O_2 are determined from the gas dynamic model (79% and 21% of air respectively) and He the background gas is calculated from equation 11. For the initial concentrations of N_2 and O_2 an extra 40 ppm of air is added in the helium channel (79% and 21% of 40 ppm respectively), due to the air impurities in the helium bottle (99.996% purity).

Table 13: Boundary conditions considered for the plasma fluid model. The letters A–O correspond to the ones found in Figure 41.

Boundary	n_e	n_ε	n_i [a)]	D
GI, IJ, JK, LM	Equation 22	Equation 23	Equation 25	Equation 27
KF	Equation 22	Equation 23	Equation 25	Applied voltage
HG, FE	$-\vec{n}\cdot\vec{\Gamma_e}=0$	$-\vec{n}\cdot\vec{\Gamma_\varepsilon}=0$	$-\vec{n}\cdot\vec{j_i}=0$	$-\vec{n}\cdot D=0$
GF	---	---	---	$-\vec{n}\cdot D=0$
EM	$-\vec{n}\cdot\vec{\Gamma_e}=0$	$-\vec{n}\cdot\vec{\Gamma_\varepsilon}=0$	$-\vec{n}\cdot\vec{j_i}=0$	Ground
MN, NO	---	---	---	Ground

[a)] Represents the heavy species in the mixture, such as the neutrals, excited and ion species

Table 14: Boundary conditions considered for the gas fluid model. The letters A–O correspond to the ones found in Figure 41.

Boundary	ω_{He}	u
AB	1	$-u_0\vec{n}$
BG, GI, IJ, JK, KF, FC, LM	Equation 34	0
CD, DE, EM	0	Equation 35

6.5 Results and discussion

Although the plasma jet appears to be continuous, in reality it consists of plasma bullets travelling at supersonic speeds [143–146]. In order to study the spatio-temporal evolution of the plasma bullet during the plasma discharge, the ICCD camera is used to take pictures of the discharge region at different moments. A filter is also used to select specific lines from the entire spectrum (shown in Figure 42). From the emission spectra of He plasma jet (Figure 42a), the dominant helium line is: 706.5 nm ($3s^3S \rightarrow 2p^3P$). The other helium lines, 587.6 nm ($3d^3D \rightarrow 2p^3P$), 667.8 nm ($3d^1D \rightarrow 2p^1P$) and 728.1 nm ($3s^1S \rightarrow 2p^1P$), have much lower emission intensity. In addition to the helium lines, N_2^+ first negative system FNS $\left(B^2\Sigma_u^+ \rightarrow X^2\Sigma_g^+\right)$, N_2 second positive system SPS $\left(C^3\Pi_u \rightarrow B^3\Pi_g\right)$, OH band ($A^2\Sigma^+ \rightarrow X^2\Pi$) and atomic oxygen triplet line ($3^5P \rightarrow 3^5S, 777\ \text{nm}$) are observed due to the mixing of the helium jet and the ambient

air. The emission intensity of N_2^+ first negative system at 391.4 nm is the most dominant in the emission spectra of the He plasma jet.

When 1000 ppm oxygen is added to the helium jet, the emission intensity of N_2^+ first negative system at 391.4 nm reduces, whereas the oxygen triplet line (777 nm) becomes the dominant contributor to the emitted light (see Figure 42b). Furthermore, the 706.5 nm line also slightly increases. In summary, for both plasma jets, He and He+O_2 (1000 ppm), the most important lines/bands are 706.5, 391.4 and 777 nm.

The most probable reaction pathways for the production of $He(3s^3S)$, $N_2^+(B^2\Sigma_u^+)$ and $O(3^5P)$ which corresponds to the responsible species behind the most important lines/bands (706.5, 391.4 and 777 nm respectively) are summarized in Table 15. It is therefore obvious that choosing the helium line at 706.5 nm is a good choice for comparison with the numerical results because there is a single reaction, L1, for the production of $He(3s^3S)$. A bandpass filter with central wavelength of 714±2 nm and 20 nm full width half-maximum bandwidth is used to obtain spatially and temporally resolved intensity distributions of discharge for helium spectral lines at 706.5 nm and 728.1 nm. In the numerical model only the transition corresponding to He line at 706.5 nm (see Table D1 in the Appendix D) is considered because the transmission factor of the bandpass filter for 706.5 nm is 1.9 times higher than for 728.1 nm. Moreover, the emission intensity of the He line at 706.5 nm is about 5-7 times higher than the emission intensity of the He line at 728.1 nm (as it can be observed in Figure 42). Therefore, the dynamics of the reaction rate for the transition of $He(3s^3S) \rightarrow He(2p^3P)$ in the numerical simulation will provide a good representation of the distribution of the discharge radiation intensity for the helium spectral line at 706.5 nm and will therefore be used for the comparison of the numerical model with the experimental results.

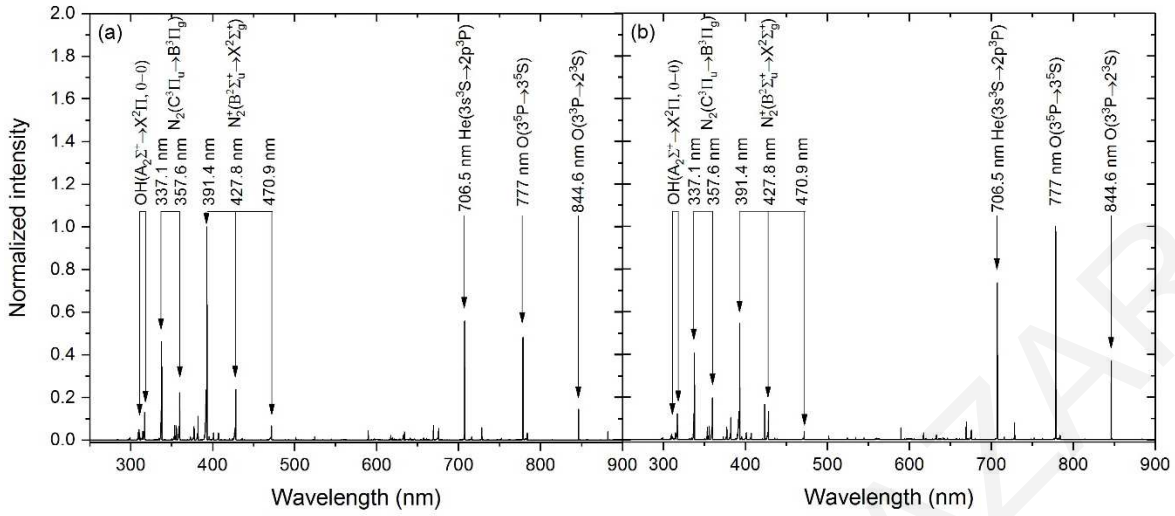

Figure 42: Optical emission spectra for (a) pure helium plasma jet and (b) He+O_2 (1000 ppm) plasma jet.

Table 15: Probable reactions for the production of He($3s^3S$), $N_2^+(B^2\Sigma_u^+)$ and $O(3^5P)$.

Species	Reaction	Probable reaction[147,148]	Transition[149]	Radiative lifetime (ns)[149,150]
$He(3s^3S)$	L1	$e^- + He \rightarrow e^- + He(3s^3S)$	$3s^3S \rightarrow 2p^3P + h\nu\ (706.5\ nm)$	64.6
	L2	$He(2s^3S) + N_2 \rightarrow He + N_2^+(B^2\Sigma_u^+) + e^-$		
	L3	$He_2(2^3\Sigma) + N_2 \rightarrow 2He + N_2^+(B^2\Sigma_u^+) + e^-$		
$N_2^+(B^2\Sigma_u^+)$	L4	$He^+ + N_2 \rightarrow He + N_2^+(B^2\Sigma_u^+)$	$B^2\Sigma_u^+ \rightarrow X^2\Sigma_g^+ + h\nu\ (391.4\ nm)$	65.8
	L5	$He_2^+ + N_2 \rightarrow 2He + N_2^+(B^2\Sigma_u^+)$		
	L6	$e^- + N_2 \rightarrow 2e^- + N_2^+(B^2\Sigma_u^+)$		
	L7	$He(2s^3S) + O_2 \rightarrow He + O(3^5P) + O$		
$O(3^5P)$	L8	$e^- + O_2^+ \rightarrow O(3^5P) + O$	$3^5P \rightarrow 3^5S + h\nu\ (777\ nm)$	27.1
	L9	$e^- + O_2 \rightarrow e^- + O(3^5P) + O$		

6.5.1 Comparison of the simulation model with the experiment for a He and He+O2 (1000 ppm) plasma jet

The helium – air mixing for the pure helium plasma jet, is presented in Figure 43. Inside the tube the gas is almost pure helium, with a very small amount (40 ppm) of air admixtures, due to the bottle impurities and outside the tube and far away from the dielectric the gas is pure air. Most of the mixing occurs between the tube and the dielectric surface with the level of air increasing in the r direction (away from the axis of symmetry) and away from the dielectric (there is almost no air on the dielectric surface, z = 2mm).

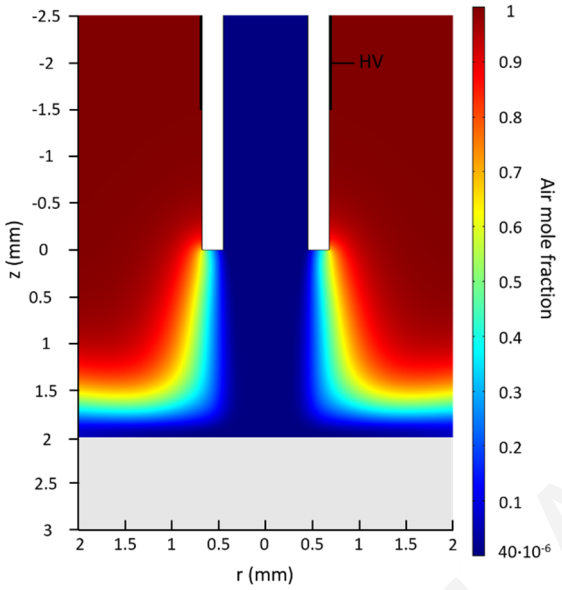

Figure 43: Helium−air mixing for the pure helium plasma jet.

The comparison of the simulation with the experimental results is accomplished by comparing the spatio-temporal resolved emission and specifically the 706.5 nm line, to the reaction rate for the transition of the helium state from $3s^3S$ to $2p^3P$. Figure 44 shows at the top the high-speed photographs of the He plasma plume in the open air, taken using a bandpass filter with 714±2 nm central wavelength for five different moments during the plasma jet evolution. The reaction rate for the transition of $He(3s^3S) \rightarrow He(2p^3P)$ is presented at the bottom of Figure 44. Here, t=0 ns corresponds to the time the maximum emission intensity coincides with the tube exit (z=0 mm). It is noted that, all the results presented here are obtained during the rise time of the applied voltage. As can be seen in Figure 44, the main features between experimental and numerical results are qualitatively similar. Specifically, both the simulated and the experimental radiation distributions form two symmetric lobes (indicating torus like shape), propagating from the tube towards the dielectric surface. The lobes radius remains almost constant up to 1 mm from the tube exit, while for z > 1 mm the torus spreads. Close to the dielectric surface (~ 0.2 – 0.3 mm) the torus compresses back towards the axis of symmetry.

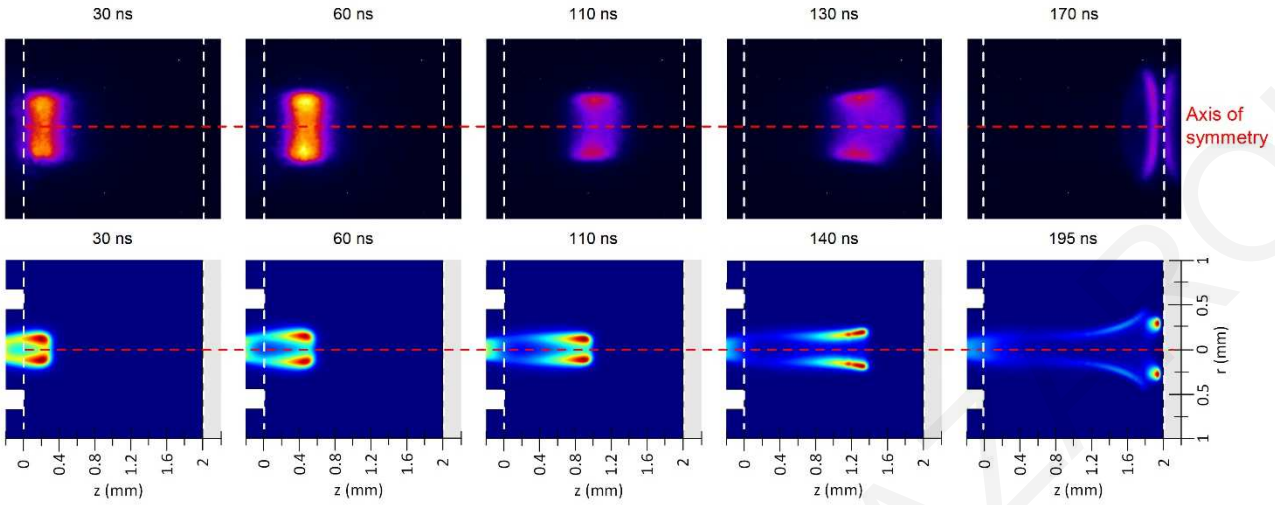

Figure 44: Measured relative intensity distributions of He line at 706.5 nm (experiment, top), compared with calculated reaction rate for the transition of He($3s^3S$) → $He(2p^3P)$ (simulation, bottom) for He plasma jet. The edges of the capillary tube are marked out by a white thick line. The tube exit (z=0 mm), the dielectric surface (z=2 mm) and the axis of symmetry (r=0 mm) are marked out by a white and red dashed line respectively, and t=0 ns corresponds to the maximum of the emission intensity being at the tube exit.

To gain further insight into the plasma bullet shape, the camera was positioned along the z-axis looking through the dielectric (see Figure 39). The measured relative intensity distribution of the He line at 706.5 nm and the reaction rate for the transition of He($3s^3S$) → He($2p^3P$) are compared in Figure 45 at the z=1 mm plane. As can be seen, the simulation and experimental results are qualitatively similar. They show that the maximum intensity of the radiation distribution of the 706.5 nm line is distributed around the axis of symmetry (r ~ 0.15 and 0.25 mm for the simulation and the experiment respectively), indicating a torus like shape of the plasma bullet. On the axis of symmetry, the radiation distribution is almost zero, as well as for r> 0.3 mm.

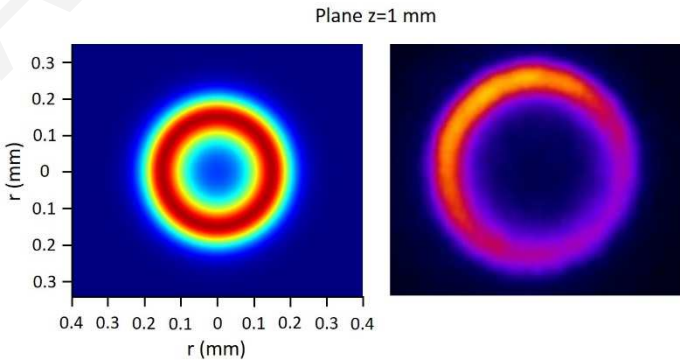

Figure 45: Measured relative intensity distributions of He line at 706.5 nm (experiment, right), compared with calculated reaction rate for the transition of He($3s^3S$) → $He(2p^3P)$ (simulation, left) for He plasma jet at the z=1 mm plane.

In order to have a more quantitative comparison, the position of the maximum radiation

intensity at 706.5 nm is compared to the peak of the reaction rate for the transition of $He(3s^3S)$ to $He(2p^3P)$ for various axial positions as shown in Figure 46. From the slope of the linear fitting of the experimental and simulation results, it is found that the experimental velocity of the excitation front (created by the He excited species) is about 8.85 ± 0.52 km/s while in the simulation this is 8.17 ± 0.22 km/s. The simulation and experimental results are in good agreement with a difference of less than 8 % which is in the acceptable limits. The linear fit of the experimental and simulation data show a determination coefficient R2 of 0.972 and 0.99 respectively. Therefore, the propagation of the two symmetric lobes from the tube towards the dielectric surface is done at similar velocities thus confirming the validity of the model.

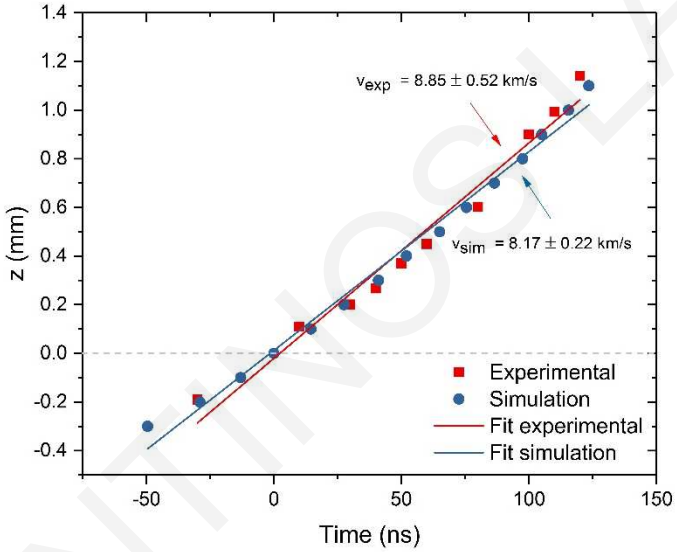

Figure 46: Position of the measured maximum intensity at 706.5 nm and simulated peak of reaction rate for the transition of $He(3s^3S)$ to $He(2p^3P)$ for pure helium jet. Time 0 ns corresponds to the radiation intensity that coincides with the tube exit (z=0 mm).

The same process is repeated for the helium plasma jet with 1000 ppm oxygen added to it. The measured relative intensity distributions of He line at 706.5 nm for five different moments during the $He+O_2$ plasma jet evolution and the reaction rate for the transition of $He(3s^3S) \rightarrow He(2p^3P)$ are presented in Figure 47. As can be seen from Figure 47 the simulation and experimental results are in good agreement. In comparison to the pure helium plasma jet case, with 1000 ppm oxygen admixture in the helium jet the emission intensity distribution of He line at 706.5 nm presents disk like shape (indicating a spherical like shape) centered on the axis of symmetry of the tube during its propagation from the tube towards the dielectric surface (see Figure 47). This is true up to ~ 1 mm from the tube exit. After 1 mm and as the plasma bullet approaches the

dielectric surface, the distribution of the line at 706.5 nm forms two distinct lobes centred on the axis of symmetry. Close to the dielectric surface (at a distance ~ 0.2-0.3 mm) it approaches again the axis of symmetry.

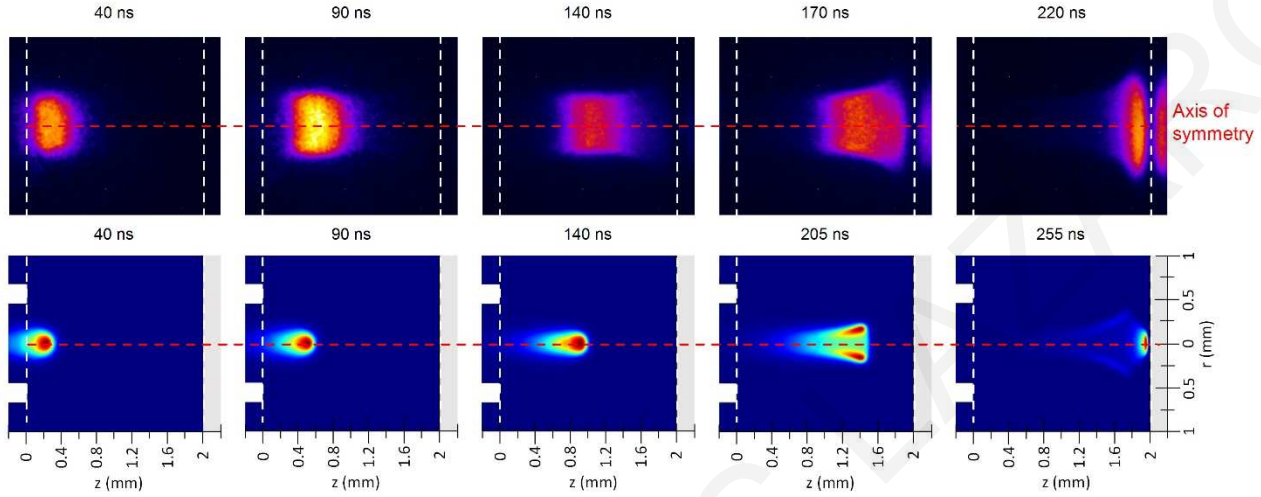

Figure 47: Measured relative intensity distributions of He line at 706.5 nm (experiment, top), compared with calculated reaction rate for the transition of He($3s^3S$) → $He(2p^3P)$ (simulation, bottom) for He+O_2 (1000 ppm) plasma jet. The edges of the capillary tube are marked out by a white thick line. The tube exit (z=0 mm), the dielectric surface (z=2 mm) and the axis of symmetry (r=0 mm) are marked out by a white and red dashed line respectively, and t=0 ns corresponds to the maximum of the emission intensity being at the tube exit.

The measured relative intensity distributions of He line at 706.5 nm and the reaction rate for the transition of He($3s^3S$) → $He(2p^3P)$ are compared in Figure 48 at plane z =1 mm from the tube exit. As it can be seen, both the simulation and experimental results, show a torus like shape of the plasma bullet. The maximum intensity of the radiation distribution occurs at a distance r ~ 0.18 mm and 0.8 mm (from the axis of symmetry) in the experiment and simulation respectively. In comparison to the pure helium plasma jet, the radiation distribution in this case is distributed closer to the axis of symmetry. Furthermore, the radiation distribution is not zero on the axis of symmetry in this case. This is due to the initial (close to the tube nuzzle, see Figure 47) sphere like shape of the plasma bullet which spreads into two lobes by the time it approaches (~ 1 mm) the dielectric surface.

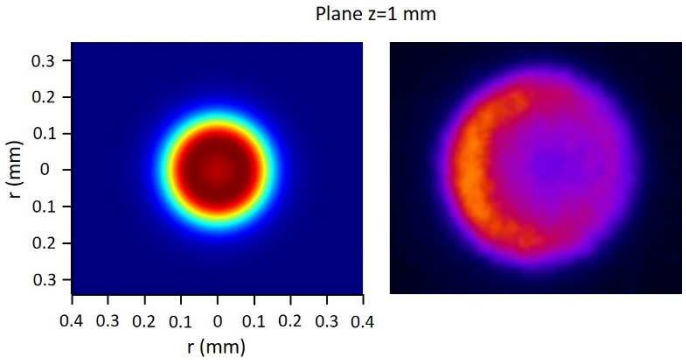

Figure 48: Measured relative intensity distributions of He line at 706.5 nm (experiment, right), compared with calculated reaction rate for the transition of He($3s^3S$) → $He(2p^3P)$ (simulation, left) for He+O_2 (1000 ppm) plasma jet at the z=1 mm plane.

The position of the maximum radiation intensity at 706.5 nm, experimentally obtained, is compared to the peak of the reaction rate for transition of He($3s^3S$) → $He(2p^3P)$ for various axial positions as shown in Figure 49. The propagation velocity of the excitation front created by He excited species, estimated from the slope of the linear fit of the experimental and simulation results is found to be 6.41 ± 0.34 km/s and 5.86 ± 0.14 km/s respectively. This demonstrates good agreement between the simulation and experimental results, with an error of less than 9 %. The linear fit of the experimental and simulation results show a determination coefficient R2 of 0.966 and 0.993 respectively. Finally, in this case, the propagation velocity of the excitation front, created by He excited species, is lower by about 27% in comparison to the pure helium plasma jet.

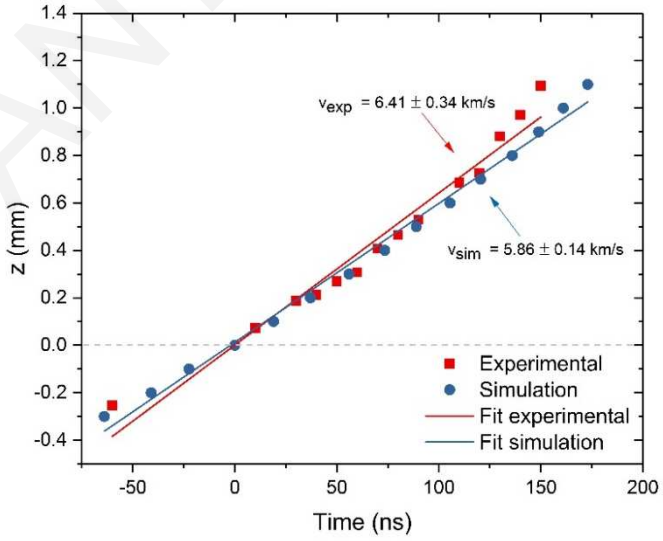

Figure 49: Position of the measured maximum intensity at 706.5 nm and simulated peak of reaction rate for the transition of He($3s^3S$) to He($2p^3P$) for He+O_2 (1000 ppm) jet. Time 0 ns corresponds to the radiation intensity that coincides with the tube exit (z=0 mm).

The above validation provide us confidence about the ability of the simulation model to capture the evolution of helium plasma jet devices with and without the presence of oxygen admixtures. This model can be subsequently used to shed light into other plasma jet devices, which are operated under different conditions i.e. amplitude of the applied voltage, frequency, electrode configuration, tube characteristics etc. Furthermore, it can be used to provide a good insight into plasma jet applications, such as biomedical applications, surface modification etc.

6.6 Conclusions

In this chapter, a two dimensional axi-symmetric model was used, for the investigation of a capillary helium plasma jet with and without the presence of oxygen admixtures. For the assessment of the validity of the simulation model, the measured distributions of the 706.5 nm He line intensity are compared with the reaction rate for the transition of $He(3s^3S)$ to $He(2p^3P)$ as calculated in the simulation model for both the pure helium and helium with 1000 ppm of oxygen plasma. Good agreement between experimental and numerical observations is obtained, for both axial and radial measurements. In particular, for the case of the pure helium plasma jet, the emitted radiation (at 706.5 nm) intensity forms a torus (ring) like shape centred on the axis of symmetry of the tube during its propagation from the tube towards the dielectric surface. On the other hand, by introducing oxygen admixtures in the helium gas, the radiation emitted by helium excited species $(3s^3S)$ shrank towards the centre of the tube axis forming a spherically symmetric shape. However, in both cases, as the plasma bullet approaches the dielectric surface (~ 1 mm) it spreads radially, while very close to the dielectric surface (~ 0.2-0.3 mm) it approaches again the axis of symmetry. In addition, the velocity of the excitation front, created by the helium excited species, decreased when oxygen admixtures were introduced in the helium jet from 8.85 ± 0.52 km/s to 6.41 ± 0.34 km/s in the experiment and 8.17 ± 0.22 km/s to 5.86 ± 0.14 km/s in the simulation.

Chapter 7

Numerical simulation of a capillary helium and helium-oxygen atmospheric pressure plasma jet: propagation dynamics and interaction with dielectric

7.1 Introduction

In this chapter the validated model presented in chapter 6 is used to shed light into the evolution of a helium plasma jet with and without the presence of oxygen admixtures, and its interaction with a dielectric surface. In particular, this chapter is mainly focus on: the most important reaction pathways behind the evolution of He and He/O_2 plasma jet, the effect of O_2 admixtures and the dielectric on the evolution and shape of plasma bullet, and the strength of the induced electric field (IEF) on the dielectric surface for pure helium and with oxygen admixtures plasma jet. Furthermore, the effects of Penning reactions and the secondary emission flux of electrons (SEFE) attributed to each ion in the mixture are also investigated through the same numerical model.

7.2 Experimental Setup

The experimental setup is shown in Figure 50. A high-voltage (HV) electrode made of a copper band is wrapped on a 20 cm long capillary soda lime glass tube (VWR International) with internal diameter (ID) of 0.9 mm and outer diameter (OD) of 1.35 mm. The HV electrode is 1 cm in length and is placed ~ 1.5 mm away from the exit of the tube. A dielectric barrier made of fussed quartz vitreosil 077 (UQG Optics LTD) of 1 mm thickness, is placed in front of the capillary tube, close to the HV electrode. The gas-gap thickness is fixed at 2 mm, in this study. The working gas (He or He+O_2) is continuously injected through the capillary tube. The flow of helium (4.6 spectral purity, Linde) and oxygen (4.5 spectral purity, Linde) is independently controlled using mass flow

controllers (MKS 1179A coupled with MKS type 247 four channel readout). The total gas flow rate is 1 slm.

High-voltage monopolar pulses are delivered from a high-voltage pulse amplifier (Trek, Inc., model PD07016) driven by an arbitrary waveform generator (Tektronix, model AFG3022C). Square positive voltage pulses with amplitude of 4.0 kV, duration of 50 μs, rise time of 7.3 μs and frequency of 10 kHz are used to excite the discharge.

In order to capture the dynamic behaviour of the plasma jet, an Intensified Charged Coupled Device (ICCD) consisting of a high resolution (1344 x 1024 pixels) CCD camera (Hamamatsu, model C8484-05G) and an image intensifier unit (Hamamatsu, model C9546-03) with an overall spectral response of 330-880 nm is used. The ICCD camera gate (~ 40 ns) was synchronized with the discharge current pulse. Additionally, an adjustable delay was used to follow the temporal evolution of the discharge current pulse. Each image was automatically stored using 1 s integration time and smoothed using a moving average filter. The temporal resolution is given by the camera gate (40 ns) and the time interval between two consecutive pictures taken along the current pulse (10 ns around current maximum and 40 ns the rest), while the spatial resolution is given by the CCD array and its objective magnification. Our experimental arrangement allows us to take pictures of the discharge gap width (2 mm) with high spatial resolution of about 8 μm.

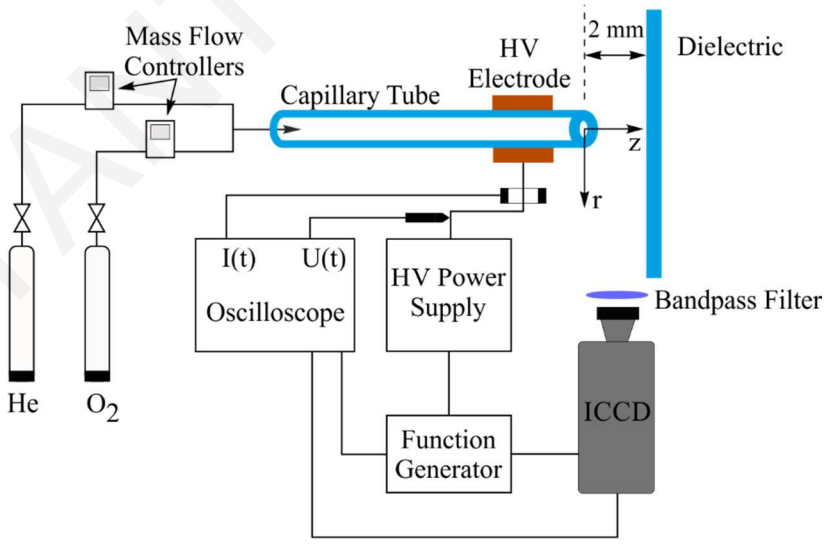

Figure 50. Experimental arrangement.

7.3 Experimental results

For the experimental study, He and He+O_2 (1000 ppm) plasma jets are considered. The ICCD camera is used to capture the dynamic evolution of the plasma bullet presented in Figure 51. The results presented in Figure 51 correspond to the rise time of the positive applied voltage, more exactly to the positive discharge current. The time of 0 ns corresponds to the time the maximum emission intensity of the plasma bullet coincides with the tube exit (z=0 mm). From Figure 51a, for the pure helium plasma jet, it can be seen that the plasma bullet forms two symmetric lobes during its propagation. These lobes indicate a torus (ring) like shape for the plasma bullet. Similar experimental observations were also made in [151,152]. For this case, the radius of the torus remains almost constant up to 1 mm (half way between the tube exit and the dielectric surface), while after 1 mm the radius starts increasing until the plasma bullet hits the dielectric surface. On the other hand, when 1000 ppm of oxygen admixture is introduced in the helium gas, the plasma bullet appears disk like and centred on the axis of symmetry during its propagation from the tube towards the dielectric surface. This is true up to 1 mm from the tube exit, and indicates a sphere like shape for the plasma bullet. The change of plasma bullet shape, from torus like shape (He plasma jet) to sphere like shape (He+O_2 (1000 ppm)), was also observed in [31,153–156], when admixtures were introduced in the helium gas. For distances longer than 1 mm and as the plasma bullet starts approaching the dielectric, the disk shape starts splitting and moves away from the axis of symmetry forming a torus. The above observations can be summarized as: (a) the addition of oxygen admixtures in the helium gas promotes the plasma bullet propagation on the axis of symmetry of the tube; (b) the presence of the dielectric surface (the slab placed in front of the tube exit) forces the plasma bullet to spread radially. Furthermore, the addition of oxygen admixtures causes a reduction of the plasma bullet speed. For the interpretation of these experimental observations, the simulation results will be analysed, for both pure helium and with 500, 1000, 1500 and 2000 ppm of oxygen.

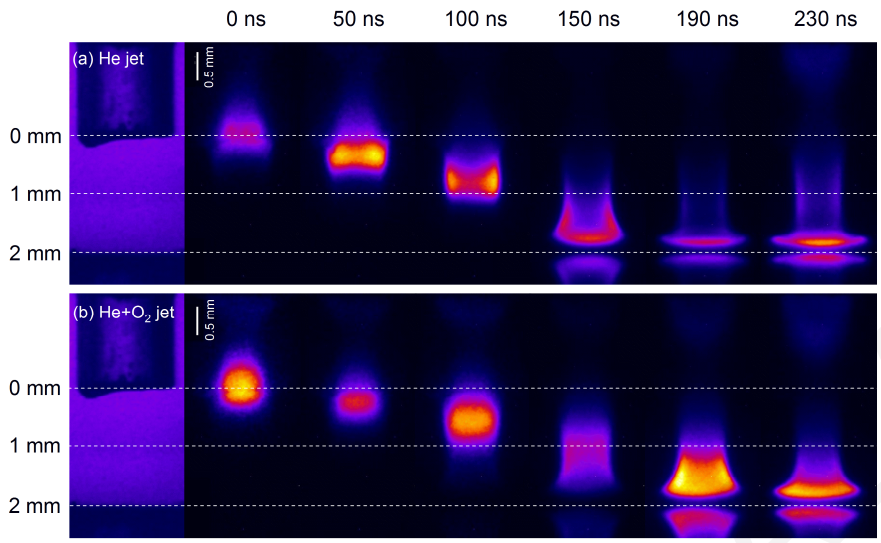

Figure 51: Spatio-temporal evolution of the plasma bullet for (a) He and (b) He+O_2 (1000 ppm) plasma jet. Time 0 ns corresponds to the plasma bullet just about the exit of the tube. The three dashed lines indicate the axial distance from the tube nozzle for z=0, 1 and 2 mm.

7.4 Analysis of the simulation results

In this section, the two-dimensional axi-symmetric model presented in chapter 6 is used to shed light into the evolution of the He and He/O_2 capillary helium plasma jet. It is noted that all the results presented in this section correspond to the rise time of the applied voltage. From the simulation results, it is observed that the evolution of the plasma jet has the characteristics of a streamer [29,152,157]. Consequently, in order to investigate its propagation, it is important to study the ionization rate on the streamer head. This will provide good insight into the evolution of the total light observed experimentally with the ICCD camera (presented in Figure 51) as it is expected to follow the propagation of the streamer. Furthermore, the interaction of the streamer with the dielectric surface and how it is affected by the introduction of oxygen admixtures is investigated in this section. In order to have comparisons with the experimental conditions the case of pure helium and with 1000 ppm admixtures of oxygen will be analysed in detail before the effects of different levels of oxygen (500-2000 ppm) are investigated. The simulation analysis will focus on the following:

- The reasons for the formation of torus shaped plasma bullet structure for the case of pure helium.
- The reasons for the change of plasma bullet structure to sphere shape once oxygen is added.

- The effect of the dielectric on the evolution of the plasma bullet.
- The effect of oxygen admixtures on the plasma bullet speed.
- The intensity of the induced electric field (IEF) on the dielectric surface for pure helium and with oxygen admixtures.

7.4.1 Evolution of the pure helium plasma jet

The helium-air mixture for the experimental setup presented in section 7.2 is obtained from the gas dynamic model and is shown in Figure 52. This shows that inside the tube prior to the exit, it is pure helium as expected. After it exits, it starts mixing with air, but it can be clearly seen that it forms a channel of almost pure helium that extends to the dielectric surface. The width of that channel is approximately the width of the tube. The mixing with air becomes more prevalent (the mole fraction of pure helium drops) away from the axis of symmetry (r = 0 mm) and as the gas propagation distance increases. This result is then fed into the plasma fluid model and the process is repeated for the case of adding 1000 ppm of oxygen to the helium gas (this is not shown here because it is indistinguishable from Figure 52).

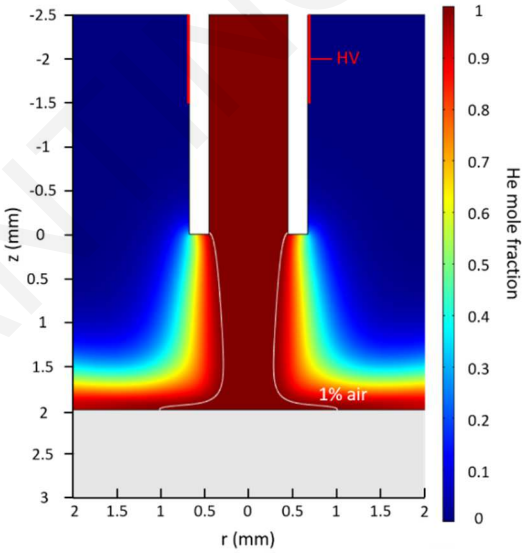

Figure 52: Helium-air mixture for the case of pure helium plasma jet obtained from the gas dynamic model. The white line shows the air at 1%.

For the analysis of the results, the evolution of the streamer is divided into three parts: first, propagation of the streamer from the tube towards the dielectric, second, interaction of the streamer with the dielectric surface, and third, propagation of the streamer along the dielectric surface. In the simulation model, the *streamer evolution is defined as the dynamic motion of the total*

ionization rate with the streamer head (plasma bullet) being the peak of that total ionization rate. The terms streamer head, plasma bullet and peak of total ionization rate will be used interchangeably throughout this study. The streamer will be analysed for the positions and times illustrated in Figure 53. The time 0 ns is set to when the streamer head coincides with the tube exit (z=0 mm). Points 1-7 in Figure 53 correspond to the case when the streamer is moving towards the dielectric and point 8 to the case when it reaches the dielectric, while points 9-11 the propagation of the streamer in the r direction (after it hits the dielectric surface).

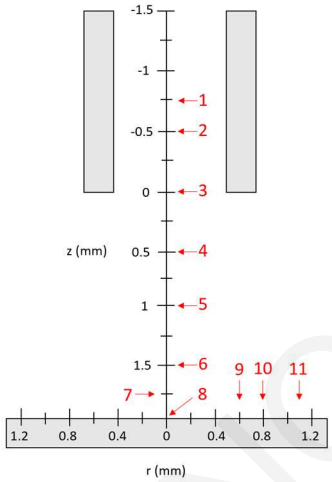

Point	Position (mm)	Time (ns)
1	z=-0.75	-152
2	z=-0.5	-96
3	z=0	0
4	z=0.5	68
5	z=1	121
6	z=1.5	164
7	z=1.75	190
8	z=1.94	204
9	r=0.6	303
10	r=0.8	403
11	r=1.1	586

Figure 53: Positions and corresponding times of the streamer head (total ionization rate) propagation for the He plasma jet. The time 0 ns corresponds to the streamer head coinciding with the tube exit (z=0 mm).

7.4.1.1 Spatio-temporal evolution of the streamer from the tube towards the dielectric

The spatio-temporal evolution of the total ionization rate is presented in Figure 54, for the same points defined in Figure 53. It is noted that the min and max values in Figure 54 are different for each sub figure, and therefore they are presented separately in each one. The applied voltage at time -152 ns (Figure 54a) is 1.85 kV and is considered the breakdown voltage, as it corresponds to the instance when the streamer starts to propagate. In particular, at this time the electric field created by the positive ions in the mixture becomes high enough to cause ionization and excitation hence propelling the streamer forward along the axis of symmetry towards the dielectric. The streamer shape changes during propagation. Initially the shape is disk like (Figure 54a) but by the time it exits the tube (Figure 54b and Figure 54c) it breaks into two lobes and then remains almost constant until it reaches 1 mm away from the dielectric (see Figure 54d and Figure 54e). From that point onwards its radius keeps increasing forming more distinct lobes (see Figure 54f and Figure

54g) until it hits (reaches) the dielectric, at which point its maximum is closer to the axis of symmetry (Figure 54h). The evolution of the streamer head (total ionization rate) presented below agrees qualitatively with the experimental results shown in Figure 51a.

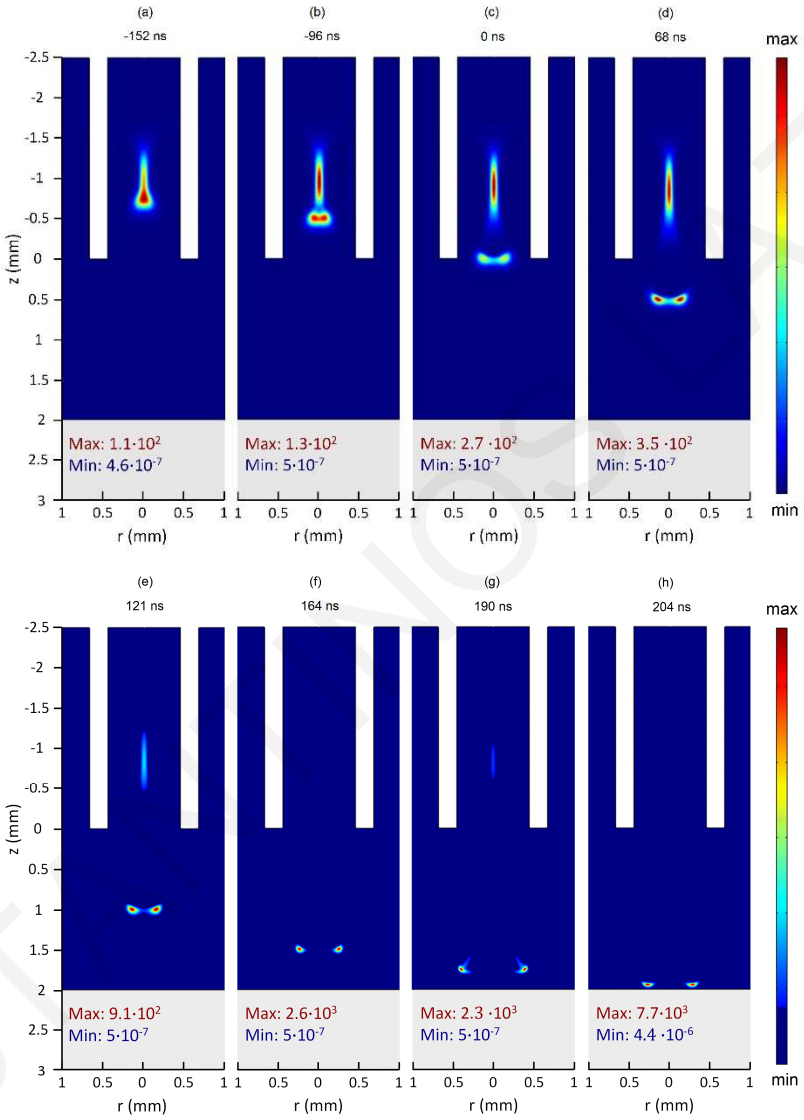

Figure 54: Simulation results of the spatio-temporal evolution of the total ionization rate (time snapshots as in Figure 53), for the He plasma jet. The total ionization rate has units of mol/m^{3}s.

7.4.1.2 Electron production

In order to understand the evolution of the plasma bullet, the electron production in front of the streamer head is further investigated. In Figure 55 the electron production rate is presented in

logarithmic scale at -152 ns which corresponds to the same time snapshot of the total ionization rate shown in Figure 54a. Figure 55 shows the electron production being maximum at z=-0.75 mm which, as expected, coincides with the streamer head in Figure 54a. Away from the streamer head at z = 0.1 mm, the electron production pointed with arrows in Figure 55, shows that there is also a relatively high electron production at the boundary with air (r~0.35 mm). These electrons are mainly produced from the Penning reactions (PR) of the nitrogen and oxygen molecules by the He_m species (R43, R51, R73 and R74, see Figure E1 in Appendix E). Those electrons will act as seeds accelerating into the tube and feeding the streamer head promoting the propagation of the streamer in the lateral direction creating a torus shape for the plasma bullet (see Figure 54b-Figure 54c). In order to ensure the validity of this conclusion, another simulation was performed (see Figure E2 in Appendix E), without considering Penning reactions in the kinetic scheme (i.e. their rate coefficients were set to zero) and the torus like shape of the plasma bullet was not observed. In this case, the propagation of the plasma bullet occurs on the axis of symmetry of the tube and has a sphere like shape. The importance of Penning reactions on the evolution of helium DBD has been shown in several studies [32,67,75,158–162].

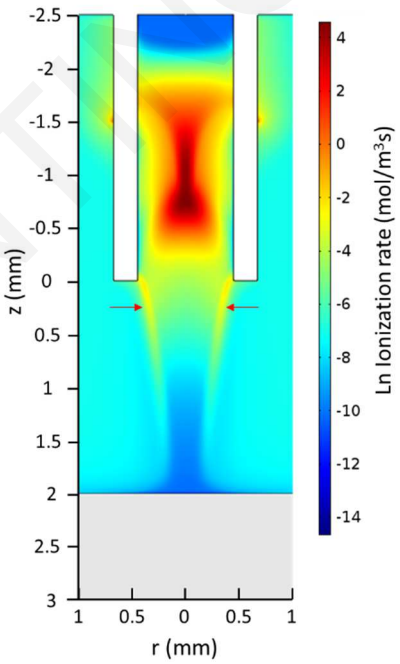

Figure 55: Simulation results of electron production rate in logarithmic scale for the He plasma jet at time -152 ns.

Once out of the tube and up to 1 mm away from the dielectric, the radius of the streamer remains almost constant, (see Figure 54d and Figure 54e). This is because the electron production

in front of the streamer head presents peak at similar radius as the torus radius of the streamer (see Figure E3a in Appendix E). As can be seen, those electrons are mainly produced through Penning reactions of He_m with N_2 and O_2 molecules. After 1 mm from the tube exit, the torus radius of the streamer increases (see Figure 54f and Figure 54g) as the production of electrons in front of the streamer occurs at larger radius. Those electrons are mainly produced through Penning reactions of He_m and He_2^m with N_2 and O_2 molecules (see Figure E3b in Appendix E).

Close to the dielectric, the shape of the plasma bullet is affected by the electrons emitted from the dielectric surface. The SEFE attributed to each ion in the mixture when the streamer is far from the dielectric and when it approaches the dielectric surface (same time snapshots as Figure 54e and Figure 54g corresponding to streamer head at 1 and 1.75 mm respectively) are presented in Figure 56a and Figure 56b respectively. As can be seen from Figure 56a, the SEFE is much higher on the sides (r~0.5 mm) than on the centre (r=0 mm). The major contributors to the SEFE are the O_4^+ ions that due to mixing with air are higher on the sides than in the centre. It is worth mentioning that the contribution of O_4^+ is dominant because most ions are eventually converted to O_4^+ (see schematic diagram of Figure 21). However, as the streamer head approaches the dielectric surface (Figure 54g) the electric field in the region between streamer head and the dielectric surface increases, and that causes the positive ions to accelerate towards the dielectric surface. This increases the SEFE from all the ions and particularly from the helium ions as seen in Figure 56b. The SEFE due to the helium ions species is increased in the centre of the dielectric, eventually causing the decrease of the streamer head torus radius as seen in Figure 54h. It is noted that when seec is set to zero, the decrease of the streamer torus radius when the plasma bullet reaches the dielectric surface is not observed (see Figure E4 in Appendix E).

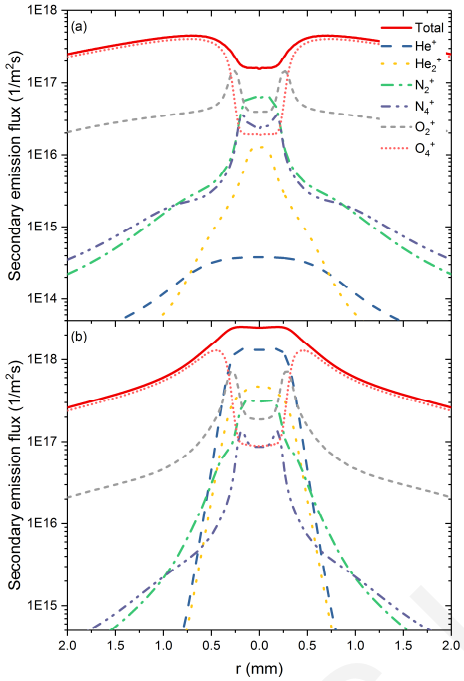

Figure 56: Simulation results of the secondary emission flux of electrons (SEFE) attributed to the different ions for the times (a) 121 ns and (b) 190 ns, for the He plasma jet.

7.4.1.3 Interaction of the streamer with the dielectric surface

As the streamer propagates towards the dielectric, it causes the accumulation of a surface charge. That surface charge induces an axial electric field that opposes and eventually negates the axial electric field of the streamer. That will stop the axial propagation of the streamer. Consequently, the radial electric field dominates, and the streamer starts propagating laterally (parallel to the dielectric). To illustrate that, the surface charge accumulation and the electric field in z and r direction along the dielectric surface are presented in Figure 57, at different times which correspond to the cases of before (121, 164 and 190 ns), during (204 ns) and after (303, 403 and 586 ns) the streamer head reaches the dielectric surface. The positions of streamer head for these times are indicated in Figure 53. As can be seen from Figure 57, as the plasma streamer approaches the dielectric surface, the electric fields (in z and r directions) on the dielectric surface start increasing. As the streamer head reaches the dielectric surface (204 ns), the electric field in z and r direction increase considerably leading to surface charge accumulation. The axial electric field, E_z, due to the interaction of the streamer with the dielectric surface is ~ 37 kV/cm. It is important to note that the axial electric field and the surface charge accumulation during the interaction of the streamer with the dielectric surface present their peaks off axis, indicating a torus-like

interaction of the plasma streamer with the dielectric surface. After that time, the surface charge accumulation continues to build up causing the reduction in the axial electric field. After some time, the radial electric field dominates, and the streamer proceeds to propagate radially (parallel to the dielectric surface). The results shown in Figure 57 associated with the streamer propagation in the radial direction (times 303, 403 and 586 ns) are analysed below when this case is investigated.

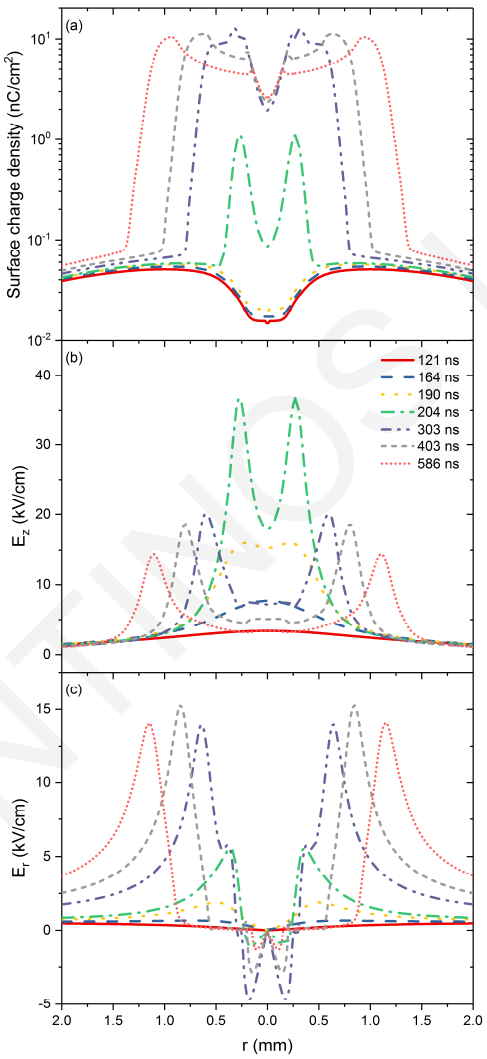

Figure 57: Simulation results of the (a) surface charge density, (b) electric field in z direction (axial) and (c) electric field in radial direction during the propagation of the streamer, for the He plasma jet.

7.4.1.4 Spatio-temporal evolution of the streamer along the dielectric surface

The spatio-temporal evolution of the total ionization rate during the propagation of the streamer along the dielectric surface is presented in Figure 58, for three different times (positions

of the streamer head from the axis of symmetry of the tube: 0.6, 0.8 and 1.1 mm, see Figure 53). It is shown that when the streamer reaches the dielectric surface, it continues parallel to it at a height of ~ 60 - 70 μm charging the surface below it (see Figure 57a). This increases the surface charge eventually shielding the axial electric field behind the streamer head (see Figure 57b). However, the axial and radial electric fields decrease gradually (Figure 57b and Figure 57c), causing the reduction of the ionization rate on the streamer head (see Figure 58). This continual reduction of ionization rate will eventually stop the propagation of the streamer. From the simulation results, it has been found that during the plasma bullet propagation along the dielectric surface the electron concentration is about $5 \cdot 10^{18}$ [m^{-3}] while the mean electron energy reduces from 20 eV to 10 eV. These results, provide a Debye length in the range of 10 to 15 μm. The sheath thickness found here (60-70 μm), as expected, corresponds to a few times the Debye length, which is in agreement with previous studies [163].

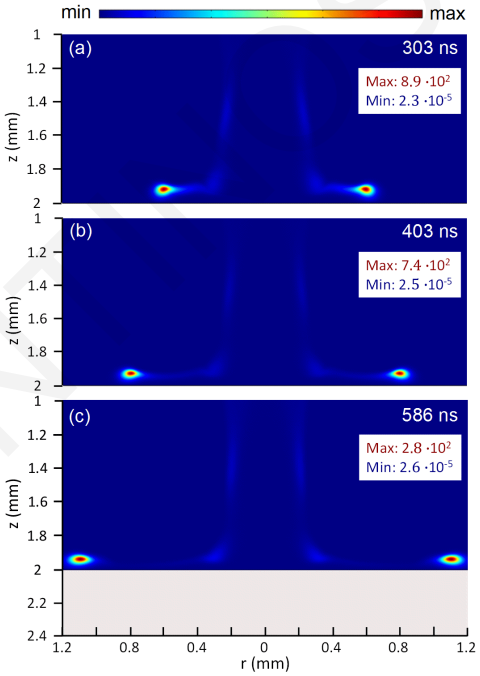

Figure 58: Simulation results of the spatio-temporal evolution of the total ionization rate along the dielectric surface (time snapshots as in Figure 53), for the He plasma jet. The total ionization rate has units of mol/m^3s.

7.4.2 Evolution of the He+O_2 (1000 ppm) plasma jet

Similar to the analysis for pure helium plasma jet, the present analysis is divided into three parts: evolution of the streamer from the tube towards the dielectric surface, interaction of the streamer with the dielectric surface and evolution of the streamer along the dielectric surface. The

spatio-temporal evolution of the total ionization rate during the streamer propagation will be analysed for the positions and times illustrated in Figure 59.

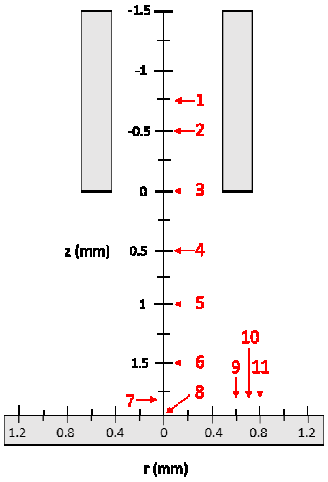

Point	Position (mm)	Time (ns)
1	z=-0.75	-181
2	z=-0.5	-114
3	z=0	0
4	z=0.5	92
5	z=1	163
6	z=1.5	227
7	z=1.8	261
8	z=1.96	267
9	r=0.6	432
10	r=0.7	506
11	r=0.8	601

Figure 59: Positions and corresponding times of the streamer head (total ionization rate) propagation for the He+O_2 (1000 ppm) plasma jet. The time 0 ns corresponds to the streamer head coinciding with the tube exit (z=0 mm).

7.4.2.1 Spatio-temporal evolution of the streamer from the tube toward the dielectric

The propagation of the streamer from the tube towards the dielectric surface for the He+O_2 (1000 ppm) plasma jet is analysed here. The total ionization rate is presented in Figure 60 for the same points as in Figure 59. As can be observed from Figure 60a, the total ionization rate initially increases in the region close to the electrodes on the axis of symmetry of the tube and has a disk like-shape. At this time (-181 ns which corresponds to the instance when the streamer starts to propagate) the applied voltage is 1.23 kV (breakdown voltage). The decrease of the breakdown voltage once oxygen admixtures are introduced in a helium barrier discharge is explained in chapter 4. Particularly, in such discharges (helium with admixtures of air components), the ions in the mixture are mainly increased due to the increase of He^+ and He_m species (see Figure 21). The increase of O_2 concentration in the mixture benefits the reactions associated with this species (such as Penning ionization reaction, charge transfer reaction etc.). As a result, a lower concentration of He_m and He^+ is required for ion production. The concentration of the former species is highly dependent on the electron temperature and consequently on the breakdown voltage. Then, in helium with admixtures of air components, the increase of air concentration results in a decrease of the breakdown voltage.

Once the streamer begins to move towards the dielectric surface, its propagation remains on the axis of symmetry up until 1 mm from the tube exit (Figure 60b-Figure 60e). After 1 mm from

the tube exit, the streamer forms two symmetric lobes centred on the axis of symmetry (Figure 60f). However, as the streamer approaches the dielectric surface, its maximum approaches the axis of symmetry of the tube (see Figure 60g and Figure 60h). The streamer exhibits qualitatively similar behaviour to the experimental results presented in section 7.3 (see Figure 51b).

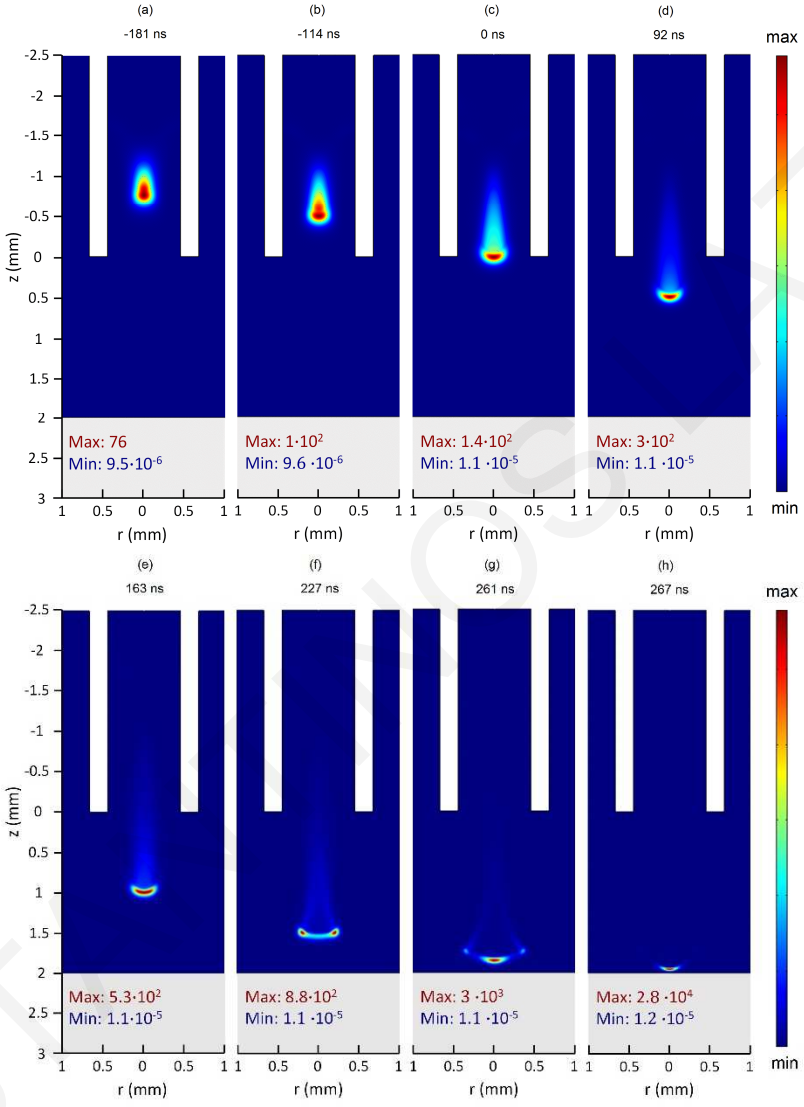

Figure 60: Simulation results of the spatio-temporal evolution of the total ionization rate (same time snapshots as in Figure 59), for He+O_2 (1000 ppm) plasma jet. The total ionization rate has units of mol/m^3s.

7.4.2.2 Electron production

In order to further understand the evolution of the plasma bullet, the electron production in front of the streamer head is investigated. In Figure 61 the electron production rate is presented in

logarithmic scale at -181 ns which corresponds to the same time snapshot of the total ionization rate shown in Figure 60a. Figure 61 shows the electron production being maximum at z=-0.75 mm which, as expected, coincides with the streamer head in Figure 60a. However, unlike the case for pure helium there is no off axis (on the side) peak production of electrons outside the tube. Therefore, the streamer does not break to form a torus shape and remains disk like propagating on the axis of symmetry (see Figure 60a-Figure 60c).

Those electrons are mainly produced from the Penning ionization of the oxygen molecules by the He_m species (R73 and R74, see Figure E5 in the Appendix E) and due to the high amount of oxygen admixtures in the helium channel, are not affected much by the mixing with atmospheric air. As a result, the electron production around the centre (for r<0.35 mm) is almost constant and does not exhibit strong peaks on the edges (r~0.35 mm). This is in contrast to the pure helium plasma where the mixing with air plays an important role in the production of electrons.

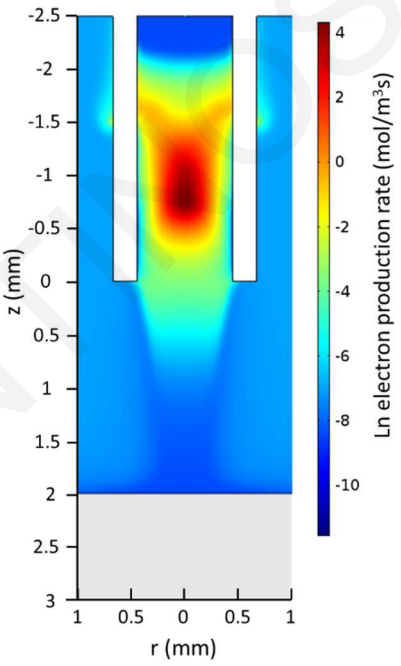

Figure 61: Simulation results of electron production rate in logarithmic scale for He+O_2 (1000 ppm) plasma jet at time – 181 ns.

Once out of the tube, the streamer continues to propagate on the axis of symmetry (see Figure 60d-Figure 60e), as electrons in front of the streamer are mainly produced in the helium channel. Those electrons are mainly produced from Penning reactions of He_m with O_2 (see Figure E6a in Appendix E). After 1 mm of the streamer from the tube exit, the maximum of electron production

in front of the streamer head occurs off axis. Those electrons feed the streamer head from the sides, promoting its propagation in the lateral direction creating a torus shape for the plasma bullet (see Figure 60f). The off axis production of electrons is mainly due to the Penning reaction of He_m and He_2^m with nitrogen molecules (see Figure E6b in Appendix E). It is noted that when the Penning reactions are eliminated from the kinetic scheme (i.e. their rate coefficients are set to zero) the torus like shape of the plasma bullet is no longer observed (see Figure E7 in Appendix E).

In order to investigate the effect of the dielectric on the plasma bullet shape, the SEFE attributed to each ion in the mixture when the streamer is far from the dielectric and when it approaches the dielectric surface (same time snapshot as Figure 60e and Figure 60g corresponding to streamer head at 1 and 1.8 mm respectively) are presented in Figure 62a and Figure 62b respectively. As can be seen from Figure 62a, the SEFE is much higher on the sides (r~0.5 mm) than in the centre (r=0 mm). However, as the streamer head continues approaching the dielectric surface, the SEFE peak is at the axis of symmetry (r = 0 mm) as shown in Figure 62b. This promotes the propagation of the streamer on the axis of symmetry of the tube making the shape more disk like again (shown in Figure 60g and Figure 60h). The major contributor to the SEFE close to the centre are the He^+ species. It is noted that when the seec is set to zero the approaching of the streamer on axis of symmetry is not observed (see Figure E8 in Appendix E).

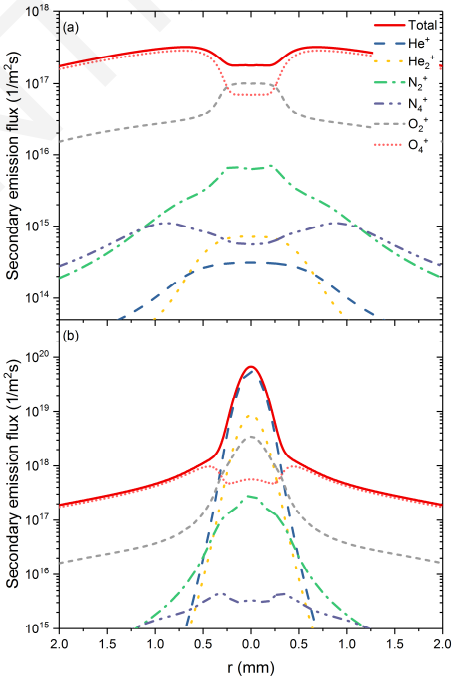

Figure 62: Simulation results of secondary emission flux of electrons (SEFE) attributed to the different ions for the times (a) 163 ns and (b) 261 ns, for $He+O_2$ (1000 ppm) plasma jet.

7.4.2.3 Interaction of the streamer with the dielectric surface

The interaction of the streamer head with the dielectric surface (Figure 60h), causes the accumulation of surface charge. That surface charge induces an axial electric field that opposes and eventually negates the axial electric field of the streamer. That will stop the axial propagation of the streamer. Consequently the radial electric field dominates and the streamer starts propagating laterally (parallel to the dielectric). To illustrate that, the surface charge density on the dielectric surface and the electric fields in z and r direction before, during and after the streamer reaches the dielectric surface are presented in Figure 63. The positions of streamer head for these times are indicated in Figure 59.

As can be seen from Figure 63, before the streamer reaches the dielectric surface (times = 163, 227 and 261 ns), the surface charge density and the electric field on the dielectric surface are low. Once the streamer reaches the dielectric (267 ns), they both increase. During the interaction of the streamer with the dielectric surface, the axial electric field reaches the value of ~51 kV/cm which is higher in comparison to the pure He plasma jet (~37 kV/cm). The difference in the peak values of E is most likely caused by the higher concentration of electrons ~ $1.25 \cdot 10^{19}$ m^{-3} in the case of He/O_2 plasma jet in comparison to ~ $5 \cdot 10^{18}$ m^{-3} for the He plasma jet. Furthermore, the electric field in the He/O_2 plasma jet does not have torus-like shape as in the pure helium plasma jet case but presents its peak on the axis of symmetry. After the streamer reaches the dielectric surface, the charge density increases until it cancels the axial electric field of the streamer. The remaining radial electric field causes the streamer to continue to propagate parallel to the dielectric. The results shown in Figure 63 associated with the streamer propagation in the radial direction (times 432, 506 and 601 ns) are analysed below.

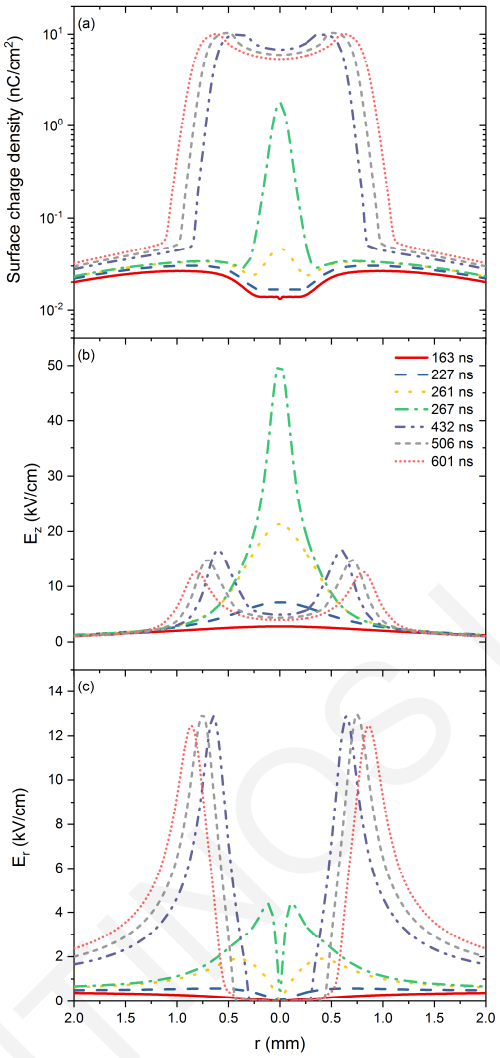

Figure 63: Simulation results of the (a) surface charge density, (b) electric field in z direction and (c) electric field in r direction during the propagation of the streamer for He+O_2 (1000ppm) plasma jet.

7.4.2.4 Propagation of the streamer along the dielectric surface

The spatio-temporal evolution of the total ionization rate during the propagation of the streamer along the dielectric surface is presented in Figure 64, for three different positions of the streamer head from the axis of symmetry of the tube (0.6, 0.7 and 0.8 mm). After the streamer reaches the dielectric surface, its propagation continues along the dielectric surface at a height about 60 - 70 μm above it. During the propagation of the streamer head, positive ions are accelerated towards the dielectric surface (charging the dielectric surface, see Figure 63a) causing the eventual shielding of the electric field behind streamer head (see Figure 63b). Furthermore, as can be observed from Figure 63b and Figure 63c, the axial and radial electric fields decrease

gradually, causing the reduction of the ionization rate on the streamer head (see Figure 64). This continual reduction of ionization rate will eventually stop the propagation of the streamer.

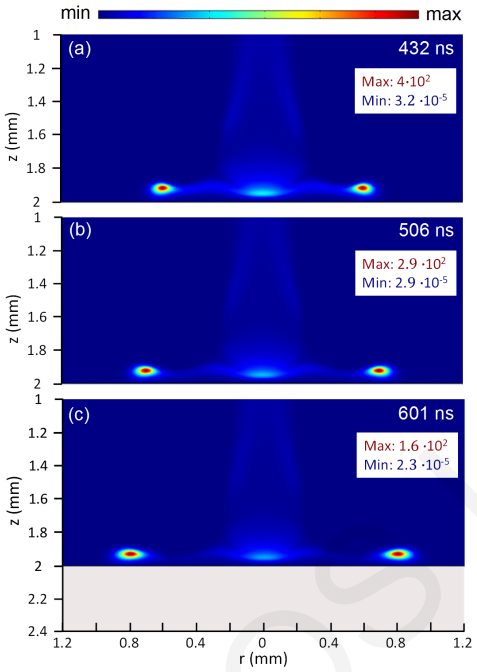

Figure 64: Simulation results of time snapshots of the total ionization rate of He+O_2 (1000 ppm) plasma jet, during the propagation of the streamer along the dielectric surface. The total ionization rate has units of mol/m^3s.

7.4.3 Effects of different level of oxygen admixtures on the plasma evolution and interaction with the dielectric surface

As oxygen admixtures vary from 500-2000 ppm the general behaviour of the streamer and its interaction with the dielectric surface does not change significantly, and therefore the detailed analysis presented in section 7.4.1 and 7.4.2 will not be repeated here. Two important parameters such as the streamer speed and IEF (during the interaction of the streamer with the dielectric surface) are presented here. The propagation speed of the streamer, derived from Figure 65, shows a significant difference between pure helium and He+O_2, albeit little variation with different admixture levels. The average speed is 7.7 km/s and 6.1 km/s for pure helium and He+O_2 plasma jet respectively. This reduction of the speed of the plasma bullet when 1000 ppm of oxygen admixtures is introduced in the helium gas is also observed experimentally (see section 7.3).

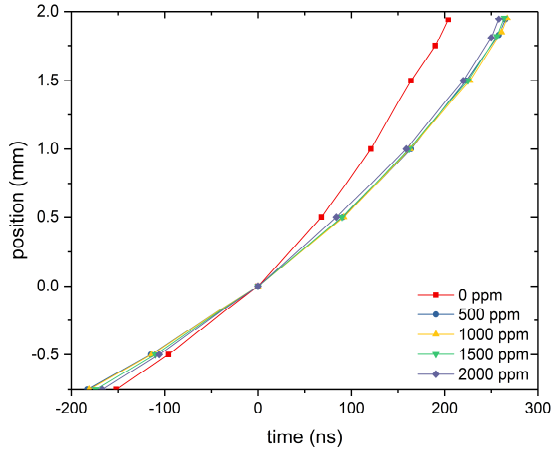

Figure 65: Simulation results of the axial position of the streamer head as a function of time.

The IEF built on the dielectric surface (during the streamer surface interaction) at different levels of oxygen admixtures in the helium gas is presented in Figure 66. The results presented correspond to the times of 204, 265, 267, 264 and 258 ns for the case of 0, 500, 1000, 1500 and 2000 ppm of oxygen admixtures in the helium gas. As can be observed, for the case of $He+O_2$ plasma jet there is a time delay for the interaction of the plasma jet with the surface. Furthermore, the $He+O_2$ plasma jet generates higher IEF in comparison to the pure helium plasma jet. Furthermore, the peak of the IEF on the dielectric surface is on the axis of symmetry for $He+O_2$ plasma jets and off the axis of symmetry for pure helium plasma jet. The maximum IEF (~ 55 kV/cm) occurs for the case of 1500 ppm of oxygen admixtures in the helium gas. Even though this will be the subject of future studies, it is worth mentioning that the higher electric fields for $He+O_2$ plasma jets could have significant implications for biomedical applications. They could make cells more susceptible to electroporation and could account for the observation that the presence of oxygen impurities in the helium plasma jet can increase cancer cell apoptosis [44,12].

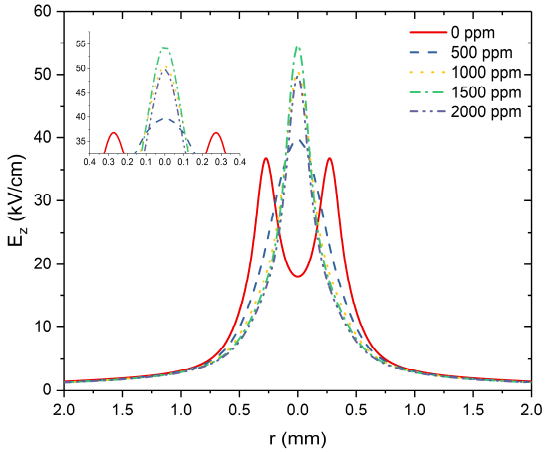

Figure 66: Induced electric field on the dielectric surface at different level of oxygen admixtures.

7.5 Conclusions

In this chapter, a two dimensional model was used to shed light into the evolution of a capillary helium plasma jet with and without the presence of oxygen admixtures and its interaction with a dielectric surface. The level of oxygen admixtures considered in this study is in the range of 500 to 2000 ppm. The simulation results show that oxygen admixtures highly affect the streamer shape, propagation speed, and the induced electric field on the dielectric surface. The shape of the plasma bullet during its propagation is controlled by the generation of seed electrons in front of the streamer head. For $He+O_2$ plasma jet, the shape of the bullet remains sphere like for propagation up to 1 mm away from the dielectric. This is because the seed electrons are mainly produced uniformly along the axis of symmetry in the helium channel. They are produced through Penning ionization of helium metastable species with the admixture of O_2 molecules. After 1 mm from the tube exit, the streamer forms two symmetric lobes centred on the axis of symmetry due to the off axis production of electrons in front of the streamer head. Those electrons are mainly produced through Penning reactions of He_m and He_2^m with N_2 molecules. In the case of pure helium jet the bullet will be torus shape because seed electrons in the helium channel are mainly generated on the edges of the channel through Penning ionization of nitrogen and oxygen molecules by He_m and He_2^m species (due to the higher N_2 and O_2 in this region from atmospheric air mixing). It should be noted that for both cases, once the streamer head gets very close to the dielectric (~ 0.1 - 0.2 mm) it is pulled towards the centre (the axis of symmetry) due to the high generation of SEFE on the axis of symmetry. Furthermore, it was observed that the plasma bullet speed decreases when

the helium plasma jet is operated in the presence of oxygen admixtures. Finally, one of the most significant results is the observation of much higher induced electric field on the dielectric surface with the introduction of the optimal amount of oxygen admixtures. This is very important, since in some applications where the APPJ is to be used to destroy (or cause the apoptosis of) diseased cells, higher electric fields mean higher electroporation of the cells and consequently higher amounts of reactive species or even therapeutic drugs successfully introduced into the cells.

Chapter 8

Conclusions and Future work

8.1 Conclusions

The influence of air impurities on the evolution of helium DBD operated at atmospheric pressure is investigated in this work through a simulation model. Deep understanding into the physics behind helium discharges and how the fundamental processes are affected by the presence of air impurities is a prerequisite for the optimization of helium DBD devices. In this work, an accurate model has been developed which is able to describe helium DBD in the presence of the dominant air constituents, i.e. nitrogen, oxygen and water. The model takes into account the analytical chemistry between the helium, nitrogen, oxygen and water species and is validated with experimental results. Due to the high complexity of the model, its development is split into three steps, starting with a simple model (pure helium) and then upgrading it by adding more details (N_2, then O_2 and finally H_2O). This systematic and gradual methodology provides confidence for the validity of the developed model.

The first model developed considers the analytical chemistry between helium and nitrogen species. In the plasma chemistry 10 species and 46 reactions channels are used. The validity of the model is ensured by comparing the simulation with experimental results. After the validation, the fundamental processes occurring during the discharge are examined, as well as the most important species. This analysis provides useful insight into the physics behind the evolution of helium DBD in the presence of nitrogen impurities. In order to further investigate the effect of nitrogen impurities on the evolution of the helium DBD the level of nitrogen impurities is varied in the range 0.1 to 500 ppm. It is observed that the nitrogen impurities significantly affect the dominant ion species at breakdown and the discharge characteristics (discharge current and breakdown voltage). Specifically, three different dominant ions were found, which are strongly dependent on the level of nitrogen impurities. These are: He_2^+ (0.1 to 35 ppm), N_2^+ (35 to 150 ppm) and N_4^+ (150 to 500 ppm). In addition, the results show that the discharge characteristics are dependent on

the dominant ion species at breakdown. This result is very important for the utilization of atmospheric pressure plasma helium devices.

Thereafter, in order to increase the accuracy of the model, the oxygen species (which constitute approximately the remaining 21% of air) are introduced in the model chemistry. The new plasma chemistry now uses 27 species and 153 reaction channels. This model is validated with experimental results and is subsequently used to investigate the influence of air traces (79% N_2 and 21% O_2) on the evolution of the helium DBD. The level of air used as impurity is in the range from 0 to 1500 ppm, which corresponds to the most commonly encountered range in atmospheric pressure discharge experiments. This is the first time where the influence of air traces on helium DBD is studied in such a wide range of compositions. The results clearly demonstrate that the plasma chemistry and consequently the discharge evolution is strongly affected by the concentration level of impurities in the mixture. The simulations show that air traces assist the discharge ignition at low concentration levels (~55 ppm) while they increase the burning voltage at higher concentration levels (~1000 ppm). Furthermore, it is found that the discharge symmetry during the voltage cycle depends strongly on the concentration of air. In order to interpret the results a detailed analysis of the processes that occur in the discharge gap is performed and the main reaction pathways of ion production are investigated. This fundamental analysis provides for the first time convincing explanation for the well-known rule of thumb that low concentration of air helps the ignition of the helium DBD, while higher levels stop the discharge ignition. All this insight and deep understanding is crucial for the **optimized** and **stable operation of plasma devices**.

In the third step water admixtures are introduced in the model. The new plasma model considers 56 species and 496 reaction channels and it is verified with experimental results in order to ensure its correctness. Subsequently, the level of dry air (79% N_2 and 21% O_2) is kept constant at 500 ppm (a plausible value for atmospheric pressure discharges without any vacuum equipment) and the effect of water admixtures (20 to 2000 ppm) on the discharge evolution is investigated. The simulation results show that the increase of water in the mixture benefits the H_2O-related reactions. This causes the discharge current peak to increase, and the discharge to ignite at lower voltages (up to 600 ppm of water). However, the further increase of water (above 600 ppm) enhances the attachment of electrons with water molecules which causes the discharge to ignite at higher voltages. Despite the higher breakdown voltage, the discharge current peak remains almost

constant, due to the high attachment of electrons with water molecules. The simulation results also show that the dominant ion for water admixtures in the range of 20 to 100 ppm is H_2O^+. By further increasing the water in the mixture, the water ion clusters are quickly converted to heavier water ion clusters. For that reason, from 100 ppm of water and up to 2000 ppm, the $H_{11}O_5^+$ is the most abundant ion in the mixture. Finally, from 20 to 2000 ppm of water admixtures, the most important negative charge species are found to be electrons.

In the final step, the helium/dry air model was used to shed light into the evolution of a capillary helium plasma jet device with and without the presence of oxygen admixtures and its interaction with a dielectric surface. The level of oxygen admixtures considered in this study is in the range of 500 to 2000 ppm. Through the model, for the first time to our knowledge, a convincing explanation is given for the well-known rule of thumb that the helium plasma jet produces **ring/torus like shape plasma bullet** propagating off axis of symmetry while with oxygen admixtures in the helium gas the plasma bullet changes to a **sphere like shape** and propagates on the axis of symmetry. The simulation results shows that the shape of the plasma bullet during its propagation is controlled by the generation of seed electrons in front of the streamer head. In the case of pure helium jet the plasma bullet is torus shape because seed electrons in the helium channel are mainly generated on the edges of the helium-air channel through Penning ionization of nitrogen and oxygen molecules by He_m and He_2^m species (due to the higher N_2 and O_2 in this region from atmospheric air mixing). On the other hand, for the $He+O_2$ plasma jet, the shape of the bullet remains sphere like during its propagation because seed electrons are mainly produced uniformly along the axis of symmetry in the helium channel, through Penning ionization of helium metastable species with the admixture of O_2 molecules. Furthermore, in this study for the first time, the effect of oxygen admixtures on the surface interaction is explored. It is shown how a **small level of oxygen impurities** can more than **double the induced electric field on the dielectric surface**. All this insight gained through the above simulation results is very important for the experimentalist working with helium and helium oxygen plasma jet devices and utilize them for biomedical applications

8.2 Future Work

Cold atmospheric pressure plasma (CAPP) has been found to be very effective in treating cancer cells without damaging normal cells. This selectivity, gives to the CAPP an important advantage over the conventional methods against cancer. In the literature there are several studies demonstrating this selectivity [9,12,11]. Up to now, it was believed that reactive oxygen and nitrogen species (RONS) produced through the CAPP devices are responsible for this selectively. However, recent advances in the field have shown that the combination of RONS and induced electric field (IEF) and not just RONS give the CAPP its unique therapeutic abilities, such as selectively treating cancer. The models that have been developed up to date for the description of a plasma-tissue interaction have many simplifications and in most of cases fail to correctly reproduce the physical description of the surface under treatment.

In the future we are planning to develop an accurate model for the description of normal and cancerous tissues, and investigate their behaviour under the interaction with a helium plasma jet device. The description of the normal and cancerous tissues will be based on their electrical characteristics. In this model, the healthy and non-healthy tissue will be incorporated and average values for their electrical characteristics will be considered. Through the model, the voltage across the tissue and the level of RONS penetration in the tissue will be computed. These results will be then fed into a new model dealing with the exact dimensions of all parts of the cells (cytoplasmic membrane, nuclear membrane, cytoplasm, nucleus, extracellular fluid) in a tissue. Through this model, accurate results for the voltage induced across the cell membrane and the level of RONS in the cells will be calculated. These results will enable us to understand the selectivity of plasma jet against cancer, with final goal the optimization of the device for this scope.

Appendix A: Rate coefficients for helium and nitrogen reactions and mesh independency analysis.

Table A1: Rate coefficients for helium and Nitrogen reactions.

Reaction No.	Reaction equation	Rate constant (m^3/s)	Threshold(eV)	Ref
1	$e^- + He \rightarrow e^- + He$	σ(E)	0	[105]
2	$e^- + He \rightarrow e^- + He_m^*$	σ(E)	19.82	[105]
3	$e^- + He \rightarrow e^- + He_m^*$	σ(E)	20.61	[105]
4	$e^- + He \rightarrow e^- + He^{**}$	σ(E)	20.96	[105]
5	$e^- + He \rightarrow e^- + He^{**}$	σ(E)	21.21	[105]
6	$e^- + He \rightarrow e^- + He^{**}$	σ(E)	22.97	[105]
7	$e^- + He \rightarrow e^- + He^{**}$	σ(E)	23.7	[105]
8	$e^- + He \rightarrow e^- + He^{**}$	σ(E)	24.02	[105]
9	$e^- + He \rightarrow 2e^- + He^+$	σ(E)	24.58	[105]
10	$e^- + He_m^* \rightarrow 2e^- + He^+$	σ(E)	4.78	[105]
11	$e^- + He_m^* \rightarrow e^- + He$	2.9×10^{-15}	-19.8	[66]
12	$e^- + He_2^* \rightarrow e^- + 2He$	3.8×10^{-15}	-17.9	[66]
13[a]	$2e^- + He^+ \rightarrow He_m^* + e^-$	6×10^{-32}	-4.78	[66]
14[a]	$He_2^+ + 2e^- \rightarrow He_m^* + He + e^-$	2.8×10^{-32}	0	[66]
15[a]	$He_2^+ + e^- + He \rightarrow He_m^* + 2He$	3.5×10^{-39}	0	[66]
16[a]	$He_2^+ + 2e^- \rightarrow He_2^* + e^-$	1.2×10^{-33}	0	[66]
17[a]	$He_2^+ + e^- + He \rightarrow He_2^* + He$	1.5×10^{-39}	0	[66]
18	$He^{**} + He \rightarrow He_2^+ + e^-$	1.5×10^{-17}	0	[66]
19	$He_m^* + He_m^* \rightarrow He_2^+ + e^-$	2.03×10^{-15}	-18.2	[66]
20	$He_m^* + He_m^* \rightarrow He^+ + He + e^-$	8.7×10^{-16}	-15.8	[66]
21[a]	$He^+ + 2He \rightarrow He_2^+ + He$	6.5×10^{-44}	0	[66]
22[a]	$He_m^* + 2He \rightarrow He_2^* + He$	1.9×10^{-46}	0	[66]
23	$He_m^* + He_2^* \rightarrow He^+ + 2He + e^-$	5×10^{-16}	-13.5	[66]
24	$He_m^* + He_2^* \rightarrow He_2^+ + He + e^-$	2×10^{-15}	-15.9	[66]
25	$He_2^* + He_2^* \rightarrow He^+ + 3He + e^-$	3×10^{-16}	-11.3	[66]
26	$He_2^* + He_2^* \rightarrow He_2^+ + 2He + e^-$	1.2×10^{-15}	-13.7	[66]
27	$He_2^* + He \rightarrow 3He$	4.9×10^{-22}	0	[66]
28	$He_m^* + N_2 \rightarrow e^- + N_2^+ + He$	7×10^{-17}	0	[66]
29	$He_2^* + N_2 \rightarrow e^- + N_2^+ + 2He$	7×10^{-17}	0	[66]
30	$He^+ + N_2 \rightarrow N_2^+ + He$	5×10^{-16}	0	[66]
31	$He^+ + N_2 \rightarrow N^+ + N + He$	7×10^{-16}	0	[66]
32	$He_2^+ + N_2 \rightarrow N_2^+ + 2He$	5×10^{-16}	0	[66]
33	$He_2^+ + N_2 \rightarrow N^+ + N + 2He$	7×10^{-16}	0	[66]
34[a,b]	$2e^- + N_2^+ \rightarrow e^- + N_2$	$5.651 \times 10^{-39} T_e^{-0.8}$	0	[66]
35[b]	$e^- + N_2^+ \rightarrow 2N$	$2.540 \times 10^{-12} T_e^{-0.5}$	0	[66]
36[b]	$e^- + N_2 \rightarrow e^- + 2N$	$1.959 \times 10^{-12} T_e^{-0.7} \exp(-1.132 \times 10^5/T_e)$	9.757	[66]
37[b]	$e^- + N \rightarrow 2e^- + N^+$	$8.401 \times 10^{-11} \exp(-1.682 \times 10^5/T_e)$	14.5	[66]
38[b]	$e^- + N \rightarrow 2e^- + N_2^+$	$4.483 \times 10^{-13} T_e^{-0.3} \exp(-1.81 \times 10^5/T_e)$	15.6	[66]
39[b]	$e^- + N_4^+ \rightarrow 2N_2$	$2 \times 10^{-12} (T_g/T_e)^{0.5}$	0	[66]

40[a]	$N_2^+ + 2N_2 \rightarrow N_4^+ + N_2$	1.9×10^{-41}	0	[66]
41[a]	$N_2^+ + He + N_2 \rightarrow N_4^+ + He$	1.9×10^{-41}	0	[66]
42	$N_4^+ + N_2 \rightarrow N_2^+ + 2N_2$	2.5×10^{-21}	0	[66]
43	$N_4^+ + He \rightarrow N_2^+ + He + N_2$	2.5×10^{-21}	0	[66]
44[a]	$He_m^* + N_2 + He \rightarrow 2He + N_2^+ + e$	3.3×10^{-42}	0	[67]
45[a]	$He_2^+ + N_2 + He \rightarrow N_2^+ + 3He$	1.36×10^{-41}	0	[67]
46[a]	$He^+ + N_2 + He \rightarrow N_2^+ + 2He$	2.2×10^{-41}	0	[67]

[a] Rate constant (m^6/s)

[b] T_e electron temperature (K) and T_g gas temperature (K)

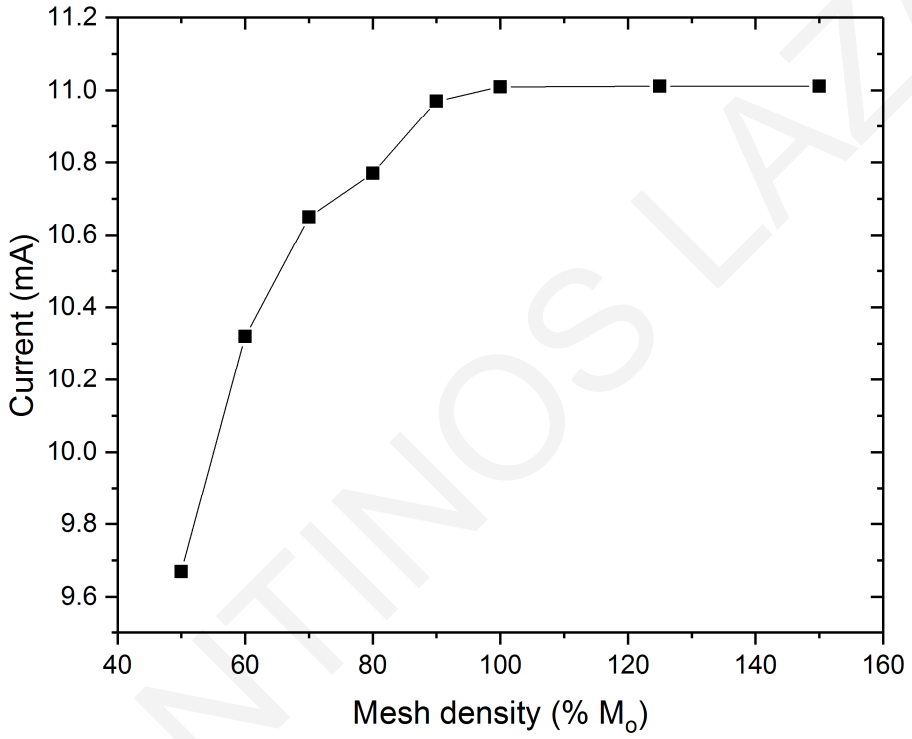

Figure A1: Simulation results of the discharge current peak for different mesh densities. Mo represents the mesh density of 1000 elements in the plasma region.

Appendix B: Rate coefficients for helium, nitrogen and oxygen reactions.

Table B1: Rate coefficients for helium, nitrogen and oxygen reactions.

Reaction No.	Reaction equation[a)]	Rate constant[b)]	Threshold (eV)	Ref
1	$e^- + He \rightarrow e^- + He$	$f(\varepsilon)$	0	[96]
2	$e^- + He \rightarrow e^- + He_m$	$f(\varepsilon)$	19.82	[96]
3	$e^- + He \rightarrow 2e^- + He^+$	$f(\varepsilon)$	24.58	[96]
4	$e^- + He_m \rightarrow 2e^- + He^+$	$f(\varepsilon)$	4.78	[164]
5	$e^- + He_m \rightarrow e^- + He$	2.9×10^{-15}	-19.82	[165,166]
6	$e^- + He_2^* \rightarrow e^- + 2He$	3.8×10^{-15}	-17.9	[165]
7	$2e^- + He^+ \rightarrow e^- + He_m$	$7.8 \times 10^{-50}(T_e/T_g)^{-4.4}$	-4.78	[167]
8	$2e^- + He_2^+ \rightarrow He_m + He + e^-$	2.8×10^{-32}	0	[165]
9	$e^- + He + He_2^+ \rightarrow He_m + 2He$	3.5×10^{-39}	0	[165]
10	$2e^- + He_2^+ \rightarrow He_2^* + e^-$	1.2×10^{-33}	0	[165]
11	$e^- + He + He_2^+ \rightarrow He_2 + He$	1.5×10^{-39}	0	[165]
12	$He_m + He_m \rightarrow He_2^+ + e^-$	$2.03 \times 10^{-15}(T_g/300)^{0.5}$	-18.2	[168]
13	$He_m + He_m \rightarrow He^+ + He + e^-$	$8.7 \times 10^{-16}(T_g/300)^{0.5}$	-15.8	[168]
14	$He^+ + 2He \rightarrow He_2^+ + He$	$1.4 \times 10^{-43}(T_g/300)^{-0.6}$	0	[168]
15	$He_m + 2He \rightarrow He_2^* + He$	2×10^{-46}	0	[168]
16	$He_m + He_2^* \rightarrow He^+ + 2He + e^-$	$5 \times 10^{-16}(T_g/300)^{0.5}$	-13.5	[165]
17	$He_m + He_2^* \rightarrow He_2^+ + He + e^-$	$2 \times 10^{-15}(T_g/300)^{0.5}$	-15.9	[165]
18	$He_2^* + He_2^* \rightarrow He^+ + 3He + e^-$	$3 \times 10^{-16}(T_g/300)^{0.5}$	-11.3	[165]
19	$He_2^* + He_2^* \rightarrow He_2^+ + 2He + e^-$	$1.2 \times 10^{-15}(T_g/300)^{0.5}$	-13.7	[165]
20	$He_2^* + He \rightarrow 2He + He$	1.5×10^{-21}	0	[106,169]
21	$e^- + He^+ \rightarrow He_m$	$6.76 \times 10^{-19} T_e^{-0.5}$	0	[170]
22	$e^- + He + He^+ \rightarrow He_m + He$	$7.4 \times 10^{-47}(T_e/T_g)^{-2}$	0	[167]
23	$e^- + He_2^+ \rightarrow He + He_m$	$7.12 \times 10^{-21}(T_e/T_g)^{-1.5}$	0	[106]
24	$e^- + He_2^+ \rightarrow 2He$	1×10^{-14}	0	[84]
25	$e^- + He_2^+ + He \rightarrow 3He$	2×10^{-39}	0	[84]
26	$He_m + 2He \rightarrow 3He$	2×10^{-46}	0	[106]
27	$e^- + He_2^* \rightarrow He_2^+ + 2e^-$	$9.75 \times 10^{-16} T_e^{0.71} e^{-3.4/T_e}$	3.4	[168]
28	$e^- + N_2 \rightarrow e^- + N_2\ (v = 1\ to\ 10)$	$f(\varepsilon)$	0.3, 0.6, 0.9, 1.1, 1.4, 1.7, 2, 2.2, 2.5, 2.7	[97]
29	$e^- + N_2 \rightarrow e^- + N_2(A)$	$f(\varepsilon)$	6.2	[97]
30	$e^- + N_2 \rightarrow e^- + N_2(A)$	$f(\varepsilon)$	7	[97]
31	$e^- + N_2 \rightarrow e^- + N_2(B)$	$f(\varepsilon)$	7.4	[97]

32	$e^- + N_2 \rightarrow e^- + N_2(B)$	$f(\varepsilon)$	7.4	[97]
33	$e^- + N_2 \rightarrow e^- + N_2(A)$	$f(\varepsilon)$	7.8	[97]
34	$e^- + N_2 \rightarrow e^- + N_2(B)$	$f(\varepsilon)$	8.2	[97]
35	$e^- + N_2 \rightarrow e^- + N_2(a)$	$f(\varepsilon)$	8.4	[97]
36	$e^- + N_2 \rightarrow e^- + N_2(a)$	$f(\varepsilon)$	8.6	[97]
37	$e^- + N_2 \rightarrow e^- + N_2(a)$	$f(\varepsilon)$	8.9	[97]
38	$e^- + N_2 \rightarrow e^- + N_2(C)$	$f(\varepsilon)$	11	[97]
39	$e^- + N_2 \rightarrow e^- + N_2(C)$	$f(\varepsilon)$	11.9	[97]
40	$e^- + N_2 \rightarrow e^- + N_2(C)$	$f(\varepsilon)$	12.3	[97]
41	$e^- + N_2 \rightarrow 2e^- + N_2^+$	$f(\varepsilon)$	15.5	[97]
42	$e^- + N_2 \rightarrow e^- + N + N$	$1 \times 10^{-14} T_e^{0.5} e^{-16/T_e}$	9.757	[171]
43	$e^- + N_4^+ \rightarrow 2N_2$	3×10^{-13}	0	[172]
44	$2e^- + N_4^+ \rightarrow 2N_2 + e^-$	3.17×10^{-42}	0	[80]
45	$2e^- + N_2^+ \rightarrow e^- + N_2$	3.17×10^{-42}	0	[100]
46	$e^- + N_2^+ \rightarrow 2N$	$4.8 \times 10^{-13} (T_e/T_g)^{-0.5}$	0	[80]
47	$N_2(A) + N_2(a) \rightarrow e^- + N_4^+$	5×10^{-17}	0	[86]
48	$N_2(a) + N_2(a) \rightarrow e^- + N_4^+$	2×10^{-16}	0	[86]
49	$N_2(B) + N_2 \rightarrow N_2 + N_2(A)$	3×10^{-17}	0	[173]
50	$N_2(C) + N_2 \rightarrow N_2 + N_2(a)$	1×10^{-17}	0	[173]
51	$N_2(a) \rightarrow N_2 + h\nu\ (117\ nm)$	1×10^2	0	[174]
52	$N_2(A) \rightarrow N_2 + h\nu\ (293\ nm)$	0.5	0	[174]
53	$N_2(B) \rightarrow N_2(A) + h\nu\ (1045\ nm)$	1.34×10^5	0	[174]
54	$N_2(C) \rightarrow N_2(B) + h\nu\ (336\ nm)$	2.45×10^7	0	[174]
55	$He_m + N_2 \rightarrow e^- + N_2^+ + He$	5×10^{-17}	0	[80]
56	$He_2^* + N_2 \rightarrow e^- + N_2^+ + 2He$	5×10^{-17}	0	[80]
57	$He^+ + N_2 \rightarrow N_2^+ + He$	6.5×10^{-14}	0	[175]
58	$He_2^+ + N_2 \rightarrow N_2^+ + 2He$	1.1×10^{-15}	0	[175]
59	$N_2^+ + He + N_2 \rightarrow N_4^+ + He$	$8.9 \times 10^{-42} (T_g/300)^{-1.54}$	0	[175]
60	$He^+ + N_2 + He \rightarrow N_2^+ + 2He$	1.1×10^{-41}	0	[175]
61	$He_2^+ + N_2 + He \rightarrow N_2^+ + 3He$	1.6×10^{-41}	0	[175]
62	$He_m + N_2 + He \rightarrow N_2^+ + 2He + e^-$	3.3×10^{-42}	0	[67]
63	$e^- + O_2 \rightarrow e^- + O_2\ (v = 1\ to\ 4)$	$f(\varepsilon)$	0.19, 0.38, 0.6, 0.8	[97]
64	$e^- + O_2 \rightarrow O + O^-$	$f(\varepsilon)$	0	[97]
65	$e^- + O_2(b) \rightarrow O + O^-$	$f(\varepsilon)$	0	[96]
66	$e^- + O_2(a) \rightarrow O + O^-$	$f(\varepsilon)$	0	[96]
67	$e^- + O_2(v) \rightarrow O + O^-$	$f(\varepsilon)$	0	[99]
68	$e^- + O_2 \rightarrow e^- + O_2(a)$	$f(\varepsilon)$	0.977	[97]
69	$e^- + O_2 \rightarrow e^- + O_2(b)$	$f(\varepsilon)$	1.627	[97]
70	$e^- + O \rightarrow e^- + O(^1S)$	$f(\varepsilon)$	4.192	[96]
71	$e^- + O_2 \rightarrow e^- + 2O$	$f(\varepsilon)$	6	[97]
72	$e^- + O_2 \rightarrow e^- + O + O(^1D)$	$f(\varepsilon)$	8.4	[97]
73	$e^- + O_2 \rightarrow e^- + O + O(^1S)$	$f(\varepsilon)$	9.97	[97]
74	$e^- + O_2 \rightarrow 2e^- + O_2^+$	$f(\varepsilon)$	12.1	[97]

75	$e^- + O_2^+ \rightarrow 2O$	$1.2 \times 10^{-14} T_e^{-0.7}$	0	[82]
76	$O^- + O_2 + O_2 \rightarrow O_3^- + O_2$	$1.1 \times 10^{-42} (T_g/300)^{-1}$	0	[81]
77	$O_2^- + O \rightarrow O^- + O_2$	$1.5 \times 10^{-16} (T_g/300)^{0.5}$	0	[82]
78	$O_2^- + O_3 \rightarrow O_3^- + O_2$	$6 \times 10^{-16} (T_g/300)^{0.5}$	0	[82]
79	$O_2(v) + O_2 \rightarrow 2O_2$	$1 \times 10^{-20} (T_g/300)^{0.5}$	0	[82]
80	$O_2^+ + O_3^- + O_2 \rightarrow O_2 + O_3 + O_2$	$2 \times 10^{-37} (T_g/300)^{-2.5}$	0	[81,86]
81	$O_4^+ + O^- + O_2 \rightarrow 2O_2 + O + O_2$	$2 \times 10^{-37} (T_g/300)^{-2.5}$	0	[81,86]
82	$O_4^+ + O_2^- + O_2 \rightarrow 3O_2 + O_2$	$2 \times 10^{-37} (T_g/300)^{-2.5}$	0	[81,86]
83	$O_4^+ + O_3^- + O_2 \rightarrow 2O_2 + O_3 + O_2$	$2 \times 10^{-37} (T_g/300)^{-2.5}$	0	[81,86]
84	$O + O^- \rightarrow e^- + O_2$	$2 \times 10^{-16} (T_g/300)^{0.5}$	0	[82]
85	$O^- + O_2(b) \rightarrow e^- + O_2 + O$	$6.9 \times 10^{-16} (T_g/300)^{0.5}$	0	[82]
86	$O^- + O_2(a) \rightarrow e^- + O_3$	$3 \times 10^{-16} (T_g/300)^{0.5}$	0	[82]
87	$O_3^- + O \rightarrow O_2^- + O_2$	$2.5 \times 10^{-16} (T_g/300)^{0.5}$	0	[82]
88	$O_4^+ + O \rightarrow O_2^+ + O_3$	3×10^{-16}	0	[86]
89	$O_4^+ + O_2 \rightarrow O_2^+ + 2O_2$	$3.3 \times 10^{-12} (T_g/300)^{-4} e^{(-5030/T_g)}$	0	[86]
90	$O(^1D) + O_2 \rightarrow O_2 + O$	$4.8 \times 10^{-18} e^{(67/T_g)}$	0	[176]
91	$O(^1D) + O_2 \rightarrow O_2(a) + O$	$1.6 \times 10^{-18} e^{(67/T_g)}$	0	[176]
92	$O(^1D) + O_2 \rightarrow O_2(b) + O$	$2.56 \times 10^{-17} e^{(67/T_g)}$	0	[176]
93	$O(^1S) + O_2(a) \rightarrow O + O_2$	1.1×10^{-16}	0	[82]
94	$O_2(b) + O_3 \rightarrow 2O_2 + O$	$7.33 \times 10^{-18} (T_g/300)^{0.5}$	0	[82]
95	$e^- + O_4^+ \rightarrow 2O_2$	$2.25 \times 10^{-13} T_e^{-0.5}$	0	[86]
96	$e^- + O + He \rightarrow O^- + He$	1×10^{-43}	0	[81]
97	$e^- + O_3 + He \rightarrow O_3^- + He$	1×10^{-43}	0	[81]
98	$He_2^* + O_2 \rightarrow 2He + O_2$	1.5×10^{-21}	0	[106]
99	$O_2(v) + He \rightarrow O_2 + He$	$1 \times 10^{-20} (T_g/300)^{0.5}$	0	[82]
100	$O^- + O_2 + He \rightarrow O_3^- + He$	$1.1 \times 10^{-42} (T_g/300)^{-1}$	0	[81]
101	$O_2^+ + O_3^- + He \rightarrow O_2 + O_3 + He$	$2 \times 10^{-37} (T_g/300)^{-2.5}$	0	[81,86]
102	$O_4^+ + O^- + He \rightarrow 2O_2 + O + He$	$2 \times 10^{-37} (T_g/300)^{-2.5}$	0	[81,86]
103	$O_4^+ + O_2^- + He \rightarrow 3O_2 + He$	$2 \times 10^{-37} (T_g/300)^{-2.5}$	0	[81,86]
104	$O_4^+ + O_3^- + He \rightarrow 2O_2 + O_3 + He$	$2 \times 10^{-37} (T_g/300)^{-2.5}$	0	[81,86]
105	$e^- + O_2 + He \rightarrow He + O_2^-$	1×10^{-43}	0	[84]
106	$O_2^+ + O_2 + He \rightarrow O_4^+ + He$	$5.8 \times 10^{-43} (T_g/300)^{-3.1}$	0	[177]
107	$He_m + O_2 \rightarrow O_2^+ + He + e^-$	$2.54 \times 10^{-16} (T_g/300)^{0.5}$	0	[82]
108	$He_2^* + O_2 \rightarrow O_2^+ + 2He + e^-$	$1 \times 10^{-16} (T_g/300)^{0.5}$	0	[178]
109	$O_2 + O + He \rightarrow O_3 + He$	$1.1 \times 10^{-46} e^{(510/T_g)}$	0	[84]
110	$He_2^+ + O_2 \rightarrow O_2^+ + 2He$	$1 \times 10^{-15} (T_g/300)^{0.5}$	0	[178]
111	$O(^1D) + He \rightarrow O + He$	1×10^{-19}	0	[82]
112	$O_2^+ + O^- + M \rightarrow O_2 + O + M$	$2 \times 10^{-37} (T_g/300)^{-2.5}$	0	[15,86]
113	$O_2^+ + O_2^- + M \rightarrow 2O_2 + M$	$2 \times 10^{-37} (T_g/300)^{-2.5}$	0	[15,86]

114	$O_2^+ + O^- + N_2 \rightarrow O_3 + N_2$	$2 \times 10^{-37}(T_g/300)^{-2.5}$	0	[15,86]
115	$O_2^+ + O_3^- + N_2 \rightarrow O_2 + O_3 + N_2$	$1 \times 10^{-37}(T_g/300)^{-2.5}$	0	[15,86]
116	$O_4^+ + O^- + N_2 \rightarrow 2O_2 + O + N_2$	$1 \times 10^{-37}(T_g/300)^{-2.5}$	0	[15,86]
117	$O_4^+ + O_2^- + N_2 \rightarrow 3O_2 + N_2$	$1 \times 10^{-37}(T_g/300)^{-2.5}$	0	[15,86]
118	$O_4^+ + O_3^- + N_2 \rightarrow 2O_2 + O_3 + N_2$	$1 \times 10^{-37}(T_g/300)^{-2.5}$	0	[15,86]
119	$N_2^+ + O^- + O_2 \rightarrow N_2 + O + O_2$	$2 \times 10^{-37}(T_g/300)^{-2.5}$	0	[15,86]
120	$N_2^+ + O^- + N_2 \rightarrow N_2 + O + N_2$	$2 \times 10^{-37}(T_g/300)^{-2.5}$	0	[15,86]
121	$N_2^+ + O_2^- + O_2 \rightarrow N_2 + O_2 + O_2$	$2 \times 10^{-37}(T_g/300)^{-2.5}$	0	[15,86]
122	$N_2^+ + O_2^- + N_2 \rightarrow N_2 + O_2 + N_2$	$2 \times 10^{-37}(T_g/300)^{-2.5}$	0	[15,86]
123	$N_2^+ + O_2 + e^- \rightarrow O_2 + N_2$	$6 \times 10^{-39}(T_e/T_g)^{-1.5}$	0	[15]
124	$O_2^+ + N_2 + e^- \rightarrow O_2 + N_2$	$6 \times 10^{-39}(T_e/T_g)^{-1.5}$	0	[15]
125	$O_2 + N + N \rightarrow O_2 + N_2$	3.9×10^{-45}	0	[15]
126	$O + O_2 + N_2 \rightarrow O_3 + N_2$	$1.1 \times 10^{-46}\exp(510/T_g)$	0	[15]
127	$O + O + N_2 \rightarrow O_2 + N_2$	$6.49 \times 10^{-47}\exp(1039/T_g)$	0	[15]
128	$O + O + N \rightarrow O_2 + N$	$3.2 \times 10^{-45}(T_g/300)^{-0.41}$	0	[15]
129	$O_3 + N_2 \rightarrow O + O_2 + N_2$	$1.6 \times 10^{-15}\exp(-11400/T_g)$	0	[15]
130	$O(^1S) + N_2 \rightarrow O + N_2$	5×10^{-23}	0	[15]
131	$O(^1D) + N_2 \rightarrow O + N_2$	$1.8 \times 10^{-17}\exp(107/T_g)$	0	[15]
132	$N_4^+ + O(^1D) \rightarrow O + N_2 + N_2^+$	1×10^{-16}	0	[15]
133	$N_4^+ + O_2 \rightarrow O_2 + N_2 + N_2^+$	2.5×10^{-16}	0	[15]
134	$N_2^+ + O_2 \rightarrow N_2 + O_2^+$	$1.04 \times 10^{-15}T_g^{-0.5}$	0	[179]
135	$N_4^+ + O_2 \rightarrow 2N_2 + O_2^+$	2.5×10^{-16}	0	[93]
136	$O_4^+ + N_2 \rightarrow O_2 + N_2 + O_2^+$	$1 \times 10^{-11}(T_g/300)^{-4.2}\exp(-5400/T_g)$	0	[15]
137	$O^- + O_2 + N_2 \rightarrow N_2 + O_3^-$	$1 \times 10^{-42}(T_g/300)^{-1}$	0	[86]
138	$e^- + O_2 + N_2 \rightarrow N_2 + O_2^-$	$1.24 \times 10^{-43}(T_g/300)^{-0.5}$	0	[81]
139	$e^- + O + N_2 \rightarrow N_2 + O^-$	1×10^{-43}	0	[81]
140	$O_2^- + N_2(A) \rightarrow e^- + O_2 + N_2$	2.1×10^{-15}	0	[173]
141	$O_2^- + N_2(B) \rightarrow e^- + O_2 + N_2$	2.5×10^{-15}	0	[86]
142	$O^- + N_2(A) \rightarrow e^- + O + N_2$	2.2×10^{-15}	0	[173]
143	$O^- + N_2(B) \rightarrow e^- + O + N_2$	1.9×10^{-15}	0	[86]
144	$N_2(A) + O_2 \rightarrow 2O + N_2$	1.7×10^{-18}	0	[173]
145	$N_2(A) + O_2 \rightarrow O_2(a) + N_2$	7.5×10^{-19}	0	[173]
146	$N_2(A) + O \rightarrow O(^1S) + N_2$	2.3×10^{-17}	0	[173]
147	$N_2(B) + O_2 \rightarrow 2O + N_2$	1.1×10^{-16}	0	[173]
148	$N_2(a) + O_2 \rightarrow 2O + N_2$	2.8×10^{-17}	0	[173]
149	$N_2(C) + O_2 \rightarrow O + O(^1S) + N_2$	3×10^{-16}	0	[173]

[a] He_m represents He(2^3S) and He(2^1S); He_2^*represents $He_2(a^3\Sigma_u^+)$; $N_2(A)$ represents $N_2\left(A^3\Sigma_u^+ (v = 0-4)\right)$, $N_2\left(A^3\Sigma_u^+ (v = 5-9)\right)$ and $N_2\left(A^3\Sigma_u^+ (v > 9)\right)$; $N_2(B)$ represents $N_2\left(B^3\Pi_g\right), N_2(W^3\Delta_u)$ and $N_2(B^3\Sigma_u^-)$; $N_2(a)$ represents $N_2(a^1\Sigma_u^-), N_2\left(a^1\Pi_g\right)$ and $N_2(W^1\Delta_u)$; $N_2(C)$ represents $N_2(C^3\Pi_u), N_2\left(E^3\Sigma_g^+\right)$ and $N_2(a^1\Sigma_g^+)$; $O_2(a)$ represents $O_2\left(a^1\Delta_g\right)$; $O_2(b)$ represents $O_2\left(b^1\Sigma_g^+\right)$; $N_2(v)$ are treated as N_2; $O_2(v)$ represents the vibrational excited states of $O_2(v = 1-4)$. M represents the background gases helium atom, Nitrogen and Oxygen molecule. [b] Rate coefficients have units of $s^{-1}, m^3s^{-1}, m^6s^{-1}$ for one, two and three body reactions respectively; T_e has units eV; T_g has units of K. $\sigma(\varepsilon)$ indicates the rate coefficient as a function of the mean electron energy calculated from the solution of Boltzmann equation (see section 4.3: Input parameters). The reference indicates the database of the cross section used.

Appendix C: Rate coefficients for helium, nitrogen, oxygen and water reactions.

Table C1: Rate coefficients for helium, nitrogen, oxygen and water reactions.

No.	Reaction equation[a)]	Rate constant[b)]	Threshold (eV)	Ref
1	$e^- + He \rightarrow e^- + He$	$f(\varepsilon)$	0	[96]
2	$e^- + He \rightarrow e^- + He_m$	$f(\varepsilon)$	19.82	[96]
3	$e^- + He \rightarrow 2e^- + He^+$	$f(\varepsilon)$	24.58	[96]
4	$e^- + He_m \rightarrow 2e^- + He^+$	$2.254 \times 10^{-13} T_e^{-0.1241} e^{-5.725/T_e}$	4.78	[80]
5	$e^- + He_m \rightarrow e^- + He$	2.9×10^{-15}	-19.82	[165,166]
6	$e^- + He_2^* \rightarrow e^- + 2He$	3.8×10^{-15}	-17.9	[165]
7	$2e^- + He^+ \rightarrow e^- + He_m$	6×10^{-32}	-4.78	[167]
8	$2e^- + He_2^+ \rightarrow He_m + He + e^-$	2.8×10^{-32}	0	[165]
9	$e^- + He + He_2^+ \rightarrow He_m + 2He$	3.5×10^{-39}	0	[165]
10	$2e^- + He_2^+ \rightarrow He_2^* + e^-$	1.2×10^{-33}	0	[165]
11	$e^- + He + He_2^+ \rightarrow He_2 + He$	1.5×10^{-39}	0	[165]
12	$He_m + He_m \rightarrow He_2^+ + e^-$	$2.03 \times 10^{-15} (T_g/300)^{0.5}$	-18.2	[168]
13	$He_m + He_m \rightarrow He^+ + He + e^-$	$8.7 \times 10^{-16} (T_g/300)^{0.5}$	-15.8	[168]
14	$He^+ + 2He \rightarrow He_2^+ + He$	$1.4 \times 10^{-43} (T_g/300)^{-0.6}$	0	[168]
15	$He_m + 2He \rightarrow He_2^* + He$	2×10^{-46}	0	[168]
16	$He_m + He_2^* \rightarrow He^+ + 2He + e^-$	$5 \times 10^{-16} (T_g/300)^{0.5}$	-13.5	[165]
17	$He_m + He_2^* \rightarrow He_2^+ + He + e^-$	$2 \times 10^{-15} (T_g/300)^{0.5}$	-15.9	[165]
18	$He_2^* + He_2^* \rightarrow He^+ + 3He + e^-$	$3 \times 10^{-16} (T_g/300)^{0.5}$	-11.3	[165]
19	$He_2^* + He_2^* \rightarrow He_2^+ + 2He + e^-$	$1.2 \times 10^{-15} (T_g/300)^{0.5}$	-13.7	[165]
20	$He_2^* + He \rightarrow 2He + He$	1.5×10^{-21}	0	[106,169]
21	$e^- + He + He^+ \rightarrow He_m + He$	$7.4 \times 10^{-47} (T_e/T_g)^{-2}$	0	[167]
22	$e^- + He_2^+ \rightarrow He + He_m$	$7.12 \times 10^{-21} (T_e/T_g)^{-1.5}$	0	[106]
23	$He_m + 2He \rightarrow 3He$	2×10^{-46}	0	[106]
24	$e^- + He_2^* \rightarrow He_2^+ + 2e^-$	$9.75 \times 10^{-16} T_e^{0.71} e^{-3.4/T_e}$	3.4	[168]
25	$e^- + N_2 \rightarrow e^- + N_2\ (v = 1\ to\ 10)$	$f(\varepsilon)$	0.3, 0.6, 0.9, 1.1, 1.4, 1.7, 2, 2.2, 2.5, 2.7	[97]
26	$e^- + N_2 \rightarrow e^- + N_2(A)$	$f(\varepsilon)$	6.2	[97]
27	$e^- + N_2 \rightarrow e^- + N_2(A)$	$f(\varepsilon)$	7	[97]
28	$e^- + N_2 \rightarrow e^- + N_2(B)$	$f(\varepsilon)$	7.4	[97]
29	$e^- + N_2 \rightarrow e^- + N_2(B)$	$f(\varepsilon)$	7.4	[97]
30	$e^- + N_2 \rightarrow e^- + N_2(A)$	$f(\varepsilon)$	7.8	[97]
31	$e^- + N_2 \rightarrow e^- + N_2(B)$	$f(\varepsilon)$	8.2	[97]
32	$e^- + N_2 \rightarrow e^- + N_2(a)$	$f(\varepsilon)$	8.4	[97]
33	$e^- + N_2 \rightarrow e^- + N_2(a)$	$f(\varepsilon)$	8.6	[97]
34	$e^- + N_2 \rightarrow e^- + N_2(a)$	$f(\varepsilon)$	8.9	[97]
35	$e^- + N_2 \rightarrow e^- + N_2(C)$	$f(\varepsilon)$	11	[97]

36	$e^- + N_2 \rightarrow e^- + N_2(C)$	$f(\varepsilon)$	11.9	[97]
37	$e^- + N_2 \rightarrow e^- + N_2(C)$	$f(\varepsilon)$	12.3	[97]
38	$e^- + N_2 \rightarrow 2e^- + N_2^+$	$f(\varepsilon)$	15.5	[97]
39	$e^- + N_2 \rightarrow e^- + N + N$	$1 \times 10^{-14} T_e^{0.5} e^{-16/T_e}$	9.757	[171]
40	$e^- + N_4^+ \rightarrow 2N_2$	3×10^{-13}	0	[172]
41	$2e^- + N_4^+ \rightarrow 2N_2 + e^-$	3.17×10^{-42}	0	[80]
42	$2e^- + N_2^+ \rightarrow e^- + N_2$	3.17×10^{-42}	0	[100]
43	$e^- + N_2^+ \rightarrow 2N$	$2.54 \times 10^{-12} T_e^{-0.5}$	0	[69]
44	$N_2(A) + N_2(a) \rightarrow e^- + N_4^+$	5×10^{-17}	0	[86]
45	$N_2(a) + N_2(a) \rightarrow e^- + N_4^+$	2×10^{-16}	0	[86]
46	$N_2(B) + N_2 \rightarrow N_2 + N_2(A)$	3×10^{-17}	0	[173]
47	$N_2(C) + N_2 \rightarrow N_2 + N_2(a)$	1×10^{-17}	0	[173]
48	$N_2(a) \rightarrow N_2 + hv\ (117\ nm)$	1×10^2	0	[174]
49	$N_2(A) \rightarrow N_2 + hv\ (293\ nm)$	0.5	0	[174]
50	$N_2(B) \rightarrow N_2(A) + hv\ (1045\ nm)$	1.34×10^5	0	[174]
51	$N_2(C) \rightarrow N_2(B) + hv\ (336\ nm)$	2.45×10^7	0	[174]
52	$He_m + N_2 \rightarrow e^- + N_2^+ + He$	5×10^{-17}	0	[80]
53	$He_2^* + N_2 \rightarrow e^- + N_2^+ + 2He$	5×10^{-17}	0	[80]
54	$He^+ + N_2 \rightarrow N_2^+ + He$	1.2×10^{-15}	0	[175]
55	$He_2^+ + N_2 \rightarrow N_2^+ + 2He$	1.1×10^{-15}	0	[175]
56	$N_2^+ + He + N_2 \rightarrow N_4^+ + He$	$8.9 \times 10^{-42} (T_g/300)^{-1.54}$	0	[175]
57	$He^+ + N_2 + He \rightarrow N_2^+ + 2He$	1.1×10^{-41}	0	[175]
58	$He_2^+ + N_2 + He \rightarrow N_2^+ + 3He$	1.6×10^{-41}	0	[175]
59	$He_m + N_2 + He \rightarrow N_2^+ + 2He + e^-$	3.3×10^{-42}	0	[67]
60	$He_2^* + N_2 \rightarrow 2He + N_2$	1.5×10^{-21}	0	[15]
61	$N_2^+ + 2N_2 \rightarrow N_4^+ + N_2$	5×10^{-41}	0	[79]
62	$N_4^+ + N_2 \rightarrow N_2^+ + 2N_2$	2.5×10^{-21}	0	[76]
63	$e^- + O_2 \rightarrow e^- + O_2\ (v = 1\ to\ 4)$	$f(\varepsilon)$	0.19, 0.38, 0.6, 0.8	[94]
64	$e^- + O_2 \rightarrow O + O^-$	$f(\varepsilon)$	0	[94]
65	$e^- + O_2(b) \rightarrow O + O^-$	$f(\varepsilon)$	0	[93]
66	$e^- + O_2(a) \rightarrow O + O^-$	$f(\varepsilon)$	0	[93]
67	$e^- + O_2(v) \rightarrow O + O^-$	$f(\varepsilon)$	0	[96]
68	$e^- + O_2 \rightarrow e^- + O_2(a)$	$f(\varepsilon)$	0.977	[94]
69	$e^- + O_2(a) \rightarrow e^- + O_2$	$f(\varepsilon)$	-0.977	b)
70	$e^- + O_2 \rightarrow e^- + O_2(b)$	$f(\varepsilon)$	1.627	[94]
71	$e^- + O \rightarrow e^- + O(^1D)$	$f(\varepsilon)$	1.968	[178]
72	$e^- + O \rightarrow e^- + O(^1S)$	$f(\varepsilon)$	4.192	[93]
73	$e^- + O_2 \rightarrow e^- + 2O$	$f(\varepsilon)$	6	[94]
74	$e^- + O_2(b) \rightarrow e^- + O(^1D) + O$	$f(\varepsilon)$	6.77	[96]
75	$e^- + O_2 \rightarrow e^- + O + O(^1D)$	$f(\varepsilon)$	8.4	[94]
76	$e^- + O_2 \rightarrow e^- + O + O(^1S)$	$f(\varepsilon)$	9.97	[94]
77	$e^- + O_2(a) \rightarrow 2e^- + O_2^+$	$f(\varepsilon)$	11.1	[96]
78	$e^- + O_2 \rightarrow 2e^- + O_2^+$	$f(\varepsilon)$	12.1	[94]
79	$e^- + O_3 \rightarrow e^- + O_2 + O$	5.88×10^{-15}	0	[179]
80	$e^- + O_2^+ \rightarrow 2O$	$1.2 \times 10^{-14} T_e^{-0.7}$	0	[79]
81	$e^- + O + O_2 \rightarrow O^- + O_2$	1×10^{-43}	0	[168]
82	$e^- + O_2 + O_2 \rightarrow O_2^- + O_2$	$2.26 \times 10^{-42} (T_g/300)^{-0.5}$	0	[180]
83	$e^- + O_2^+ + O_2 \rightarrow 2O_2$	$2.49 \times 10^{-41} (T_e)^{-1.5}$	0	[168]
84	$2e^- + O_2^+ \rightarrow e^- + O_2$	$7.18 \times 10^{-39} (T_e)^{-4.5}$	0	[83]

85	$O^- + O_2 + O_2 \rightarrow O_3^- + O_2$	$1.1 \times 10^{-42}(T_g/300)^{-1}$	0	[78]
86	$O_2^- + O \rightarrow O^- + O_2$	$1.5 \times 10^{-16}(T_g/300)^{0.5}$	0	[79]
87	$O_2^- + O_3 \rightarrow O_3^- + O_2$	$6 \times 10^{-16}(T_g/300)^{0.5}$	0	[79]
88	$O_2^+ + O_3^- + O_2 \rightarrow O_2 + O_3 + O_2$	$2 \times 10^{-37}(T_g/300)^{-2.5}$	0	[78,83]
89	$O_4^+ + O^- + O_2 \rightarrow 2O_2 + O + O_2$	$2 \times 10^{-37}(T_g/300)^{-2.5}$	0	[78,83]
90	$O_4^+ + O_2^- + O_2 \rightarrow 3O_2 + O_2$	$2 \times 10^{-37}(T_g/300)^{-2.5}$	0	[78,83]
91	$O_4^+ + O_3^- + O_2 \rightarrow 2O_2 + O_3 + O_2$	$2 \times 10^{-37}(T_g/300)^{-2.5}$	0	[78,83]
92	$O + O^- \rightarrow e^- + O_2$	$2 \times 10^{-16}(T_g/300)^{0.5}$	0	[79]
93	$O^- + O_2(b) \rightarrow e^- + O_2 + O$	$6.9 \times 10^{-16}(T_g/300)^{0.5}$	0	[79]
94	$O^- + O_2(a) \rightarrow e^- + O_3$	$3 \times 10^{-16}(T_g/300)^{0.5}$	0	[79]
95	$O_3^- + O \rightarrow O_2^- + O_2$	$2.5 \times 10^{-16}(T_g/300)^{0.5}$	0	[79]
96	$O_4^+ + O \rightarrow O_2^+ + O_3$	3×10^{-16}	0	[83]
97	$O_4^+ + O_2 \rightarrow O_2^+ + 2O_2$	$3.3 \times 10^{-12}(T_g/300)^{-4} e^{(-5030/T_g)}$	0	[83]
98	$O(^1D) + O_2 \rightarrow O_2 + O$	$4.8 \times 10^{-18} e^{(67/T_g)}$	0	[174]
99	$O(^1D) + O_2 \rightarrow O_2(a) + O$	$1.6 \times 10^{-18} e^{(67/T_g)}$	0	[174]
100	$O(^1D) + O_2 \rightarrow O_2(b) + O$	$2.56 \times 10^{-17} e^{(67/T_g)}$	0	[174]
101	$O(^1S) + O_2(a) \rightarrow O + O_2$	1.1×10^{-16}	0	[79]
102	$O_2(b) + O_3 \rightarrow 2O_2 + O$	$7.33 \times 10^{-18}(T_g/300)^{0.5}$	0	[79]
103	$e^- + O_4^+ \rightarrow 2O_2$	$2.25 \times 10^{-13} T_e^{-0.5}$	0	[83]
104	$e^- + O + He \rightarrow O^- + He$	1×10^{-43}	0	[78]
105	$e^- + O_3 + He \rightarrow O_3^- + He$	1×10^{-43}	0	[78]
106	$He_2^* + O_2 \rightarrow 2He + O_2$	1.5×10^{-21}	0	[103]
107	$O_2(v) + M \rightarrow O_2 + M$	$1 \times 10^{-20}(T_g/300)^{0.5}$	0	[79]
108	$O^- + O_2 + He \rightarrow O_3^- + He$	$1.1 \times 10^{-42}(T_g/300)^{-1}$	0	[78]
109	$O_2^+ + O_3^- + He \rightarrow O_2 + O_3 + He$	$2 \times 10^{-37}(T_g/300)^{-2.5}$	0	[78,83]
110	$O_4^+ + O^- + He \rightarrow 2O_2 + O + He$	$2 \times 10^{-37}(T_g/300)^{-2.5}$	0	[78,83]
111	$O_4^+ + O_2^- + He \rightarrow 3O_2 + He$	$2 \times 10^{-37}(T_g/300)^{-2.5}$	0	[78,83]
112	$O_4^+ + O_3^- + He \rightarrow 2O_2 + O_3 + He$	$2 \times 10^{-37}(T_g/300)^{-2.5}$	0	[78,83]
113	$e^- + O_2 + He \rightarrow He + O_2^-$	1×10^{-43}	0	[81]
114	$O_2^+ + O_2 + He \rightarrow O_4^+ + He$	$5.8 \times 10^{-43}(T_g/300)^{-3.1}$	0	[175]
115	$He_m + O_2 \rightarrow O_2^+ + He + e^-$	$2.54 \times 10^{-16}(T_g/300)^{0.5}$	0	[79]
116	$He + He_m + O_2 \rightarrow O_2^+ + 2He + e^-$	1.6×10^{-43}	0	[181]
117	$He_2^* + O_2 \rightarrow O_2^+ + 2He + e^-$	$1 \times 10^{-16}(T_g/300)^{0.5}$	0	[176]
118	$O_2 + O + He \rightarrow O_3 + He$	$1.1 \times 10^{-46} e^{(510/T_g)}$	0	[81]
119	$He_2^+ + O_2 \rightarrow O_2^+ + 2He$	$1 \times 10^{-15}(T_g/300)^{0.5}$	0	[176]
120	$O(^1D) + He \rightarrow O + He$	1×10^{-19}	0	[79]
121	$O_2^+ + O^- + M \rightarrow O_2 + O + M$	$2 \times 10^{-37}(T_g/300)^{-2.5}$	0	[11,83]
122	$O_2^+ + O_2^- + M \rightarrow 2O_2 + M$	$2 \times 10^{-37}(T_g/300)^{-2.5}$	0	[11,83]
123	$O_2^+ + O^- + N_2 \rightarrow O_3 + N_2$	$2 \times 10^{-37}(T_g/300)^{-2.5}$	0	[11,83]
124	$O_2^+ + O_3^- + N_2 \rightarrow O_2 + O_3 + N_2$	$1 \times 10^{-37}(T_g/300)^{-2.5}$	0	[11,83]

125	$O_4^+ + O^- + N_2 \rightarrow 2O_2 + O + N_2$	$1 \times 10^{-37}(T_g/300)^{-2.5}$	0	[11,83]
126	$O_4^+ + O_2^- + N_2 \rightarrow 3O_2 + N_2$	$1 \times 10^{-37}(T_g/300)^{-2.5}$	0	[11,83]
127	$O_4^+ + O_3^- + N_2 \rightarrow 2O_2 + O_3 + N_2$	$1 \times 10^{-37}(T_g/300)^{-2.5}$	0	[11,83]
128	$N_2^+ + O^- + O_2 \rightarrow N_2 + O + O_2$	$2 \times 10^{-37}(T_g/300)^{-2.5}$	0	[11,83]
129	$N_2^+ + O^- + N_2 \rightarrow N_2 + O + N_2$	$2 \times 10^{-37}(T_g/300)^{-2.5}$	0	[11,83]
130	$N_2^+ + O_2^- + O_2 \rightarrow N_2 + O_2 + O_2$	$2 \times 10^{-37}(T_g/300)^{-2.5}$	0	[11,83]
131	$N_2^+ + O_2^- + N_2 \rightarrow N_2 + O_2 + N_2$	$2 \times 10^{-37}(T_g/300)^{-2.5}$	0	[11,83]
132	$N_2^+ + O_2 + e^- \rightarrow O_2 + N_2$	$6 \times 10^{-39}(T_e/T_g)^{-1.5}$	0	[11]
133	$O_2^+ + N_2 + e^- \rightarrow O_2 + N_2$	$6 \times 10^{-39}(T_e/T_g)^{-1.5}$	0	[11]
134	$O_2 + N + N \rightarrow O_2 + N_2$	3.9×10^{-45}	0	[11]
135	$O + O_2 + N_2 \rightarrow O_3 + N_2$	$1.1 \times 10^{-46}\exp(510/T_g)$	0	[11]
136	$O + O + N_2 \rightarrow O_2 + N_2$	$6.49 \times 10^{-47}\exp(1039/T_g)$	0	[11]
137	$O + O + N \rightarrow O_2 + N$	$3.2 \times 10^{-45}(T_g/300)^{-0.41}$	0	[11]
138	$O_3 + N_2 \rightarrow O + O_2 + N_2$	$1.6 \times 10^{-15}\exp(-11400/T_g)$	0	[11]
139	$O(^1S) + N_2 \rightarrow O + N_2$	5×10^{-23}	0	[11]
140	$O(^1D) + N_2 \rightarrow O + N_2$	$1.8 \times 10^{-17}\exp(107/T_g)$	0	[11]
141	$N_4^+ + O(^1D) \rightarrow O + N_2 + N_2^+$	1×10^{-16}	0	[11]
142	$N_4^+ + O_2 \rightarrow O_2 + N_2 + N_2^+$	2.5×10^{-16}	0	[11]
143	$N_2^+ + O_2 \rightarrow N_2 + O_2^+$	$1.04 \times 10^{-15}T_g^{-0.5}$	0	[177]
144	$N_4^+ + O_2 \rightarrow 2N_2 + O_2^+$	4×10^{-16}	0	[90]
145	$O_4^+ + N_2 \rightarrow O_2 + N_2 + O_2^+$	$1 \times 10^{-11}(T_g/300)^{-4.2}\exp(-5400/T_g)$	0	[11]
146	$O^- + O_2 + N_2 \rightarrow N_2 + O_3^-$	$1 \times 10^{-42}(T_g/300)^{-1}$	0	[83]
147	$e^- + O_2 + N_2 \rightarrow N_2 + O_2^-$	$1.24 \times 10^{-43}(T_g/300)^{-0.5}$	0	[78]
148	$e^- + O + N_2 \rightarrow N_2 + O^-$	1×10^{-43}	0	[78]
149	$O_2^- + N_2(A) \rightarrow e^- + O_2 + N_2$	2.1×10^{-15}	0	[171]
150	$O_2^- + N_2(B) \rightarrow e^- + O_2 + N_2$	2.5×10^{-15}	0	[83]
151	$O^- + N_2(A) \rightarrow e^- + O + N_2$	2.2×10^{-15}	0	[171]
152	$O^- + N_2(B) \rightarrow e^- + O + N_2$	1.9×10^{-15}	0	[83]
153	$N_2(A) + O_2 \rightarrow 2O + N_2$	1.7×10^{-18}	0	[171]
154	$N_2(A) + O_2 \rightarrow O_2(a) + N_2$	7.5×10^{-19}	0	[171]
155	$N_2(A) + O \rightarrow O(^1S) + N_2$	2.3×10^{-17}	0	[171]
156	$N_2(B) + O_2 \rightarrow 2O + N_2$	1.1×10^{-16}	0	[171]
157	$N_2(a) + O_2 \rightarrow 2O + N_2$	2.8×10^{-17}	0	[171]
158	$N_2(C) + O_2 \rightarrow O + O(^1S) + N_2$	3×10^{-16}	0	[171]
159	$e^- + H_2O \rightarrow e^- + H_2O$	$f(\varepsilon)$	0	[93]
160	$e^- + H_2O \rightarrow OH + H^-$	$f(\varepsilon)$	0	[93]
161	$e^- + H_2O \rightarrow H_2 + O^-$	$f(\varepsilon)$	0	[93]
162	$e^- + H_2O \rightarrow H + OH^-$	$f(\varepsilon)$	0	[93]
163	$e^- + H_2O \rightarrow e^- + H + OH$	$f(\varepsilon)$	7	[93]
164	$e^- + H_2O \rightarrow e^- + H_2 + O(^1D)$	$f(\varepsilon)$	7.4	[182]
165	$e^- + H_2 \rightarrow e^- + 2H$	$f(\varepsilon)$	8.9	[183]
166	$e^- + H_2O \rightarrow e^- + H + OH(A)$	$f(\varepsilon)$	9	[183]
167	$e^- + H_2O \rightarrow 2e^- + H_2O^+$	$f(\varepsilon)$	12.61	[93]
168	$e^- + H \rightarrow 2e^- + H^+$	$f(\varepsilon)$	13.6	[94]
169	$e^- + H_2 \rightarrow 2e^- + H_2^+$	$f(\varepsilon)$	15.4	[94]

170	$e^- + OH \rightarrow e^- + O + H$	$2.08 \times 10^{-13} T_e^{-0.76} \exp(-6.9/T_e)$	6.9	[184]
171	$e^- + OH \rightarrow 2e^- + OH^+$	$2 \times 10^{-16} T_e^{1.78} \exp(-13.8/T_e)$	13.8	[184]
172	$e^- + HO_2 \rightarrow e^- + O_2 + H$	3.1×10^{-15}	0	[179]
173	$e^- + H_2O_2 \rightarrow e^- + 2OH$	2.36×10^{-15}	0	[179]
174	$e^- + H_2O_2 \rightarrow e^- + HO_2 + H$	3.1×10^{-17}	0	[179]
175	$e^- + OH + He \rightarrow He + OH^-$	3×10^{-43}	0	[185]
176	$e^- + O_2 + H_2O \rightarrow O_2^- + H_2O$	1.4×10^{-41}	0	[168]
177	$e^- + H_2O_2 \rightarrow H_2O + O^-$	$1.57 \times 10^{-16} T_e^{-0.55}$	0	[186]
178	$e^- + H_2O_2 \rightarrow OH + OH^-$	$2.7 \times 10^{-16} T_e^{-0.5}$	0	[186]
179	$e^- + H_5O_2^+ \rightarrow 2H_2O + H$	$1.62 \times 10^{-12} T_e^{-0.15}$	0	[187]
180	$e^- + H_4O_2^+ \rightarrow H_2O + OH + H$	$9.6 \times 10^{-13} T_e^{-0.2}$	0	[187]
181	$e^- + H_7O_3^+ \rightarrow 3H_2O + H$	$2.24 \times 10^{-12} T_e^{-0.08}$	0	[188]
182	$e^- + H_9O_4^+ \rightarrow 4H_2O + H$	3.6×10^{-12}	0	[188]
183	$e^- + H_{11}O_5^+ \rightarrow 5H_2O + H$	4×10^{-12}	0	[189]
184	$e^- + H_{13}O_6^+ \rightarrow 6H_2O + H$	4×10^{-12}	0	[189]
185	$e^- + H_{15}O_7^+ \rightarrow 7H_2O + H$	4×10^{-12}	0	[189]
186	$e^- + H_{17}O_8^+ \rightarrow 8H_2O + H$	4×10^{-12}	0	[189]
187	$e^- + H_{19}O_9^+ \rightarrow 9H_2O + H$	4×10^{-12}	0	[189]
188	$H^- + He \rightarrow He + H + e^-$	$8 \times 10^{-18} (T_g/300)^{0.5}$	0	[78]
189	$H^- + O_2 \rightarrow HO_2 + e^-$	1.2×10^{-15}	0	[190]
190	$He^+ + H_2O \rightarrow H^+ + OH + He$	2.04×10^{-16}	0	[167]
191	$He^+ + H_2O \rightarrow OH^+ + H + He$	2.86×10^{-16}	0	[167]
192	$He^+ + H_2O \rightarrow H_2O^+ + He$	6.05×10^{-17}	0	[167]
193	$HeH^+ + H \rightarrow H_2^+ + He$	9.1×10^{-16}	0	[167]
194	$HeH^+ + H_2O \rightarrow H_3O^+ + He$	4.3×10^{-16}	0	[191]
195	$He_2^+ + H_2O \rightarrow HeH^+ + He + OH(A)$	1.3×10^{-16}	0	[192]
196	$He_2^+ + H_2O \rightarrow OH^+ + H + 2He$	2.1×10^{-16}	0	[78]
197	$He_2^+ + H_2O \rightarrow H^+ + OH + 2He$	2.1×10^{-16}	0	[78]
198	$He_2^+ + H_2O \rightarrow HeH^+ + OH + He$	2.1×10^{-16}	0	[78]
199	$He_2^+ + H_2O \rightarrow H_2^+ + O + 2He$	2.1×10^{-16}	0	[78]
200	$O_2^+ + H_2O + N_2 \rightarrow H_2O_3^+ + N_2$	$2.6 \times 10^{-40} (T_g/300)^{-4}$	0	[187]
201	$O_2^+ + H_2O + He \rightarrow H_2O_3^+ + He$	$2.6 \times 10^{-40} (T_g/300)^{-4}$	0	[187]
202	$O_2^+ + H_2O + O_2 \rightarrow H_2O_3^+ + O_2$	$2.6 \times 10^{-40} (T_g/300)^{-4}$	0	[193]
203	$O_4^+ + H_2O + N_2 \rightarrow H_2O_3^+ + O_2 + N_2$	$1.5 \times 10^{-40} (T_g/300)^{2}$	0	[187]
204	$H_2O^+ + O_2 \rightarrow O_2^+ + H_2O$	3.3×10^{-16}	0	[194]
205	$H_2O_3^+ + O_2 \rightarrow O_4^+ + H_2O$	$2 \times 10^{-16} \exp(-2300/T_g)$	0	[194]
206	$O_4^+ + H_2O \rightarrow O_2 + H_2O_3^+$	1.7×10^{-15}	0	[194]
207	$N_2^+ + H_2O \rightarrow N_2 + H_2O^+$	3×10^{-15}	0	[193]
208	$N_4^+ + H_2O \rightarrow 2N_2 + H_2O^+$	2.4×10^{-15}	0	[195]
209	$H^+ + O_2 \rightarrow H + O_2^+$	2×10^{-15}	0	[167]
210	$H^+ + H_2O \rightarrow H + H_2O^+$	6.9×10^{-15}	0	[167]
211	$H^- + H_2O \rightarrow OH^- + H_2$	3.8×10^{-15}	0	[167]
212	$H_2^+ + He \rightarrow HeH^+ + H$	1.3×10^{-16}	0	[167]
213	$H_2^+ + O_2 \rightarrow O_2^+ + H_2$	8×10^{-16}	0	[167]
214	$H_2^+ + H_2O \rightarrow H_2O^+ + H_2$	3.9×10^{-15}	0	[167]
215	$H_2^+ + H_2O \rightarrow H_3O^+ + H$	3.4×10^{-15}	0	[167]
216	$O^- + H_2O \rightarrow OH^- + OH$	1.4×10^{-15}	0	[196]
217	$OH^+ + O \rightarrow O_2^+ + H$	7.1×10^{-16}	0	[167]
218	$OH^+ + O_2 \rightarrow O_2^+ + OH$	3.8×10^{-16}	0	[168]

219	$OH^+ + H_2O \rightarrow H_2O^+ + OH$	1.5×10^{-15}	0	[197]
220	$OH^+ + H_2O \rightarrow H_3O^+ + O$	1.3×10^{-15}	0	[198]
221	$H_2O^+ + H_2O \rightarrow H_3O^+ + OH$	1.85×10^{-15}	0	[168]
222	$H_2O_3^+ + H_2O \rightarrow H_4O_2^+ + O_2$	1×10^{-15}	0	[187]
223	$H_2O_3^+ + H_2O \rightarrow H_3O^+ + OH + O_2$	3×10^{-16}	0	[196]
224	$H_4O_2^+ + H_2O \rightarrow H_5O_2^+ + OH$	1.4×10^{-15}	0	[187]
225	$H_3O^+ + H_2O + M \rightarrow H_5O_2^+ + M$	$3.2 \times 10^{-39}(T_g/300)^{-4}$	0	[195]
226	$H_5O_2^+ + H_2O + M \rightarrow H_7O_3^+ + M$	$7.4 \times 10^{-39}(T_g/300)^{-7.5}$	0	[195]
227	$H_7O_3^+ + H_2O + M \rightarrow H_9O_4^+ + M$	$2.5 \times 10^{-39}(T_g/300)^{-8.1}$	0	[195]
228	$H_9O_4^+ + M \rightarrow H_7O_3^+ + H_2O + M$	$2 \times 10^{12} T_g^{-8.1} \exp(-8360/T_g)$	0	[195]
229	$H_9O_4^+ + H_2O + M \rightarrow H_{11}O_5^+ + M$	$3.3 \times 10^{-40}(T_g/300)^{-14}$	0	[195]
230	$H_{11}O_5^+ + M \rightarrow H_9O_4^+ + H_2O + M$	$6.3 \times 10^{24} T_g^{-14} \exp(-5750/T_g)$	0	[195]
231	$H_{11}O_5^+ + H_2O + M \rightarrow H_{13}O_6^+ + M$	$4 \times 10^{-41}(T_g/300)^{-15.3}$	0	[195]
232	$H_{13}O_6^+ + M \rightarrow H_{11}O_5^+ + H_2O + M$	$2.62 \times 10^{27} T_g^{-15.3} \exp(-5000/T_g)$	0	[195]
233	$H_{13}O_6^+ + H_2O + M \rightarrow H_{15}O_7^+ + M$	$4.5 \times 10^{-42}(T_g/300)^{-16}$	0	[195]
234	$H_{15}O_7^+ + M \rightarrow H_{13}O_6^+ + H_2O + M$	$1.98 \times 10^{29} T_g^{-16} \exp(-5000/T_g)$	0	[195]
235	$H_{15}O_7^+ + H_2O + M \rightarrow H_{17}O_8^+ + M$	$4.5 \times 10^{-42}(T_g/300)^{-16}$	0	[195]
236	$H_{17}O_8^+ + M \rightarrow H_{15}O_7^+ + H_2O + M$	$1.98 \times 10^{29} T_g^{-16} \exp(-5000/T_g)$	0	[195]
237	$H_{17}O_8^+ + H_2O + M \rightarrow H_{19}O_9^+ + M$	$4.5 \times 10^{-42}(T_g/300)^{-16}$	0	[195]
238	$H_{19}O_9^+ + M \rightarrow H_{17}O_8^+ + H_2O + M$	$1.98 \times 10^{29} T_g^{-16} \exp(-5000/T_g)$	0	[195]
239	$O^- + H_2O + M \rightarrow H_2O_2^- + M$	1.3×10^{-40}	0	[199]
240	$OH^- + H_2O + M \rightarrow H_3O_2^- + M$	2.5×10^{-40}	0	[199]
241	$H_2O_2^- + H_2O \rightarrow H_3O_2^- + OH$	1×10^{-17}	0	[199]
242	$H_3O_2^- + H_2O + M \rightarrow H_5O_3^- + M$	3.5×10^{-40}	0	[199]
243	$He^+ + OH^- + M \rightarrow OH + He + M$	$2 \times 10^{-37}(T_g/300)^{-2.5}$	0	[14]
244	$He_2^+ + O^- + M \rightarrow O + 2He + M$	$2 \times 10^{-37}(T_g/300)^{-2.5}$	0	[14]
245	$He_2^+ + OH^- + M \rightarrow OH + 2He + M$	$2 \times 10^{-37}(T_g/300)^{-2.5}$	0	[14]
246	$He_2^+ + H_2O_2^- + M \rightarrow 2He + O + H_2O + M$	$2 \times 10^{-37}(T_g/300)^{-2.5}$	0	[14]
247	$He_2^+ + H_3O_2^- + M \rightarrow 2He + OH + H_2O + M$	$2 \times 10^{-37}(T_g/300)^{-2.5}$	0	[14]
248	$He_2^+ + H_5O_3^- + M \rightarrow 2He + OH + 2H_2O + M$	$2 \times 10^{-37}(T_g/300)^{-2.5}$	0	[14]
249	$O_2^+ + OH^- \rightarrow O_2 + OH$	$2 \times 10^{-13}(T_g/300)^{-0.5}$	0	[14]
250	$O_2^+ + H_2O_2^- + M \rightarrow O_2 + O + H_2O + M$	$2 \times 10^{-37}(T_g/300)^{-2.5}$	0	[14]
251	$O_2^+ + H_3O_2^- + M \rightarrow O_2 + OH + H_2O + M$	$2 \times 10^{-37}(T_g/300)^{-2.5}$	0	[14]
252	$O_2^+ + H_5O_3^- + M \rightarrow O_2 + OH + 2H_2O + M$	$2 \times 10^{-37}(T_g/300)^{-2.5}$	0	[14]
253	$OH^+ + O^- \rightarrow HO_2$	$2 \times 10^{-13}(T_g/300)^{-0.5}$	0	[14]
254	$OH^+ + O_2^- \rightarrow OH + O_2$	$2 \times 10^{-13}(T_g/300)^{-0.5}$	0	[14]
255	$OH^+ + H_2O_2^- + M \rightarrow O + OH + 2H_2O + M$	$2 \times 10^{-37}(T_g/300)^{-2.5}$	0	[14]
256	$OH^+ + H_5O_3^- + M \rightarrow 2OH + 2H_2O + M$	$2 \times 10^{-37}(T_g/300)^{-2.5}$	0	[14]
257	$H_2O^+ + O^- + M \rightarrow O + H_2O + M$	$2 \times 10^{-37}(T_g/300)^{-2.5}$	0	[14]
258	$H_2O^+ + OH^- + M \rightarrow OH + H_2O + M$	$2 \times 10^{-37}(T_g/300)^{-2.5}$	0	[14]
259	$H_2O^+ + H_2O_2^- + M \rightarrow O + 2H_2O + M$	$2 \times 10^{-37}(T_g/300)^{-2.5}$	0	[14]

260	$H_2O^+ + H_3O_2^- + M \rightarrow OH + 2H_2O + M$	$2 \times 10^{-37}(T_g/300)^{-2.5}$	0	[14]
261	$H_2O^+ + H_5O_3^- + M \rightarrow OH + 3H_2O + M$	$2 \times 10^{-37}(T_g/300)^{-2.5}$	0	[14]
262	$H_2O_3^+ + O^- + M \rightarrow H_2O + O + O_2 + M$	$2 \times 10^{-37}(T_g/300)^{-2.5}$	0	[14]
263	$H_2O_3^+ + O_2^- + M \rightarrow H_2O + 2O_2 + M$	$2 \times 10^{-37}(T_g/300)^{-2.5}$	0	[14]
264	$H_2O_3^+ + H_5O_3^- + M \rightarrow 3H_2O + OH + O_2 + M$	$2 \times 10^{-37}(T_g/300)^{-2.5}$	0	[14]
265	$H_9O_4^+ + H_2O_2^- + M \rightarrow 5H_2O + OH + M$	$2 \times 10^{-37}(T_g/300)^{-2.5}$	0	[14]
266	$H_9O_4^+ + H_5O_3^- + M \rightarrow 7H_2O + M$	$2 \times 10^{-37}(T_g/300)^{-2.5}$	0	[14]
267	$H_{11}O_5^+ + H_2O_2^- + M \rightarrow OH + 6H_2O + M$	$2 \times 10^{-37}(T_g/300)^{-2.5}$	0	[14]
268	$H_{11}O_5^+ + H_5O_3^- + M \rightarrow 8H_2O + M$	$2 \times 10^{-37}(T_g/300)^{-2.5}$	0	[14]
269	$H_{13}O_6^+ + H_2O_2^- + M \rightarrow OH + 7H_2O + M$	$2 \times 10^{-37}(T_g/300)^{-2.5}$	0	[14]
270	$H_{13}O_6^+ + H_5O_3^- + M \rightarrow 9H_2O + M$	$2 \times 10^{-37}(T_g/300)^{-2.5}$	0	[14]
271	$H_{15}O_7^+ + H_2O_2^- + M \rightarrow OH + 8H_2O + M$	$2 \times 10^{-37}(T_g/300)^{-2.5}$	0	[83,200]
272	$H_{15}O_7^+ + H_5O_3^- + M \rightarrow 10H_2O + M$	$2 \times 10^{-37}(T_g/300)^{-2.5}$	0	[83,200]
273	$H_{17}O_8^+ + H_2O_2^- + M \rightarrow OH + 9H_2O + M$	$2 \times 10^{-37}(T_g/300)^{-2.5}$	0	[83,200]
274	$H_{17}O_8^+ + H_5O_3^- + M \rightarrow 11H_2O + M$	$2 \times 10^{-37}(T_g/300)^{-2.5}$	0	[83,200]
275	$H_{19}O_9^+ + H_2O_2^- + M \rightarrow OH + 10H_2O + M$	$2 \times 10^{-37}(T_g/300)^{-2.5}$	0	[83,200]
276	$H_{19}O_9^+ + H_5O_3^- + M \rightarrow 12H_2O + M$	$2 \times 10^{-37}(T_g/300)^{-2.5}$	0	[83,200]
277	$H_9O_4^+ + O^- + M \rightarrow 4H_2O + OH + M$	$2 \times 10^{-37}(T_g/300)^{-2.5}$	0	[14]
278	$H_9O_4^+ + O_2^- + M \rightarrow 4H_2O + O_2 + H + M$	$2 \times 10^{-37}(T_g/300)^{-2.5}$	0	[14]
279	$H_{11}O_5^+ + O^- + M \rightarrow 5H_2O + OH + M$	$2 \times 10^{-37}(T_g/300)^{-2.5}$	0	[14]
280	$H_{11}O_5^+ + O_2^- + M \rightarrow 5H_2O + O_2 + H + M$	$2 \times 10^{-37}(T_g/300)^{-2.5}$	0	[14]
281	$H_{13}O_6^+ + O^- + M \rightarrow 6H_2O + OH + M$	$2 \times 10^{-37}(T_g/300)^{-2.5}$	0	[14]
282	$H_{13}O_6^+ + O_2^- + M \rightarrow 6H_2O + O_2 + H + M$	$2 \times 10^{-37}(T_g/300)^{-2.5}$	0	[14]
283	$He_m + H \rightarrow H^+ + He + e^-$	1.1×10^{-15}	0	[50]
284	$He_m + H_2 \rightarrow H_2^+ + He + e^-$	2.9×10^{-17}	0	[201]
285	$He_m + OH \rightarrow OH^+ + He + e^-$	7.8×10^{-16}	0	[14]
286	$He_m + H_2O \rightarrow H_2O^+ + He + e^-$	6.6×10^{-16}	0	[191]
287	$He_m + H_2O \rightarrow H + OH^+ + He + e^-$	1.5×10^{-16}	0	[191]
288	$He_m + H_2O \rightarrow OH + H^+ + He + e^-$	2.6×10^{-17}	0	[191]
289	$He_m + H_2O \rightarrow OH + HeH^+ + e^-$	8.5×10^{-18}	0	[191]
290	$He_m + H_2O_2 \rightarrow He + OH^+ + OH + e^-$	7.8×10^{-16}	0	[14]
291	$He_2^* + H_2 \rightarrow H_2^+ + 2He + e^-$	2.2×10^{-16}	0	[202]
292	$He_2^* + OH \rightarrow OH^+ + 2He + e^-$	6×10^{-16}	0	[14]
293	$He_2^* + H_2O \rightarrow H_2O^+ + 2He + e^-$	6×10^{-16}	0	[203]
294	$He_2^* + H_2O \rightarrow 2He + H_2O$	1.5×10^{-21}	0	[167]
295	$He + OH(A) \rightarrow He + OH$	1.5×10^{-20}	0	[192]
296	$He + H + O_2 \rightarrow He + HO_2$	$2 \times 10^{-44}(T_g/300)^{-0.8}$	0	[204]
297	$He + H + OH \rightarrow He + H_2O$	$1.56 \times 10^{-43}(T_g/300)^{-2.6}$	0	[205]
298	$H + O_3 \rightarrow OH + O_2$	$2.71 \times 10^{-17}(T_g/300)^{0.75}$	0	[206]
299	$H + HO_2 \rightarrow H_2 + O_2$	$1.1 \times 10^{-18} T_g^{0.56} \exp(-346/T_g)$	0	[168]
300	$H + HO_2 \rightarrow 2OH$	$2.35 \times 10^{-16} \exp(-373.7/T_g)$	0	[168]

301	$O + OH \rightarrow H + O_2$	$6 \times 10^{-17} T_g^{-0.186} \exp(-154/T_g)$	0	[168]
302	$O + HO_2 \rightarrow OH + O_2$	$2.9 \times 10^{-17} \exp(200/T_g)$	0	[168]
303	$O(^1D) + H_2O_2 \rightarrow H_2O + O_2$	5.2×10^{-16}	0	[168]
304	$O(^1D) + H_2O \rightarrow 2OH$	$1.62 \times 10^{-16} \exp(64.95/T_g)$	0	[206]
305	$O(^1D) + H_2O \rightarrow O + H_2O$	1.2×10^{-17}	0	[174]
306	$O_2(b) + H_2O \rightarrow O_2(a) + H_2O$	$4.52 \times 10^{-18} \exp(89/T_g)$	0	[207]
307	$2OH \rightarrow H_2O + O$	$2.5 \times 10^{-21} T_g^{1.14} \exp(-50/T_g)$	0	[206]
308	$2OH \rightarrow H_2O_2$	$1.5 \times 10^{-17} (T_g/300)^{-0.37}$	0	[204]
309	$OH + HO_2 \rightarrow O_2 + H_2O$	$4.38 \times 10^{-17} \exp(110.9/T_g)$	0	[168]
310	$OH + H_2O_2 \rightarrow H_2O + HO_2$	$4.53 \times 10^{-18} \exp(-288.9/T_g)$	0	[168]
311	$OH(A) + H_2O \rightarrow H_2O + OH$	$4.9 \times 10^{-16} (T_g/300)^{0.5}$	0	[208]
312	$OH(A) + H_2O_2 \rightarrow HO_2 + H_2O$	2.93×10^{-16}	0	[209]
313	$OH(A) \rightarrow OH + hv$	1.25×10^{6}	0	[192]

Note: [a] M represents the background gases helium atom, Nitrogen and Oxygen molecule. [b] Rate coefficients have units of $s^{-1}, m^3 s^{-1}, m^6 s^{-1}$ for one, two and three body reactions respectively; T_e has units of eV; T_g has units of K. $f(\varepsilon)$ indicates the rate coefficient as a function of the mean electron energy calculated from the solution of Boltzmann equation. The reference indicates the database of the cross section used. [b] The cross sections are calculated by detailed balancing.

Appendix D: Rate coefficients for helium, nitrogen and oxygen reactions.

Table D1: Rate coefficients for helium, nitrogen and oxygen reactions.

Reaction No.	Reaction equation[a)]	Rate constant[b)]	Threshold (eV)	Ref
1	$e^- + He \rightarrow e^- + He$	$f(\varepsilon, n)$	0	[93]
2	$e^- + He \rightarrow e^- + He_m$	$f(\varepsilon, n)$	19.82	[93]
3	$e^- + He \rightarrow 2e^- + He^+$	$f(\varepsilon, n)$	24.58	[93]
4	$e^- + He_m \rightarrow 2e^- + He^+$	$2.254 \times 10^{-13} T_e^{-0.1241} e^{-5.725/T_e}$	4.78	[77]
5	$e^- + He_m \rightarrow e^- + He$	2.9×10^{-15}	-19.82	[163,164]
6	$e^- + He_2^m \rightarrow e^- + 2He$	3.8×10^{-15}	-17.9	[163]
7	$2e^- + He^+ \rightarrow e^- + He_m$	$7.8 \times 10^{-50} (T_e/T_g)^{-4.4}$	-4.78	[165]
8	$2e^- + He_2^+ \rightarrow He_m + He + e^-$	2.8×10^{-32}	0	[163]
9	$e^- + He + He_2^+ \rightarrow He_m + 2He$	3.5×10^{-39}	0	[163]
10	$2e^- + He_2^+ \rightarrow He_2^m + e^-$	1.2×10^{-33}	0	[163]
11	$e^- + He + He_2^+ \rightarrow He_2^m + He$	1.5×10^{-39}	0	[163]
12	$He_m + He_m \rightarrow He_2^+ + e^-$	$2.03 \times 10^{-15} (T_g/300)^{0.5}$	-18.2	[166]
13	$He_m + He_m \rightarrow He^+ + He + e^-$	$8.7 \times 10^{-16} (T_g/300)^{0.5}$	-15.8	[166]
14	$He^+ + 2He \rightarrow He_2^+ + He$	$1.4 \times 10^{-43} (T_g/300)^{-0.6}$	0	[166]
15	$He_m + 2He \rightarrow He_2^m + He$	2×10^{-46}	0	[166]
16	$He_m + He_2^m \rightarrow He^+ + 2He + e^-$	$5 \times 10^{-16} (T_g/300)^{0.5}$	-13.5	[163]
17	$He_m + He_2^m \rightarrow He_2^+ + He + e^-$	$2 \times 10^{-15} (T_g/300)^{0.5}$	-15.9	[163]
18	$He_2^m + He_2^m \rightarrow He^+ + 3He + e^-$	$3 \times 10^{-16} (T_g/300)^{0.5}$	-11.3	[163]
19	$He_2^m + He_2^m \rightarrow He_2^+ + 2He + e^-$	$1.2 \times 10^{-15} (T_g/300)^{0.5}$	-13.7	[163]
20	$e^- + He^+ \rightarrow He_m$	$6.76 \times 10^{-19} T_e^{-0.5}$	0	[168]
21	$e^- + He + He^+ \rightarrow He_m + He$	$7.4 \times 10^{-47} (T_e/T_g)^{-2}$	0	[165]
22	$e^- + He_2^+ \rightarrow He + He_m$	$7.12 \times 10^{-21} (T_e/T_g)^{-1.5}$	0	[103]
23	$e^- + He_2^m \rightarrow He_2^+ + 2e^-$	$9.75 \times 10^{-16} T_e^{0.71} e^{-3.4/T_e}$	3.4	[166]
24	$e^- + N_2 \rightarrow e^- + N_2$	$f(\varepsilon, n)$	0	[94]
25	$e^- + N_2 \rightarrow e^- + N_2\ (v = 1\ to\ 4)$	$f(\varepsilon, n)$	0.3, 0.6, 0.9, 1.1	[94]
26	$e^- + N_2 \rightarrow e^- + N_2(A^3\Sigma_u^+\ (v = 0-4))$	$f(\varepsilon, n)$	6.2	[94]
27	$e^- + N_2 \rightarrow e^- + N_2(A^3\Sigma_u^+\ (v = 5-9))$	$f(\varepsilon, n)$	7	[94]
28	$e^- + N_2 \rightarrow e^- + N_2(B^3\Pi_g)$	$f(\varepsilon, n)$	7.4	[94]
29	$e^- + N_2 \rightarrow e^- + N_2(W^3\Delta_u)$	$f(\varepsilon, n)$	7.4	[94]
30	$e^- + N_2 \rightarrow e^- + N_2(A^3\Sigma_u^+\ (v > 9))$	$f(\varepsilon, n)$	7.8	[94]
31	$e^- + N_2 \rightarrow e^- + N_2(B^3\Sigma_u^-)$	$f(\varepsilon, n)$	8.2	[94]
32	$e^- + N_2 \rightarrow e^- + N_2(a^1\Sigma_u^-)$	$f(\varepsilon, n)$	8.4	[94]

33	$e^- + N_2 \rightarrow e^- + N_2(a^1\Pi_g)$	$f(\varepsilon, n)$	8.6	[94]
34	$e^- + N_2 \rightarrow e^- + N_2(W^1\Delta_u)$	$f(\varepsilon, n)$	8.9	[94]
35	$e^- + N_2 \rightarrow e^- + N_2(C^3\Pi_u)$	$f(\varepsilon, n)$	11	[94]
36	$e^- + N_2 \rightarrow e^- + N_2(E^3\Sigma_g^+)$	$f(\varepsilon, n)$	11.9	[94]
37	$e^- + N_2 \rightarrow e^- + N_2(a^1\Sigma_g^+)$	$f(\varepsilon, n)$	12.3	[94]
38	$e^- + N_2 \rightarrow 2e^- + N_2^+$	$f(\varepsilon, n)$	15.5	[94]
39	$e^- + N_4^+ \rightarrow 2N_2$	3×10^{-13}	0	[170]
40	$2e^- + N_4^+ \rightarrow 2N_2 + e^-$	3.17×10^{-42}	0	[77]
41	$2e^- + N_2^+ \rightarrow e^- + N_2$	3.17×10^{-42}	0	[97]
42	$e^- + N_2^+ \rightarrow 2N$	$2.36 \times 10^{-14}(T_e)^{-0.5}$	0	[97]
43	$He_m + N_2 \rightarrow e^- + N_2^+ + He$	5×10^{-17}	0	[77]
44	$He_2^m + N_2 \rightarrow e^- + N_2^+ + 2He$	5×10^{-17}	0	[77]
45	$He^+ + N_2 \rightarrow N_2^+ + He$	6.5×10^{-16}	0	[173]
46	$He_2^+ + N_2 \rightarrow N_2^+ + 2He$	1.1×10^{-15}	0	[173]
47	$N_2^+ + He + N_2 \rightarrow N_4^+ + He$	$8.9 \times 10^{-42}(T_g/300)^{-1.54}$	0	[173]
48	$N_2^+ + N_2 + N_2 \rightarrow N_4^+ + N_2$	5×10^{-41}	0	[83]
49	$He^+ + N_2 + He \rightarrow N_2^+ + 2He$	1.1×10^{-41}	0	[173]
50	$He_2^+ + N_2 + He \rightarrow N_2^+ + 3He$	1.6×10^{-41}	0	[173]
51	$He_m + N_2 + He \rightarrow N_2^+ + 2He + e^-$	3.3×10^{-42}	0	[64]
52	$e^- + O_2 \rightarrow e^- + O_2$	$f(\varepsilon, n)$	0	[94]
53	$e^- + O_2 \rightarrow e^- + O_2\ (v = 1\ to\ 4)$	$f(\varepsilon, n)$	0.19, 0.38, 0.6, 0.8	[94]
54	$e^- + O_2 \rightarrow O + O^-$	$f(\varepsilon, n)$	0	[94]
55	$e^- + O_2 \rightarrow e^- + O_2(a)$	$f(\varepsilon, n)$	0.977	[94]
56	$e^- + O_2 \rightarrow e^- + O_2(b)$	$f(\varepsilon, n)$	1.627	[94]
57	$e^- + O_2 \rightarrow e^- + 2O$	$f(\varepsilon, n)$	6	[94]
58	$e^- + O_2 \rightarrow e^- + O + O(^1D)$	$f(\varepsilon, n)$	8.4	[94]
59	$e^- + O_2 \rightarrow e^- + O + O(^1S)$	$f(\varepsilon, n)$	9.97	[94]
60	$e^- + O_2 \rightarrow 2e^- + O_2^+$	$f(\varepsilon, n)$	12.1	[94]
61	$e^- + O_2^+ \rightarrow 2O$	$1.2 \times 10^{-14} T_e^{-0.7}$	0	[79]
62	$e^- + O_2 + O_2 \rightarrow O_2^- + O_2$	$2.26 \times 10^{-42}(T_g/300)^{-0.5}$	0	[180]
63	$e^- + O_2^+ + O_2 \rightarrow 2O_2$	$2.49 \times 10^{-41}(T_e)^{-1.5}$	0	[168]
64	$2e^- + O_2^+ \rightarrow e^- + O_2$	$7.18 \times 10^{-39}(T_e)^{-4.5}$	0	[83]
65	$O_4^+ + O^- + O_2 \rightarrow 2O_2 + O + O_2$	$2 \times 10^{-37}(T_g/300)^{-2.5}$	0	[78,83]
66	$O_4^+ + O_2^- + O_2 \rightarrow 3O_2 + O_2$	$2 \times 10^{-37}(T_g/300)^{-2.5}$	0	[78,83]
67	$O_4^+ + O_2 \rightarrow O_2^+ + 2O_2$	$3.3 \times 10^{-12}(T_g/300)^{-4} e^{(-5030/T_g)}$	0	[83]
68	$e^- + O_4^+ \rightarrow 2O_2$	$2.25 \times 10^{-13} T_e^{-0.5}$	0	[83]
69	$O_4^+ + O^- + He \rightarrow 2O_2 + O + He$	$2 \times 10^{-37}(T_g/300)^{-2.5}$	0	[78,83]
70	$O_4^+ + O_2^- + He \rightarrow 3O_2 + He$	$2 \times 10^{-37}(T_g/300)^{-2.5}$	0	[78,83]
71	$e^- + O_2 + He \rightarrow He + O_2^-$	1×10^{-43}	0	[81]
72	$O_2^+ + O_2 + He \rightarrow O_4^+ + He$	$5.8 \times 10^{-43}(T_g/300)^{-3.1}$	0	[175]
73	$He_m + O_2 \rightarrow O_2^+ + He + e^-$	$2.54 \times 10^{-16}(T_g/300)^{0.5}$	0	[79]
74	$He + He_m + O_2 \rightarrow O_2^+ + 2He + e^-$	1.6×10^{-43}	0	[181]
75	$He_2^m + O_2 \rightarrow O_2^+ + 2He + e^-$	$1 \times 10^{-16}(T_g/300)^{0.5}$	0	[176]

76	$He_2^+ + O_2 \rightarrow O_2^+ + 2He$	$1 \times 10^{-15}(T_g/300)^{0.5}$	0	[176]
77	$O_2^+ + O^- + M \rightarrow O_2 + O + M$	$2 \times 10^{-37}(T_g/300)^{-2.5}$	0	[11,83]
78	$O_2^+ + O_2^- + M \rightarrow 2O_2 + M$	$2 \times 10^{-37}(T_g/300)^{-2.5}$	0	[11,83]
79	$O_2^+ + O^- + M \rightarrow O_3 + M$	$2 \times 10^{-37}(T_g/300)^{-2.5}$	0	[11,83]
80	$O_4^+ + O^- + N_2 \rightarrow 2O_2 + O + N_2$	$1 \times 10^{-37}(T_g/300)^{-2.5}$	0	[11,83]
81	$O_4^+ + O_2^- + N_2 \rightarrow 3O_2 + N_2$	$1 \times 10^{-37}(T_g/300)^{-2.5}$	0	[11,83]
82	$N_2^+ + O^- + M \rightarrow N_2 + O + M$	$2 \times 10^{-37}(T_g/300)^{-2.5}$	0	[11,83]
83	$N_2^+ + O_2^- + M \rightarrow N_2 + O_2 + M$	$2 \times 10^{-37}(T_g/300)^{-2.5}$	0	[11,83]
84	$N_2^+ + O_2 + e^- \rightarrow O_2 + N_2$	$6 \times 10^{-39}(T_e/T_g)^{-1.5}$	0	[11]
85	$O_2^+ + N_2 + e^- \rightarrow O_2 + N_2$	$6 \times 10^{-39}(T_e/T_g)^{-1.5}$	0	[11]
86	$N_4^+ + O_2 \rightarrow O_2 + N_2 + N_2^+$	2.5×10^{-16}	0	[11]
87	$N_2^+ + O_2 \rightarrow N_2 + O_2^+$	$1.04 \times 10^{-15} T_g^{-0.5}$	0	[177]
88	$N_4^+ + O_2 \rightarrow 2N_2 + O_2^+$	2.5×10^{-16}	0	[90]
89	$O_4^+ + N_2 \rightarrow O_2 + N_2 + O_2^+$	$1 \times 10^{-11}(T_g/300)^{-4.2}\exp(-5400/T_g)$	0	[11]
90	$e^- + O_2 + N_2 \rightarrow N_2 + O_2^-$	$1.24 \times 10^{-43}(T_g/300)^{-0.5}$	0	[78]
91	$e^- + He \rightarrow e^- + He(3s^3S)$	$f(\varepsilon, n)$	22.719	[94]
92	$He(3s^3S) \rightarrow He(2p^3P) + hv\ (706\ nm)$	1.547	0	[145]
93	$O_2^+ + O_2 + O_2 \rightarrow O_2 + O_4^+$	$2.4 \times 10^{-32}(T_g/300)^{-3.2}$	0	[83]

[a] He_m represents $He(2s^3S)$ and $He(2s^1S)$; He_2^m represents $He_2(a^3\Sigma_u^+)$; $O_2(a)$ represents $O_2(a^1\Delta_g)$ and are treated as O_2; $O_2(b)$ represents $O_2(b^1\Sigma_g^+)$ and are treated as O_2; $N_2(v)$ represents the vibrational excited states of $N_2(v = 1-4)$ and are treated as N_2; $N_2(A^3\Sigma_u^+\ (v = 0-4))$, $N_2(A^3\Sigma_u^+\ (v = 5-9))$, $N_2(A^3\Sigma_u^+\ (v > 9))$, $N_2(B^3\Pi_g)$, $N_2(W^3\Delta_u)$, $N_2(B^3\Sigma_u^-)$, $N_2(a^1\Sigma_u^-)$, $N_2(a^1\Pi_g)$, $N_2(W^1\Delta_u)$, $N_2(C^3\Pi_u)$, $N_2(E^3\Sigma_g^+)$, $N_2(a^1\Sigma_g^+)$ are treated as N_2; $O_2(v)$ represents the vibrational excited states of $O_2(v = 1-4)$ and are treated as O_2; $O(^1D)$ and $O(^1S)$ are treated as O. M represents the background gases helium atom, nitrogen and oxygen molecule. [b] Rate coefficients have units of $s^{-1}, m^3s^{-1}, m^6s^{-1}$ for one, two and three body reactions respectively; $T_e = 2/3\varepsilon$ has units eV; T_g has units of K. $f(\varepsilon, n)$ indicates the rate coefficient as a function of the mean electron energy and air mole fraction calculated from the solution of Boltzmann equation. The reference indicates the database of the cross section used.

Appendix E: Supplementary simulation results for the plasma jet

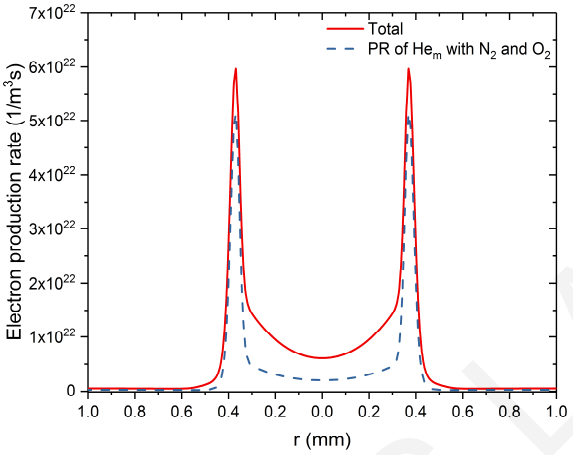

Figure E1: Simulation results of the electron production rate for the He plasma jet at z=0.1 mm and time -152 ns (i.e. streamer head location at z=-0.75 mm, same time snapshot as Figure 54a).

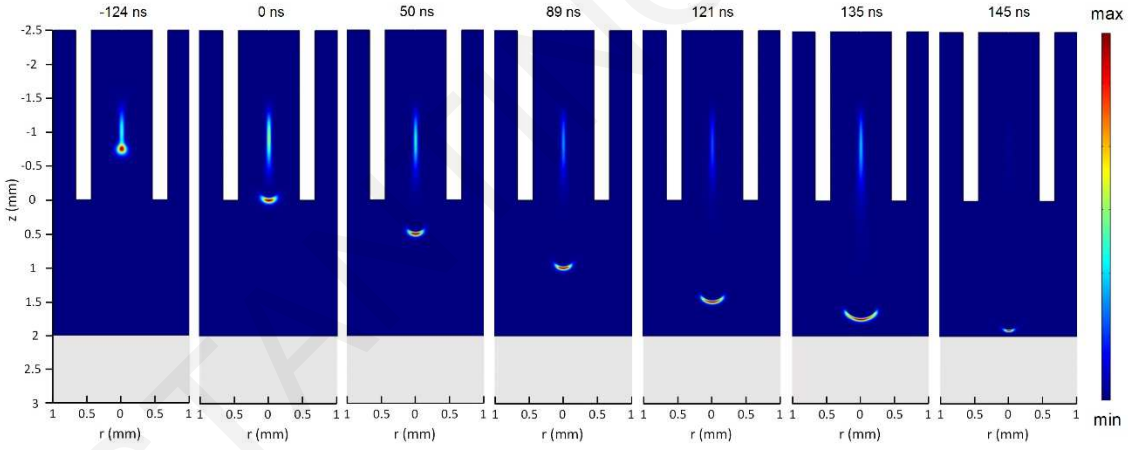

Figure E2: Simulation results of the spatio-temporal evolution of the total ionization rate for He plasma jet without considering the Penning reactions in the kinetic scheme.

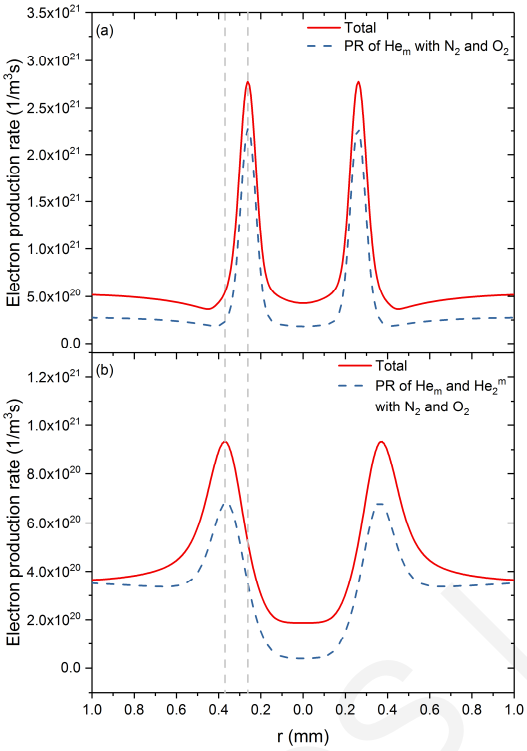

Figure E3: Simulation results of the electron production rate for the He plasma jet (a) at z=1 mm and time 0 ns (i.e. streamer head location at z=0 mm, same time snapshot as Figure 54c), (b) at z=1.85 and time 121 ns (i.e. streamer head location at z=1 mm, same time snapshot as Figure 54e). The dotted grey lines are a visual aid to highlight the peak shift between the two curves.

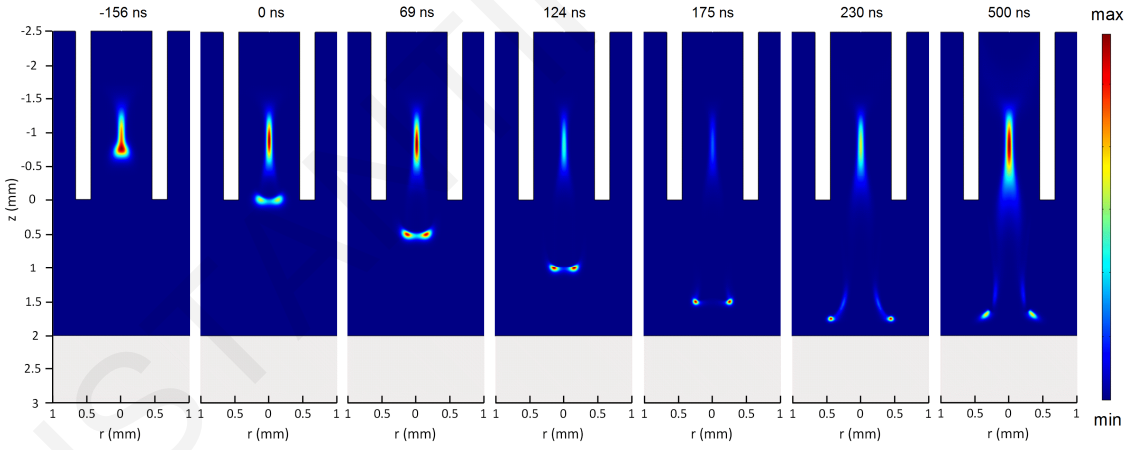

Figure E4: Simulation results of the spatio-temporal evolution of the total ionization rate for He plasma jet where the seec is set to zero.

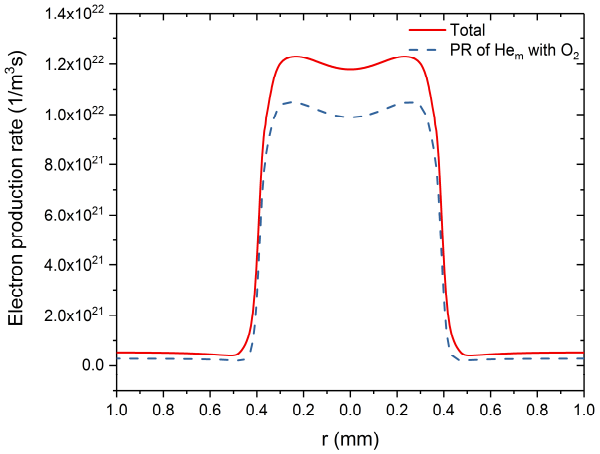

Figure E5: Simulation results of the electron production rate for the He+O_2 (1000ppm) plasma jet at z=0.1 mm and time -181 ns (i.e. plasma bullet location z= -0.75 mm, same time snapshot as Figure 60a).

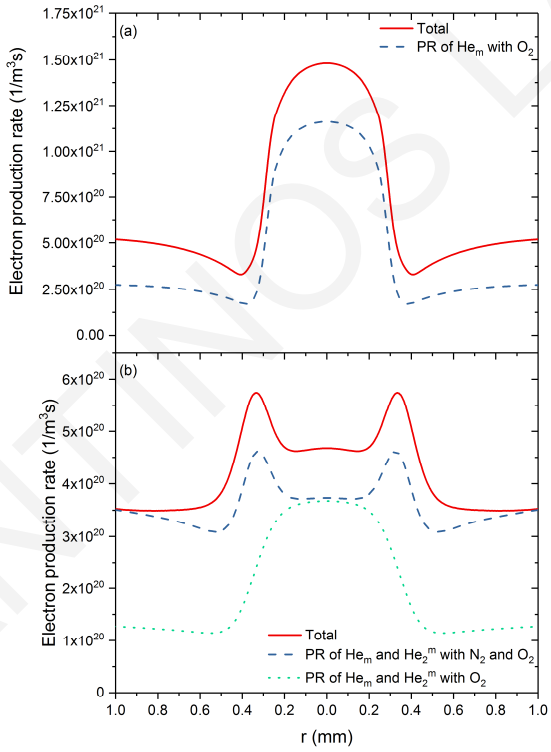

Figure E6: Simulation results of the electron production rate for the He+O_2 (1000 ppm) plasma jet (a) at z=1 mm and time 0 ns (i.e. the plasma bullet location just about the exit of the tube, same time snapshot as Figure 60c), (b) at z=1.85 and time 163 ns (i.e. plasma bullet location z= 1 mm, same time snapshot as Figure 60e).

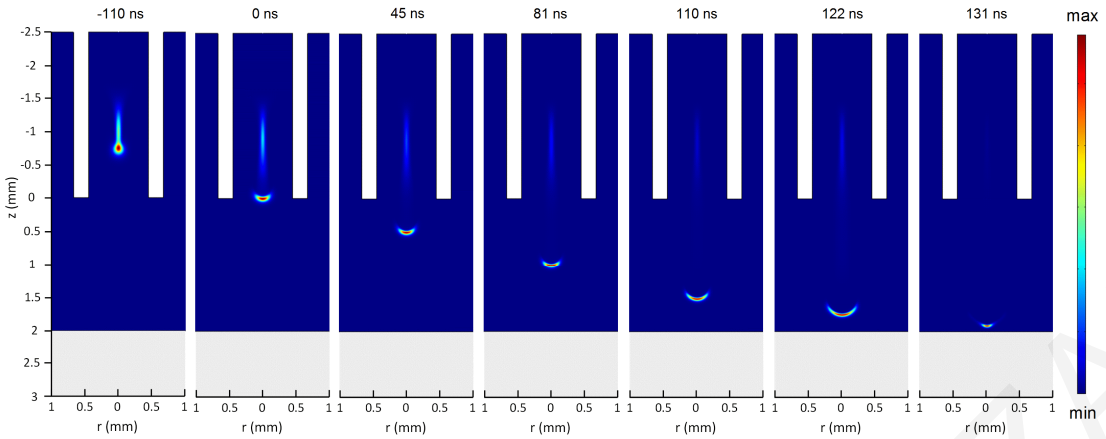

Figure E7: Simulation results of the spatio-temporal evolution of the total ionization rate for He+O_2 (1000 ppm) plasma jet without considering the Penning reactions in the kinetic scheme.

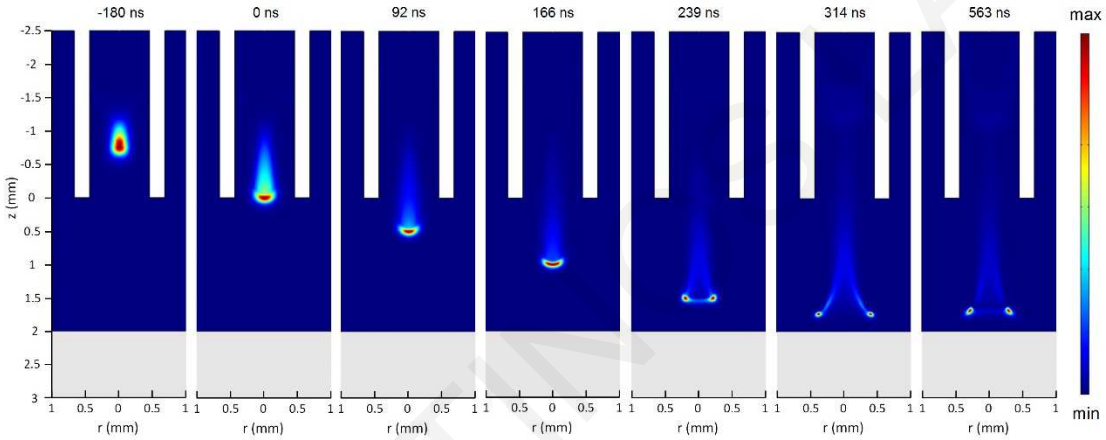

Figure E8: Simulation results of the spatio-temporal evolution of the total ionization rate for He+O_2 (1000 ppm) plasma jet where the seec is set to zero.

References

[1] Mariotti D, Belmonte T, Benedikt J, Velusamy T, Jain G and Švrček V 2016 Low-Temperature Atmospheric Pressure Plasma Processes for “Green” Third Generation Photovoltaics *Plasma Process. Polym.* **13** 70–90

[2] Belmonte T, Pintassilgo C D, Czerwiec T, Henrion G, Hody V, Thiebaut J M and Loureiro J 2005 Oxygen plasma surface interaction in treatments of polyolefines *Surf. Coatings Technol.* **200** 26–30

[3] Kong M G, Kroesen G, Morfill G, Nosenko T, Shimizu T, van Dijk J and Zimmermann J L 2009 Plasma medicine: an introductory review *New J. Phys.* **11** 115012

[4] Nastuta A V, Topala I, Grigoras C, Pohoata V and Popa G 2011 Stimulation of wound healing by helium atmospheric pressure plasma treatment *J. Phys. D. Appl. Phys.* **44** 105204

[5] Laroussi M 2005 Low Temperature Plasma-Based Sterilization: Overview and State-of-the-Art *Plasma Process. Polym.* **2** 391–400

[6] Mfopara A, Kirkpatrick M J and Odic E 2008 Dilute Methane Treatment by Atmospheric Pressure Dielectric Barrier Discharge: Effects of Water Vapor *Plasma Chem. Plasma Process.* **29** 91–102

[7] Laroussi M 2015 Low-Temperature Plasma Jet for Biomedical Applications: A Review *IEEE Trans. Plasma Sci.* **43** 703–12

[8] Lee H W, Nam S H, Mohamed A-A H, Kim G C and Lee J K 2010 Atmospheric Pressure Plasma Jet Composed of Three Electrodes: Application to Tooth Bleaching *Plasma Process. Polym.* **7** 274–80

[9] Keidar M 2015 Plasma for cancer treatment *Plasma Sources Sci. Technol.* **24** 033001

[10] O’Connell D, Cox L J, Hyland W B, McMahon S J, Reuter S, Graham W G, Gans T and Currell F J 2011 Cold atmospheric pressure plasma jet interactions with plasmid DNA *Appl. Phys. Lett.* **98** 043701

[11] Murakami T, Niemi K, Gans T, O’Connell D and Graham W G 2013 Chemical kinetics and reactive species in atmospheric pressure helium–oxygen plasmas with humid-air impurities *Plasma Sources Sci. Technol.* **22** 015003

[12] Murakami T, Niemi K, Gans T, O’Connell D and Graham W G 2013 Interacting kinetics of neutral and ionic species in an atmospheric-pressure helium–oxygen plasma with humid air impurities *Plasma Sources Sci. Technol.* **22** 045010

[13] Murakami T, Niemi K, Gans T, O'Connell D and Graham W G 2014 Afterglow chemistry of atmospheric-pressure helium–oxygen plasmas with humid air impurity *Plasma Sources Sci. Technol.* **23** 025005

[14] Liu D X, Bruggeman P, Iza F, Rong M Z and Kong M G 2010 Global model of low-temperature atmospheric-pressure He + H 2 O plasmas *Plasma Sources Sci. Technol.* **19** 025018

[15] Liu D X, Iza F, Wang X H, Kong M G and Rong M Z 2011 He+O2+H2O plasmas as a source of reactive oxygen species *Appl. Phys. Lett.* **98** 221501

[16] Schröter S, Gibson A R, Kushner M J, Gans T and O'Connell D 2018 Numerical study of the influence of surface reaction probabilities on reactive species in an rf atmospheric pressure plasma containing humidity *Plasma Phys. Control. Fusion* **60** 014035

[17] Navrátil Z, Brandenburg R, Trunec D, Brablec a, St'ahel P, Wagner H-E and Kopecký Z 2006 Comparative study of diffuse barrier discharges in neon and helium *Plasma Sources Sci. Technol.* **15** 8–17

[18] Babaeva N Y and Naidis G V. 2018 Modeling of Plasmas for Biomedicine *Trends Biotechnol.* **36** 603–14

[19] Naidis G V 2010 Modelling of streamer propagation in atmospheric-pressure helium plasma jets *J. Phys. D. Appl. Phys.* **43** 402001

[20] Naidis G V 2011 Modelling of plasma bullet propagation along a helium jet in ambient air *J. Phys. D. Appl. Phys.* **44** 215203

[21] Breden D, Miki K and Raja L L 2011 Computational study of cold atmospheric nanosecond pulsed helium plasma jet in air *Appl. Phys. Lett.* **99** 111501

[22] Jánský J and Bourdon A 2011 Simulation of helium discharge ignition and dynamics in thin tubes at atmospheric pressure *Appl. Phys. Lett.* **99** 161504

[23] Breden D, Miki K and Raja L L 2012 Self-consistent two-dimensional modeling of cold atmospheric-pressure plasma jets/bullets *Plasma Sources Sci. Technol.* **21** 034011

[24] Naidis G V. 2012 Modeling of helium plasma jets emerged into ambient air: Influence of applied voltage, jet radius, and helium flow velocity on plasma jet characteristics *J. Appl. Phys.* **112** 103304

[25] Boeuf J-P, Yang L L and Pitchford L C 2013 Dynamics of a guided streamer ("plasma bullet") in a helium jet in air at atmospheric pressure *J. Phys. D. Appl. Phys.* **46** 015201

[26] Liu X Y, Pei X K, Lu X P and Liu D W 2014 Numerical and experimental study on a pulsed-dc plasma jet *Plasma Sources Sci. Technol.* **23** 035007

[27] Naidis G V. 2015 On the Ring-Shaped Structure of Helium Plasma Jets *IEEE Trans.*

Plasma Sci. **43** 733–6

[28] Bourdon A, Darny T, Pechereau F, Pouvesle J-M, Viegas P, Iséni S and Robert E 2016 Numerical and experimental study of the dynamics of a μ s helium plasma gun discharge with various amounts of N 2 admixture *Plasma Sources Sci. Technol.* **25** 035002

[29] Norberg S A, Johnsen E and Kushner M J 2015 Formation of reactive oxygen and nitrogen species by repetitive negatively pulsed helium atmospheric pressure plasma jets propagating into humid air *Plasma Sources Sci. Technol.* **24** 035026

[30] Logothetis D, Papadopoulos P K, Svarnas P and Vafeas P 2016 Comparison of two electro-hydrodynamic force models for the interaction between helium jet flow and an atmospheric-pressure "plasma jet" p 150019

[31] Lietz A M, Johnsen E and Kushner M J 2017 Plasma-induced flow instabilities in atmospheric pressure plasma jets *Appl. Phys. Lett.* **111** 114101

[32] Ning W, Dai D, Zhang Y, Han Y and Li L 2018 Effects of trace of nitrogen on the helium atmospheric pressure plasma jet interacting with a dielectric substrate *J. Phys. D. Appl. Phys.* **51** 125204

[33] Norberg S A, Johnsen E and Kushner M J 2015 Helium atmospheric pressure plasma jets touching dielectric and metal surfaces *J. Appl. Phys.* **118** 013301

[34] Norberg S A, Johnsen E and Kushner M J 2016 Helium atmospheric pressure plasma jets interacting with wet cells: delivery of electric fields *J. Phys. D. Appl. Phys.* **49** 185201

[35] Wang L, Zheng Y and Jia S 2016 Numerical study of the interaction of a helium atmospheric pressure plasma jet with a dielectric material *Phys. Plasmas* **23** 103504

[36] Yan W and Economou D J 2016 Simulation of a non-equilibrium helium plasma bullet emerging into oxygen at high pressure (250–760 Torr) and interacting with a substrate *J. Appl. Phys.* **120** 123304

[37] Yan W and Economou D J 2017 Gas flow rate dependence of the discharge characteristics of a helium atmospheric pressure plasma jet interacting with a substrate *J. Phys. D. Appl. Phys.* **50** 415205

[38] Topala I and Nagatsu M 2015 Capillary plasma jet: A low volume plasma source for life science applications *Appl. Phys. Lett.* **106** 054105

[39] Brandt S, Klute F D, Schütz A and Franzke J 2017 Dielectric barrier discharges applied for soft ionization and their mechanism *Anal. Chim. Acta* **951** 16–31

[40] Kim S J, Chung T H, Bae S H and Leem S H 2010 Induction of apoptosis in human breast cancer cells by a pulsed atmospheric pressure plasma jet *Appl. Phys. Lett.* **97** 023702

[41] Mirpour S, Ghomi H, Piroozmand S, Nikkhah M, Tavassoli S H and Azad S Z 2014 The Selective Characterization of Nonthermal Atmospheric Pressure Plasma Jet on Treatment of Human Breast Cancer and Normal Cells *IEEE Trans. Plasma Sci.* **42** 315–22

[42] Meyyappan M and Kreskovsky J P 1990 Glow discharge simulation through solutions to the moments of the Boltzmann transport equation *J. Appl. Phys.* **68** 1506–12

[43] Meunier J, Belenguer P and Boeuf J P 1995 Numerical model of an ac plasma display panel cell in neon?xenon mixtures *J. Appl. Phys.* **78** 731–45

[44] Gogolides E and Sawin H H 1992 Continuum modeling of radio-frequency glow discharges. I. Theory and results for electropositive and electronegative gases *J. Appl. Phys.* **72** 3971

[45] Hagelaar G J M and Pitchford L C 2005 Solving the Boltzmann equation to obtain electron transport coefficients and rate coefficients for fluid models *Plasma Sources Sci. Technol.* **14** 722–33

[46] Kee R J, Coltrin M E and Glarborg P 2003 *Chemically Reacting Flow Theory and Practice* (Wiley)

[47] Bird R B, Stewart W E and Lightfoot E N 2002 *Transport phenomena* vol 15 (Wiley)

[48] Neufeld P D 1972 Empirical Equations to Calculate 16 of the Transport Collision Integrals Ω(l, s) *J. Chem. Phys.* **57** 1100

[49] Brokaw R S 1969 Predicting Transport Properties of Dilute Gases *Ind. Eng. Chem. Process Des. Dev.* **8** 240–53

[50] Hagelaar G J M, Kroesen G M W, van Slooten U and Schreuders H 2000 Modeling of the microdischarges in plasma addressed liquid crystal displays *J. Appl. Phys.* **88** 2252

[51] Papadopoulos P K, Vafeas P, Svarnas P, Gazeli K, Hatzikonstantinou P M, Gkelios A and Clément F 2014 Interpretation of the gas flow field modification induced by guided streamer (“plasma bullet”) propagation *J. Phys. D. Appl. Phys.* **47** 425203

[52] Wilke C R 1950 A Viscosity Equation for Gas Mixtures *J. Chem. Phys.* **18** 517–9

[53] Day M A 1990 The no-slip condition of fluid dynamics *Erkenntnis* **33** 285–96

[54] COMSOL Multiphysics® v. 4.4. www.comsol.com. COMSOL AB, Stockholm, Sweden.

[55] Massines F, Gherardi N, Naudé N and Ségur P 2009 Recent advances in the understanding of homogeneous dielectric barrier discharges *Eur. Phys. J. Appl. Phys.* **47** 22805

[56] Massines F, Rabehi A, Decomps P, Gadri R Ben, Ségur P and Mayoux C 1998 Experimental and theoretical study of a glow discharge at atmospheric pressure controlled

by dielectric barrier *J. Appl. Phys.* **83** 2950

[57] Gherardi N, Khamphan C, Ricard A, Massines F, Ségur P, Gherardi N, Khamphan C and Ricard A 2003 Physics and chemistry in a glow dielectric barrier discharge at atmospheric pressure: diagnostics and modelling *Surf. Coatings Technol.* **174-175** 8–14

[58] Chiper A S, Cazan R and Popa G 2008 On the Secondary Discharge of an Atmospheric-Pressure Pulsed DBD in He with Impurities *IEEE Trans. Plasma Sci.* **36** 2824–30

[59] Chiper A S, Nastuta A V, Rusu G B and Popa G 2009 On surface elementary processes and polymer surface modifications induced by double pulsed dielectric barrier discharge *Nucl. Instruments Methods Phys. Res. Sect. B Beam Interact. with Mater. Atoms* **267** 313–6

[60] Asandulesa M, Topala I, Pohoata V and Dumitrascu N 2010 Influence of operational parameters on plasma polymerization process at atmospheric pressure *J. Appl. Phys.* **108** 093310

[61] Chelouah A, Marode E, Hartmann G and Achat S 1994 A new method for temperature evaluation in a nitrogen discharge *J. Phys. D. Appl. Phys.* **27** 940–5

[62] Chiper A S, Aniţa V, Agheorghiesei C, Pohoaţa V, Aniţa M and Popa G 2004 Spectroscopic Diagnostics for a DBD Plasma in He/Air and He/N2 Gas Mixtures *Plasma Process. Polym.* **1** 57–62

[63] Lin K-M, Hung C-T, Hwang F-N, Smith M R, Yang Y-W and Wu J-S 2012 Development of a parallel semi-implicit two-dimensional plasma fluid modeling code using finite-volume method *Comput. Phys. Commun.* **183** 1225–36

[64] Pouvesle J M 1982 Modeling of the charge transfer afterglow excited by intense electrical discharges in high pressure helium nitrogen mixtures *J. Chem. Phys.* **77** 817

[65] Pechereau F and Bourdon A 2014 Influence of nitrogen admixtures in helium on the propagation dynamics of an atmospheric pressure plasma jet *XXII ESCAMPIG* pp 340–1

[66] Yuan X and Raja L L 2003 Computational study of capacitively coupled high-pressure glow discharges in helium *IEEE Trans. Plasma Sci.* **31** 495–503

[67] Ellis H W, Pai R Y, McDaniel E W, Mason E A and Viehland L A 1976 Transport properties of gaseous ions over a wide energy range *At. Data Nucl. Data Tables* **17** 177–210

[68] Viehland database, www.lxcat.net, retrieved on Feb 23, 2014.

[69] Hung C-T, Chiu Y-M, Hwang F-N, Chiang M-H, Wu J-S and Wang Y-C 2010 Investigation of the Atmospheric Helium Dielectric Barrier Discharge Driven by a Realistic Distorted-Sinusoidal Voltage Power Source *Plasma Chem. Plasma Process.* **31** 1–21

[70] Martens T, Bogaerts A, Brok W and van Dijk J 2007 Computer simulations of a dielectric barrier discharge used for analytical spectrometry. *Anal. Bioanal. Chem.* **388** 1583–94

[71] Martens T, Bogaerts A, Brok W J M and Dijk J V. 2008 The dominant role of impurities in the composition of high pressure noble gas plasmas *Appl. Phys. Lett.* **92** 041504

[72] Martens T, Bogaerts A, Brok W J M and van Dijk J 2010 The influence of impurities on the performance of the dielectric barrier discharge *Appl. Phys. Lett.* **96** 091501

[73] Jansky J, Algwari Q T, O'Connell D and Bourdon A 2012 Experimental–Modeling Study of an Atmospheric-Pressure Helium Discharge Propagating in a Thin Dielectric Tube *IEEE Trans. Plasma Sci.* **40** 2912–9

[74] Lazzaroni C, Chabert P, Lieberman M A, Lichtenberg A J and Leblanc A 2012 Analytical–numerical global model of atmospheric-pressure radio-frequency capacitive discharges *Plasma Sources Sci. Technol.* **21** 035013

[75] Jánský J and Bourdon A 2014 Simulation of two counter-propagating helium discharges at atmospheric pressure *Plasma Sources Sci. Technol.* **23** 025001

[76] Lazarou C, Koukounis D, Chiper A S, Costin C, Topala I and Georghiou G E 2015 Numerical modeling of the effect of the level of nitrogen impurities in a helium parallel plate dielectric barrier discharge *Plasma Sources Sci. Technol.* **24** 035012

[77] Lieberman M a 2015 Analytical model of atmospheric pressure, helium/trace gas radio-frequency capacitive Penning discharges *Plasma Sources Sci. Technol.* **24** 025009

[78] Liu D-X, Rong M-Z, Wang X-H, Iza F, Kong M G and Bruggeman P 2010 Main Species and Physicochemical Processes in Cold Atmospheric-pressure He + O2 Plasmas *Plasma Process. Polym.* **7** 846–65

[79] Stafford D S and Kushner M J 2004 O[sub 2]([sup 1]Δ) production in He⁄O[sub 2] mixtures in flowing low pressure plasmas *J. Appl. Phys.* **96** 2451

[80] Turner M M 2016 Uncertainty and sensitivity analysis in complex plasma chemistry models *Plasma Sources Sci. Technol.* **25** 015003

[81] Stalder K R, Vidmar R J, Nersisyan G and Graham W G 2006 Modeling the chemical kinetics of high-pressure glow discharges in mixtures of helium with real air *J. Appl. Phys.* **99** 093301

[82] Iqbal M M and Turner M M 2015 Influence of Gap Spacing between Dielectric Barriers in Atmospheric Pressure Discharges *Contrib. to Plasma Phys.* **55** 444–58

[83] Kossyi I A, Kostinsky A Y, Matveyev A A and Silakov V P 1992 Kinetic scheme of the non-equilibrium discharge in nitrogen-oxygen mixtures *Plasma Sources Sci. Technol.* **1** 207–20

[84] Belmonte T, Cardoso R P, Henrion G and Kosior F 2007 Collisional–radiative modelling of a helium microwave plasma in a resonant cavity *J. Phys. D. Appl. Phys.* **40** 7343–56

[85] Alves L L 2007 Fluid modelling of the positive column of direct-current glow discharges *Plasma Sources Sci. Technol.* **16** 557–69

[86] www.lxcat.laplace.univ-tlse.fr/

[87] Longo S and Capitelli M 1994 A simple approach to treat anisotropic elastic collisions in Monte Carlo calculations of the electron energy distribution function in cold plasmas *Plasma Chem. Plasma Process.* **14** 1–13

[88] Biagi S F 1999 Monte Carlo simulation of electron drift and diffusion in counting gases under the influence of electric and magnetic fields *Nucl. Instruments Methods Phys. Res. Sect. A Accel. Spectrometers, Detect. Assoc. Equip.* **421** 234–40

[89] Alves L L, Bartschat K, Biagi S F, Bordage M C, Pitchford L C, Ferreira C M, Hagelaar G J M, Morgan W L, Pancheshnyi S, Phelps A V, Puech V and Zatsarinny O 2013 Comparisons of sets of electron–neutral scattering cross sections and swarm parameters in noble gases: II. Helium and neon *J. Phys. D. Appl. Phys.* **46** 334002

[90] Brandenburg R, Maiorov V A, Golubovskii Y B, Wagner H-E, Behnke J and Behnke J F 2005 Diffuse barrier discharges in nitrogen with small admixtures of oxygen: discharge mechanism and transition to the filamentary regime *J. Phys. D. Appl. Phys.* **38** 2187–97

[91] Pancheshnyi S, Biagi S, Bordage M C, Hagelaar G J M, Morgan W L, Phelps a. V and Pitchford L C 2012 The LXCat project: Electron scattering cross sections and swarm parameters for low temperature plasma modeling *Chem. Phys.* **398** 148–53

[92] Bordage M C, Biagi S F, Alves L L, Bartschat K, Chowdhury S, Pitchford L C, Hagelaar G J M, Morgan W L, Puech V and Zatsarinny O 2013 Comparisons of sets of electron–neutral scattering cross sections and swarm parameters in noble gases: III. Krypton and xenon *J. Phys. D. Appl. Phys.* **46** 334003

[93] Morgan database, www.lxcat.net, retrieved on September 25, 2015

[94] IST-Lisbon database, www.lxcat.net, retrieved on September 25, 2015

[95] Alves L L 2014 The IST-LISBON database on LXCat *J. Phys. Conf. Ser.* **565** 012007

[96] TRINITI database, www.lxcat.net, retrieved on September 25, 2015

[97] Raja L L 2003 Computational study of capacitively coupled high-pressure glow discharges in helium *IEEE Trans. Plasma Sci.* **31** 495–503

[98] Yang A, Wang X, Rong M, Liu D and Iza F 2011 1-D fluid model of atmospheric-pressure rf He + O2 cold plasmas : Parametric study and critical evaluation 1-D fluid model of atmospheric-pressure rf He 1 O 2 cold plasmas : Parametric study and critical

evaluation **113503**

[99] Babaeva N Y and Kushner M J 2013 Reactive fluxes delivered by dielectric barrier discharge filaments to slightly wounded skin *J. Phys. D. Appl. Phys.* **46** 025401

[100] Bogaczyk M, Wild R, Stollenwerk L and Wagner H-E 2012 Surface charge accumulation and discharge development in diffuse and filamentary barrier discharges operating in He, N 2 and mixtures *J. Phys. D. Appl. Phys.* **45** 465202

[101] Zhang P and Kortshagen U 2006 Two-dimensional numerical study of atmospheric pressure glows in helium with impurities *J. Phys. D. Appl. Phys.* **39** 153–63

[102] http://www.comsol.com/plasma-module

[103] Golubovskii Y B, Maiorov V A, Behnke J and Behnke J F 2003 Modelling of the homogeneous barrier discharge in helium at atmospheric pressure *J. Phys. D. Appl. Phys.* **36** 39–49

[104] Dosoudilová L, Tschiersch R, Bogaczyk M, Navrátil Z, Wagner H-E and Trunec D 2015 Investigation of helium barrier discharges with small admixtures of oxygen *J. Phys. D. Appl. Phys.* **48** 355204

[105] Abd-Allah Z, Sawtell D A G, McKay K, West G T, Kelly P J and Bradley J W 2015 Mass spectrometric investigation of the ionic species in a dielectric barrier discharge operating in helium-water vapour mixtures *J. Phys. D. Appl. Phys.* **48** 085202

[106] McKay K, Donaghy D, He F and Bradley J W 2017 Studying Townsend and glow modes in an atmospheric-pressure DBD using mass spectrometry *Plasma Sources Sci. Technol.* **27** 015002

[107] Gorbanev Y, O'Connell D and Chechik V 2016 Non-Thermal Plasma in Contact with Water: The Origin of Species *Chem. - A Eur. J.* **22** 3496–505

[108] Bruggeman P, Iza F, Lauwers D and Gonzalvo Y A 2010 Mass spectrometry study of positive and negative ions in a capacitively coupled atmospheric pressure RF excited glow discharge in He–water mixtures *J. Phys. D. Appl. Phys.* **43** 012003

[109] Bruggeman P J, Kushner M J, Locke B R, Gardeniers J G E, Graham W G, Graves D B, Hofman-Caris R C H M, Maric D, Reid J P, Ceriani E, Fernandez Rivas D, Foster J E, Garrick S C, Gorbanev Y, Hamaguchi S, Iza F, Jablonowski H, Klimova E, Kolb J, Krcma F, Lukes P, Machala Z, Marinov I, Mariotti D, Mededovic Thagard S, Minakata D, Neyts E C, Pawlat J, Petrovic Z L, Pflieger R, Reuter S, Schram D C, Schröter S, Shiraiwa M, Tarabová B, Tsai P A, Verlet J R R, von Woedtke T, Wilson K R, Yasui K and Zvereva G 2016 Plasma–liquid interactions: a review and roadmap *Plasma Sources Sci. Technol.* **25** 053002

[110] Kawamura E, Lieberman M A and Lichtenberg A J 2016 Standing striations due to ionization instability in atmospheric pressure He/H 2 O radio frequency capacitive

discharges *Plasma Sources Sci. Technol.* **25** 054009

[111] Kawamura E, Lieberman M A and Lichtenberg A J 2018 Ionization instability induced striations in low frequency and pulsed He/H 2 O atmospheric pressure plasmas *Phys. Plasmas* **25** 013535

[112] Ding K, Lieberman M A and Lichtenberg A J 2014 Hybrid model of neutral diffusion, sheaths, and the α to γ transition in an atmospheric pressure He/ H 2 O bounded rf discharge *J. Phys. D. Appl. Phys.* **47** 305203

[113] Kawamura E, Lieberman M a, Lichtenberg a J, Chabert P and Lazzaroni C 2014 Particle-in-cell and global simulations of α to γ transition in atmospheric pressure Penning-dominated capacitive discharges *Plasma Sources Sci. Technol.* **23** 035014

[114] Kawamura E, Lieberman M A and Lichtenberg A J 2017 Ionization instability induced striations in atmospheric pressure He/H 2 O RF and DC discharges *J. Phys. D. Appl. Phys.* **50** 145204

[115] Tavant A and Lieberman M A 2016 Hybrid global model of water cluster ions in atmospheric pressure Ar/ H 2 O RF capacitive discharges *J. Phys. D. Appl. Phys.* **49** 465201

[116] Große-Kreul S, Hübner S, Benedikt J and von Keudell A 2016 Sampling of ions at atmospheric pressure: ion transmission and ion energy studied by simulation and experiment *Eur. Phys. J. D* **70** 103

[117] Große-Kreul S, Hübner S, Schneider S, von Keudell A and Benedikt J 2016 Methods of gas purification and effect on the ion composition in an RF atmospheric pressure plasma jet investigated by mass spectrometry *EPJ Tech. Instrum.* **3** 6

[118] Hodoroaba B, Gerber I C, Ciubotaru D, Mihaila I, Dobromir M, Pohoata V and Topala I 2018 Carbon “fluffy” aggregates produced by helium–hydrocarbon high-pressure plasmas as analogues to interstellar dust *Mon. Not. R. Astron. Soc.* **481** 2841–50

[119] Viehland L A and Kirkpatrick C C 1995 Relating ion/neutral reaction rate coefficients and cross-sections by accessing a database for ion transport properties *Int. J. Mass Spectrom. Ion Process.* **149-150** 555–71

[120] Bogaczyk M, Nemschokmichal S, Wild R, Stollenwerk L, Brandenburg R, Meichsner J and Wagner H-E 2012 Development of Barrier Discharges: Operation Modes and Structure Formation *Contrib. to Plasma Phys.* **52** 847–55

[121] http://www.pardiso-project.org/

[122] Massines F, Gherardi N, Naudé N and Ségur P 2005 Glow and Townsend dielectric barrier discharge in various atmosphere *Plasma Phys. Control. Fusion* **47** B577–88

[123] Lazarou C, Belmonte T, Chiper A S S and Georghiou G E E 2016 Numerical modelling

of the effect of dry air traces in a helium parallel plate dielectric barrier discharge *Plasma Sources Sci. Technol.* **25** 055023

[124] Gazeli K, Noël C, Clément F, Daugé C, Svarnas P and Belmonte T 2013 A study of helium atmospheric-pressure guided streamers for potential biological applications *Plasma Sources Sci. Technol.* **22** 025020

[125] Hensel K, Kučerová K, Tarabová B, Janda M, Machala Z, Sano K, Mihai C T, Ciorpac M, Gorgan L D, Jijie R, Pohoata V and Topala I 2015 Effects of air transient spark discharge and helium plasma jet on water, bacteria, cells, and biomolecules *Biointerphases* **10** 029515

[126] Svarnas P, Matrali S H, Gazeli K and Antimisiaris S G 2015 Assessment of Atmospheric-Pressure Guided Streamer (Plasma Bullet) Influence on Liposomes with Different Composition and Physicochemical Properties *Plasma Process. Polym.* **12** 655–65

[127] Lunov O, Zablotskii V, Churpita O, Jäger A, Polívka L, Syková E, Dejneka A and Kubinová Š 2016 The interplay between biological and physical scenarios of bacterial death induced by non-thermal plasma *Biomaterials* **82** 71–83

[128] Ehlbeck J, Schnabel U, Polak M, Winter J, von Woedtke T, Brandenburg R, von dem Hagen T and Weltmann K-D 2011 Low temperature atmospheric pressure plasma sources for microbial decontamination *J. Phys. D. Appl. Phys.* **44** 013002

[129] Shaw D, West A, Bredin J and Wagenaars E 2016 Mechanisms behind surface modification of polypropylene film using an atmospheric-pressure plasma jet *Plasma Sources Sci. Technol.* **25** 065018

[130] Abuzairi T, Okada M, Bhattacharjee S and Nagatsu M 2016 Surface conductivity dependent dynamic behaviour of an ultrafine atmospheric pressure plasma jet for microscale surface processing *Appl. Surf. Sci.* **390** 489–96

[131] Xian Y, Lu X, Wu S, Chu P K and Pan Y 2012 Are all atmospheric pressure cold plasma jets electrically driven? *Appl. Phys. Lett.* **100** 123702

[132] Guaitella O and Sobota A 2015 The impingement of a kHz helium atmospheric pressure plasma jet on a dielectric surface *J. Phys. D. Appl. Phys.* **48** 255202

[133] Brullé L, Vandamme M, Riès D, Martel E, Robert E, Lerondel S, Trichet V, Richard S, Pouvesle J-M and Le Pape A 2012 Effects of a Non Thermal Plasma Treatment Alone or in Combination with Gemcitabine in a MIA PaCa2-luc Orthotopic Pancreatic Carcinoma Model ed C J Eaves *PLoS One* **7** e52653

[134] Motrescu I and Nagatsu M 2016 Nanocapillary Atmospheric Pressure Plasma Jet: A Tool for Ultrafine Maskless Surface Modification at Atmospheric Pressure *ACS Appl. Mater. Interfaces* **8** 12528–33

[135] Klute F D, Michels A, Schütz A, Vadla C, Horvatic V and Franzke J 2016 Capillary

Dielectric Barrier Discharge: Transition from Soft Ionization to Dissociative Plasma *Anal. Chem.* **88** 4701–5

[136] Horvatic V, Michels A, Ahlmann N, Jestel G, Veza D, Vadla C and Franzke J 2015 Time- and spatially resolved emission spectroscopy of the dielectric barrier discharge for soft ionization sustained by a quasi-sinusoidal high voltage *Anal. Bioanal. Chem.* **407** 6689–96

[137] Horvatic V, Michels A, Ahlmann N, Jestel G, Veza D, Vadla C and Franzke J 2015 Time-resolved spectroscopy of a homogeneous dielectric barrier discharge for soft ionization driven by square wave high voltage *Anal. Bioanal. Chem.* **407** 7973–81

[138] Russell T W F, Robinson A S and Wagner N J Convective Heat and Mass Transfer *Mass and Heat Transfer* (Cambridge: Cambridge University Press) pp 246–300

[139] Tschiersch R, Nemschokmichal S, Bogaczyk M and Meichsner J 2017 Surface charge measurements on different dielectrics in diffuse and filamentary barrier discharges *J. Phys. D. Appl. Phys.* **50** 105207

[140] Teschke M, Kedzierski J, Finantu-Dinu E G, Korzec D and Engemann J 2005 High-speed photographs of a dielectric barrier atmospheric pressure plasma jet *IEEE Trans. Plasma Sci.* **33** 310–1

[141] Lu X and Laroussi M 2006 Dynamics of an atmospheric pressure plasma plume generated by submicrosecond voltage pulses *J. Appl. Phys.* **100** 063302

[142] Mericam-Bourdet N, Laroussi M, Begum A and Karakas E 2009 Experimental investigations of plasma bullets *J. Phys. D. Appl. Phys.* **42** 055207

[143] Topala I and Dumitrascu N 2011 Evolution of Bullets in Helium Atmospheric Pressure Plasma Jet *IEEE Trans. Plasma Sci.* **39** 2342–3

[144] Yao C-W, Chang Z-S, Ma H, Xu G, Mu H and Zhang G-J 2016 Experimental Research on Mode Transitions of Atmospheric Pressure Helium Dielectric Barrier Discharge *IEEE Trans. Plasma Sci.* **44** 2576–88

[145] Chiper A S and Popa G 2013 Temporally, spatially, and spectrally resolved barrier discharge produced in trapped helium gas at atmospheric pressure *J. Appl. Phys.* **113** 213302

[146] Kramida, A., Ralchenko, Yu., Reader J and N A T 2015 NIST Atomic Spectra Database (Version 5). National Institute of Standards and Technology, Gaithersburg, MD. http://physics.nist.gov/asd

[147] Hoder T, Brandenburg R, Basner R, Weltmann K-D, Kozlov K V and Wagner H-E 2010 A comparative study of three different types of barrier discharges in air at atmospheric pressure by cross-correlation spectroscopy *J. Phys. D. Appl. Phys.* **43** 124009

[148] Lu X, Laroussi M and Puech V 2012 On atmospheric-pressure non-equilibrium plasma jets and plasma bullets *Plasma Sources Sci. Technol.* **21** 034005

[149] Lu X, Naidis G V, Laroussi M and Ostrikov K 2014 Guided ionization waves: Theory and experiments *Phys. Rep.* **540** 123–66

[150] Xian Y, Yue Y, Liu D, Yang Y, Lu X and Pan Y 2014 On the Mechanism of Ring-Shape Structure of Plasma Bullet *Plasma Process. Polym.* **11** 1169–74

[151] Chang Z, Yao C, Mu H and Zhang G 2014 Study on the Property Evolution of Atmospheric Pressure Plasma Jets in Helium *Plasma Sci. Technol.* **16** 83–8

[152] Wu S, QuanJun Huang, Zhan Wang and XinPei Lu 2011 The Effect of Nitrogen Diffusion From Surrounding Air on Plasma Bullet Behavior *IEEE Trans. Plasma Sci.* **39** 2286–7

[153] Leiweke R J, Sands B L and Ganguly B N 2011 Effect of Gas Mixture on Plasma Jet Discharge Morphology *IEEE Trans. Plasma Sci.* **39** 2304–5

[154] Shashurin A and Keidar M 2015 Experimental approaches for studying non-equilibrium atmospheric plasma jets *Phys. Plasmas* **22** 122002

[155] Sakiyama Y, Graves D B, Jarrige J and Laroussi M 2010 Finite element analysis of ring-shaped emission profile in plasma bullet *Appl. Phys. Lett.* **96** 041501

[156] Belinger A, Naudé N and Gherardi N 2017 Transition from diffuse to self-organized discharge in a high frequency dielectric barrier discharge ed N Gherardi and T Hoder *Eur. Phys. J. Appl. Phys.* **79** 10802

[157] Schregel C-G, Carbone E A D, Luggenhölscher D and Czarnetzki U 2016 Ignition and afterglow dynamics of a high pressure nanosecond pulsed helium micro-discharge: I. Electron, Rydberg molecules and He (2 3 S) densities *Plasma Sources Sci. Technol.* **25** 054003

[158] Carbone E A D, Schregel C-G and Czarnetzki U 2016 Ignition and afterglow dynamics of a high pressure nanosecond pulsed helium micro-discharge: II. Rydberg molecules kinetics *Plasma Sources Sci. Technol.* **25** 054004

[159] Nemschokmichal S, Tschiersch R and Meichsner J 2016 The influence of negative ions in helium–oxygen barrier discharges: II. 1D fluid simulation and adaption to the experiment *Plasma Sources Sci. Technol.* **25** 055024

[160] Yan W, Liu F, Sang C and Wang D 2014 Two-dimensional modeling of the cathode sheath formation during the streamer-cathode interaction *Phys. Plasmas* **21** 013504

[161] Graves D B 2014 Low temperature plasma biomedicine: A tutorial review *Phys. Plasmas* **21** 080901

[162] Janev R K, Langer W D, Post D E and Evans K 1987 *Elementary Processes in Hydrogen-Helium Plasmas* (Berlin, Heidelberg: Springer Berlin Heidelberg)

[163] Deloche R, Monchicourt P, Cheret M and Lambert F 1976 High-pressure helium afterglow at room temperature *Phys. Rev. A* **13** 1140–76

[164] Stevefelt J 1982 Reaction kinetics of a high pressure helium fast discharge afterglow *J. Chem. Phys.* **76** 4006

[165] Konstantinovskii R S, Shibkov V M and Shibkova L V 2005 Effect of a Gas Discharge on the Ignition in the Hydrogen – Oxygen System **46** 821–34

[166] Wang Q, Economou D J and Donnelly V M 2006 Simulation of a direct current microplasma discharge in helium at atmospheric pressure *J. Appl. Phys.* **100** 023301

[167] Millar T J, Farquhar P R A and Willacy K 1997 The UMIST database for astrochemistry 1995 **185** 139–85

[168] Gordillo-Vázquez F J 2008 Air plasma kinetics under the influence of sprites *J. Phys. D. Appl. Phys.* **41** 234016

[169] Castillo M, Méndez I, Islyaikin A M, Herrero V J and Tanarro I 2005 Low-pressure DC air plasmas. investigation of neutral and ion chemistry. *J. Phys. Chem. A* **109** 6255–63

[170] Sommerer T J and Kushner M J 1992 Numerical investigation of the kinetics and chemistry of rf glow discharge plasmas sustained in He, N2, O2, He/N2/O2, He/CF4/O2, and SiH4/NH3 using a Monte Carlo-fluid hybrid model *J. Appl. Phys.* **71** 1654

[171] Tochikubo F, Uchida S, Yasui H and Sato K 2009 Numerical Simulation of NO Oxidation in Dielectric Barrier Discharge with Microdischarge Formation *Jpn. J. Appl. Phys.* **48** 076507

[172] Capitelli M, Ferreira C M, Gordiets B F and Osipov A I 2000 *Plasma Kinetics in Atmospheric Gases* vol 31 (Berlin, Heidelberg: Springer Berlin Heidelberg)

[173] Margot J, Petrov G M, Matte J P, Pe I, Sadi T, Hubert J, Tran K C, Alves L L, Loureiro J, Ferreira C M and Guerra V 2000 Numerical Modeling of a He – N 2 Capillary Surface ´ re **20**

[174] Atkinson R, Baulch D L, Cox R A, Hampson R F, Kerr J A, Rossi M J and Troe J 1997 Evaluated Kinetic, Photochemical and Heterogeneous Data for Atmospheric Chemistry: Supplement V. IUPAC Subcommittee on Gas Kinetic Data Evaluation for Atmospheric Chemistry *J. Phys. Chem. Ref. Data* **26** 521

[175] Good A 1975 Third-order ion-molecule clustering reactions *Chem. Rev.* **75** 561–83

[176] Cardoso R P, Belmonte T, Henrion G and Sadeghi N 2006 Influence of trace oxygen on He(2 3 S) density in a He–O 2 microwave discharge at atmospheric pressure: behaviour

of the time afterglow *J. Phys. D. Appl. Phys.* **39** 4178–85

[177] Kelly S and Turner M M 2013 Atomic oxygen patterning from a biomedical needle-plasma source *J. Appl. Phys.* **114** 123301

[178] Morgan database, www.lxcat.net, retrieved on August 3, 2016.

[179] Soloshenko I A, Tsiolko V V, Pogulay S S, Terent'yeva A G, Bazhenov V Y, Shchedrin A I, Ryabtsev A V and Kuzmichev A I 2007 The component content of active particles in a plasma-chemical reactor based on volume barrier discharge *Plasma Sources Sci. Technol.* **16** 56–66

[180] Park G Y, Hong Y J, Lee H W, Sim J Y and Lee J K 2010 A Global Model for the Identification of the Dominant Reactions for Atomic Oxygen in He/O 2 Atmospheric-Pressure Plasmas *Plasma Process. Polym.* **7** 281–7

[181] Niemi K, Waskoenig J, Sadeghi N, Gans T and O'Connell D 2011 The role of helium metastable states in radio-frequency driven helium–oxygen atmospheric pressure plasma jets: measurement and numerical simulation *Plasma Sources Sci. Technol.* **20** 055005

[182] Yousfi M and Benabdessadok M D 1996 Boltzmann equation analysis of electron-molecule collision cross sections in water vapor and ammonia *J. Appl. Phys.* **80** 6619

[183] Itikawa database, www.lxcat.net, retrieved on August 3, 2016.

[184] Riahi R, Teulet P, Ben Lakhdar Z and Gleizes A 2006 Cross-section and rate coefficient calculation for electron impact excitation, ionisation and dissociation of H2 and OH molecules *Eur. Phys. J. D* **40** 223–30

[185] Axford S D T and Hayhurst A N 1996 Mass Spectrometric Sampling of Negative Ions from Flames of Hydrogen and Oxygen: The Kinetics of Electron Attachment and Detachment in Hot Mixtures of HFormulaO, OFormula, OH and HOFormula *Proc. R. Soc. A Math. Phys. Eng. Sci.* **452** 1007–33

[186] Nandi D, Krishnakumar E, Rosa A, Schmidt W-F and Illenberger E 2003 Dissociative electron attachment to H2O2: a very effective source for OH and OH− generation *Chem. Phys. Lett.* **373** 454–9

[187] Bortner M H and Baurer T 1979 *Defense Nuclear Agency Reaction Rate Handbook* (Section 24 Revision No. 7, March 1978, NTIS AD-7636 99, 1979)

[188] Huang C-M, Whitaker M, Biondi M A and Johnsen R 1978 Electron-temperature dependence of recombination of electrons with H3O+·(H2O)n-series ions *Phys. Rev. A* **18** 64–7

[189] Brian J 1990 The dissociative recombination of molecular ions *Phys. Rep.* **186** 215–48

[190] Dunkin D B 1970 Rate Constants for the Thermal Energy Reactions of H−. with O2, NO,

CO, and N2O *J. Chem. Phys.* **53** 987

[191] Sanders R A and Muschlitz E E 1977 Chemiionization and secondary ion reactions in H2O and D2O *Int. J. Mass Spectrom. Ion Phys.* **23** 99–108

[192] Binns W R and Ahl J L 1978 Excitation and quenching reactions in E-beam excited He/H2O and He/CH3CN systems *J. Chem. Phys.* **68** 538

[193] Hamden M 1989 Gas Phase Ion-Molecule Reaction Rate Constants Through 1986. Yasumasa Ikezoe, Shingo Matsuoka, Masahiro Takebe and Albert Viggiano (eds). Maruzen Company Ltd, Tokyo. 1987. (viii) + 244 pp. US$ 150.00 *Rapid Commun. Mass Spectrom.* **3** iii – iii

[194] Vidmar R J and Stalder K R 2004 *AFOSR Final Performance Report. Computations of the power to sustain plasma in air with relevance to aerospace technology. Final report prepared for Air Force Office of Scientific Research* (No: AFRISRARRE040123. Contact No. F49620-01-0414)

[195] Sieck L W, Heron J T and Green D S 2000 Chemical Kinetics Database and Predictive Schemes for Humid Air Plasma Chemistry. Part I: Positive Ion–Molecule Reactions *Plasma Chem. Plasma Process.* **20** 235–58

[196] Ferguson E E 1973 Rate constants of thermal energy binary ion-molecule reactions of aeronomic interest *At. Data Nucl. Data Tables* **12** 159–78

[197] Eichwald O, Yousfi M, Hennad A and Benabdessadok M D 1997 Coupling of chemical kinetics, gas dynamics, and charged particle kinetics models for the analysis of NO reduction from flue gases *J. Appl. Phys.* **82** 4781

[198] Jianli Z, Juncheng Z, Ji S, Hongchen G, Xiangsheng W and Weimin G 2009 Scale-Up Synthesis of Hydrogen Peroxide from H 2 /O 2 with Multiple Parallel DBD Tubes *Plasma Sci. Technol.* **11** 181–6

[199] Fritzenwallner J and Kopp E 1998 Model calculations of the negative ion chemistry in the mesosphere with special emphasis on the chlorine species and the formation of cluster ions *Adv. Sp. Res.* **21** 891–4

[200] Kushner M J 1999 Strategies for Rapidly Developing Plasma Chemistry Models *Bull. Am. Phys. Soc.* **44** 63

[201] Park G, Lee H, Kim G and Lee J K 2008 Global Model of He/O 2 and Ar/O 2 Atmospheric Pressure Glow Discharges *Plasma Process. Polym.* **5** 569–76

[202] Takao S, Kogoma M, Oka T, Imamura M and Arai S 1980 Optical absorption spectra and kinetic behavior of helium excited diatomic molecule (a 3Σu+) *J. Chem. Phys.* **73** 148

[203] Ricard A, Décomps P and Massines F 1999 Kinetics of radiative species in helium pulsed discharge at atmospheric pressure *Surf. Coatings Technol.* **112** 1–4

[204] GRI-MECH 3 Reaction Rate Database. http://www.me.berkeley.edu/gri-mech/

[205] Tsang W and Hampson R F 1986 Chemical Kinetic Data Base for Combustion Chemistry. Part I. Methane and Related Compounds *J. Phys. Chem. Ref. Data* **15** 1087

[206] NIST chemical kinetic database. http://kinetics.nist.gov/kinetics/index.jsp

[207] Dunlea E J, Talukdar R K and Ravishankara A R 2005 Kinetic Studies of the Reactions of O 2 (b 1 Σ g +) with Several Atmospheric Molecules *J. Phys. Chem. A* **109** 3912–20

[208] Koike T and Morinaga K 1982 Further studies of the rate constant for chemical excitation of OH in shock waves. *Bull. Chem. Soc. Jpn.* **55** 52–4

[209] Deng L, Shi W, Yang H, Sha G and Zhang C 2004 Improved method for measuring absolute O2(a1Δg) concentration by O2(a1Δg→X3Σ−g) IR radiation *Rev. Sci. Instrum.* **75** 4455